TESIS DE LA UNIVERSIDAD
DE ZARAGOZA

2021

358

Giovanni Arico

Cosmology with baryons: modelling the cosmic matter distribution for Large-Scale Structure analyses.

Director/es

Dr. D. Raúl E. Ángulo De La Fuente
Dr. D. Carlos Hernández-Monteagudo

ISSN 2254-7606

Prensas de la Universidad
Universidad Zaragoza

Servicio de Publicaciones

ISSN 2254-7606

Universidad
Zaragoza
1542

Tesis Doctoral

COSMOLOGY WITH BARYONS: MODELLING THE COSMIC MATTER DISTRIBUTION FOR LARGE-SCALE STRUCTURE ANALYSES.

Autor

Giovanni Arico

Director/es

Dr. D. Raúl E. Ángulo De La Fuente
Dr. D. Carlos Hernández-Monteagudo

UNIVERSIDAD DE ZARAGOZA
Escuela de Doctorado

2021

Universidad Zaragoza

Facultad de Física
Departamento de Física Teorica

Cosmology with baryons: modelling the cosmic matter distribution for Large-Scale Structure analyses

PhD thesis

Candidate:

Giovanni Aricò

Supervisors:

Prof. Dr. Raul E. Angulo
Prof. Dr. Carlos Hernández-Monteagudo

July 27, 2021

DIPC

Universidad Zaragoza
1542

CEFCA
Centro de Estudios de Física del Cosmos de Aragón

Abstract

The interplay between gravitational and hydrodynamical forces in shaping the structure of the Universe is complex and still largely unknown. Gravitational forces are dominant on large scales, where the density perturbations are small and thus describable by linear-order solutions of the Boltzmann equations. However, on small scales, non-linearities arise, and therefore analytical approaches break down. The gas is furthermore perturbed by hydrodynamical forces, and several astrophysical processes take place. Galaxy formation triggers supernovae explosions and energy injection from accreting supermassive black holes, perturbing the mass distribution and reshaping the gravitational potential, causing subsequently a back-reaction on the collision-less dark matter. The lack of accurate modelling of such baryonic processes is one of the main sources of uncertainties in Large Scale Structure analyses, and its impact is expected to dramatically increase in the next observational campaigns planned.

In this thesis, we develop a framework to consistently model the spatial distribution and time evolution of dark matter, gas, and galaxies, in the Large Scale Structure of the universe. The core of our framework is given by large, high-resolution N-body simulations, which ensure robust modelling of non-linearities on small scales, and accurate predictions on large scales. In a post-processing phase, we displace the particles in our simulations to explore different cosmological and baryonic scenarios, by combining two state-of-the-art algorithms: cosmology-rescaling and baryon correction model. We implement extended and optimised versions of these algorithms, to reach the accuracy required by next-generation surveys, and we systematically test them, both separately and jointly. Finally, we use modern machine learning techniques, and specifically artificial neural networks, trained to learn the connections between cosmological and astrophysical parameters and relevant summary statistics of the cosmic matter field, as measured in our simulations. In this way, our predictions can be delivered at a negligible computational cost, and the linear, nonlinear and baryonic contributions can be computed separately. Our neural network emulators are publicly available and can be easily incorporated into a weak lensing pipeline. By using our framework, the modelling of the cosmic matter field can be extended to unprecedentedly small scales, in a highly accurate and flexible fashion, and additionally with a consistent speeding-up in the computational time. We expect that the techniques developed and the results presented here will be useful for a broad range of applications in Large Scale Structure analyses, and in particular in the exploitation of weak lensing and galaxy surveys.

Resumen

La interacción entre las fuerzas gravitatorias e hidrodinámicas en la formación de la estructura del Universo es compleja y aún se desconoce en gran medida. Las fuerzas gravitatorias son dominantes a gran escala, donde las perturbaciones de la densidad son pequeñas y, por tanto, se pueden describir mediante una teoría lineal. Sin embargo, en las escalas pequeñas surgen no linealidades y, por lo tanto, la teoría analítica no es suficiente. El gas es perturbado tanto por las fuerzas hidrodinámicas como por la gravedad, y tienen lugar varios procesos astrofísicos. La formación de galaxias desencadena explosiones de supernovas y la inyección de energía de los agujeros negros supermasivos que se acrecientan, perturbando la distribución de la masa y remodelando el potencial gravitatorio, lo que provoca posteriormente una reacción inversa en la materia oscura.

La falta de una modelización precisa de estos procesos bariónicos es una de las principales fuentes de incertidumbre en los actuales estudios de lentes gravitatorias débiles, y se espera que su impacto aumente drásticamente en las próximas campañas de observación previstas.

En esta tesis, queremos desarrollar un marco para modelar de forma consistente la distribución espacial y la evolución temporal de la materia oscura, el gas y las galaxias, en la Estructura a Gran Escala del Universo. Utilizamos un enfoque basado en simulaciones, variando simultáneamente la cosmología y los procesos astrofísicos. El núcleo de nuestro marco está dado por grandes simulaciones de alta resolución, que garantizan una modelización robusta de las no linealidades a pequeñas escalas, y predicciones precisas a grandes escalas. En una fase de posprocesamiento, desplazamos las partículas en nuestras simulaciones para explorar diferentes escenarios cosmológicos y bariónicos, mediante la combinación de dos algoritmos de última generación: el modelo de escalado cosmológico y el de corrección bariónica. Implementamos versiones extendidas y optimizadas de ambos algoritmos, para alcanzar la precisión requerida por los estudios de próxima generación, y los probamos sistemáticamente por separado y en combinación. Por último, utilizamos técnicas modernas de aprendizaje automático, y en concreto redes neuronales artificiales, entrenadas para aprender las conexiones entre los parámetros cosmológicos y astrofísicos y las estadísticas relevantes del campo de materia cósmica, tal y como se miden en nuestras simulaciones. De este modo, nuestras predicciones pueden realizarse con un coste computacional insignificante, y la contribución lineal, no lineal y bariónica puede calcularse por separado. Nuestros emuladores de redes neuronales están disponibles públicamente y pueden incorporarse fácilmente a una analisis de lentes gravitatorias débiles. Utilizando nuestro marco de trabajo,

la modelización de la densidad cosmica puede extenderse a escalas pequeñas sin precedentes, de forma muy precisa y con una aceleración consistente en el tiempo de cálculo. Esperamos que las técnicas desarrolladas y los resultados presentados aquí sean útiles para una amplia gama de aplicaciones en los análisis de estructuras a gran escala, y en particular en studios de lentes gravitatorias débiles y galaxias.

Acronyms

ΛCDM Λ Cold Dark Matter. 1, 2, 137, 143

AGN Active Galactic Nuceli. 47, 48, 52, 54–56, 67, 70, 77, 141, 148, 188

AIC Akaike Information Creterion. 129, 132–134, 140, 147

BAO Baryonic Acoustic Oscillations. 140, 147

BCM Baryon Correction Model. XI–XIII, XV, 4, 49–51, 53–59, 61–63, 65, 67–70, 72–74, 76, 79, 81–83, 98–100, 103, 107, 108, 119, 137, 138, 141, 144, 148, 187, 188, 193

CDM Cold Dark Matter. 2

CMB Cosmic Microwave Background. 1, 2, 23, 24, 34

DES Dark Energy Survey. 3

EoS Equation of State. 2, 3

EPT Eulerian Perturbation Theory. 3

GrO Gravity Only. XI, 48–50, 52, 53, 55, 56, 58, 59, 61–65, 91, 99, 119, 188, 201

HSC Subaru Hyper Suprime-Cam Lensing Survey. 3

KiDS Kilo-Degree Survey. 3

LPT Lagrangian Perturbation Theory. 3

LSS Lage Scale Structure. 2, 3, 5, 141, 142

LSST Legacy Survey of Space and Time. 2, 3, 140, 147

MCMC Monte Carlo Markov Chain. 5, 139, 145

NFW Navarro-Frenk-White. 55, 58, 63, 91, 187, 188

PSF Point Spread Function. 3

SHAM Sub-Halo Abundance Matching. 141, 148

Index

List of Figures

List of Tables

Introduction

From ancient times, humans have speculated on the nature of the Universe and its origins. For millennia, our representation of the Universe was shaped by myths and legends, inspired by the natural events that were observed. In the last century, cosmology has finally turned into a quantitative science.

0.1 Cosmological context

The development of special and general relativity, the discovery of the expansion of the Universe, and the Cosmic Microwave Background (CMB), have provided a strong theoretical and observational ground for the hot Big Bang model. In the last decades, cosmology has entered its precision era. The exquisite observations made by satellites and large ground telescopes, the progress of theoretical models, and the increasing power of computers have allowed the transition from s of magnitudes to percent errors. The inflationary theory, first proposed by Alan Guth in 1979, solved some of the long-standing theoretical problems in cosmology (Guth, 1981). The discovery of the anisotropy in the CMB, and the following experiments to measure them (COBE, WMAP, Planck), have provided us a precise estimation of the energy content and geometry of the Universe (Mather et al., 1994; Komatsu et al., 2011; Planck Collaboration et al., 2018). Moreover, from the light of distant supernovae, it was discovered the late acceleration in the expansion of the Universe (Riess et al., 1998). All these probes led to the establishment of the current standard cosmological model, the geometrically-flat Λ Cold Dark Matter (ΛCDM). In the standard model, the common baryonic matter makes up only 20% of the total matter in the Universe, being the rest unknown "cold dark matter". The energy budget today is dominated by an unknown source of energy, the "dark energy", which is driving the actual acceleration of the Universe. Even if the Universe expands, the dark energy density stays constant: from here the name "cosmological constant", Λ, was introduced by Einstein a century ago.

Despite being able to accurately reproduce a very large set of different observations, from the power spectrum of the CMB to the galaxy distribution today, ΛCDM lacks a solid theoretical justification. If we assume Λ to be the zero-point energy of the quantum vacuum, its observed energy differs from the theoretically expected one by $\sim$120 s of magnitude.

We do not know the physical nature of the Cold Dark Matter (CDM) and we lack empirical evidence for inflation. Moreover, the latest and most accurate observations highlight a tension between cosmological parameters inferred at high redshifts, with CMB experiments, and low redshifts Lage Scale Structure (LSS) surveys (see e.g. Verde et al., 2019; Perivolaropoulos and Skara, 2021). These tensions could reflect an improper account of systematic errors, which become increasingly important given the accuracy of the experiments, but could also be the hint of an unknown underlying physics, e.g. a breakdown of general relativity, new fundamental particles, scalar fields, etc. Several models beyond ΛCDM have been explored. One of the most explored extensions of the ΛCDM includes massive neutrinos. This scenario is robustly supported by experiments detecting the solar neutrinos oscillations in lepton flavor. Considering massive neutrinos affects the expansion and the growth of Structures in the Universe, but does not solve the aforementioned tensions. Another popular generalisation of the ΛCDM is obtained by allowing the EoS of dark energy to evolve with cosmic time, i.e. dropping the cosmological constant paradigm. Other models have been proposed, for instance "modified-gravity" $f(R)$ models, where a generic dependence on the Ricci scalar (R) is introduced in the Einstein-Hilbert action yielding Einstein's field equations for gravity, or models where it is considered an interaction between dark matter and dark energy.

0.2 On LSS surveys

Current data do not allow to distinguish between the different cosmological models proposed, and it is not clear if by refining the precision and robustness of future experiments the current tension between the parameters will increase (pointing therefore to a model break-down) or be alleviated (suggesting some data systematics issues). The next generation "stage IV" LSS surveys will have potentially a constraining power close to CMB experiments. Additionally, LSS observations are intrinsically more sensitive to dark energy, which kick-in at late times, comparing to the CMB. Stage IV surveys, e.g. Euclid and Legacy Survey of Space and Time (LSST), should constrain the dark energy EoS at 1% level (Amendola et al., 2018; LSST Science Collaboration et al., 2009).

The full exploitation of the data from the forthcoming observational campaigns poses serious theoretical and computational challenges. The sheer amount of expected data is striking, being in some cases tens of Terabytes collected per night, with all the difficulties of transfer, storage, and analysis that this implies. The handling of systematic errors will be critical, given the expected precision of these surveys.

Among them, weak lensing surveys are particularly complex to model. These surveys measure the cosmic shear, that is the spatial correlation of the shapes of distant, background galaxies, caused by the foreground LSS gravitational field which acts as a lens (see e.g.

Hoekstra and Jain, 2008; Mandelbaum, 2018, for a review). Cosmic shear is sensitive to the total cosmic matter interposed between the source galaxies and the observer, measuring directly the projected matter power spectrum, convolved by a geometrical lensing kernel. In this way, it is possible to probe the growth of structure in the Universe, as well as dark matter and dark energy.

Unfortunately, the signal is very small (about 1%), and the extraction of the cosmological information is complicated by the need of modelling the Point Spread Function (PSF), ellipticities, photometric redshifts, and intrinsic alignment of galaxies.

The poor knowledge of the baryonic physics in the LSS is arguably the main source of uncertainty of the ongoing weak lensing surveys, and it is expected to have even a more dramatic impact in upcoming stage IV surveys, e.g. Euclid (Laureijs et al., 2011), the Nancy Grace Roman Space Telescope (Spergel et al., 2015), and the Vera Rubin Observatory LSST (Ivezić et al., 2019). Present-day Stage III surveys such as Dark Energy Survey (DES) (Troxel et al., 2018), Kilo-Degree Survey (KiDS) (Asgari et al., 2020a), and the Subaru Hyper Suprime-Cam Lensing Survey (HSC) (Hikage et al., 2019), by directly probing the evolution of the cosmic matter distribution are already providing competitive constraints on the total cosmic matter content, the growth of structures in the Universe, and the dark energy EoS. Nevertheless, much of the information encoded in the data is currently not used. In fact, the analyses must be limited to large scales, where the baryonic contribution is expected to be negligible, because of the lack of reliable modelling on small scales.

Last but not least, the huge volumes covered by the next surveys, combined with the high resolution of the observations, require theoretical modelling of the statistical signal over an unprecedented dynamical range. This implies the need to model simultaneously several physical processes on very different scales.

0.3 About this thesis

The aim of this thesis is to develop a framework that models the relevant physical processes at the level of precision required for stage IV weak-lensing surveys. In practice, we are interested in knowing how the matter density field, including dark matter, gas, and galaxies, evolves as a function of scale and redshift.

Analytical models, such as Lagrangian and Eulerian Perturbation Theory (LPT and EPT), can deliver accurate predictions of the matter density field at large scales. However, on small scales, where over-densities are large, perturbation theory breaks down due to non-linearities. Moreover, on relatively small scales, hydrodynamical interactions and astrophysical processes cannot be neglected. Additionally, a poorly understood bias function links the galaxy distribution to the underlying matter field.

Currently, numerical simulations are the most accurate method to study the evolution of the cosmic matter density field. Gravity-only N-body simulations deliver accurate predictions of matter and halo distributions across a wide dynamical range of scales, taking advantage of the power of modern supercomputers and the high parallelisation of recent algorithms. Different algorithms have been shown to converge at 1% level (Schneider et al., 2016; Angulo et al., 2020), and the simulated volumes approach the ones of forthcoming surveys. Nevertheless, the computational cost of these simulations does not allow direct use in cosmological analysis, where a fast exploration of the parameter space is required.

Magneto-hydrodynamical simulations attempt to evolve simultaneously the gravity and hydrodynamical forces evolution, included various astrophysical processes. Due to their complexity, these kinds of simulations are computationally more expensive than the gravity-only ones. This means that these simulations have typically smaller volumes, which are statistically not representative of the next-generation surveys. Moreover, relevant astrophysical processes at small scales cannot be resolved, and consequently are“manually” added as sub-grid processes using *ad-hoc* analytical prescriptions. Different implementations of sub-grid physics may cause a substantial discrepancy between the predictions of different codes.

The approach followed in this thesis has been developed within the `bacco` simulation project[2] (Angulo et al., 2020). This project seeks to provide highly accurate predictions of dark matter, gas, and galaxy distributions as a function of cosmological parameters, by running only a few high-resolution gravity-only simulations. In this framework, the cosmological space is explored with the aid of “cosmology-rescaling” algorithms (Angulo and White, 2010). These algorithms look for the transformation in time and space which minimises the variance of the amplitude of linear fluctuations between the original cosmology of a simulation and a desired target one. Then, the output of the simulation is manipulated, and by rescaling the box length at the appropriate time (snapshot), the final density field will be remarkably close to the one expected if the simulation was run within the target cosmology. Keeping the nonlinear properties of the original simulation, this method can potentially reduce the computational cost of a target simulation from millions of CPU hours to CPU minutes.

The central part of the thesis is devoted to adding in post-processing baryons to gravity-only simulations. This is accomplished by designing a Baryon Correction Model (BCM), a.k.a. *baryonification* algorithm (Schneider and Teyssier, 2015a; Schneider et al., 2019; Aricò et al., 2020b, 2021a), which displaces the particles inside the simulations to mimic the dynamical effects of different baryonic components. In this way, it is possible to model the gas accretion and ejection, and the condensation of gas in central and satellite

---

[2] `http://www.dipc.org/bacco/`

galaxies, in an accurate and fast fashion. Also, the back-reaction on the dark matter caused by the baryonic gravitational potential is estimated and taken into account.

This approach has several advantages: it has only a few physically-motivated free parameters, and the non-linearities are fully accounted due to the underlying N-body simulation. Moreover, the free parameters can be constrained by using both observations and hydrodynamical simulations. On the other hand, it is more flexible and not as computational expensive comparing to hydrodynamical simulations.

Both the cosmology scaling and baryonification algorithm have been highly optimised, so that a full simulation with an arbitrary cosmology and baryonic physics can be obtained in a time scale of few seconds - few minutes, depending on the size of the original N-body simulation used. Nevertheless, the direct use of these simulations for parameter inference would be computationally prohibiting. In fact, typically a Monte Carlo Markov Chain (MCMC) analysis requires an order of 10^5 evaluations to be carried out. To overcome this problem, we build emulators of the relevant summary statistics. Emulators are multidimensional interpolators of a computationally expensive function, originally proposed in cosmology by Heitmann et al. (2014). In our case, we tried both Gaussian Processes and artificial neural networks, finding the latter ones more suited for large training sets. Thus, we train our machine on different power spectra, including the linear, the non-linear, and one featuring baryonic effects. Using these emulators, we can provide highly accurate predictions of e.g. the cosmic shear correlation function, allowing the modelling of scales usually inaccessible, and speeding up the cosmological analysis by a factor of 100 with respect to traditional methodologies.

Each of the chapters of this thesis is adapted from a different paper, thus it is self-contained and could in principle be read independently from the others. The outline is the following:

- In §1 (adapted from Aricò et al., 2021b), we describe how we compute the linear and perturbation theory for LSS, and how we speed the calculations up using neural network emulators;

- In §2 (adapted from Angulo et al., 2020), we introduce the simulations employed, and the rescaling algorithm used to explore different cosmological scenarios. Finally, we describe the non-linear boost emulator built by rescaling the cosmologies of our simulations;

- In §3 (adapted from Aricò et al., 2020b), we describe the implementation of the baryonification algorithm, and test its accuracy in the power spectrum against full hydrodynamical simulations. We also quantify the cosmological information contained in the matter power spectrum at different scales, and the possible loss of information due to uncertainties in baryonic physics;

- In §4 (adapted from Aricò et al., 2021a), we extend the baryonification algorithm to include satellite galaxies and re-accreted gas. We test this implementation against hydrodynamical simulations, going to higher-order statistics, considering both the matter power spectrum and bispectrum;
- In §5 (adapted from Aricò et al., 2020a), we combine the cosmology rescaling with the baryonification to build a neural network emulator of the baryonic boost factor, which depends from both cosmology and astrophysics. We apply the emulator to test the cosmological dependencies of astrophysical processes, and to look for a minimal parametrisation of the baryonic physics;
- We summarise and give our conclusions in §5.6.

Chapter 1

Accelerating Boltzmann solvers and perturbation theory with emulators

The linear matter power spectrum is an essential ingredient in all theoretical models for interpreting large-scale-structure observables. Although Boltzmann codes such as `CLASS` or `CAMB` are very efficient at computing the linear spectrum, the analysis of data usually requires 10^4-10^6 evaluations, which means this task can be the most computationally expensive aspect of data analysis. In this chapter, adapted from "Accelerating Large-Scale-Structure data analyses by emulating Boltzmann solvers and Lagrangian Perturbation Theory" (Aricò et al., 2021b), we address this problem by building a neural network emulator that provides the linear theory matter power spectrum in about one millisecond with 0.3% accuracy over $10^{-3} \leq k[h\,\mathrm{Mpc}^{-1}] < 30$. We train this emulator with more than 150,000 measurements, spanning a broad cosmological parameter space that includes massive neutrinos and dynamical dark energy. We show that the parameter range and accuracy of our emulator is enough to get unbiased cosmological constraints in the analysis of a *Euclid*-like weak lensing survey. Complementing this emulator, we train 15 other emulators for the cross-spectra of various linear fields in Eulerian space, as predicted by 2nd-order Lagrangian Perturbation theory, which can be used to accelerate perturbative bias descriptions of galaxy clustering. Our emulators are especially designed to be used in combination with emulators for the nonlinear matter power spectrum and for baryonic effects, all of which are publicly available at `http://www.dipc.org/bacco`.

1.1 Introduction

The optimal exploitation of Large Scale Structure (LSS) data is one of the most important challenges in modern cosmology. For this, multiple theoretical models have been developed based on perturbation theory, the halo model, excursion set theory, or N-body simulations. Regardless of the nature of the modelling, essentially all approaches rely on predictions of the linear matter power spectrum as a function of cosmological parameters.

The linear matter power spectrum can be accurately computed by taking moments of the Bolztmann equation describing the co-evolution of all species (neutrinos, cold dark matter, radiation, etc.) in the Universe. This truncated Bolztmann hierarchy can be solved very efficiently by publicly available codes such as `CMBFast` (Seljak and Zaldarriaga, 1996), `CAMB` (Lewis et al., 2000), and `CLASS` (Lesgourgues, 2011a), which can provide the matter power spectrum in 1-10 seconds of computing, depending on the desired accuracy.

Estimating cosmological parameters from LSS observations typically requires 10^4 - 10^6 evaluations of the relevant theoretical model. Thus, the computational cost of estimating the linear power spectrum can reach thousands of CPU hours. Traditionally, this has not been an issue because other aspects of the modelling (e.g. the calculation of loops in perturbation theory) were significantly more expensive. This situation, however, in changing with the use of *emulators*.

Emulators are a mathematical tool that allow for an efficient multidimensional interpolation of a given function. Popular choices in the field of LSS are Gaussian Processes (e.g. Heitmann et al., 2014; McClintock and Rozo, 2019; Bocquet et al., 2020), polynomial chaos expansions (e.g. Knabenhans et al., 2019; Euclid Collaboration et al., 2020) and neural networks (e.g. Kobayashi et al., 2020; Aricò et al., 2020a; Zennaro et al., 2021). In all cases, a small number of (computationally expensive) predictions at different locations of a parameter space are used to build the emulator which can then be evaluated in any other point of the parameter space.

Multiple emulators have been built for LSS summary statistics (usually based on the results of N-body simulations), which include the nonlinear matter power spectrum, halo mass function, halo bias, and the effect of baryons (e.g. Heitmann et al., 2014; Knabenhans et al., 2019; Winther et al., 2019; McClintock et al., 2019; Zhai et al., 2019; Bird et al., 2019; Bocquet et al., 2020; Schneider et al., 2020; Angulo et al., 2020; Euclid Collaboration et al., 2020; Aricò et al., 2020a; Zennaro et al., 2021).

Regardless the technique, the emulated quantity is usually the ratio with respect to the linear theory expectation (e.g. the nonlinear over the linear power spectrum). This reduces the dynamical range of the function and removes some of the cosmology-dependence, allowing a more robust and accurate emulation. Since the evaluation of an emulator takes a negligible amount of CPU time, the calculation of the linear power spectrum becomes the bottleneck of the analysis. A possible way to tackle this is to reduce the number of evaluations needed in parameter constraints. Specifically, one technique proposed by several authors is to directly emulate the likelihood function (e.g. McClintock and Rozo, 2019; Leclercq, 2018; Pellejero-Ibañez et al., 2020).

Even for efficient parameter samplers, reducing the computational cost of Boltzmann solvers at fixed precision would be of great benefit. This would allow a more accurate determination of the respective likelihood functions and a faster exploration of different models and data. An option for speeding up these calculations was proposed by Albers et al. (2019) who trained a neural network to replace the most time consuming parts of the code `CLASS` . Another alternative is to directly build an emulator for the linear power spectrum. This has been attempted by `PICO` (Fendt and Wandelt, 2007) using a fifth-order polynomial expansion to interpolate between pre-computed CMB temperature power spectra, and by `CosmoNET` (Auld et al., 2007, 2008) using neural networks to emulate CMB fluctuations and the matter power spectrum. Having been developed over a decade ago, these works were limited by the size of their training sets which contained of the order of 1,000 measurements and by the computational cost of the training itself.

Here we take advantage of all the recent development in neural networks and computer architecture to develop a new emulator for the linear matter power spectrum with a focus on the analysis of forthcoming LSS experiments. Our emulator covers a 8-dimensional ΛCDM parameter space including massive neutrinos and dynamical dark energy: σ_8, Ω_c, Ω_b, n_s, h, M_ν, w_0 and w_a, where we reach about 0.3% precision for $10^{-3} \leq k[h\,\mathrm{Mpc}^{-1}] < 30$ in a region around the parameter values preferred by current data analyses. The accuracy somewhat degrades to 1% when going to extreme cosmological models. Additionally, we build an emulator for the 15 different cross-spectra that enter a 2nd order Lagrangian bias expansion of galaxy clustering, which we compute using 2nd-order Lagrangian perturbation theory.

Our neural networks provide predictions in about one millisecond on a single CPU core and have negligible memory requirements. Furthermore, they are designed to be employed together with our emulators for the nonlinear matter power spectrum (Angulo et al., 2020), baryonic effects (Aricò et al., 2020a), and galaxy bias expansion (Zennaro et al., 2021). All these emulators are part of the `baccoemu` project, and they are publicly available[1] and updated continuously to improve their accuracy.

The outline of this paper is the following: in §1.2 we present our linear matter power spectrum and quantify its accuracy; in §1.3 we introduce our Lagrangian Perturbation Theory spectra emulators; in §1.4 we employ the linear matter power spectrum emulator to show that it provides unbiased results for the analysis of a mock *stage-IV* cosmic shear survey; we provide our conclusions in §1.5.

---

[1] `http://www.dipc.org/bacco`

Cosmology	σ_8	Ω_c	Ω_b	n_s	h	M_ν [eV]	w_0	w_a
Standard	[0.73, 0.9]	[0.23, 0.4]	[0.04, 0.06]	[0.92, 1.01]	[0.6, 0.8]	[0.0, 0.4]	[-1.15, -0.85]	[-0.3, 0.3]
Extended	[0.6, 1.]	[0.15, 0.6]	[0.03, 0.07]	[0.9, 1.1]	[0.5, 0.9]	[0.0, 0.5]	[-1.3, -0.7]	[-0.5, 0.5]

Table 1.1: The range of cosmological parameter values defining the two hyperspaces over which we train our neural network emulator. σ_8 is the *cold* mass linear mass variance in $8\,h^{-1}\mathrm{Mpc}$ spheres; Ω_c and Ω_b are the density of cold matter and baryons in units of the critical density of the Universe; n_s is the primordial spectral index; h is the dimensionless Hubble parameter $h = H_0/(100\,\mathrm{km\,s^{-1}Mpc^{-1}})$; M_ν is the sum of neutrinos masses in eV; and w_0 and w_a are parameters describing the time-evolving dark energy equation of state via $w(z) = w_0 + (1-a)\,w_\mathrm{a}$.

1.2 Linear matter power spectrum emulator

In this section, we describe our emulator for the linear cold matter power spectrum. We start by defining our parameter space (§1.2.1), then we describe our training and validation sets (§1.2.2), as well as our neural network setup (§1.2.3). We finish by validating our predictions for the growth function, baryonic acoustic oscillations, and the neutrino-induced suppression on the power spectrum (§1.2.4).

1.2.1 Parameter space

We consider 8 cosmological parameters: the *cold* mass linear variance in $8\,h^{-1}\mathrm{Mpc}$ spheres, σ_8; the density of cold matter and baryons in units of the critical density of the universe, Ω_c and Ω_b; the primordial spectral index, n_s; the dimensionless Hubble parameter, $h \equiv H_0/(100\,\mathrm{km\,s^{-1}Mpc^{-1}})$; the sum of neutrinos masses in units of eV, M_ν; and a time-evolving dark energy equation of state defined through a CPL parameterisation (Chevallier and Polarski, 2001; Linder, 2003), $w(z) = w_0 + (1-a)\,w_\mathrm{a}$.

We define two separate cosmological hyperspaces. The first one, hereafter dubbed as *standard*, spans values roughly 10σ around Planck best-fitting parameters (Planck Collaboration et al., 2018). We note that this hyper-volume is identical to that adopted in the nonlinear, baryonic, and bias emulators of Angulo et al. (2020); Aricò et al. (2020a); Zennaro et al. (2021), respectively. The second cosmological parameter space, dubbed as *extended*, is defined by parameter ranges roughly twice as large, with which we aim at expanding the possible usage of the emulator to different kind of analyses and applications. For both cases, we consider a redshift range $z \in [0, 3]$. The cosmological parameters and the respective ranges of both hyperspaces are provided in Table 1.1.

1.2.2 Training and validation sets

We define our training set by evenly sampling the parameter space with a Latin-Hypercube (LH) algorithm, a statistical method which maximise the distance between the sampling points. Specifically, our neural networks will be trained with the co-addition of various LH samples. The first one is a 20,000-point LH defined in the *standard* cosmological space. The second one is a LH of 100,000 points, defined in the *extended* cosmological space. We note that the *standard* space is more densely sampled, and thus we expect our emulator to be more accurate in this region.

As a validation set, we build a 2,000-point LH defined in the *standard* hyper-space. To this, we add 10,000 points distributed according to a LH in the region of the *extended* space not included in the *standard* space, hereafter dubbed *outer* space.

We build 4 additional LHs, of 10,000-points each, defined on the $M_\nu = 0$ and on the $z = 0$ subspaces for both the *standard* and *extended* spaces. We use 90% of the points in each LH in the training set, and add the remaining 10% to the validation set. In this way, we improve our predictions for cases with massless neutrinos and at $z = 0$, both of which of particular cosmological interest but that might display degraded performances since they are located on the edge of the parameter hyperspace.

Overall, our training set is made of 156,000 models, whereas our validation set contains 16,000. We employ the Boltzmann solver `CLASS` to compute the cold-matter power spectrum in each of the 172,000 points. We make our predictions on a fixed grid in wavenumber, with 200 $k-$bins between $10^{-3} \leq k[h\,\mathrm{Mpc}^{-1}] \leq 30$, and at the redshift indicated by the LH sampling. In Appendix A we provide details of our specific `CLASS` setup and a comparison with `CAMB` . We highlight that we will emulate the power spectrum of cold dark matter plus baryons (i.e. *cold* matter), which differs from the total mass case for massive neutrinos. We made this choice since the cold matter power spectrum has been shown to be a better prediction for the various LSS statistics (e.g. Castorina et al., 2015; Zennaro et al., 2019).

Before the training, we take the logarithm of the power spectra, normalising them by their mean in each k-bin. We find that, for the size of our training set, this is sufficient to reduce the variance of the data, and that using the ratio of the power spectra with some approximated method, e.g. Eisenstein and Hu (1999), does not improve sensibly the emulation. We have also tried to split the training set in two different components and emulating them separately, e.g. power spectrum at $z = 0$ and growth function, or smooth power spectrum and BAO oscillations, but we did not find any obvious advantage in any of these strategies.

Finally, we perform a Principal Component Analysis (PCA) decomposition and retain the first 32 eigenvectors, which combined are enough to reproduce the power spectrum at the 0.03% level; this effectively filters out small scale noise, which aids the neural network training.

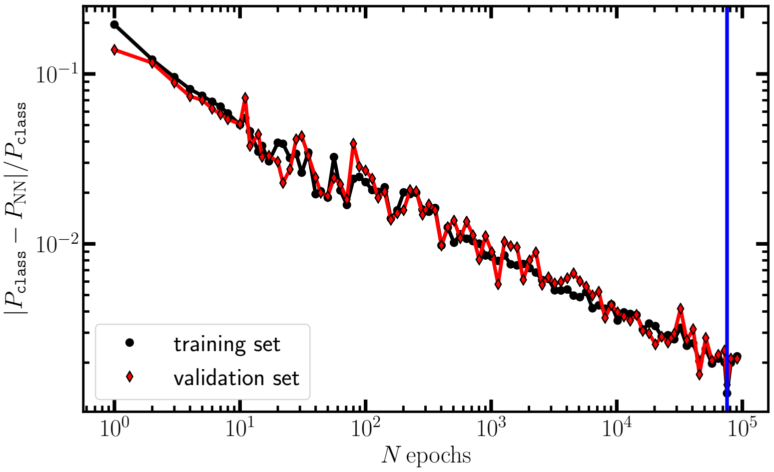

Figure 1.1: The mean absolute fractional error of our neural network, $\lambda = \left\langle \frac{|P_{\mathrm{NN}} - P_{\mathtt{CLASS}}|}{P_{\mathtt{CLASS}}} \right\rangle$, as a function of the number of epochs employed for its training. Black circles and red diamonds show the results when λ is evaluated on the training and the validation set, respectively. The vertical blue line marks the minimum of λ in the validation set and thus the training we will adopt thereafter in this paper.

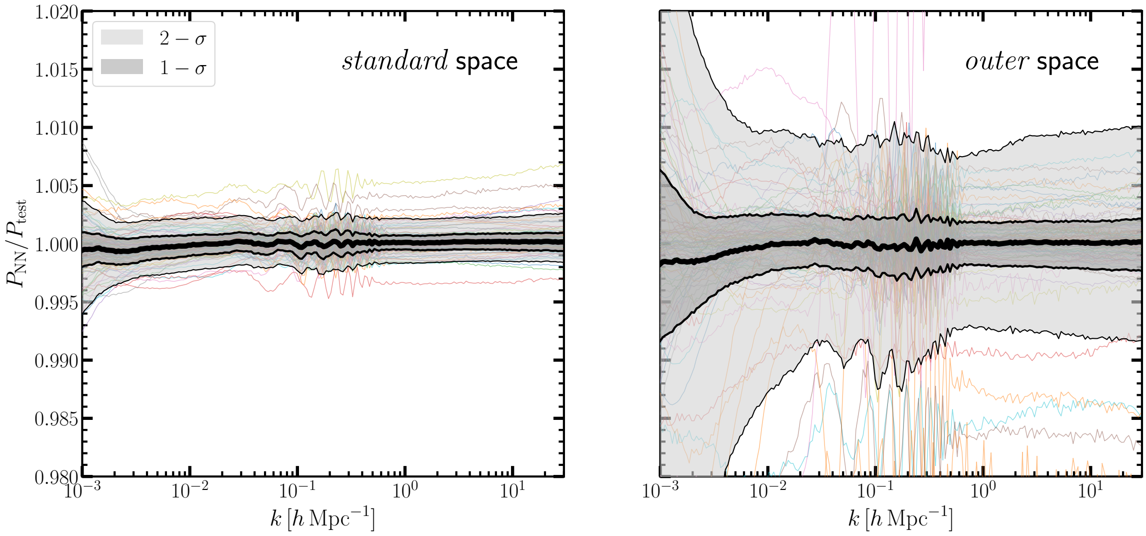

Figure 1.2: The accuracy of our neural network predictions for the linear matter power spectrum for multiple cosmologies and redshifts. We display the ratio of the power spectra computed by our emulator, P_{NN}, to that of the Boltzmann solver `CLASS` , $P_{\mathtt{CLASS}}$, in the *standard* (left panel) and in the *outer* (right panel) cosmological parameter spaces (c.f. Table 1.1). In the *outer* space, *all* the cosmological parameters have values not included in the *standard* space. The shaded regions enclose 68% and 95% of the cosmologies in our validation set, and the mean is shown as a thick grey line. As an example, thin coloured lines show the results for 100 randomly selected cosmologies.

1.2.3 Neural network setup

We build our emulator using a feed-forward neural network trained with 156,000 power spectrum measurements. Compared to Gaussian Processes, neural networks have the advantage of significantly lower computational and memory requirements, especially for large training sets. We employ the publicly-available libraries `Keras` and `TensorFlow` (Chollet et al., 2015; Abadi et al., 2016) to build a relatively simple architecture with two hidden layers of 400 neurons each, and a Rectified Linear Unit as an activation function. We use an Adam optimiser with a batch size of 750, and define as loss function the mean absolute fractional error. This quantity, to be minimised during the training procedure, is defined as

$$\lambda = \left\langle \frac{|P_{\rm NN} - P_{\tt CLASS}|}{P_{\tt CLASS}} \right\rangle , \tag{1.1}$$

where $P_{\rm NN}$ is the power spectrum predicted by the neural network, $P_{\tt CLASS}$ is the `CLASS` power spectrum, and the mean $\langle ... \rangle$ runs over the training points.

To avoid overfitting, we monitor the loss function λ computed over both the training and the validation datasets. We stop the training when the loss function evaluated on the validation set does not decrease for more than 10,000 epochs (to avoid being stuck in local minima). This resulted into a training of approximately 10^5 epochs, being the final loss function of the order of 1.5×10^{-3}. The whole training took approximately 24 hours.

In Fig. 1.1 we display the loss function λ computed in the training and validation sets, as a function of the number of epochs employed in the training. We see that the neural network return progressively more accurate results, with the loss function decreasing roughly as $N_{\rm epoch}^{-0.2}$. We can also see that the accuracy is roughly identical in the training and validation sets, which suggests the network has learnt relevant features in the power spectrum data, rather than any specific source of noise. We note that it appears that further training could yield to an even more accurate neural network without overfitting. However, as the improvement scales slowly with $N_{\rm epochs}$, it becomes impractical to train for much longer (i.e. the computational cost of the training becomes prohibitively high).

1.2.4 Validation of the emulator

We test the accuracy of our emulator using the validation set described in §1.2.2. We recall that this sample contains roughly 10% of the training data, distributed between the *standard* and *outer* cosmological spaces.

In Fig. 1.2 we display the ratio of the power spectrum computed with our emulator to that of `CLASS` . Shaded regions contain 68 and 95$\%$ of the measurements in the *standard* and *outer* space (left and right panel, respectively). We display 100 randomly-selected ratios for comparison.

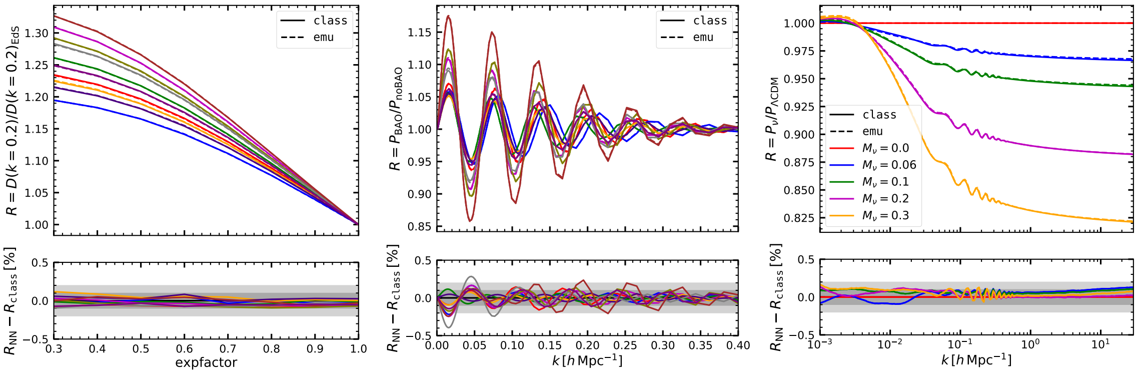

Figure 1.3: Validation of the predictions of our neural-network emulator for the linear matter power spectrum. *Left panel:* Growth factor at $k = 0.2\,h\,\mathrm{Mpc}^{-1}$ as a function of expansion factor. *Middle panel:* The ratio of the linear power spectrum over its smooth (or de-wiggled) counterpart which isolates the contribution of baryonic acoustic oscillations to the power spectrum. In both of these panels we show 10 randomly-selected cosmological models. *Right panel:* The ratio of the power spectrum computed including neutrinos of a various mass, as specified in the legend, over its respective neutrino massless case. In all three cases, we show the results obtained with `CLASS` as solid lines, and with our emulator as dashed lines. In the bottom panels, we display the compare these predictions indicating differences of 0.1 and 0.2% as shaded regions.

We can see that, in the *standard* cosmological space, our emulator is unbiased at the 0.01% level, and 68% of the validation set lies within 0.1%, while 95% within 0.3%. In the *outer* cosmological space, the accuracy is about $\approx 1\%$ for most of the scales, although it tends to degrade toward very large scales, $k < 0.002\,h\,\mathrm{Mpc}^{-1}$. Nevetheless, we highlight the *standard* cosmological space is expected to contain the full range of currently allowed cosmologies. In any case, even in the *outer* space, our emulator accuracy is significantly higher than that of current predictions for the nonlinear matter power spectrum for which state-of-the-art N-body codes agree at $\sim 2\%$ for $k \sim 10h\,\mathrm{Mpc}^{-1}$ (Schneider et al., 2016; Angulo et al., 2020; Springel et al., 2020). Moreover, in general we expect in the *extended space* an accuracy in-between the one found in the *standard* and *outer* space, being the latter a very particular case when *all* the parameters simultaneously have very extreme values. Therefore, any uncertainty of our emulator is arguably subdominant for LSS data analyses.

We further test our emulator in Fig. 1.3 by examining its predictions for the redshift dependence of growth factor, the baryonic acoustic oscillations, and the neutrino-induced suppression of the matter power spectrum. In each case we illustrate the accuracy by displaying the emulator and `CLASS` predictions for a small number of selected cosmologies within our *standard* space.

In the left panel of Fig. 1.3 we show the linear growth factor, $D(k) \equiv \sqrt{P(k,z)/P(k,z=0)}$ over the Einstein-de-Sitter solution, $D \propto a$, computed using our emulator and `CLASS` at 10 different cosmological models. We see that the emulator predictions are very accurate, within 0.1%, as expected from the performance shown previously. Also, the accuracy does not depend on the expansion factor, which indicates that the performance of our emulator is the same at all redshifts.

Given their importance for LSS analyses, we explicitly check how well the Baryonic Acoustic Oscillation (BAO) feature is recovered. In the middle panel of Fig. 1.3 we display the ratio between linear power spectrum and its de-wiggled counterpart, $P/P_{\rm no-wiggle}$, which highlights the contribution of the BAO to the power spectrum. We compute $P_{\rm no-wiggle}$ by performing a discrete sine transform of the linear theory power spectrum, smoothing the result, and returning to Fourier space with an inverse sine transform (e.g Baumann et al., 2018). We can see how each oscillation is remarkably well reproduced by our emulator, with small in-phase deviations of the order of 0.3%. This suggests the accuracy of our emulator is also high enough for BAO analyses.

To close this section, we examine the dependency of the power spectrum on massive neutrinos. The rightmost panel of Fig. 1.3 shows the ratio of the power spectrum computed with increasingly massive neutrinos, $M_\nu = [0.06, 0.1, 0.2, 0.3]$ eV, over the massless case, $M_\nu = 0$ eV, keeping fixed the primordial spectral amplitude $A_{\rm s}$ and the matter density $\Omega_{\rm m}$. As with our previous tests, we find that the distortion caused by neutrinos – a suppression at small scales proportional to the neutrino mass fraction – is accurately recovered by our emulator at 0.2% level.

1.3 Lagrangian perturbation theory emulator

Besides predicting the clustering of matter, another challenge for present-day and forthcoming cosmological surveys is to predict the clustering of galaxies. In this section we build emulators for several matter statistics as predicted by Lagrangian Perturbation Theory (LPT) that are typically employed in models for the power spectrum of galaxies.

1.3.1 Lagrangian bias expansion

Among the many possible models to describe the clustering of galaxies, a particularly promising one is a perturbative Lagrangian bias expansion (Matsubara, 2008). In this formalism, the power spectrum of galaxies, $P_{\rm gg}$, and the matter-galaxy cross-power spectrum, $P_{\rm gm}$, at second order are given as:

$$\begin{aligned} P_{\rm gg} &= \sum_{i,j\in\{1,\delta,\delta^2,s^2,\nabla^2\delta\}} (2-\delta_{ij}) b_i b_j \, P_{ij}, \\ P_{\rm gm} &= \sum_{i\in\{1,\delta,\delta^2,s^2,\nabla^2\delta\}} b_i \, P_{i1}, \end{aligned} \tag{1.2}$$

where, b_1, b_2, b_{s^2}, and $b_{\nabla^2\delta}$ are free “bias” parameters; δ is the linear density field, s^2 is the shear field defined as $s^2 \equiv s_{ij}s_{ij}$ where $s_{ij} \equiv \partial_i\partial_j\nabla^{-2}\delta - \delta_{D,ij}\delta(q)$, and $\nabla^2\delta$ the Laplacian

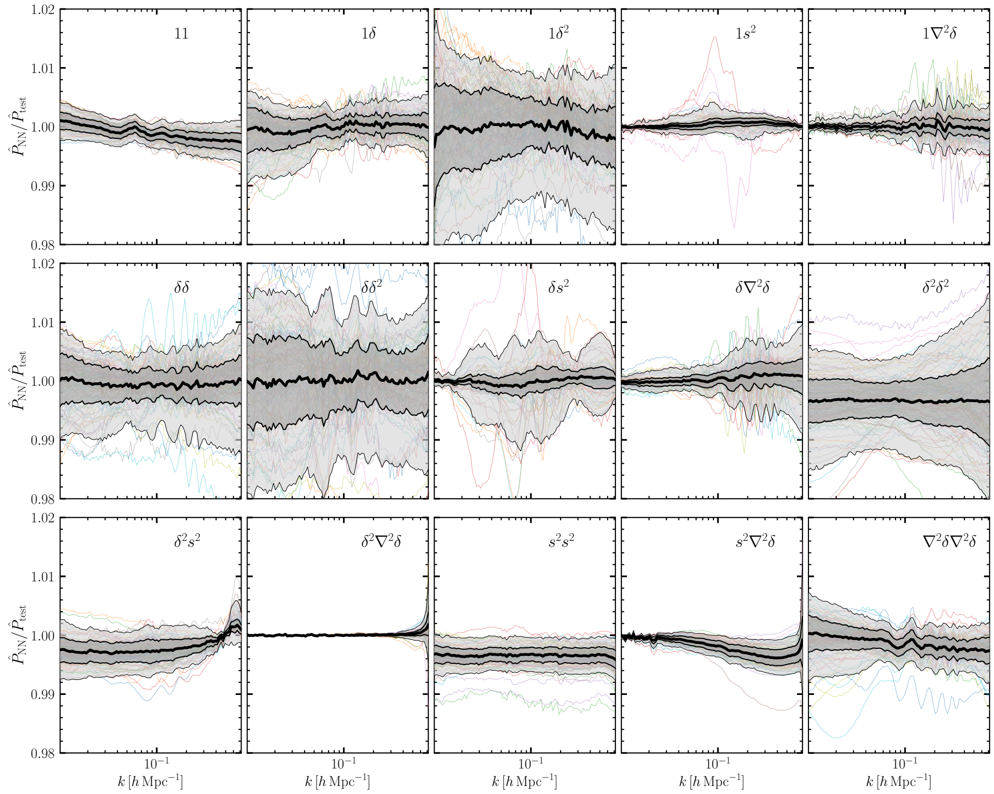

Figure 1.4: The accuracy of our emulators for the cross-spectrum of linear fields in Eulerian coordinates predicted by Lagrangian Perturbation Theory. The two fields defining the cross-spectra are indicated in the legend of each panel, where 1 is an homogeneous Lagrangian field; δ and δ^2 are the linear density field and its square, respectively; s^2 is the shear field; and $\nabla^2\delta$ is the Laplacian of the linear density field. In each panel we display the ratio of the emulator prediction over the same quantity computed by directly solving the relevant LPT expression. Shaded regions enclose 68% and 95% of the measurements in our validation set, and the mean is is marked by the thick black line. For comparison we show a randomly-selected set of cosmologies as coloured lines.

of the linear density; and $P_{ij} = \langle |\delta_i(\boldsymbol{k})\delta_j^*(\boldsymbol{k})| \rangle$ (see Zennaro et al., 2021, for details).

In other words, the clustering of galaxies is given as a weighted sum of 15 cross-spectra of five Lagrangian fields, $\delta^{\mathrm{L}} \in \{1, \delta, \delta^2, s^2, \nabla^2\delta\}$, advected to Eulerian coordinates:

$$1 + \delta^{\mathrm{E}}(\boldsymbol{x}) = \int \mathrm{d}^3q\, \delta^{\mathrm{L}}(\boldsymbol{q})\delta_{\mathrm{D}}(\boldsymbol{x} - \boldsymbol{q} - \boldsymbol{\Psi}(\boldsymbol{q})) \tag{1.3}$$

where δ_{D} is a Dirac's delta. The displacement field $\Psi(\boldsymbol{q})$ (and thus the cross-spectra) can be computed perturbatively at a given order, or, as proposed recently, measured directly from N-body simulations. The latter can accurately describe the power spectrum of galaxies down to much smaller scales than using perturbative solutions, which opens up the possibility of an accurate modelling of galaxy clustering (Modi et al., 2020).

In fact, Zennaro et al. (2021) and Kokron et al. (2021) have built emulators for these spectra as a function of cosmology from simulation suites. However, even in this case, large scales are described with perturbation theory owing to the noise (cosmic variance) in the N-body displacements. Additionally, the emulation is performed for the ratio of the N-body spectra over the perturbative solution, which, as for the matter power spectrum, improves the quality of the emulation.

The LPT terms can be computed with publicly available codes (such as `velocileptors`, Chen et al., 2020) or, as in Zennaro et al. (2021), by solving the three dimensional LPT integrals with a adaptive quadrature algorithm. Both implementations are very efficient and produce the LPT spectra in around 1 second of computing time, depending on accuracy parameters and machine architecture. However, this can become the most costly step in the context of obtaining the galaxy model from an emulator.

In this section, we build an emulator for each of the 15 terms to speed up this process. Specifically, we emulate the terms $P_{11}, P_{1\delta}$, and $P_{\delta\delta}$ where we expand δ at first order in Lagrangian perturbation theory; this is enough for the applications mentioned. All remaining terms are computed expanding densities at second order in Lagrangian perturbation theory, retaining only contributions of order (11) and (22). We refer the reader to Zennaro et al. (2021) for the explicit expression of each of these spectra in LPT. It is important to note that we assume the linear power spectrum entering our LPT calculations to be smoothed on a scale $k_{\mathrm{s}} = 0.75h\,\mathrm{Mpc}^{-1}$.

1.3.2 LPT emulator

We build the LPT emulators in the *standard* hyper-parameter space (c.f. Table 1.1) and over the expansion factor range: $a \in [0.4, 1.]$ (note that this redshift range is slightly smaller than that employed in § 1.2.1). We note that the cosmological parameter space matches the ones used by Zennaro et al. (2021), where we presented non-linear boost-factors for these spectra. We then compute the LPT predictions in 91 logarithmic bins over the range $10^{-2} < k[h\,\mathrm{Mpc}^{-1}] < 0.75$.

We sample the parameter space with a single LH with 18,000 points. In each of these points, we compute the 15 Lagrangian cross power spectra as described above. As noted by Zennaro et al. (2021), some of these spectra can be negative. In these cases, we emulate the quantity:

$$\hat{P}_{ij} = P_{ij} + |\min(P_{ij})| + 0.1. \tag{1.4}$$

so that the spectra are always positive. As in the case of the linear matter power spectrum, prior to the training we take the logarithm of the power spectra, and subtract the mean in each k-bin. We then perform a PCA decomposition prior to the training, retaining for each spectrum a number of PC sufficient to recover the power spectrum at 0.01%, which ranges from 5 to 20 PCA vectors.

We use 90% of the sample as our training dataset and the remaining 10% as our validation set. The architecture of the neural network used to emulate the LPT power spectra is the same as that described in § 1.2.3, i.e. 2 hidden layers with 400 neurons each.

We quantify the accuracy of our emulators in Fig. 1.4, which shows the ratio of the emulation prediction in the validation set over the spectra computed with LPT. Overall, the accuracy of the 15 spectra is around better than 1%. In particular, we best recover the terms 11, $1s^2$, $\delta^2\nabla^2\delta$, s^2s^2, and $s^2\nabla^2\delta$, with an accuracy of 0.5% or better. On the contrary, the terms $1\delta^2$, and $\delta\delta^2$ are emulated at better than 2%. This accuracy is higher than that of the nonlinear emulators, thus the LPT emulation uncertainty should add a subdominant contribution to the global modelling error. Nevertheless, as with our linear emulator, it is straightforward to add further points to the training set, if higher accuracy is required.

1.4 Parameter constraints from mock cosmic shear power spectra

In this section, we illustrate the use of our linear power spectrum emulator with a simple application: we infer cosmological parameters from a mock lensing power spectrum using either our linear emulator or directly the output of `CLASS` . In this way, we will confirm that the accuracy of our emulator is adequate in the context of LSS data analysis.

Our mock data corresponds to the auto and cross power spectra of weak lensing shear measurements for 10 equi-populated redshift bins $z_i \in [0.1, 2.5]$. We adopt the specifics of a *stage-IV* survey, and in particular those of the Euclid mission (Amendola et al., 2018). The cross-spectrum of cosmic shear is given by:

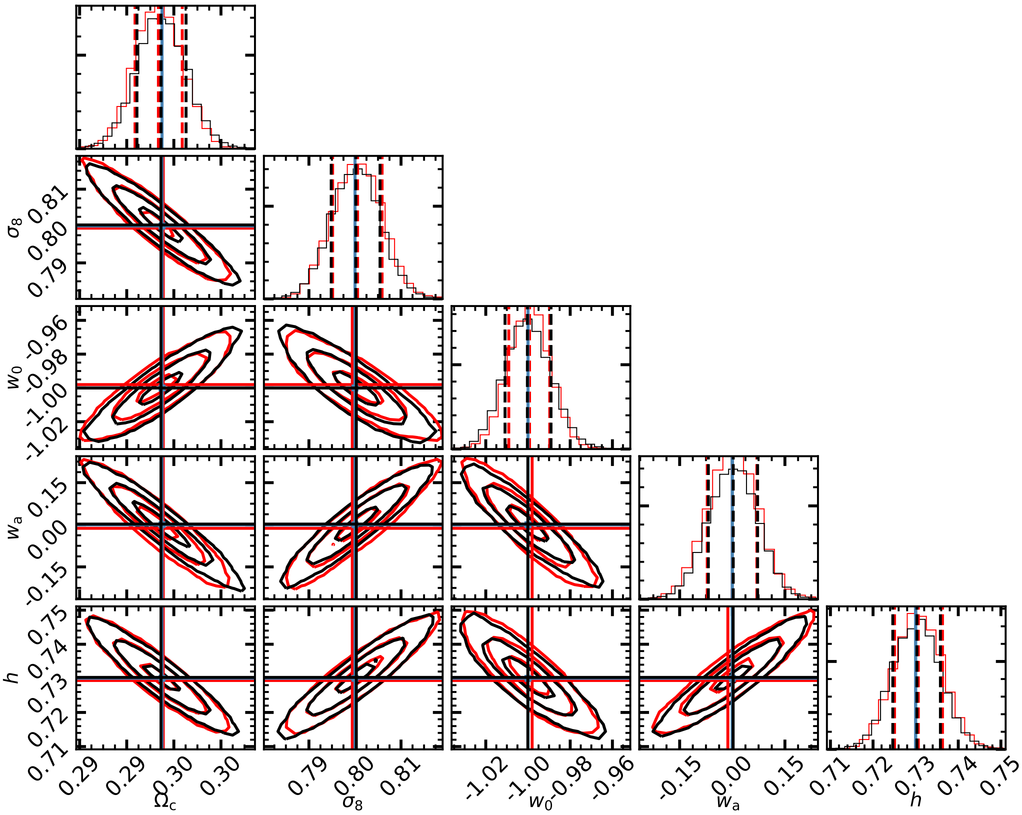

Figure 1.5: The marginalised posterior distributions on cosmological parameters obtained from mock weak lensing data. Our mock data is comprised by the shear power spectrum and cross-spectra using 10 tomographic bins over $z \in [0., 2.5]$, and a redshift distribution of background galaxies, shape noise, and cosmic variance expected for a *stage-IV* Euclid-like survey. The contours in each panel show 1,2, and 3 σ levels obtained by performing an MCMC analysis using the linear matter power spectrum directly provided by the Boltzmann solver `CLASS` (black lines and contours) or by our emulator (red lines and contours). Blue lines indicate the cosmological parameters adopted in our mock data, whereas black and red lines show the best-fitting values obtained by our analysis.

$$C_{\gamma_i,\gamma_j}(\ell) = \int_0^{\chi_{\rm H}} \frac{g_i(\chi)g_j(\chi)}{\chi^2} P\left(\frac{\ell}{\chi}, z(\chi)\right) d\chi, \tag{1.5}$$

where $P(k, z)$ is the linear matter power spectrum (given by `CLASS` for our mock data), and $g_i(\chi)$ is the the lensing kernel of the i-th redshift bin:

$$g_i(\chi) = \frac{3}{2}\Omega_{\rm m}\left(\frac{H_0}{c}\right)^2 \frac{\chi}{a}\int_{z(\chi)}^{z_{\rm H}} {\rm d}z'\, n_i(z)\frac{\chi(z') - \chi(z)}{\chi(z')}, \tag{1.6}$$

where c is the light speed and $\chi(z)$ is the comoving distance to z. We assume a redshift distribution of galaxies in the i-th bin $n_i(z) \propto z^2 \exp\left(-\frac{z\sqrt{2}}{z_i}\right)$, with z_i roughly setting the redshift where the galaxy number density peaks. The galaxy distribution in each bin is normalised such that $\int_0^\infty {\rm d}z\, n_i(z) = 1$.

For simplicity, we only consider the Gaussian contribution of the covariance:

$$\begin{aligned}\mathrm{Cov}^{\rm G}_{\gamma_i,\gamma_j,\gamma_m,\gamma_n}(\ell_1, \ell_2) = \frac{\delta_{\ell_1,\ell_2}}{N_\ell}\Bigg[&\left(C_{\gamma_i,\gamma_m} + \delta_{im}\frac{\sigma_{\rm e}^2}{2\bar{n}^i_{\rm eff}}\right)\left(C_{\gamma_j,\gamma_n} + \delta_{jn}\frac{\sigma_{\rm e}^2}{2\bar{n}^j_{\rm eff}}\right) + \\ &\left(C_{\gamma_i,\gamma_n} + \delta_{in}\frac{\sigma_{\rm e}^2}{2\bar{n}^i_{\rm eff}}\right)\left(C_{\gamma_j,\gamma_m} + \delta_{jm}\frac{\sigma_{\rm e}^2}{2\bar{n}^j_{\rm eff}}\right)\Bigg]\end{aligned} \tag{1.7}$$

where $N_\ell = (2\ell + 1)\Delta\ell f_{\rm sky}$ is the number of independent multipoles falling in a bin centered in ℓ with width $\Delta\ell$, $f_{\rm sky}$ is the fraction of the sky covered by the survey, $\sigma_{\rm e}$ and $\bar{n}^i_{\rm eff}$ are the RMS ellipticity and the effective projected number density of the source galaxies in the i bin, respectively (Barreira et al., 2018). The presence of the Kronecker deltas δ_{ℓ_i,ℓ_j} forces the Gaussian term to be diagonal, and δ_{ij} to have shape noise terms only for matching redshift bins. We adopt a fiducial setup of $f_{\rm sky} = 0.36$, $\sigma_{\rm e} = 0.37$, $\bar{n}^i_{\rm eff} = 30\,\mathrm{arcmin}^{-2}$.

We fit the mock data over 20 logarithmically-spaced multipoles between $\ell \in [20, 5000]$, using the affine invariant MCMC sampler `emcee` (Foreman-Mackey et al., 2013) and employing 10 walkers of 10,000 steps each, considering a burn-in phase of 1,000 steps. Our data model is given by Eq. 1.5 computed with a linear power spectrum provided by either `CLASS` or by our emulator, and letting free the cosmological parameters $\Omega_{\rm c}$, σ_8, h, w_0, and $w_{\rm a}$. Using 1 CPU, a single call to `CLASS` takes $\approx$ 0.5 seconds ($\approx$ 7 seconds when having massive neutrinos), whereas the emulator evaluation takes $\approx$ 1 milliseconds.

In Fig. 1.5, we display the posterior distributions estimated with the MCMC analysis using `CLASS` and the emulator (black and red lines, respectively). We see that by using the linear emulator, we recover unbiased parameters at less than 0.05σ. Moreover, the 1D marginalised PDFs, the parameters degeneracy, and the contours are all almost indistinguishable from those using directly `CLASS` . Overall, the results show a remarkable agreement between both approaches, which suggests that the accuracy of our linear emulator is sufficient for the analyses of forthcoming LSS surveys.

1.5 Summary

In this chapter, we have presented and validated a set of fast and accurate emulators aimed at speeding up the analysis of forthcoming LSS data. These emulators can provide their predictions in about one millisecond of computing time and cover a broad 8-dimensional cosmological parameter space that includes massive neutrinos and dynamical dark energy.

First, we have built and validated an emulator for the linear cold matter power spectrum, which is faster than a typical Boltzmann solver by a factor of 1000. The accuracy of the emulator is subpercent over $10^{-3} < k < 30$ (Fig. 1.2) and it also accurately predicts the growth of fluctuations, the baryonic acoustic oscillations, and the suppression of clustering induced by massive neutrinos (Fig. 1.3). Our second set of emulators predict multiple cross-spectra of Lagrangian fields relevant for a 2nd-order perturbative model of galaxy bias. We compute these fields with 1 and 2-order Lagrangian perturbation theory which can then be emulated with percent accuracy (Fig. 1.4). Finally, we have shown that the accuracy of the linear emulator can be used to provide unbiased cosmological constraints for a tomographic analysis of a Euclid-like weak lensing survey (Fig. 1.5).

The emulators presented in this work are part of the `baccoemu` project[2], and have been specifically designed to be used with those we have previously built for the nonlinear matter power spectrum (Angulo et al., 2020), the modifications induced by baryonic physics (Aricò et al., 2020a), and galaxy bias (Zennaro et al., 2021). All together, they can contribute towards a comprehensive, fast, and accurate cosmological exploitation of LSS data.

---

[2] `http://bacco.dipc.org/emulator.html`.

Chapter 2

The BACCO Simulation Project: rescaling the cosmology of simulations

In this chapter, adapted from "The BACCO Simulation Project: Exploiting the full power of large-scale structure for cosmology" Angulo et al. (2020), we present the BACCO project, a simulation framework specially designed to provide highly-accurate predictions for the distribution of mass, galaxies, and gas as a function of cosmological parameters. We describe our main suite of simulations ($L \sim 2\,\mathrm{Gpc}$ and 4320^3 particles) and present various validation tests. Using a cosmology-rescaling technique, we predict the nonlinear mass power spectrum over the redshift range $0 < z < 1.5$ and over scales $10^{-2} < k/(h\,\mathrm{Mpc}^{-1}) < 5$ for 800 points in an 8-dimensional cosmological parameter space. For an efficient interpolation of the results, we build a Gaussian Process emulator which we test against other widely-used methods. Over the whole range of scales considered, we expect our predictions to be accurate at the 2% level for parameters in the minimal ΛCDM model and to 3% when extended to dynamical dark energy and massive neutrinos. We make our emulator publicly available under `http://www.dipc.org/bacco`.

2.1 Introduction

Over the last two decades, our understanding of the Universe has grown tremendously: the accelerated expansion of the Universe and the existence of dark matter are becoming firmly established. Furthermore, there are strong constraints on the micro-physical properties of dark matter and neutrinos, and on the statistics of the primordial cosmic fluctuations (e.g. Alam et al., 2017; Planck Collaboration et al., 2018; Gilman et al., 2020).

Despite the progress, there are several tensions among current data when interpreted within the context of the ΛCDM model. For instance, the value of the Hubble parameter inferred from local supernovae is significantly larger than that inferred from the analysis of the CMB (e.g. Riess, 2019; Freedman et al., 2019). Another example is that the amplitude of fluctuations, $S_8 = \sqrt{\Omega_m/0.3}\,\sigma_8$, as determined from low-redshift lensing measurements, appears smaller than that inferred from CMB (e.g. Asgari et al., 2020b).

In the current era of precision cosmology, the large amount of available large-scale structure (LSS) data promises accurate measurements of cosmological parameters with small systematic errors. These future measurements could shed light on the aforementioned tensions, confirming or ruling out the ΛCDM paradigm (e.g. Weinberg et al., 2013). Many observational campaigns that seek to obtain this data are under construction or with an imminent start (e.g. Euclid, DESI, J-PAS).

To fully exploit the upcoming LSS data and obtain these cosmological constraints, extremely accurate theoretical models are required. This is an active area of research with different approaches being adopted in the literature. On the one hand, recent advances in perturbation theory have increased considerably the range of scales that can be treated analytically (e.g. Desjacques et al., 2018). These scales are, however, still in the quasi-linear regime. On the other hand, cosmological numerical simulations are by far the most accurate method to model smaller and non-linear scales (where, in principle, much more additional constraining power resides). As with analytical models, simulations have also steadily increased their robustness and accuracy (e.g. Kuhlen et al., 2012).

Traditionally, numerical simulations were very expensive computationally and suffered from large cosmic-variance errors, thus they were only used to calibrate fitting functions or combined with perturbation theory to provide predictions for nonlinear structure as a function of cosmology (e.g. Smith et al., 2003; Takahashi et al., 2012). This has changed recently, as the available computational power keeps increasing and so-called emulators become more popular. In this approach, a suite of simulations of different cosmologies are interpolated to provide predictions in the nonlinear regime and for biased tracers of the LSS (e.g. Heitmann et al., 2014; Nishimichi et al., 2018; Liu et al., 2018; DeRose et al., 2019; Giblin et al., 2019; Wibking et al., 2019).

To keep computational cost under control, traditional emulators are typically restricted to a small region in parameter space which is sampled with a small number of simulations ($\sim 50-100$), and the individual simulations are low resolution or simulate a relatively small cosmic volume. This limits their usability in actual data analyses and/or add a significant source of uncertainty.

Here we take advantage of several recent advances to solve these limitations. First, we employ a very efficient N-body code to carry out a suite of 6 large-volume high-resolution simulations, which allows to resolve all halos and subhalos with mass $> 5 \times 10^{10} h^{-1}\mathrm{M}_{\odot}$, together with their merger histories. We employ initial conditions with suppressed variance, which allows to predict robustly even scales comparable to our simulated volume. These simulations are combined with cosmology-rescaling algorithms, so that predictions can be obtained for any arbitrary set of cosmological parameters. Overall, this approach allows us to make highly accurate predictions for the large-scale phase-space structure of dark matter, galaxies, and baryons.

Our approach has many advantages over others in the literature. Firstly, we can predict the matter distribution over a broad range of scales, with high force accuracy and over a large cosmic volume. This allows for detailed modellings of the distribution of gas and the impact of “baryonic effects” (Schneider et al., 2019; Chisari et al., 2019; Aricò et al., 2020b). We can also resolve collapsed dark matter structures and their formation history, which enables sophisticated modelling of the galaxies that they are expected to host (e.g. Henriques et al., 2020; Moster et al., 2018; Chaves-Montero et al., 2016). In addition, the cosmological parameter space is large and densely sampled, so that emulator uncertainties are kept under a desired level. Finally, the parameter space includes non-standard ΛCDM parameters, dynamical dark energy and massive neutrinos.

As an initial application of our framework, we have used our suite of specially-designed simulations to predict the nonlinear mass power spectrum over the range $0 < z < 1.5$ for 800 different cosmologies within an 8-dimensional parameter space defined by a $\sim 10\sigma$ volume around Planck’s best-fit values. From these, we construct and present a Gaussian emulator so that these predictions are easily accessible to other researchers. Overall, we reach a few percent accuracy over the whole range of parameters considered.

This chapter is structured as follows. Section 2.2 is devoted to presenting our numerical simulations and to the description and validation of numerical methods. In Section 2.3 we describe the construction of an emulator for the nonlinear power spectrum. In particular, Section 2.3.1 discusses our strategy for selecting training cosmologies, Section 2.3.1 discusses our power spectra measurements. Finally, in Section 2.3.2 we compare our predictions with other approaches. We summarise our results and discuss the implications of our work in Section 2.4.

2.2 Numerical methods

2.2.1 The BACCO Simulations

The “BACCO simulations" is a suite of 6 N-body simulations that follow the nonlinear growth of dark matter structure within a cubic region of L=$1440 h^{-1}\mathrm{Mpc}$ on a side. These calculations are performed for three different sets of cosmological parameters with two realizations each. The matter distribution is represented by 4320^3 (~ 80 billion) particles.

The three cosmologies adopted by our BACCO simulations are provided in Table 2.1. We dub these cosmologies `narya`, `nenya`, and `vilya`[1]. These sets are inconsistent with the latest

---

[1] `narya`, `vilya`, and `nenya` are the most powerful rings after Sauron’s “One Ring” in “The Lord of the

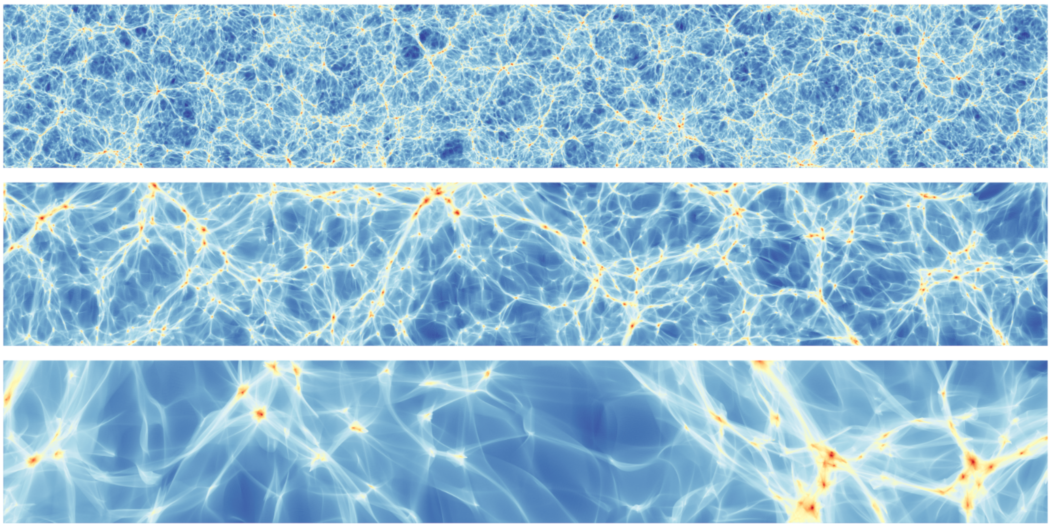

Figure 2.1: The projected mass density field in `nenya`, one of our six BACCO simulations, at $z = 0$. Each image corresponds to a 25 h^{-1}Mpc deep projection employing a tri-cubic Lagrangian interpolation method. Top, middle, and bottom panels progressively zoom into a $1440\,h^{-1}$Mpc, $360\,h^{-1}$Mpc, and $90\,h^{-1}$Mpc-wide region of the simulation.

observational constraints, but they were intentionally chosen to so that they can be efficiently combined with cosmology-rescaling algorithms (Angulo and White, 2010). Specifically, Contreras et al. (2020a) showed that these 3 cosmologies are optimal, in terms of accuracy and computational cost, to cover all the cosmologies within a region of $\sim 10\sigma$ around the best values found by a recent analysis of the Planck satellite (Planck Collaboration et al., 2014b).

For `narya` and `vilya` we stored 50 snapshots, equally log-spaced in expansion factor, a, and adopt a Plummer-equivalent softening length of $\epsilon = 6.7h^{-1}$kpc. As pointed out by Contreras et al. (2020a), most of the cosmological parameter volume is covered by rescaling `nenya`, thus we have increased the force resolution and frequency of its outputs to $\epsilon = 5h^{-1}$kpc and 100 snapshots, respectively. All simulations were started at $a = 0.02$ using 2nd-order Lagrangian Perturbation theory, and were evolved up to $a = 1.25$ so that they can be accurately scaled to cosmologies with large amplitude of fluctuations.

For each of the three cosmologies, we carry out two realizations with an initial mode amplitude fixed to the ensemble mean, and opposite Fourier phases (Angulo and Pontzen, 2016; Pontzen et al., 2016). These "Paired-&-Fixed" initial conditions allow for a significant reduction of cosmic variance in the resulting power spectrum in the linear and quasi-linear scales (which are the most affected by cosmic variance), as it has been tested extensively in recent works (Chuang et al., 2019; Villaescusa-Navarro et al., 2018; Klypin et al., 2020).

The BACCO simulations were carried out in the Summer of 2019 at Marenostrum-IV at the Barcelona Supercomputing Center (BSC) in Spain. We ran our N-body code in a hybrid distributed/shared memory setup employing 8192 cores using 4096 MPI tasks. The

---

Rings" mythology.

run time was 7.2 million CPU hours, equivalent of 35 days of wall-clock time. The total storage required for all data products is about 80 TB.

To compare against recent emulator projects, we notice these simulations have 10 times better mass resolution, 4 times better force resolution, and 2×3 the volume of those used by the AEMULUS project (DeRose et al., 2019); 50 times the volume and 3 times better mass resolution than MassiveNuS (Liu et al., 2018); 6 times better mass resolution, 50% larger volume, and twice the spatial resolution than those in the EUCLID emulator project (Euclid Collaboration et al., 2019); 10 times more particles and slightly better force resolution than the runs of the DarkEmulator (Nishimichi et al., 2018); 2 times better mass resolution and similar force resolution and volume to the simulations in the `Mira-Titan` Universe project (Heitmann et al., 2014).

In Fig. 2.1 we display the projected matter density field of `nenya` at $z = 0$. Each panel shows a region of the simulated volume, the top panel a region $1440\,h^{-1}\mathrm{Mpc}$ wide – the full simulation side-length –, whereas middle and bottom panels zoom in regions 960 and $360\,h^{-1}\mathrm{Mpc}$ wide, respectively. We display the density field as estimated via a tri-cubic Lagrangian tessellation using only 1080^3 particles. Note that thanks to this interpolation, no particle discreteness is visible and filaments and voids become easily distinguishable.

2.2.2 The simulation code

The N-body code we employ is an updated version of `L-Gadget3` (Springel, 2005; Angulo et al., 2012). This code was originally developed for the Millennium-XXL project and was successfully executed with more than 10,000 CPUs employing 30Tb of RAM. Compared with previous versions of `Gadget`, `L-Gadget3` features an hybrid OpenMP/P-thread/MPI parallelisation strategy and improved domain decomposition algorithms.

In addition to these improvements, our updated `L-Gadget3` version stores all outputs in the HDF5 format, implements the possibility of simulating massive neutrinos via the linear response approach (Ali-Haïmoud and Bird, 2013), and features an improvement in the Tree-PM force split and in Kick-Drift operators. The output data structure is such to allow a straightforward reconstruction of the full phase-space distribution via tri-cubic Lagrangian interpolation (Hahn and Angulo, 2016; Stücker et al., 2019).

Table 2.1: The cosmological parameters of the three "BACCO" simulations presented in this chapter: Vilya, Nenya and Narya. All the simulations have been run with a ΛCDM cosmology with $\sigma_8 = 0.9$, $M_\nu = 0$, $w_0 = -1$ and $w_a = 0$, and have a box side of 1440 h^{-1}Mpc and 4320^3 particles.

	Ω_m	Ω_b	$\mathrm{n_s}$	h	m_p $[h^{-1}\mathrm{M}_\odot]$	ϵ $[h^{-1}\mathrm{kpc}]$
Vilya	0.27	0.06	0.92	0.65	2.77×10^9	6.7
Nenya	0.315	0.05	1.01	0.60	3.2×10^9	5
Narya	0.36	0.05	1.01	0.70	3.7×10^9	6.7

The code carries out a large fraction of the required post-processing on the fly. Specifically, this includes the 2LPT initial conditions generator, group finding via Friends-of-Friends algorithms and an improved version of `SUBFIND` (Springel et al., 2001) that is also able to track tidally-disrupted structures, and a descendant finder and merger tree construction (c.f. §2.2.2).

Thanks to the in-lining of these tools, it is not necessary to store the full particle load at every snapshot, which significantly reduces the I/O and long-term storage requirements. The dark matter distribution is, however, very useful in many applications, thus `L-Gadget3` is able to store a subset of particles sampling homogeneously the initial Lagrangian distribution.

SubFind and Group finders

The identification of bound structures is a key aspect of N-body simulations, thus `L-Gadget3` features a version of the `SUBFIND` algorithm with several improvements.

The first improvement is the ability to track subhalos on-the-fly across snapshots – defining progenitor and descendants –, computing various additional quantities such as peak halo mass, peak maximum circular velocity, infall subhalo mass, and mass accretion rate, among others. These properties become useful when modelling galaxy formation within gravity-only simulations (e.g. Chaves-Montero et al., 2016; Moster et al., 2018).

The second improvement of our updated version of `SUBFIND` is the use of the subhalo catalogue in the previous snapshot to better identify structures. In the original algorithm, particles are first sorted according to the local density, then when a saddle point is detected, the most massive group at that point is considered as the primary structure. This, however, can cause inconsistencies across time, as small changes can lead to fluctuations in the structure considered as primary. In our version of `SUBFIND` instead, when a saddle point is detected, we consider as primary the substructure whose main progenitor is the most massive. This has proven to return more stable merger trees and quantities that are not local in time (e.g. peak maximum circular velocity).

Finally, during their evolution, substructures can disappear from a simulation due to artifacts in the structure finder, finite numerical resolution, or because its mass falls below the resolution limit owing to tidal stripping. The last of our improvements to `SUBFIND` is the ability to track all subhalos with no recognizable descendant, keeping the position and velocity of their most bound particle. This is a indispensable feature to correctly model the small-scale galaxy clustering in dark matter simulations (Guo and White, 2014).

At every output time, we store FoF groups and `SUBFIND` subhalos with more than 10 particles. In total, there are approximately 129 billion groups and 214 billion subhalos in our outputs. This means our simulations are able to resolve halos with mass $5 \times 10^{10} h^{-1}\mathrm{M}_{\odot}$, and subhalos with a number density of $0.1\, h^3\mathrm{Mpc}^{-3}$ at $z = 0$.

2.2.3 Validation

Time and force resolution

In order to quantify the accuracy of our results, we have carried out a suite of small, $L = 64\,h^{-1}\mathrm{Mpc}$ box, simulations where we systematically vary the numerical parameters around those adopted in the BACCO simulations. Specifically, we consider the time-integration accuracy, force calculation accuracy, softening length, and mass resolution.

In Fig. 2.2 we compare the nonlinear power spectrum between these test runs and one that adopts the same numerical parameters and mean interparticle separation as our main BACCO simulations. Solid and dashed lines denote the results at $z = 0$ and $z = 1$, respectively. In all panels the grey shaded region indicates $\pm 1\%$ agreement.

In the top panel we display simulations with different mass resolutions, $N^{1/3}/L = [2, 3, 4]$. The main effect of mass resolution is how well small non-linear structures are resolved. We see no significant effect up to $k \sim 5h\,\mathrm{Mpc}^{-1}$ and a mild increase, of about 1% in the power at $k \sim 10h\,\mathrm{Mpc}^{-1}$ when improving the mass resolution.

The main source of inaccuracies in the force calculation are the terms neglected in the oct-tree multipole expansion. Specifically, `Gadget` considers only the monopole contribution down to tree-nodes of mass M and size ℓ that fulfill $\frac{GM^2}{r^2}\left(\frac{\ell}{r}\right) > \alpha|\vec{a}|$ for a particle at a distance r and acceleration $|\vec{a}|$. Thus, the accuracy in the force calculation is controlled by the parameter α. In the second panel we vary this parameter and see that with exception of $\alpha = 0.01$, i.e. twice poorer force resolution than that in BACCO, the power spectrum is converged at a sub-percent level.

As in previous versions of `Gadget`, time-steps in `L-Gadget3` are computed individually for each particle as $\sqrt{2\eta\epsilon/|\vec{a}|}$, where ϵ is the softening and $|\vec{a}|$ is the magnitude of the acceleration in the previous timestep. The parameter η therefore controls how accurately orbits are integrated. In the third panel we vary this parameter increasing/decreasing it by a factor of 4/2 with respect to our fiducial value, $\eta = 0.05$. We see that the power spectrum varies almost negligibly with less than a 0.5% impact up to $k \sim 10h\,\mathrm{Mpc}^{-1}$.

Perhaps the most important degree of freedom in a numerical simulation is the softening length, ϵ, a parameter that smooths two-body gravitational interactions (note that in `Gadget`, forces become Newtonian at a distance 2.7ϵ). In the fourth panel we compare three simulations with 50% higher and lower values of ϵ to values equal to $1/140$ and $1/35-th$ of the mean interparticle separation. On small scales we see that the amount of power increases systematically the lower the value of the softening length. In particular, our fiducial configuration underestimates the power by $1(2.5)\%$ at $k \sim 5(10)\,h\,\mathrm{Mpc}^{-1}$.

In summary, our results appear converged to better than 1% up to $k \sim 5h\,\mathrm{Mpc}^{-1}$, and to $\sim 3\%$ up to $k \sim 10\,h\,\mathrm{Mpc}^{-1}$. The main numerical parameter preventing better convergence

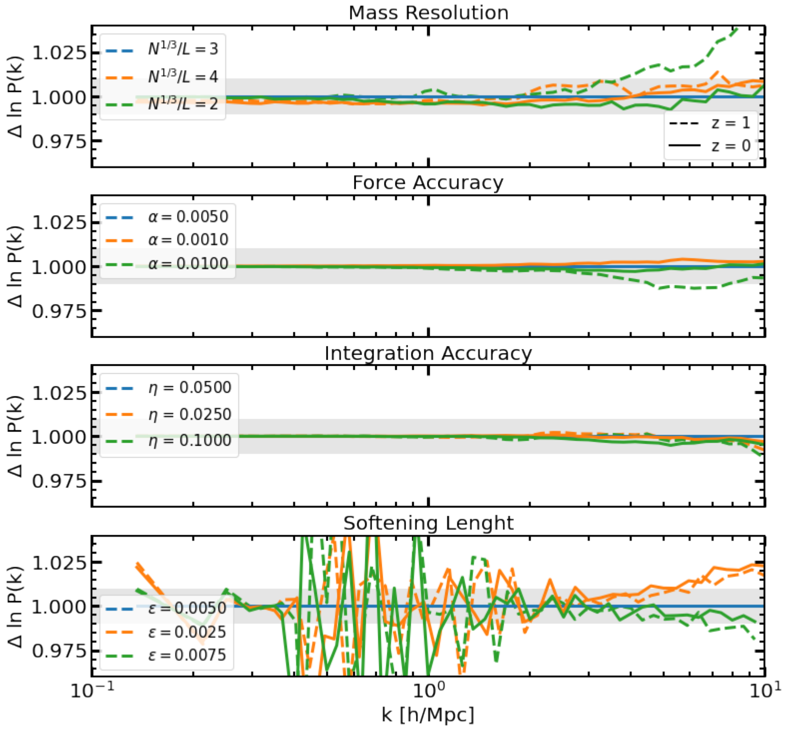

Figure 2.2: The impact of numerical parameters in our simulated nonlinear mass power spectra at $z = 0$ and $z = 1$. We display fractional differences with respect to the measurements in a simulation that adopts the same accuracy parameters as our main BACCO simulations. The grey bands indicate a region of $\pm 1\%$.

is the softening length. To mitigate its impact, we have adopted the following empirical correction to our power spectrum results

$$P(k) \to P(k)\ \left[1 + 1.62 \times 10^{-2} (\mathrm{erfc}(\ln(k/\epsilon) - 3.1) - 2)\right] \tag{2.1}$$

where ϵ is the softening length in units of $h\,\mathrm{Mpc}^{-1}$, and erfc is the complementary error function. We we found this expression by fitting the effect seen in the bottom panel of Fig. 2.2. We will apply this correction by default which brings the expected nominal accuracy of our power spectrum predictions to $\sim 1\%$ on all scales considered.

The EUCLID comparison project

To further validate our N-body code and quantify the accuracy of our numerical simulations, we have carried out the main simulation of the “Euclid code comparison project”, presented in Schneider et al. (2016). This simulation consists of 2048^3 particles of mass $1.2 \times 10^9\ h^{-1}\mathrm{M}_\odot$ in a $500\ h^{-1}\mathrm{Mpc}$ box, and has been carried out with several N-body codes: `RAMSES` (Teyssier, 2002), `PkdGrav3` (Potter et al., 2017), `Gagdet3` , and recently with `ABACUS` by Garrison et al. (2019).

Our realisation of this simulation adopts the same force and time-integration accuracy parameters as of main BACCO simulations, and the same softening lenght as `nenya`, $\epsilon =$

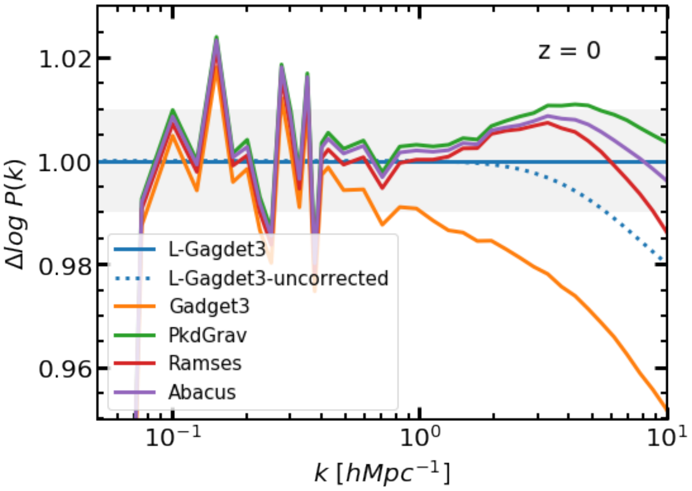

Figure 2.3: The nonlinear mass power spectrum at $z = 0$ of the "Euclid code comparison project". Each coloured curve displays the predictions of a different N-body code, as indicated by the legend, and we display ratios relative to our simulation result corrected by finite numerical resolution. Note that all N-body codes agree to better than 1% precision up to $k \sim 10h\,\mathrm{Mpc}^{-1}$, with the exception of the original `Gadget3` run presented in Schneider et al (2016).

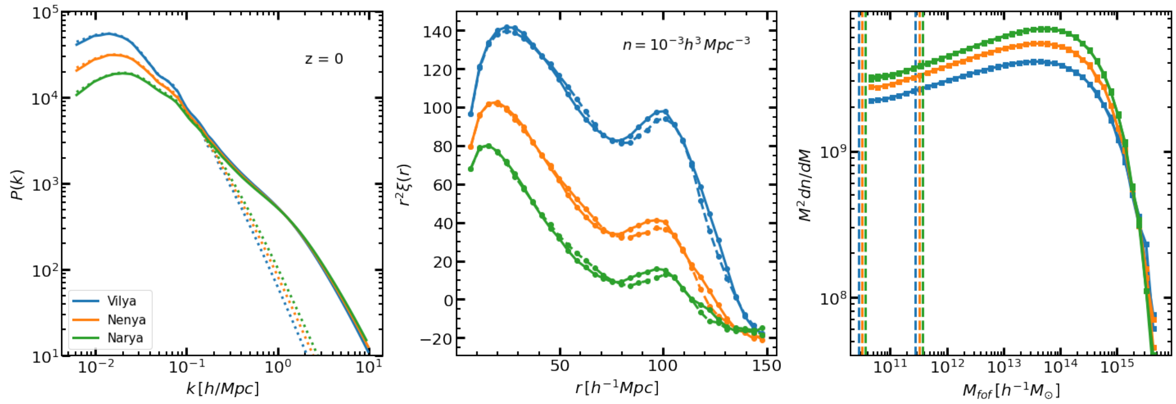

Figure 2.4: Predictions from the BACCO simulations, `vilya`, `nenya`, and `narya`, at $z = 0$. Left panel shows the nonlinear mass power spectrum as solid lines, and linear perturbation theory as dotted lines. The middle panel shows the redshift-space correlation function for subhalos with a number density of $10^{-3}\,h^3\,\mathrm{Mpc}^{-3}$, where solid and dashed lines show the results for each of the two opposite-phase simulations. The right panel shows the Friends-of-Friends halo mass function, with vertical dashed lines indicating the mass limit resolved with 10 and 100 particles.

$5\,h^{-1}\mathrm{kpc}$. The full calculation required 6230 timesteps and took 3×10^5 CPU hours employing 1024 MPI Tasks.

In Fig. 2.3 we compare the resulting power spectra at $z = 0$. We display the ratio with respect to our `L-Gadget3` results including the correction provided in Eq. 2.1. For comparison, we display the uncorrected measurement as a blue dashed line. Note the spikes on large scales are caused by noise due to a slighly different k-binning in the spectra.

Our results, `PkdGrav`, `RAMSES`, and that of `ABACUS` agree to a remarkable level – they differ by less than 1% up to $k \sim 10h\,\mathrm{Mpc}^{-1}$. This is an important verification of the absolute accuracy of our results, but it is also an important cross-validation of all these 4 N-body codes. Interestingly, the `Gadget3` result presented in Schneider et al. (2016) is clearly in tension with the other 4 codes. Since the underlying core algorithms in our code and in `Gadget3` are the same, the difference is likely a consequence of numerical parameters adopted by Schneider et al. (2016) not being as accurate as those for the other runs. In the future, it will be important to conduct code comparison projects were numerical parameters are chosen so that each code provides results converged to a given degree.

The BACCO simulations

Having validated our numerical setup, we now present an overview of the results of our BACCO simulations at $z = 0$ in Fig. 2.4.

In the left panel we show the nonlinear power spectrum in real space. Firstly, we see the low level of random noise in our predictions owing to the "Paired-&-Fixed" method. On large scales, we have checked that our results agree at the 0.5% level with respect to the linear theory solution, which we compute for each cosmology using the Bolztmann code `CLASS` (Lesgourgues, 2011a). Also on large scales, we see that the three simulations display significantly different power spectra, despite the three of them having identical values for σ_8. This is mostly a consequence of their different primordial spectral index, n_s. In contrast, on scales smaller than $k \sim 0.2h\,\mathrm{Mpc}^{-1}$, the spectra become much more similar as their linear spectra also do (shown by dotted lines).

In the middle panel we show the monopole of the redshift-space correlation functions for subhalos with a spatial number density equal to $10^{-3}\,h^3\mathrm{Mpc}^{-3}$ selected according to their peak maximum circular velocity. This is roughly analogous to a stellar mass selection above $5 \times 10^{10}h^{-1}\mathrm{M}_{\odot}$. We see a significant difference in the correlation amplitude among simulations. This hints at the potential constraining power of LSS if a predictive model for the galaxy bias is available. We display each of the two "Paired-&-Fixed" simulations in each cosmology as solid and dashed lines. Unlike in the power spectrum plot, the effect of pairing the initial phase fields is visible.

Finally, in the right panel of Fig. 2.4 we display the mass function of halos identified by the FoF algorithm. As in previous cases, there are clear differences among cosmologies. The minimum halo mass in our simulations is $\sim 3-4\times 10^{10}\,h^{-1}\mathrm{M}_{\odot}$, which should suffice to model galaxies with star formation rates above $10\,h^{-1}\mathrm{M}_{\odot}$/year at $z\sim 1$ (Orsi and Angulo, 2018), as expected to be observed by surveys like EUCLID, DESI, or J-PAS (Favole et al., 2017).

In the next section we will employ our BACCO simulations to predict the nonlinear mass power spectrum as a function of cosmology.

2.3 Nonlinear mass power spectrum Emulator

Our aim is to make fast predictions for the nonlinear power spectrum over the whole region of currently-viable cosmologies. In this section we describe how we achieve this by building (§2.3.1) and testing of a matter power spectrum emulator (§2.3.2).

Our basic strategy is the following:

- First, we define a target region in cosmological parameter space (§2.3.1) and iteratively select a set of training points that minimise the emulator uncertainty (§2.3.1).

- Second, we use the cosmology-rescaling approach over the outputs of our BACCO simulations (§2.3.1) to predict the power spectra in those training cosmologies (§2.3.1).

- Finally, we use Gaussian processes to build an emulator for the power spectra over the linear expectation (§2.3.1).

We test the performance and accuracy of our emulator (§2.3.2) and compare it against widely-used methods to predict the nonlinear power spectrum (§2.3.2).

2.3.1 Building the emulator

The parameter space

We aim to cover 8 parameters of the ΛCDM model extended with massive neutrinos and dynamical dark energy. Specifically, we consider the parameter range:

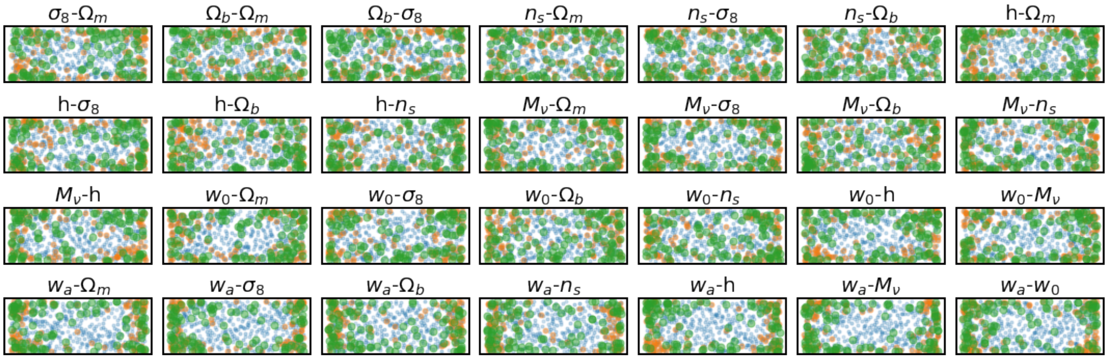

Figure 2.5: Distribution of cosmologies employed to build our BACCO emulator. Blue symbols display the location of cosmologies in our initial training set, whereas orange and green symbols display those subsequently selected by our iterative method. In each plot, the limits coincide with the full range of values considered (c.f. Eq 2.2).

$$
\begin{aligned}
\sigma_8 &\in [0.73, 0.9] \\
\Omega_{\rm m} &\in [0.23, 0.4] \\
\Omega_b &\in [0.04, 0.06] \\
n_s &\in [0.92, 1.01] \\
h\,[100\,{\rm km\,s^{-1}Mpc^{-1}}] &\in [0.6, 0.8] \\
M_\nu\,[{\rm eV}] &\in [0.0, 0.4] \\
w_0 &\in [-1.15, -0.85] \\
w_a &\in [-0.3, 0.3]
\end{aligned}
\tag{2.2}
$$

where M_ν is the total mass in neutrinos, σ_8 is the r.m.s. linear *cold mass* (dark matter plus baryons) variance in $8h^{-1}{\rm Mpc}$ spheres, and w_0 and w_a define the time evolution of the dark energy equation of state: $w(z) = w_0 + (1-a)w_a$. The parameter range we consider for (σ_8, Ω_m, Ω_b, n_s) corresponds to a $\sim 10\sigma$ region around the best-fit parameters of the analysis of Planck Collaboration et al. (2014a). For the dimensionless Hubble parameter, h, we expand the range to cover a 4σ region around current low-redshift measurements from supernovae data (Riess, 2019).

We assume a flat geometry, i.e. $\Omega_k = 0$ and $\Omega_m + \Omega_w + \Omega_\nu = 1$. We keep fixed the effective number of relativistic species to $N_{\rm eff} = 3.046$, and the temperature of the CMB $T_{\rm CMB} = 2.7255$ K and neglect the impact of radiation (i.e. $\Omega_r = 0$). Note, however, that it is relatively straightforward to relax these assumptions and include in our framework varying curvature, relativistic degrees of freedom, or other ingredients.

For comparison, we notice that the range of parameters covered by our emulator is approximately twice as large as that of the `Euclid emulator` (with the exception of w_0, which is similar), which implies a parameter space volume ~ 200 times larger, and that it covers cosmological parameters beyond the minimal ΛCDM: dynamical dark energy and massive neutrinos. In contrast, our parameter space is similar to that considered by the `Mira-Titan` Universe project (Heitmann et al., 2006; Lawrence et al., 2017), however, as we will discuss next, we cover the space with approximately 20 times the number of sampling points.

Training Cosmology Set

The next step is to define the cosmologies with which we will train our emulator. This is usually done by sampling the desired space with a Latin-Hypercube (e.g. Heitmann et al., 2006). We adopt a slightly different strategy based on the idea of iterative emulation of Pellejero-Ibañez et al. (2020) (see also Rogers et al., 2019), where we preferentially select training points in regions of high emulator uncertainty.

Let us first define the emulated quantity:

$$Q(k,z) \equiv \log(P(k,z)/P_{\rm linear}(k,z)) \tag{2.3}$$

where $P_{\rm linear}$ is the linear theory power spectrum and $P(k)$ is the measured nonlinear power spectrum of *cold* matter (i.e. excluding neutrinos). Emulating this quantity, rather than the full nonlinear power spectra, reduces significantly the dynamical range of the emulation, simplifying the problem and thus delivering more accurate results (see e.g. Euclid Collaboration et al., 2019).

To build our training set, we first construct a Latin-Hypercube with 400 points. We then build an emulator for Q, which provides the expectation value and variance for the emulated quantity (c.f. §2.3.1 for more details). We then evaluate the emulator over a Latin-Hypercube built with 2,000 points, and select the 100 points expected to have the largest uncertainty in their predictions. We add these points to our training set and re-build the emulator. We repeat this procedure 4 times.

We display the final set of training cosmologies, comprised of 800 points, in Fig. 2.5. Blue symbols indicate the initial training cosmologies, whereas orange and green symbols do so for the 2nd and 4th iteration, respectively. We can appreciate that most points in the iterations are located near the boundaries of the cosmological space, which minimise extrapolation.

It is worth mentioning that we sample our space significantly better than typical emulators. For instance, the `Mira-Titan` and `Euclid Emulator` projects employ 36 and 100 simulations, respectively. This implies that we can keep the emulator errors under any desired level, which could be problematic otherwise, as parameter-dependent uncertainties in models, could in principle bias parameter estimates. On the other hand, sampling points can be designed optimally so that emulation errors are much smaller than a naive Latin Hypercube

(Heitmann et al., 2014; Rogers et al., 2019), however, this can be only be done optimally for a single summary statistic: what could be optimal for the matter power spectrum, is not necessarily the best for, e.g, the quadrupole of the galaxy power spectrum.

Cosmology rescaling

Our next step is to predict nonlinear structure for each of our training cosmologies. For this, we employ the latest incarnation of the cosmology-rescaling algorithm, originally introduced by Angulo and White (2010).

In short, the cosmology-rescaling algorithm seeks a coordinate and time transformation such that the linear rms variance coincides in the original and target cosmologies. This transformation is motivated by extended Press-Schechter arguments, and returns highly accurate predictions for the mass function and properties of collapsed objects. On large scales, the algorithm uses 2nd-order Lagrangian Perturbation Theory to modify the amplitude of Fourier modes as consistent with the change of cosmology. On small scales, the internal structure of halos is modified using physically-motivated models for the concentration-mass-redshift relation (e.g. Ludlow et al., 2016).

The accuracy of the cosmology algorithm has been tested by multiple authors (Ruiz et al., 2011; Angulo and Hilbert, 2015; Mead and Peacock, 2014a; Mead et al., 2015; Renneby et al., 2018; Contreras et al., 2020a), and it has been recently extended to the case of massive neutrinos by Zennaro et al. (2019). Specifically, by comparing against a suite of N-body simulations, Contreras et al. (2020a) explicitly showed that the cosmology rescaling achieves an accuracy of $\lesssim 3\%$ up to $k = 5h\,\mathrm{Mpc}^{-1}$ over the same range of cosmological parameter values we consider here (c.f. Eq. 2.2). The largest errors appear on small scales and for dynamical dark energy parameters but, when restricted to the 6 parameters of the minimal ΛCDM model, the rescaling returns 1% accurate predictions. Note that the level of accuracy is set by the performance of current models for the concentration-mass-redshift relation (which usually are not calibrated for beyond ΛCDM parameters), and future progress along those lines should feedback into higher accuracy for our emulator.

For our task at hand, we first split the parameter space into three disjoint regions where `nenya`, `narya`, or `vilya` will be employed (Contreras et al., 2020b). Then, we load in memory a given snapshot of a given simulation and then rescale it to the corresponding subset of the 800 cosmologies. We employ 10 snapshots per simulation.

The full rescaling algorithm takes approximately 2 minutes (on 12 threads using OpenMP parallelization) per cosmology and redshift. Thus, all the required computations for building the emulator required approximately $10,000$ CPU hours – a negligible amount compared to that employed to run a single state-of-the-art N-body simulation.

Power Spectrum Measurements

We estimate the power spectrum in our rescaled simulation outputs using Fast Fourier Transforms. We employ a cloud-in-cells assignment scheme over two interlaced grids (Sefusatti et al., 2016) of $N = 1024^3$ points. To achieve efficient measurements at higher wavenumbers, we repeat this procedure after folding the simulation box 4 times in each dimension. We measure the power spectrum in 120 evenly-spaced bins in $\log k$, from $k = 0.01$ to $5h\,\mathrm{Mpc}^{-1}$, and transition from the full to the folded measurement at half the Nyquist frequency. We have explicitly checked that this procedure returns sub-percent accurate power spectrum measurements over the full range of scales considered.

Although our BACCO simulations have high mass resolution, for computational efficiency, hereafter we will consider a subset of 1080^3 particles (uniformly selected in Lagrangian space) as our dark matter catalogue. This catalogue, however, is affected by discreteness noise. For a Poisson sampling of N points over a box of sidelength L, the power spectrum receives a contribution equal to $(L/N)^3$. However, this might not be an accurate estimate for our discreteness noise since our sampling is homogeneous in Lagrangian coordinates. We have estimated its actual contribution as a third-order polynomial by comparing the spectra of the full and undiluted samples at different redshifts. We found that the amplitude is proportional to ~ 0.6 times the Poisson noise at $z = 0$, and that it progressively decreases in amplitude at higher redshifts, to reach ~ 0.2 times the Poisson noise at $z = 2$.

All our power spectrum measurements will be corrected by discreteness noise by subtracting the term described above, and further corrected for finite numerical accuracy following section §2.2.3. However, this procedure is not perfect, and we still detect $\sim 2\%$ residuals at $z \sim 1$ at $k \sim 5h\,\mathrm{Mpc}^{-1}$. This will contribute to uncertainties in our emulator, which, however, are smaller than systematic uncertainties induced by the cosmology scaling.

Emulator Data

In total, we employ more than 16,000 power spectrum measurements; 400+400 training cosmologies at approximately 10 different cosmic times for two paired simulations. Grey shaded regions in Fig. 2.6 show the range covered by this data at $z = 0$ and $z = 1$, with the inset focusing on the range of wavemodes where baryonic acoustic oscillations are found. Blue and red lines show two randomly-chosen cosmologies.

On the largest scales, we can see that our rescaled simulations agree almost perfectly with linear theory. Although expected, it provides further validation of the dataset. On intermediate scales, we can see an oscillatory behaviour – better appreciated in the figure insets. This is a consequence of the nonlinear smearing of baryonic acoustic oscillations

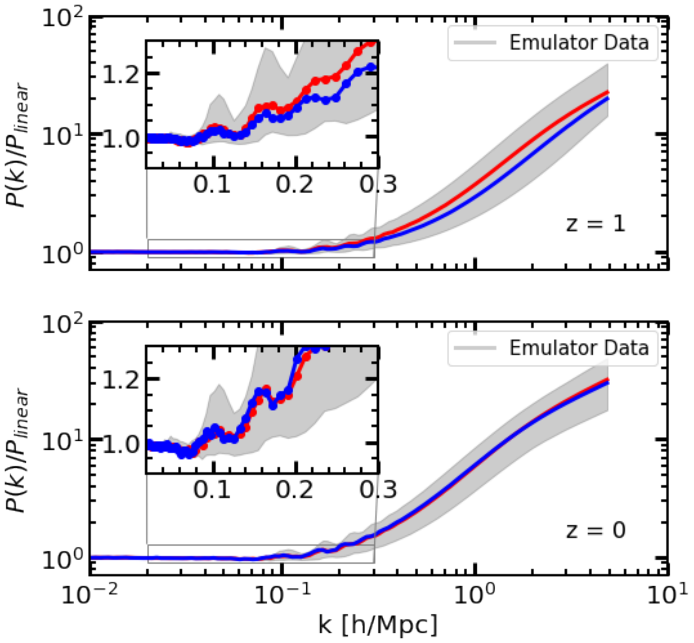

Figure 2.6: Nonlinear power spectra at $z = 0$ and $z = 1$ over the linear theory expectations, as predicted by rescaled BACCO simulations. Grey regions indicate the range covered by the training set employed to construct our emulator. Blue and red lines display two particular, randomly-chosen, measurements.

caused mostly by large-scale flows. At higher redshifts, the amplitude of this feature decreases since BAO are better described by linear theory. On smaller highly nonlinear scales, we see an increase of more than one order of magnitude with different cosmologies differing by even factors of 3-4.

Principal Component Analysis

To reduce the dimensionality of our power spectrum measurements, we have performed a principal components (PC) analysis over our whole dataset, after subtracting the mean. We have kept the 8 k-vectors with the highest eigenvalues, which together can explain all but 10^{-3} of the data variance.

In the top panel of Fig. 2.7 we show the amplitude of these PCs, as indicated by the legend. The most important vector is a smooth function of wavenumber and roughly captures the overall impact of nonlinear evolution. Subsequent vectors describe the smearing of the BAO and further nonlinear modifications. It is worth noting that only the 7th and 8th PC vectors display any noticeable noise, owing to the highly precise input dataset.

In the bottom panel of the Fig. 2.7 we display the ratio of the full $Q \equiv \log(P/P_{\rm linear})$ over that reconstructed using the first PCs aforementioned. We show the results for a random 2% of the power spectrum in our training data. We can see that almost all of them are recovered to better than 0.5%. It is interesting to note that the residuals, although increase on intermediate scales, are mostly devoid of structure, which suggests that including additional PCs will simply

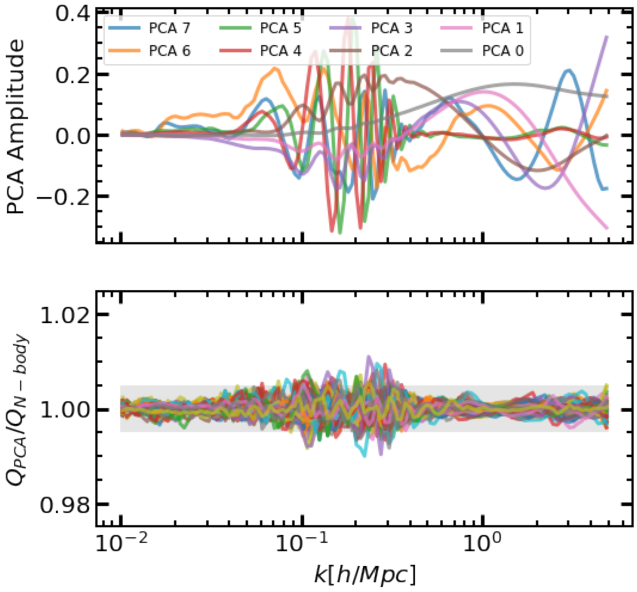

Figure 2.7: Top: The amplitude of the first 8 vectors of a principal component analysis of our power spectrum data. Bottom: Ratio between the original and PCA-reconstructed $Q \equiv \log(P/P_{\rm linear})$ for a random 2% of our data at $z = 0$. The grey band indicates a region of $\pm 0.5\%$, which can be considered as an indication of the statistical noise in our data.

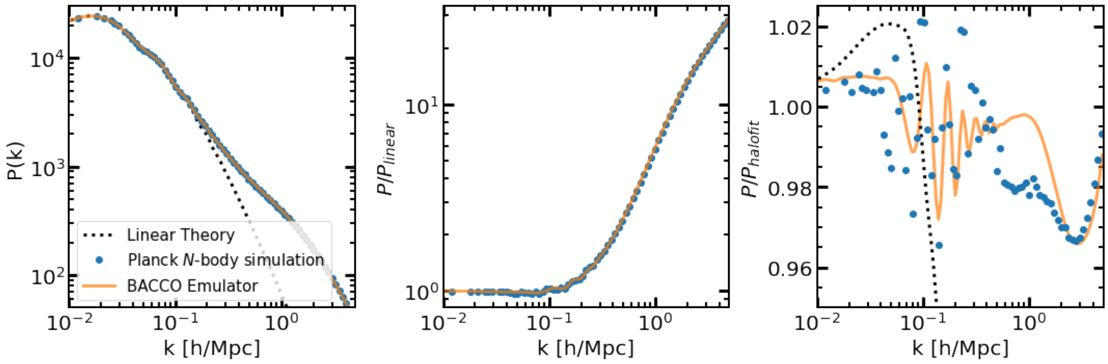

Figure 2.8: Comparison between the nonlinear power spectrum at $z = 0$ as predicted by a full N-body simulation and our BACCO emulator for a set of cosmological parameters consistent with recent analyses of the Planck satellite data. The left panel shows the full power spectrum, whereas middle and rightmost panel show the same data relative to the expectations of linear theory or halofit, respectively. The emulator and simulation predictions agree to better than $\sim 2\%$ over the full range of scales considered.

recover more accurately the intrinsic noise in our dataset rather than systematic dependencies on cosmology.

To confirm this idea, we have repeated our emulation but keeping twice as many PCs. Although the description of the values of Q in our dataset gained accuracy (decreasing the differences down to $\sim 0.25\%$), the performance of the emulator at predicting other cosmologies did not increase. This supports the idea that PCs beyond the 8-*th* are simply capturing particular statistical fluctuations in the training set, rather than cosmology-induced features.

Gaussian processes

To interpolate between our training data, and thus predict $Q(k, z)$ for any cosmology, we will employ Gaussian Processes Regression. Note that other options are possible, such as polynomial chaos expansion, or deep neural networks.

In short, Gaussian processes assume that every subset of points in a given space is jointly Gaussian distributed with zero mean and covariance K. The covariance is *a priori* unknown but it can be estimated from a set of observations (e.g. our training set). Once the covariance is specified, the Gaussian process can predict the full probability distribution function anywhere in the parameter space.

In our case, we measure the amplitude associated to each PC in each training set. We then build a separate Gaussian Process for each of our PCs, using the package `GPy` (GPy, 2012). We assume the covariance kernel to be described by a squared exponential, with correlation length and variance set to the values that best describe the correlation among our data, found by maximising the marginal likelihood.

For a given target cosmology in our parameter space, we can predict the amplitude associated to each PC and then reconstruct the full $Q(k, z)$ vector. Any given evaluation takes approximately 180 milliseconds.

2.3.2 Testing the emulator

A first example

We present a first look at our emulator results in Fig. 2.8, where we show the nonlinear power spectrum at $z = 0$ for a cosmology consistent with a recent analysis of Planck data. Specifically, we consider: $\sigma_8 = 0.8102$, $\Omega_m = 0.30964$, $\Omega_b = 0.04897$, $n_s = 0.9665$, $h = 0.6766$, $M_\nu = 0.0$, $w_0 = -1.0$, $w_a = 0.0$. The left panel shows the full power spectrum, the middle panel do so relative to linear theory, and the rightmost panel relative to `HaloFit` calibrated by Takahashi et al. (2012).

For comparison, we include as orange circles, the results of a full N-body simulation

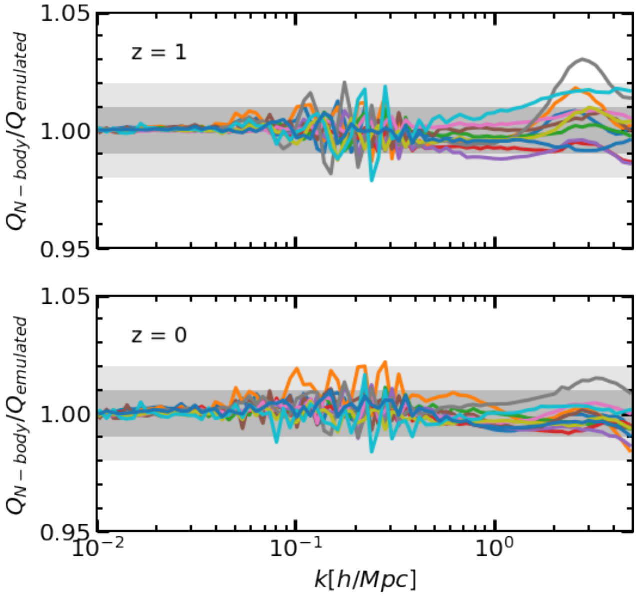

Figure 2.9: Comparison between $Q \equiv \log(P/P_{\rm linear})$ predicted by our emulator and that computed directly by scaling our BACCO simulations to the desired cosmology. Top and bottom panels display results at $z = 1$ and $z = 0$, respectively, for 10 cosmologies that span our whole parameter space.

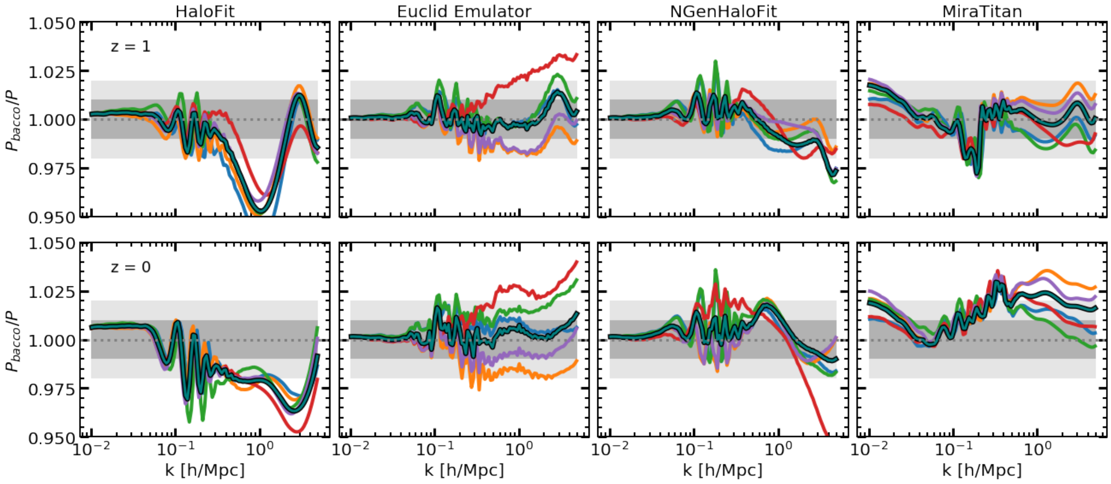

Figure 2.10: Comparison between nonlinear power spectrum predicted by our emulator and by four other methods. From left to right, panels display a comparison against `Halofit`, `Euclid Emulator`, `NGenHaloFit`, and `MiraTitan`. Top and bottom rows show results for $z = 1$ and $z = 0$, respectively. Each coloured curve represents a different cosmology within the parameter space where the `Euclid Emulator` has been calibrated. We highlight the "Euclid reference" cosmology as a thick line. Grey bands indicate ± 1 and $\pm 2\%$ regions.

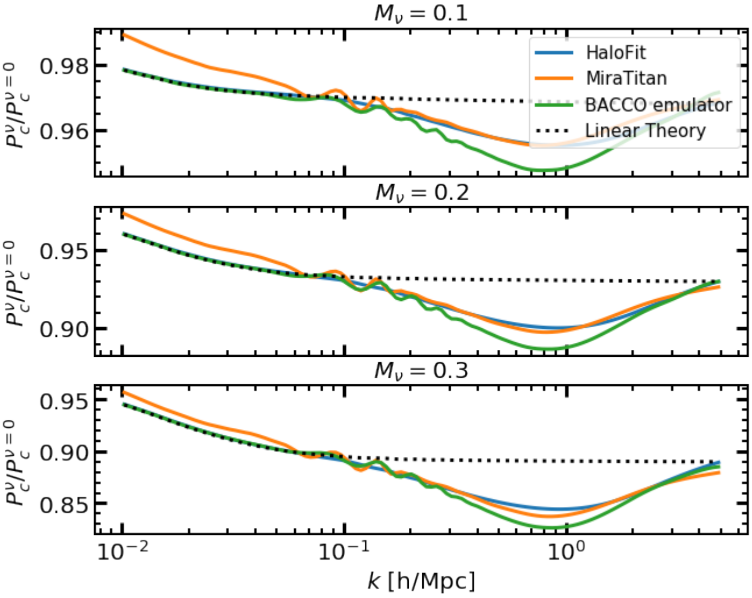

Figure 2.11: The ratio between the *cold* matter power spectra in massive neutrino cosmologies, P_c^ν, and the case without any massive neutrino, $P_c^{\nu=0}$. We show the predictions of linear theory (dotted line) and of three models: `HaloFit`, `Mira-Titan` emulator and our BACCO emulator.

with the same mass resolution and numerical parameters as those of our main BACCO suite, but in a smaller box, $L = 512\,h^{-1}\mathrm{Mpc}$. Also as in our BACCO suite, the initial conditions have been "Paired-&-Fixed" for this simulation.

Overall, we can see that the BACCO emulator and the N-body simulation agree to a remarkable level, being indistinguishable by eye in the leftmost and middle panels. In particular, on large scales, both agree with linear theory (which only can be appreciated thanks to the "Paired-&-Fixed" initial conditions); on intermediate scales, both also predict a BAO featured smeared out compared to linear theory.

In the rightmost panel we can see these aspects in more detail. Firstly, we note that the simulation and emulator results agree to about 1% on all the scales considered. This is consistent with the expected accuracy of the cosmology rescaling method, but also note that due to its somewhat small volume, the cosmic variance in the N-body simulation results are not negligible. It is also interesting to note the systematic disagreement with the predictions from `halofit`. In following subsections we will explore these differences further.

Accuracy

To start testing the accuracy of our emulator, we have defined 10 cosmologies distributed over the target parameter space (c.f.§2.3.1) using a Latin hypercube. We then rescale our BACCO outputs to those parameters and compare the results against our emulation predictions. This essentially tests how accurate the PCA decomposition and emulation via Gaussian Process Regression are.

In Fig. 2.9 we show the ratio of the emulated to the rescaled nonlinear power spectrum at $z = 0$ and $z = 1$ for the 10 cosmologies mentioned before (we recall that nor $z = 0$ nor $z = 1$ were explicitly included in the emulator). We can see that on all scales our results are better than $\pm 2\%$ percent, and that most of the cosmologies are predicted to better that 1% at $z = 0$. Although this is already a high accuracy, we note that more and more rescaled results can be added over time to progressively improve the quality of the emulation. We can also appreciate oscillatory features around the wavenumbers where BAO are located, this suggest that emulating more finely binned power spectra, could recover them more precisely.

We recall that this level of uncertainty is comparable to the accuracy expected by the cosmology rescaling algorithm: 1% for parameters of the minimal ΛCDM and $\sim 3\%$ when considering massive neutrinos and dynamical dark energy.

Comparison with HaloFit, EuclidEmulator, and NgenHaloFit

We now compare our emulation results against four widely-used methods to predict the nonlinear evolution: `HaloFit` (Takahashi et al., 2012), the `Euclid Emulator` (Euclid Collaboration et al., 2019), `NGenHalofit` (Smith and Angulo, 2019), and `Mira-Titan` (Lawrence et al., 2017). Since not all of them have been calibrated over the whole parameter space covered by our emulator, we have restricted the comparison to the volume covered by the `Euclid Emulator`. We note that of our 800 training cosmologies, only 2 of them fall within this parameter volume.

In Fig. 2.10 we display the ratio of those predictions to that of our BACCO emulator. Coloured lines show 10 cosmologies set by a latin hypercube inside the `Euclid Emulator` parameter space. In addition, we show as a heavy line the Euclid reference cosmology: $\Omega_{\rm cdm} = 0.26067$, $\sigma_8 = 0.8102$, $\Omega_{\rm b} = 0.04897$, $n_s = 0.9665$, $h = 0.6766$, $M_\nu = 0$, $w_0 = -1$, $w_a = 0$, employed by (Euclid Collaboration et al., 2019).

On large scales, $k < 0.08 h\,{\rm Mpc}^{-1}$, our emulator agrees almost perfectly with `NGenHalofit` and the `Euclid Emulator`. `Halofit`, on the other hand shows a small constant power deficit, whereas the `Mira-Titan` displays a weakly scale-dependent offset. Over this range of scales, `Mira-Titan` is given by TimeRG perturbation theory (Pietroni, 2008; Upadhye et al., 2014), which might indicate inaccuracies in that approach.

On intermediate scales, $0.08 < k/[h\,{\rm Mpc}^{-1}] < 0.5$, our results agree very well with those of `NGenHalofit`; for almost all cosmologies the differences are within the expected accuracy of our emulator. In contrast, we see that `Halofit` overestimates the amount of power by about 2% at $z = 0$ and it does not correctly captures the BAO nonlinear smearing (as was already noted by Euclid Collaboration et al., 2019). On the other hand, `MiraTitan` underestimates the power by up to 2.5% at $z = 0$, and displays a strong feature at $k \sim 0.2 h\,{\rm Mpc}^{-1}$ at $z = 1$. Over this range of scales `MiraTitan` employs a suite of low-resolution, large volume simulations, thus the disagreement could be due to an insufficient numerical accuracy in their simulations.

On small scales, $k > 0.5h\,\mathrm{Mpc}^{-1}$, we continue to see differences among the three methods. For halofit, `NGenHaloFit` and `Mira-Titan`, they are systematic, roughly independent of cosmology, and decrease at higher redshift. This suggests that the origin is mostly caused by the different numerical accuracy in the underlying simulations. Specifically, the simulations used by Smith and Angulo (2019) employ a softening length $\epsilon = 8h^{-1}\mathrm{kpc}$, which according to Eq. 2.1 is expected to produce an underestimation of 1.5% at $k = 5h\,\mathrm{Mpc}^{-1}$. In addition, the transition between their high and low-resolution runs occurs at $k \sim 0.6h\,\mathrm{Mpc}^{-1}$ which might be related to the deficit we observe at $k \sim 0.7 - 0.7h\,\mathrm{Mpc}^{-1}$ at $z = 0$.

In contrast, the differences with respect to `Euclid Emulator` vary significantly for different cosmologies. Specifically, for the Euclid Reference Cosmology, the agreement is subpercent on all scales. However, for our other test cosmologies, differences have a spread of $\sim 5\%$, even at $k < 1h\,\mathrm{Mpc}^{-1}$. We do not see this behaviour with other methods, which might suggest that there are significant uncertainties in the emulated power spectra of the `Euclid Emulator` beyond their quoted precision.

Finally, we note that there is a 1% "bump" at $k \sim 3h\,\mathrm{Mpc}^{-1}$ in all $z = 1$ panels, which is originated by our imperfect shotnoise correction.

The previous comparison was done in a rather restricted cosmological parameter volume, which served as a strong test of our accuracy. However, one of the biggest advantages of our method is the ability to predict much more extreme cosmologies even with non-standard ingredients. We provide an example of this next.

In Fig. 2.11 we show the predictions for the effects of massive neutrinos on the $z = 0$ cold matter (baryons plus dark matter) power spectrum. We display the ratio between cases with various neutrino masses, P_c^{ν}, relative to that without massive neutrinos P_c^{ν}. In all cases we use $A_s = 2.1 \times 10^{-9}$ and fix all the other cosmological parameters to those of the "Euclid reference cosmology". We only display the predictions of `HaloFit` and `Mira-Titan`, since `NGenHaloFit` nor the `Euclid Emulator` have been calibrated in the case of massive neutrinos.

We can see that on large scales, our predictions agree with both linear theory and `HaloFit`. For very massive neutrino cases, there is also a good agreement with `MiraTitan`, but there is a significant disagreement for $M_\nu = 0.1$, this might be caused by the scale-dependent features on large scales seed in the previous figure. On intermediate scales, all predictions also agree on the broadband shape of the neutrino-induced suppression, but our emulator is also able to capture the slightly different BAO suppression expected when massive neutrinos are present. On small scales, all three methods describe the well-known neutrino-induced spoon-like suppression, disagreeing slightly on the magnitude of the maximum suppression. Note however, we expect our emulator to predict more precisely the full shape of the nonlinear power spectrum, owing to the systematic uncertainties in `HaloFit` and `Mira-Titan` discussed before.

2.4 Summary

In this chapter, we have presented the BACCO simulation project: a framework that aims at delivering high-accuracy predictions for the distribution of dark matter, galaxies, and gas as a function of cosmological parameters.

The basic idea consists in combining recent developments in numerical cosmology – N-body simulations, initial conditions with suppressed variance, and cosmology-rescaling methods – to quickly predict the nonlinear distribution of matter in a cosmological volume. The main advantage of our approach is that it requires only a small number of N-body simulations, thus they can be of high resolution and volume. This in turn allows sophisticated modelling of the galaxy population (for instance in terms of subhalo abundance matching, semi-empirical or semi-analytic galaxy formation model), and of baryons (including the effects of cooling, star formation and feedback) in the mass distribution.

The main suite of simulations of the BACCO project consists in 3 sets of "Paired-&-Fixed" simulations, each of them of a size $L = 1440\,h^{-1}\mathrm{Mpc}$ and with 80 billion particles. Their cosmologies were carefully chosen so that they maximise the accuracy of our predictions (Fig. 2.1 and Table 2.1) while minimising computational resources. We have validated the accuracy of our numerical setup with a suite of small N-body simulations (Fig. 2.2) and by presenting a realization of the Euclid comparison project (Fig. 2.3). These tests indicate our simulations have an accuracy of 1% up to $k \sim 5h\,\mathrm{Mpc}^{-1}$.

We have employed our BACCO simulations to predict more than 16,000 nonlinear power spectra at various redshifts and for 800 different cosmologies (Figs. 2.5 and 2.6). These cosmologies span essentially all the currently allowed region of parameter space of ΛCDM extended to massive neutrinos and dynamical dark energy. Using these results, we built an emulator for the 8 most important principal components of the ratio of the nonlinear power spectrum over the linear expectation (Fig. 2.7). We show our emulation procedure to be accurate at the $1-2\%$ level over $0 < z < 1.5$ and $10^{-2} < k/(h\,\mathrm{Mpc}^{-1}) < 5$ (Figs. 2.8 and 2.9). Therefore, our accuracy is currently limited by that of cosmology rescaling methods. We compared our predictions against four popular methods to quickly predict the power spectrum in the minimal ΛCDM scenario (Fig. 2.10) and in the presence of massive neutrinos (Fig. 2.11).

Since predicting a given cosmology requires an almost negligible amount of CPU time in our BACCO framework, we foresee the accuracy of our emulator to continuously improve as we include more cosmologies in the training set. Extensions to more parameters should also be possible, as, for instance, the number of relativistic degrees of freedom or curvature, can be easily incorporated in cosmology-rescaling methods. Additionally, there are several aspects of such methods that are likely to improve in the future, which should feedback into more accurate predictions and emulated power spectra.

On the other hand, effects induced by baryons on the shape of the nonlinear mass power spectrum can be of 10-30% (e.g. Chisari et al., 2019). Thus, they are much larger than current uncertainties in our emulation, cosmology-rescaling, or even shotnoise. These effects of star formation, gas cooling, and feedback from supermassive black holes are quite uncertain and differ significantly between different hydrodynamical simulations. However, they can be accurately modelled in post-processing using dark-matter only simulations (Schneider and Teyssier, 2015b). Specifically, Aricò et al. (2020b) showed that the effects of 7 different state-of-the-art hydrodynamical simulations could all be modelled to better than 1% within simple but physically-motivated models. In the next chapters, we will implement such models and extend our matter emulation to simultaneously include cosmological and astrophysical parameters.

Chapter 3

Baryonification: exploring astrophysical scenarios

In this chapter, adapted from the paper “Modelling the large-scale mass density field of the Universe as a function of cosmology and baryonic physics” (Aricò et al., 2020b), we present and test a framework that models the three-dimensional distribution of mass in the Universe as a function of cosmological and astrophysical parameters. Our approach combines two different techniques: a rescaling algorithm that modifies the cosmology of gravity-only N-body simulations, and a baryonification algorithm which mimics the effects of astrophysical processes induced by baryons, such as star formation and AGN feedback. We show how this approach can accurately reproduce the effects of baryons on the matter power spectrum of various state-of-the-art hydrodynamical simulations (EAGLE, Illustris, Illustris-TNG, Horizon-AGN, and OWLS, Cosmo-OWLS and BAHAMAS), to better than 1% from very large down to small, highly nonlinear, scales ($k \sim 5\,h\,\mathrm{Mpc}^{-1}$), and from $z = 0$ up to $z \sim 2$. We highlight that, thanks to the heavy optimisation of our algorithms, we can obtain these predictions for arbitrary baryonic models and cosmology (including massive neutrinos and dynamical dark energy models) with an almost negligible CPU cost. With these tools in hand we explore the degeneracies between cosmological and astrophysical parameters in the nonlinear mass power spectrum. Our findings suggest that after marginalising over baryonic physics, cosmological constraints inferred from weak gravitational lensing should be moderately degraded.

3.1 Introduction

Measuring the spatial distribution and growth of mass in the Universe is one of the main probes of the cosmic acceleration and the nature of dark matter (see e.g. Weinberg et al., 2013). Consequently, weak gravitational lensing, which directly maps the cosmic gravitational potential and thus the matter distribution, is among the primary targets of several current and future cosmological surveys (KIDS, DES, HSC SSP, Euclid, LSST).

One of the main advantages of weak lensing is that, since dark matter dominates the mass budget in the Universe, its theory modelling should mostly rely on well-understood physics such as General Relativity. However, although gravitational interactions dominate the nonlinear evolution of mass in the Universe, processes induced by baryonic interactions cannot be ignored. In fact, the accuracy of future measurements will be such that, if neglected, baryonic physics could easily induce a large bias on the cosmological constraints inferred (Semboloni et al., 2011; Schneider et al., 2020).

Similarly, various other cosmological observables depend on the distribution of baryons and dark matter on large scales and thus are affected by the same baryonic physics. For instance, thermal and kinetic Sunyaev-Zeldovich effects can probe the cosmological parameters and the law of gravity, but are also sensitive to the distribution and the (thermo-) dynamical state of the gas in and around haloes (Sunyaev and Zeldovich, 1970; McCarthy et al., 2014; Hojjati et al., 2017; Park et al., 2018). Therefore, in addition to quantifying the impact of e.g. intrinsic alignment of galaxies, non-thermal pressure, or uncertainties in the redshift distribution of background galaxies, the effects of baryons also need to be modelled and understood to great precision in modern cosmology.

Currently, the most accurate way to predict the joint evolution of dark matter and baryons is through cosmological hydrodynamical simulations. These simulations seek to follow the relevant astrophysical processes for galaxy formation along with the nonlinear evolution of the mass field. In general, they predict a suppression of the mass clustering at intermediate scales ($k \sim 1\,h\,\mathrm{Mpc}^{-1}$), and an enhancement on small scales ($k > 10\,h\,\mathrm{Mpc}^{-1}$) with respect to the results from Gravity Only (GrO) simulations. The former effect is predominantly due to feedback from AGN and supernovae, whereas the latter to the condensation of baryons into stars (for a review, see Chisari et al., 2019).

Despite a broad agreement among different state-of-the-art simulations, there are discrepancies on the amplitude, redshift evolution, and scales affected by baryonic effects. This is likely a consequence of differences in the numerical scheme, and in the (uncertain but necessary) implementation of various sub-grid recipes (Chisari et al., 2018; van Daalen et al., 2020). Furthermore, since most astrophysical processes included in hydrodynamical simulations cannot be predicted ab-initio, they have to be calibrated against observations – a process which has an intrinsic uncertainty, involve many free parameters, and could moreover depend on the assumed cosmology. All this suggests that we are far from a deterministic modelling of astrophysical processes, and that the impact of baryons is still not understood at a quantitative level. Therefore, the modifications predicted by simulations should not be used at face value in cosmological parameter estimations, and more flexible methods should be seeked.

Different approaches have been adopted to incorporate baryonic effects into the data analysis pipelines. For instance, marginalising over nuisance parameters (e.g Harnois-Déraps et al., 2015); identifying the range of scales potentially affected by baryonic physics and exclude them in data analyses (e.g. Troxel et al., 2018) (but at the expense of discarding a potentially huge amount of cosmological information); or to perform a Principal Components Analysis (PCA) and remove the first components (Eifler et al., 2015; Huang et al., 2019).

More general attempts to describe the mass field in the presence of baryons are found in several extensions of the halo-model (e.g. Semboloni et al., 2011; Mohammed et al., 2014; Fedeli, 2014; Mead et al., 2015; Debackere et al., 2020); in terms of response functions calibrated using Separate Universe simulations (Barreira et al., 2019); in perturbative modelling (Lewandowski et al., 2015); displacing particles according to the expected gas pressure (Dai et al., 2018); or even using machine learning (Tröster et al., 2019).

In this work we follow another approach, namely the Baryon Correction Model (BCM), initially proposed by Schneider and Teyssier (2015a) and extended in Schneider et al. (2019). The main idea behind this technique is to split mass elements into 4 categories: galaxies, hot bound gas in haloes, ejected gas and dark matter, whose abundance and spatial distribution are parametrised with physically-motivated recipes. The position of particles in a GrO simulation is then perturbed accordingly.

The advantages of this approach are multiple. Firstly, it is physically motivated and does not rely on any specific hydrodynamical simulation. The approach also captures the nonlinear regime, it takes into account environmental effects, and it provides the three-dimensional matter density field. Finally, it has only a few free parameters which could be constrained directly by observations. Unfortunately, the approach is computationally expensive and relies on the existence of a suite of high-resolution simulations with varying cosmological parameters, both of which limit its usability in real data analyses.

Here, we propose a modified version of the BCM that solves these issues. Our version captures the essence of the original approach but with different assumptions and in a computationally efficient manner. We also extend the model to identify individual simulation particles as part of galaxies, hot gas, cold (ejected) gas, or dark matter. Importantly, we also demonstrate that our modified version of the BCM can be accurately combined with the cosmology-scaling algorithm presented in Angulo and White (2010), so that the BCM can be applied on top of any set of cosmological parameters.

Putting these two ingredients together, we predict the mass power spectrum simultaneously as a function of cosmology and astrophysical parameters. To test the accuracy of our approach, we employ a single GrO simulation with which we reproduce, to better than 1%, the power spectrum suppression as predicted by various state-of-the-art simulations (EAGLE, Illustris, Illustris-TNG, OWLS, Cosmo-OWLS, BAHAMAS and Horizon-AGN) which adopt different cosmologies and galaxy formation prescriptions. Furthermore, we test the flexibility of our model at $z \leq 2$, for OWLS, Cosmo-OWLS, BAHAMAS and Horizon-AGN. We find that the accuracy of our model does not degrade at high redshifts, indicating that our assumptions hold over all the broad range of scales and cosmic times considered. As an initial application of the framework developed in this manuscript, we explore the impact of baryons in extracting cosmological information from the mass power spectrum. We stress also the importance of quantifying and correctly propagating the uncertainties of the data model employed, which can be the leading source of error in the forthcoming weak-lensing surveys.

This chapter is organised as follows: in §3.2 we present the N-body simulations used in our work, in §3.3 we introduce our baryonic model and quantify its impact in the mass power spectrum; in §3.4 we briefly describe the cosmology rescaling algorithm, its implementation, and its combination to the BCM; in §3.5 we fit state-of-the-art hydrodynamical simulations and provide the best-fitting parameters at $z = 0$, studying also their redshift evolution. We explore the cosmological information in the power spectrum in §3.6. We discuss our results and conclude in §3.7.

3.2 Numerical Simulations

3.2.1 Gravity-Only Simulations

Our GrO simulations were run with `L-GADGET-3` (Angulo et al., 2012), an optimised and memory-efficient version of `GADGET` (Springel, 2005). The initial conditions were generated on-the-fly at $z = 49$ using 2nd-order Lagrangian Perturbation theory and have suppressed cosmic variance thanks to the "fixed and paired" technique (Angulo and Pontzen, 2016). Gravitational forces were computed using a Tree-PM algorithm with a Plummer-equivalent softening length of $\epsilon_s = 6.7\,h^{-1}\mathrm{kpc}$. The force and time integration accuracy parameters were chosen so that $z = 0$ power spectra are accurate at the $\sim 1\%$ level at $k \sim 5\,h\,\mathrm{Mpc}^{-1}$.

We have built (sub)halo catalogues with a Friends-of-Friends algorithm and a modified version of `SUBFIND` (Springel et al., 2001). The FoF linking length is 20% of the mean inter-particle separation, $\ell = 67\,h^{-1}\mathrm{kpc}$. We kept objects gravitationally bound and resolved with at least 20 particles. Additionally, for all the simulations we stored a set of particles (homogeneously selected in Lagrangian space) diluted by a factor of 4^3, which we will use as our dark matter catalogue.

We have run a set of three (paired) simulations, with box sides of 64, 128, 256 $h^{-1}\mathrm{Mpc}$ and 192^3, 384^3, 768^3 particles of mass $m_p \approx 3.2 \times 10^9\ h^{-1}\mathrm{M}_{\odot}$. Therefore, Milky-Way like haloes are resolved with ~ 300 particles. The particle mass was also chosen to achieve a high accuracy on the nonlinear power spectrum (Schneider et al., 2016).

The cosmological parameters were chosen to maximise the accuracy of the rescaling algorithm over a wide range of cosmologies. Specifically: the density of cold dark matter, baryons and dark energy, in units of the critical density, are $\Omega_{\rm cdm} = 0.265$, $\Omega_{\rm b} = 0.05$, $\Omega_\Lambda = 0.685$ respectively, the Hubble parameter $H_0 = 60$ km s^{-1} Mpc^{-1}, the spectral index of the primordial power spectrum $n_s = 1.01$, the amplitude of the linear fluctuation of the matter density field at $8\,h^{-1}{\rm Mpc}$, $\sigma_8 = 0.9$, the optical depth at recombination $\tau = 0.0952$, the dark energy equation-of-state parameters assuming a Chevallier-Polarski-Linder parametrisation, (Chevallier and Polarski, 2001; Linder, 2003), $w_0 = -1$ and $w_a = 0$, and the sum of the neutrino masses $\sum m_\nu = 0$ eV. We refer to Contreras et al. (2020a) for further details.

To test the accuracy of the combination of cosmology scaling and baryonic model, we have carried out another paired simulation adopting the Planck 2013 cosmology (Planck Collaboration et al., 2014b, hereafter Planck13): $\Omega_{\rm cdm} = 0.2588$, $\Omega_b = 0.0482$, $\Omega_\Lambda = 0.6928$, $H_0 = 67.77$ km s^{-1} Mpc^{-1}, $n_s = 0.961$, $\sigma_8 = 0.828$, $\tau = 0.0952$, $w_0 = -1$, $w_a = 0$, $\sum m_\nu = 0$. This second simulation has the same number of particles and initial white-noise field as our main simulation, but a box size of $272.4\,h^{-1}{\rm Mpc}$ (instead of $256\,h^{-1}{\rm Mpc}$). This volume was chosen to exactly match the box size of our largest simulation after its cosmology was rescaled to Planck13.

All the power spectra shown throughout this chapter, unless stated otherwise, are computed by assigning particles in two 512^3 interlaced grids employing a *cloud-in-cell* mass assignment scheme, and using Fast Fourier Transforms. This results into a power spectrum estimation accurate to 1% up to the grid Nyquist frequency (see Sefusatti et al., 2016). We have checked that using a *triangular shaped cloud* scheme our results do not change.

The shot noise contribution is estimated as $1/\bar{n}$, and subtracted. $\bar{n}\,P(k)$ reaches 0.01 at $k \sim 5\,h\,{\rm Mpc}^{-1}$, a scale 4 times larger than the typical wavenumber affected by our choice of softening length ($k \sim \pi(2.7\,\epsilon_s)^{-1} \approx 20\,h\,{\rm Mpc}^{-1}$). Therefore, we will focus on scales $k \lesssim 5h\,{\rm Mpc}^{-1}$, where we expect numerical noise in our results to be less than 1%.

3.2.2 Hydrodynamical Simulations

To test the performance of our BCM, we will compare its predictions against measurements from various hydrodynamical simulations. In alphabetical order, these simulations are:

- BAHAMAS (McCarthy et al., 2017): run with `GADGET3`, calibrated to reproduce the present-day stellar mass function and halo gas mass fractions, with the specific purpose of studying the baryonic impact on the cosmic mass distribution. The simulation we use in this work has a box size of L=$400\,h^{-1}{\rm Mpc}$ and it has been run employing a Planck15 cosmology with massive neutrinos (Planck Collaboration 2015 results XIII, 2016) ($\Omega_{\rm cdm}$, $\Omega_{\rm b}$, Ω_Λ, A_s, h, n_s, τ, $\sum m_\nu$)=(0.2589, 0.0486, 0.6911, 2.116×10^{-9}, 0.6774, 0.9667, 0.066, 0.06).

- Cosmo-OWLS (Le Brun et al., 2014): this set of simulations is an extension of the OWLS simulations, designed to study cluster-size astrophysics. We use a simulation which include metal-dependent radiative cooling, star formation, stellar and AGN feedback, and have a L=$400\,h^{-1}\mathrm{Mpc}$ box with a WMAP7 cosmology (Ω_{cdm}, Ω_{b}, Ω_{Λ}, A_s, h, n_s, τ)=(0.226, 0.0455, 0.72845, 2.185×10^{-9}, 0.704, 0.967, 0.085).

- EAGLE (Schaye et al., 2015; Hellwing et al., 2016): a SPH hydrodynamical simulation in a L=$68\,h^{-1}\mathrm{Mpc}$ box that includes modelling for star formation, thermal AGN feedback, black-hole growth and metal enrichment. The cosmology employed is consistent with Planck13 (Ω_{cdm}, Ω_{b}, Ω_{Λ}, A_s, h, n_s, τ)=(0.2588, 0.0482, 0.6928, 2.1492×10^{-9}, 0.6777, 0.9611, 0.0952).

- Illustris (Vogelsberger et al., 2014b): a $75\,h^{-1}\mathrm{Mpc}$ box simulated with the adaptive moving mesh code `AREPO` (Springel, 2010). Similarly to EAGLE, it includes a wide range of astrophysical recipes, although their implementation and calibration differ. In particular, its thermal AGN feedback has been shown to be over-effective, blowing away most of the baryons inside haloes (van Daalen et al., 2020). The cosmology employed is consistent with WMAP9 (Ω_{cdm}, Ω_{b}, Ω_{Λ}, A_s, h, n_s, τ)=(0.227, 0.0456, 0.7274, 2.175×10^{-9}, 0.704, 0.9631, 0.081).

- IllustrisTNG-300 (Springel et al., 2018): a $205\,h^{-1}\mathrm{Mpc}$ box simulated with the same code and an updated version of the physics modelling of *Illustris*. Most notably, it features a new kinetic AGN feedback, more in agreement with observations with respect to the previous only-thermal one. The cosmology employed is a Planck15 with massless neutrinos (Ω_{cdm}, Ω_{b}, Ω_{Λ}, A_s, h, n_s, τ, $\sum m_{\nu}$)=(0.2589, 0.0486, 0.6911, 2.081×10^{-9}, 0.6774, 0.9667, 0.066, 0).

- Horizon-AGN (Dubois et al., 2014): a $100\,h^{-1}\mathrm{Mpc}$ box run with the Adaptive Mesh Refinement (AMR) algorithm `RAMSES` (Teyssier, 2002), which focus on the effects of AGN on various cosmic quantities. The cosmology employed is WMAP7-like (Ω_{cdm}, Ω_{b}, Ω_{Λ}, A_s, h, n_s, τ)=(0.226, 0.0455, 0.7284, 1.988×10^{-9}, 0.704, 0.967, 0.085).

- OWLS (Schaye et al., 2010; van Daalen et al., 2011): suite of simulations designed to study different baryonic effects on the cosmic density field. The simulation used in this work has a box of $100\,h^{-1}\mathrm{Mpc}$ and includes AGN feedback. The cosmology employed is from WMAP7 (Ω_{cdm}, Ω_{b}, Ω_{Λ}, A_s, h, n_s, τ)=(0.226, 0.0455, 0.7284, 1.988×10^{-9}, 0.704, 0.967, 0.085).

The power spectra for the mass field together with those for a GrO version of each simulation were kindly provided to us or made publicly available by the authors. To facilitate their comparison, we rebin the original $P(k)$ measurements into the same k bins.

3.3 Modified Baryon Correction Model

In this section we describe how we model baryonic processes in a given output of a GrO simulation. Our approach follows closely the BCM proposed by Schneider and Teyssier (2015a), with further assumptions to simplify it and speed-up its execution. Most of the recipes of the BCM are given in terms of the host halo mass and radius. Here, we will assume these to be M_{200} and r_{200}, the mass and size of a sphere whose average density is equal to 200 times the critical density of the Universe.

3.3.1 Overwiew

The main idea behind the BCM is to capture baryonic effects by explicitly modelling four components: galaxies, hot gas inside haloes, expelled gas and dark matter:

- *Galaxies* are placed at the minimum of the potential of dark matter (DM) haloes. The mass of galaxies is given by subhalo abundance matching (Behroozi et al., 2013), whereas their internal profile is given by a power law with an exponential cut-off at a scale radius set by observations (Kravtsov et al., 2018).

- *Hot gas* is assumed to be in hydrostatic equilibrium inside DM haloes. The amount of hot gas, $M_{\rm bg}$, is given as a function of the universal baryon fraction, approaching unity for halo masses $M_{\rm h} \gg M_c$, and decreasing as a power law $(M_{\rm h}/M_c)^{\beta}$ for smaller masses, where M_c and β are free parameters. The gas profile is described as a power-law with a polytropic index given by the concentration of the host halo, and on scales larger than half virial radius we assume that the gas perfectly traces dark matter.

- *Gas ejected* from its halo is assumed to be distributed isotropically up to a scale $\sim 10\,\eta\, r_{200}$. Its density profile is described as a constant with an exponential suppression, consistent with assuming an initial Maxwell-Boltzmann distribution for the velocity of ejected mass particles. The amount of mass ejected is simply given by mass conservation: $M_{\rm ej} = M_{\rm h} - M_{\rm g} - M_{\rm dm} - M_{\rm bg}$.

- *Dark matter* is assumed to be initially described by a Navarro-Frenk-White profile with the same concentration as in the GrO calculation. Posteriorly, the profile is quasi-adiabatically relaxed to account for the modification in the potential induced by the three components described above.

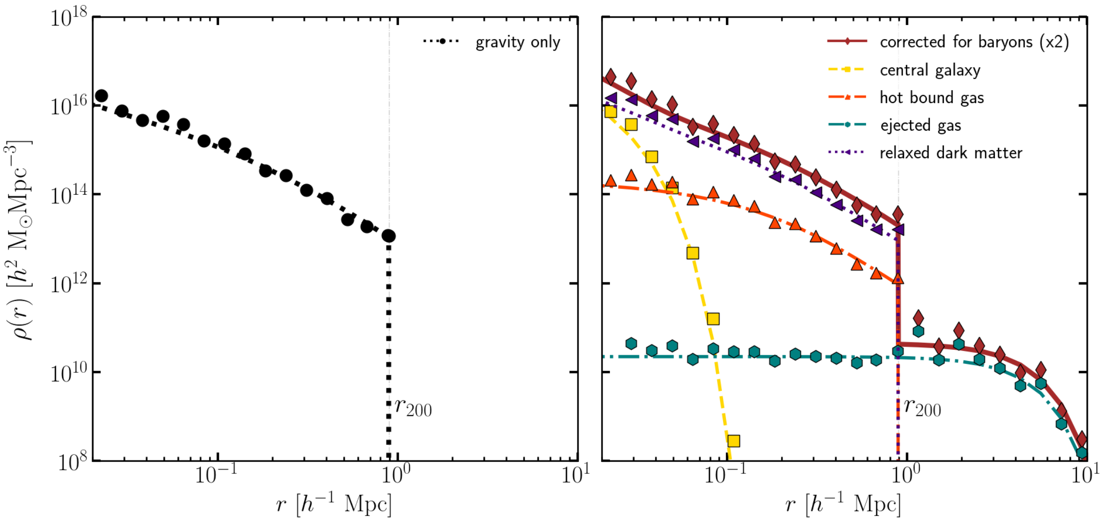

Figure 3.1: Density profiles of a halo of mass 1.2×10^{14} h^{-1} $M_\odot$ and concentration $c \approx 4$ at $z = 0$. *Left Panel:* The black circles and dashed line are the measured gravity-only profile and its fit, respectively. The initial profile is truncated at r_{200}. *Right Panel:* The brown solid line represents the theoretical total corrected profile, while the diamonds the measurements after the displacement of the particles. All the BCM components are displayed according to the legend. Notice how the gas ejected by the AGN feedback is the only component beyond r_{200}. The total BCM theoretical and measured density profiles are multiplied by a factor of 2 for display purposes.

Parameter	Description	Fiducial Value ($z = 0$)
M_c	Halo mass scale for retaining half of the total gas	$3.3 \cdot 10^{13}\, h^{-1}M_\odot$
M_1	Characteristic halo mass for galaxy mass fraction	$8.63 \cdot 10^{11}\, h^{-1}M_\odot$
η	Maximum distance of gas ejection	0.54
β	Slope of the gas fraction as a function of halo mass	0.12

Table 3.1: Parameters specifying our model for baryonic physics, and their fiducial values, obtained fitting the BAHAMAS simulation, used throughout this chapter. See §3.3 for details on the baryonic model, and §3.5 for details on how the parameters were found.

The model has four free parameters (η, M_c, β, M_1) with clear physical meaning: M_c is the characteristic halo mass for which half of the gas is retained; β is the slope of the hot gas fraction - halo mass relation; M_1 is the characteristic halo mass for which the central galaxy has a given mass fraction ϵ ($\epsilon = 0.023$ at $z = 0$) and η sets the range of distances reached by the AGN feedback. These parameters (all present in the original BCM, even if with slightly different physical meaning and if M_1 was fixed) are summarized in Table 3.1, and further details on the whole procedure are given in Appendix B.

For a given halo, we can therefore obtain a prediction for the relative difference for the cumulative mass profile before and after modeling baryons. We then perturb the position of particles inside a halo by applying a displacement $\Phi(r) = r(M_{\mathrm{BC}}) - r(M_{\mathrm{GrO}})$ so that they capture the expected modification induced by baryons.

Finally, we tag each particle in our simulation to be part of one of our four components, and rescale its mass to match the total expected mass in each component. This allows to extend the model to other gas properties e.g. temperature and pressure, and thus to simultaneously model weak lensing and other observables such as X-ray emission or thermal/kinetic Sunyaev-Zeldovich signals. More details of this procedure are provided in Appendix C.

3.3.2 A first example

To illustrate our model in practice, we have applied it to the haloes of one of the N-body simulation described in §3.2. In this section we will use the fiducial BCM parameters given in ST15, i.e. $M_c = 1.2 \times 10^{14}\ h^{-1}\ \mathrm{M}_{\odot}$, $\eta = 0.5$, $\beta = 0.6$, $M_1 = 2.2 \times 10^{11}\ h^{-1}\ \mathrm{M}_{\odot}$.

In Fig. 3.1 we show a halo of $10^{14}\ h^{-1}\ M_{\odot}$ and concentration parameter ~ 4 at $z = 0$. The left panel shows the density profile from the GrO simulation whereas the right panel shows the result after the BCM is applied. In both panels, the symbols represent the measurements, whereas lines denote the respective analytic descriptions. We can see that the GrO profile is well described by a NFW profile up to its critical radius r_{200}. Beyond r_{200}, we do not attempt to model the mass distribution, and thus the GrO profile is simply set to zero. On the contrary, the halo density profile significantly departs from a NFW after baryons are modelled.

On very small scales, the density essentially follows that of the central galaxy. The hot gas has a NFW slope on large scales but a flatter profile in the inner region. The dark matter is perturbed by the gravitational potential of the other components, resulting in a steeper profile in the inner region and a flatter profile at large radii, albeit the effect is so small that it is not visible by eye.

Beyond the halo boundaries, where the GrO model is null, the density profile is totally constituted by the ejected material. This means in practice that, after the displacement of the particles, the effective density profile in the halo outskirts will be equal to the one given by the GrO simulation plus the ejected component of the BCM.

The displacement field and cumulative mass profiles for this halo are shown in Fig. 3.2. Since we consider initially only the mass within r_{200}, the GrO profile is constant for $r > r_{200}$. After modelling baryons, the mass increases up to a scale set by the strength of the AGN feedback. We can also see that the displacement field is largest close to the halo boundary. This implies that these are the mass elements that will be ejected out and describe the expelled gas component.

The distortions of the halo density profiles translate directly into modifications to the mass power spectrum. In Fig. 3.3 we show the ratio of the power spectrum to the GrO one. Coloured lines display the results for the total mass field and for each of the BCM components separately. Consistent with the expectation set by the density profiles, the mass power spectrum is suppressed on intermediate scales owing to the ejected mass, on small scales, the central galaxy counteracts this effect and the power spectrum is enhanced. In §3.3.4 we will investigate systematically these modifications with respect to BCM parameter values. Fig. 3.3 also presents the results for the ST15 method as dashed lines. Although both models agree qualitatively, they disagree in detail. We discuss general and specific differences among them in the next subsection.

Comparison with Schneider & Teyssier (2015)

The main difference of our BCM with respect to that of Schneider and Teyssier (2015a) is that we assume that baryonic physics acts *only* over mass elements within the host halo. Notice that this assumption does not imply a null effect on the large-scale clustering (since the ejected gas does reach large scales), but implies instead that particles perturbed by baryons were initially inside haloes. On the contrary, ST15 attempt to model the mass profiles up to infinity, which in practice means that the displacement tends to zero only at very large distances from the halo centre, and it also implies that in general the displacement of a given mass element receives (a non-commutative) contribution of every single halo in the simulated volume. Furthermore, this approach requires modelling the distribution and clustering of field particles (not belonging to any halo), an operation computationally expensive that cannot anyway take into account halo local environments.

By truncating the profiles at r_{200}, thus forcing the displacement of the particles to be zero beyond r_{200}, we avoid all these potential issues and remove the non-locality of the model (which appears rather numerical than physical). This also yields a better numerical efficiency as particles inside different haloes can be treated separately, which allows a trivial parallelisation of the algorithm. Our BCM also does not require modelling the mass distribution outside halos, both computationally expensive and uncertain on a halo-by-halo

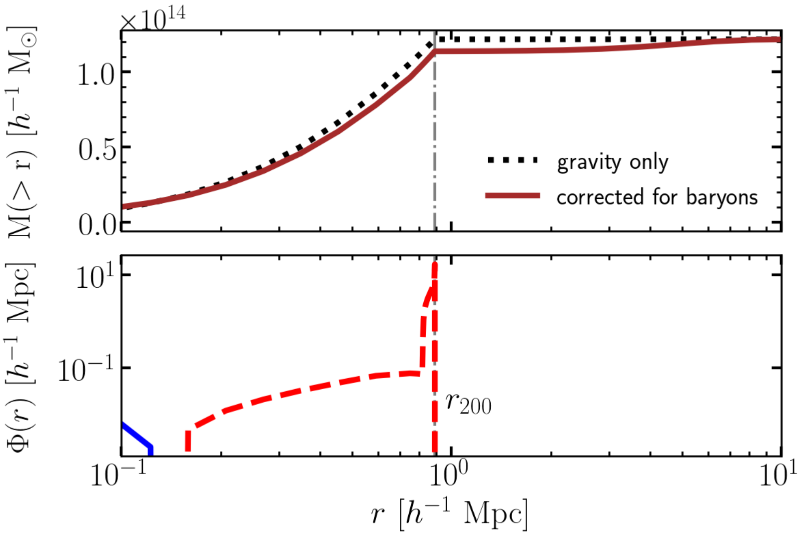

Figure 3.2: *Upper panel:* Initial gravity-only ($M_{\rm GrO}$, black dotted line) and *baryon corrected* ($M_{\rm BC}$, brown solid line) mass profiles. Notice that $M_{\rm GrO}$ is constant after r_{200}, while $M_{\rm BC}$ tends asymptotically to $M_{\rm GrO}$ at large radii, because of the ejected mass. *Lower panel:* Displacement field $\Phi(r) = r(M_{\rm BC}) - r(M_{\rm GrO})$. In radial shells where $M_{\rm GrO} < M_{\rm BC}$ we have that $\Phi < 0$ (blue solid line), thus the particles infall toward the centre of the halo. On the contrary, $M_{\rm GrO} > M_{\rm BC}$ implies that $\Phi > 0$ (red dashed line) and the particles are pushed away from the centre. Notice also that when approaching r_{200} the displacement becomes of the order of tens of Mpc.

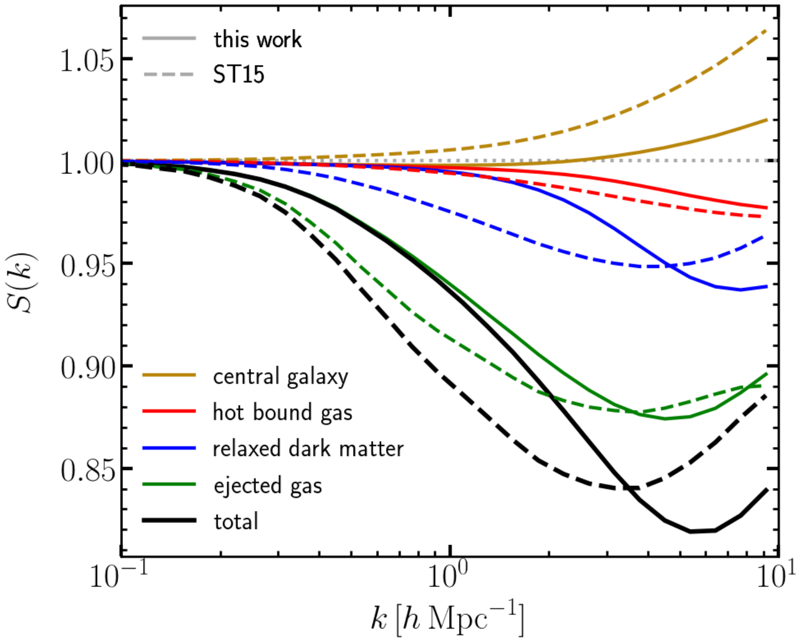

Figure 3.3: Baryonic effects on the matter power spectrum, defined as $S(k) \equiv P/P_{\rm GrO}$, considering one by one the components of the standard ST15 (dashed lines) and new (solid lines) version the BCM at z=0. The total impact (black) is given by the sum of central galaxy (gold), hot bound gas(red), relaxed dark matter (blue), ejected gas (green) contributions.

basis.

In our approach we employ similar analytical density profiles and free parameters as those described in Schneider and Teyssier (2015a). However, the differences discussed above imply that the BCM parameters affect the nonlinear power spectrum in a somewhat different way. We now explore the differences in the power spectrum predictions between the ST15 BCM and our version. To do so, we have implemented this BCM following step by step the prescriptions of Schneider and Teyssier (2015a), and applied it to our GrO simulation. We compare the power spectra in Fig. 3.3 for both models as dashed and solid lines.

For the same model parameters, our implementation predicts less suppression of the power spectrum up to $k \sim 3h\,\mathrm{Mpc}^{-1}$, and larger suppression on smaller scales. We can understand these discrepancies by examining each BCM component separately (displayed as coloured lines in Fig. 3.3).

On small scales, $k \approx 5\,h\,\mathrm{Mpc}^{-1}$, the predicted enhancement due to galaxies is smaller than that in ST15 by 2-3 times. Since our halo masses are smaller than in ST15, galaxies are also effectively less massive, which translates into a smaller enhancement of power. We notice that the abundance matching performed by Behroozi et al. (2013) and used in Kravtsov et al. (2018) is calibrated with M_{200} critical, so, unlike ST15, we expect our galaxy mass function to be consistent with observations. Because of the lower halo mass, haloes also have less gas, both ejected and in equilibrium. Therefore, we expect a weaker impact of gas components on the matter power spectrum, which is indeed what is displayed by blue and green lines. Finally, in the ST15 implementation the dark matter quasi-adiabatic relaxation causes a suppression of ≈ 5 %, affecting large scales, whereas in ours the effect is negligible at $k < 2\ h\,\mathrm{Mpc}^{-1}$. This is also expected by the weaker modification of the gravitational potential caused by the baryons, combined with the assumption that the halo back reaction is negligible at scales larger than r_{200}.

3.3.3 Numerical implementation

The concentration of each of these haloes is found by fitting a NFW form to the mass profile computed over 20 bins uniformly spaced in $\log(r/r_{200})$ over the range $[3\,\epsilon_s/r_{200}, 1]$. We compute the baryonic corrections for haloes with more than 640 particles (10 subsampled particles), i.e. $M_\mathrm{h} \geq 2 \cdot 10^{12}\,h^{-1}\mathrm{M}_\odot$. We note that, although we might expect a bias $\approx 8\%$ in the concentration estimation of haloes sampled with $\approx$ 600 particles (Poveda-Ruiz et al., 2016), 98% of the baryonic effect on the matter power spectrum is given by haloes more massive than $10^{13}\,h^{-1}\mathrm{M}_\odot$, as shown in Appendix D. We resolve the latter haloes with more than 3000 particles, thus expecting a bias $\leq 2\%$ in the concentration estimation.

To increase the computational efficiency of the BCM, the density profiles are computed and stored directly on-the-fly by our N-body code. Furthermore, at each output, particles are sorted according to halo membership, and their relative distances to the parent halo centre stored. Additionally, the concentrations of all the haloes are computed and stored in post-processing for each snapshot of the simulation. All this allows to be able to quickly apply the BCM exploiting OpenMP and MPI parallelisation. On average, the whole procedure takes ≈ 5 (≈ 0.5) seconds on 4 threads when applied to our biggest (smallest) simulation.

The BCM displacement field is found by inverting the mass profiles, and in this case the truncation produces a thin shell of very large displacement at radii approaching r_{200}. The shape of this thin shell affects the matter density field at all the scales larger than r_{200}, thus we refine the radial bins in that region to have more precision in the matter distribution on large scales.

3.3.4 Impact of baryons on the power spectrum

In this subsection we study the range of possible distortions of the matter power spectrum allowed by the BCM.

In Fig. 3.4 we display the mass power spectra obtained after applying the BCM to our fiducial GrO N-body simulation. Each panel varies a single parameter of the model while keeping the other three fixed. Bluer (redder) colors represent low (high) parameter values.

The top left panel varies M_c, the typical mass of haloes that have lost half of their gas, in a logarithmic range $[12, 16]\, h^{-1}\mathrm{M}_{\odot}$. For low values of M_c, the power spectrum barely changes owing to the relatively minor contribution that $\lesssim 10^{13}\, h^{-1}\mathrm{M}_{\odot}$ haloes have to the mass power spectrum. As M_c increases, however, more haloes lose baryons and the power spectrum is suppressed more.

The larger the halo mass, the larger the scale over which baryons are redistributed by feedback, thus the power spectrum suppression affects progressively larger scales. Eventually, when $M_c \sim 10^{15}\, h^{-1}\mathrm{M}_{\odot}$ the abundance of haloes drops and the power spectrum converges.

How rapid the baryon fraction decreases with halo mass is controlled by β, which is varied in the logarithmic range $[-1, 1]$ (bottom left panel). We can see that the impact of this parameter is smaller if compared to that of M_c. Higher values produce a faster transition to haloes devoid of gas, and consequently the power spectrum is tilted, being more suppressed on small scales and less on large scales. On the contrary, for lower values the power spectrum is more suppressed on large scales, and less on small scales.

The top right panel varies η (in the same range as β) and consequently the radius up to which the ejected gas will settle in. The larger the value of η, the further the gas is expelled and therefore the larger the scales that are suppressed. In principle there is no bound on the minimum wavenumber affected, in fact, in the limit of $\eta \to \infty$, all wavelengths are affected.

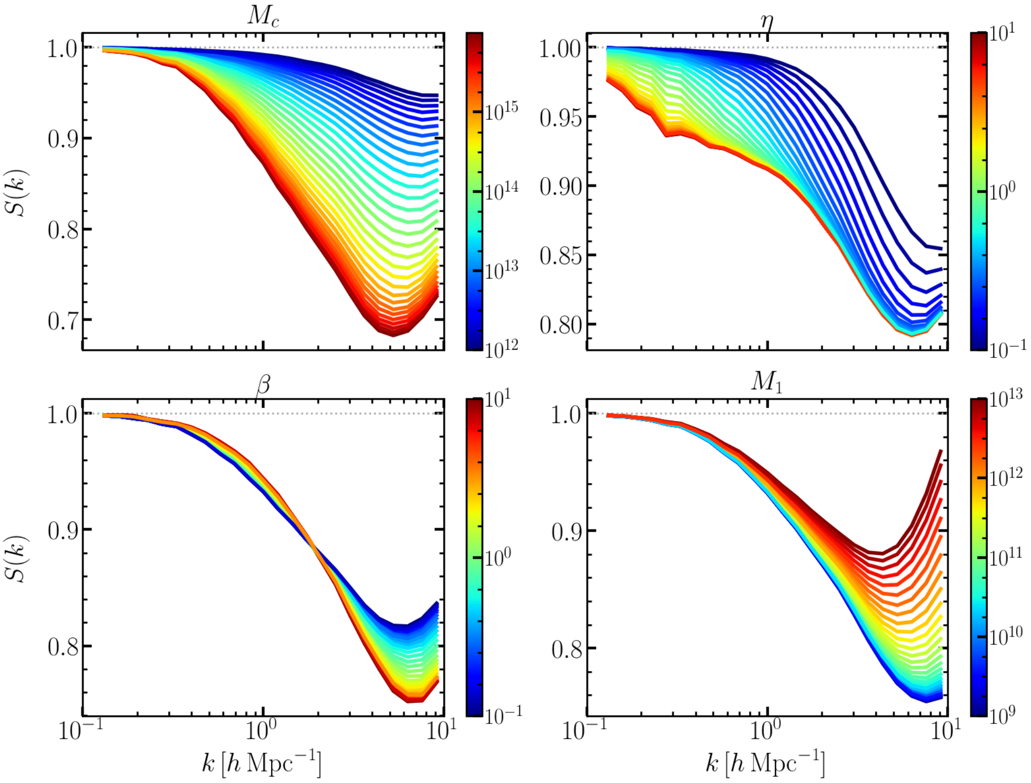

Figure 3.4: Modifications to the matter power spectrum at $z = 0$ caused by baryons, $S(k) \equiv P/P_{\mathrm{GrO}}$. Each panel varies one of the four free parameters of the baryon correction model (M_c, η, β, M_1) while keeping the other three fixed at their fiducial value.

On the other hand, as η decreases, the expelled gas remains very close to its initial position and the power spectrum barely changes.

Finally, the bottom right panel varies M_1, the typical mass of haloes with a central galaxy of $0.023\,M_1\,h^{-1}\mathrm{M}_{\odot}$, in the logarithmic range $[9,13]\,h^{-1}\mathrm{M}_{\odot}$. There are two separate trends visible in this plot. Firstly, as we increase M_1 a larger fraction of baryons is transformed into stars, which in turn reduces the amount of expelled gas and consequently, the power spectrum suppression is reduced up to $k \approx 3\,h\,\mathrm{Mpc}^{-1}$. On smaller scales, the contribution of stars in the modelled galaxies becomes important, which increases the amplitude of these Fourier modes.

Overall, we see that the BCM has flexibility to model many different physical scenarios, but, at the same time, not every possible $P(k)$ modification is allowed. In fact, the modifications are constrained to certain regions and have very specific dependences with the wavelength. Therefore, it is not guaranteed that the model is able to accurately reproduce the predictions of state-of-the art hydrodynamical simulations. We explore this in §3.5.

3.4 Cosmology scaling of gravity-only simulations

The BCM enables a flexible modelling of baryonic effects provided a suite of high-resolution GrO simulations with varying cosmological parameters. Here we will show that these GrO predictions can be obtained accurately and efficiently using cosmology-rescaling techniques.

The main idea of a cosmology rescaling is to transform the length, time, and mass units of the outputs of a N-body simulation, so that it predicts the nonlinear structure expected in arbitrary-many nearby cosmologies (Angulo and White, 2010; Angulo and Hilbert, 2015). The algorithm has been extensively tested (Ruiz et al., 2011; Renneby et al., 2018; Mead and Peacock, 2014a,b; Mead et al., 2015; Zennaro et al., 2019; Contreras et al., 2020a), and has recently been extended to cover massive neutrino cosmologies (Zennaro et al., 2019), where the redshift and scale dependence of the growth factor induced by the neutrinos is computed with the public code `reps` (Zennaro et al., 2017).

Here we employ the latest incarnation of the cosmology-rescaling, which, in addition to the units transformation, includes a correction of large-scale modes using 2nd order Lagrangian Perturbation Theory and a correction of small-scale modes. For the latter, the algorithm displaces the particles inside haloes to account for the cosmology-dependence of the concentration-mass-redshift relation. For further details we refer the reader to (Contreras et al., 2020a).

In order to maximise the accuracy of the method, we should have a snapshot taken exactly at the transformed cosmic time. In general, if we rescale a pre-existing simulation, we can apply only the time transformations allowed by the finite number of snapshots stored,

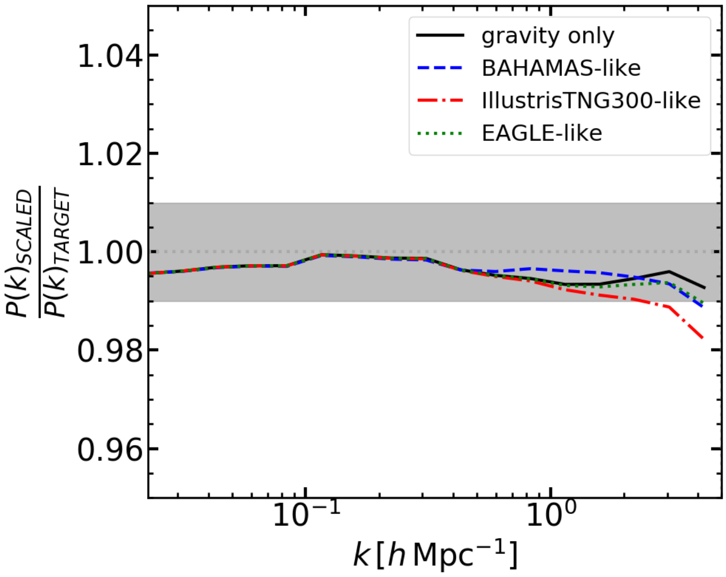

Figure 3.5: Ratio of the mass power spectra at $z = 0$ of two simulations in the cosmology preferred by Planck13: one scaled from our fiducial cosmology, $P_{\rm scaled}(k)$, and the other carried out directly with Planck13, $P_{\rm target}(k)$. Black lines display results of GrO simulations, whereas coloured lines do so for simulations where baryons are explicitly modelled in the BCM with parameters mimicking EAGLE, Illustris-TNG, and BAHAMAS, as indicated by the legend. The grey band marks a discrepancy of 1%.

decreasing the accuracy of the method. Obviously, the more snapshots stored the higher the accuracy achieved. We have stored 94 snapshots on the expansion factor interval $a = [0.02, 1.25]$ (notice that the simulation is run "to the future", $z < 0$, making possible the scaling to extreme cosmologies). To increase even more the accuracy of the method, we apply the algorithm to the two snapshots closest to the scaling target time, interpolating afterwards the chosen summary statistics. Having two snapshots taken at cosmic expansion factors a_0 and a_1, and scaled expansion factor a_* such that $a_0 < a_* < a_1$, the interpolated scaled power spectrum reads

$$P(a_*) = P(a_0) \cdot \left(1 - \frac{a_* - a_0}{a_1 - a_0}\right) + P(a_1) \cdot \left(\frac{a_* - a_0}{a_1 - a_0}\right), \tag{3.1}$$

where $P(a_0)$ and $P(a_1)$ are the power spectra measured rescaling the two snapshots at a_0 and a_1, respectively.

Scaling of the halo catalogue

The halo catalogue is directly rescaled, to avoid to run `SUBFIND` on the rescaled distribution of particles. Within the standard scaling algorithm, the density profiles should be simply $\rho_*(r) = m_*/s_*^3 \rho(r)$, where $m_* = s_*^3 \Omega_{\rm m,T}/\Omega_{\rm m,O}$ is the mass scale factor, s_* is the length scale factor and the "T" and "O" subscripts refer to the target and original cosmologies, respectively. Accordingly, the NFW parameters should be rescaled as $r_{s,*} = s_* r_s$ and $\rho_{c,*} = m_*/s_*^3 \rho_c$. The concentration correction adds an extra displacement which we take into account as $\rho_*^\dagger(r) = \rho_*(r) + \Delta\rho(r)$, where $\Delta\rho(r)$ is the difference between the NFW profiles of two haloes with the concentration computed within target and scaled cosmology. The scale radius of the NFW is then $r_{s,*}^\dagger = r_{s,*} + \Delta r_s$ and the characteristic density $\rho_{c,*}^\dagger = \rho_{c,*} + \Delta\rho_c$. The critical radius and mass r_{200} and M_{200} are then found with a minimisation over the new NFW halo profile and within the target cosmology.

Joint performance of cosmology scaling and BCM

The scaling algorithm provides highly accurate predictions for the mass power spectrum – better than 3% at $z \leq 1$ over the whole range of ΛCDM-based cosmologies currently viable, and over a wide range of scales $0.01 - 5\, h\,\mathrm{Mpc}^{-1}$ (Contreras et al., 2020a). Similarly, the halo mass function is reproduced with an accuracy better than 10% (Angulo and White, 2010). In the following we will show that the algorithm also provides high-quality predictions for the mass clustering when used along with the BCM.

To quantify the accuracy of the method, we have rescaled our fiducial simulation (c.f. §3.2) to the cosmological parameters preferred by Planck13. We then apply the BCM to the rescaled output and compare to the results obtained by applying the BCM to a simulation directly carried out with a Planck13 cosmology.

Fig. 3.5 shows the ratio of the power spectra at $z = 0$ for three different sets of BCM values. These sets were chosen so that they accurately describe the baryonic effects in the EAGLE, Illustris-TNG, and BAHAMAS simulations. For comparison, we also show the precision when just rescaling GrO outputs. For all models considered the accuracy of the cosmology rescaling is preserved at a very high level, adding no more than 1% additional uncertainty over the rescaling of GrO simulations. Notice that we find similar results for Illustris, Horizon-AGN, OWLS and Cosmo-OWLS, even if not shown in figure for display purposes.

3.5 Fitting the state-of-the-art hydrodynamical simulations

In this section we will explore if the BCM is able to correctly describe the baryonic effects predicted in seven different state-of-the-art hydrodynamical simulations: EAGLE, Illustris, Illustris-TNG, Horizon-AGN, OWLS, Cosmo-OWLS, and BAHAMAS. These simulations adopt different cosmological parameters, sub-grid physics, and values for the free parameters (owing to different strategies and observations used to calibrate them). Therefore, this exercise will test our ability to simultaneously model cosmology and astrophysics.

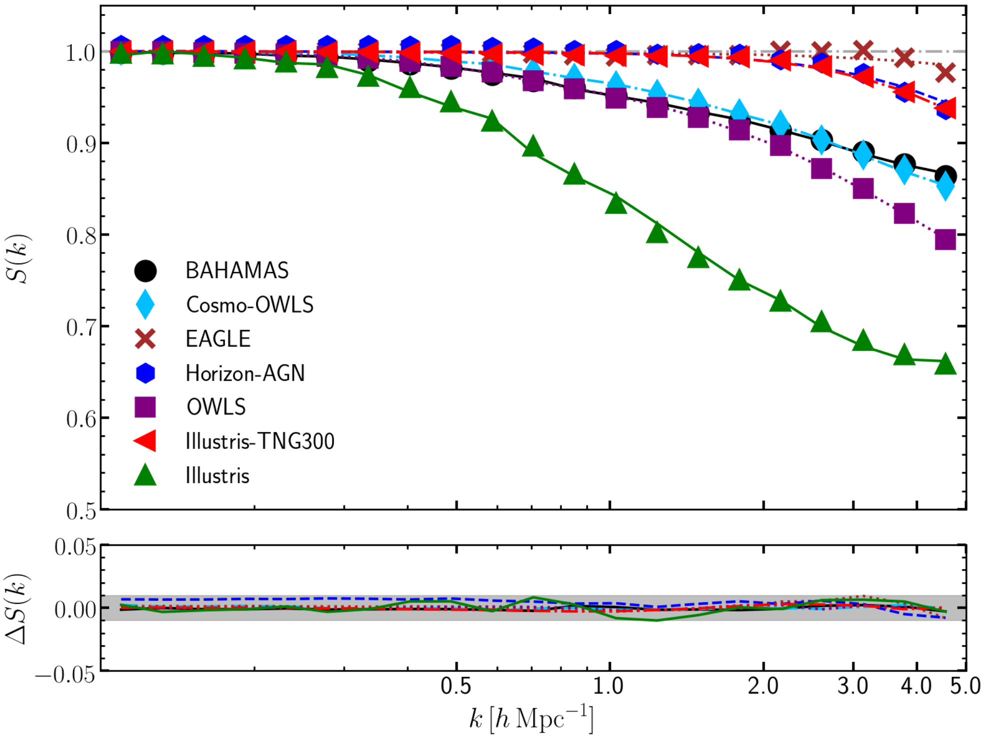

Figure 3.6: *Upper Panel:* Measurements of the baryonic impact to the matter power spectrum, $S(k) \equiv P/P_{\mathrm{GrO}}$, in different hydrodynamical simulations according to the legend (symbols), compared against our respective best-fits (solid lines). *Lower Panel:* Difference between measurements and best-fits. The grey shaded band marks the 1% difference.

3.5.1 Simulation data & BCM parameter sampling

For each of the seven hydrodynamical simulations, we fit the ratio of the mass power spectrum with respect to its GrO counterpart: $S(k) = P_{\mathrm{hydro}}/P_{\mathrm{GrO}}$. We interpolate $S(k)$ in 20 data points uniformly spaced in log-k over the range $[0.1 - 5]\ h\,\mathrm{Mpc}^{-1}$, to have consistent measurements for all the simulations. We use an empirical approach to estimate the covariance of $S(k)$. First, we assume:

$$\mathcal{C}_{S,ij} = \mathcal{E}(k_i)\mathcal{K}(k_j, k_i)\mathcal{E}^T_j(k_j), \tag{3.2}$$

where $\mathcal{E}$ is an envelope function that describes the typical amplitude of the uncertainty as a function of wavenumber, and $\mathcal{K}(k)$ the correlation of this uncertainty, which we model as a Gaussian distributed random variable $\mathcal{K} = \mathcal{N}(|k_i - k_j|, \ell)$.

We set the magnitude of each term based on the intra-data variance as a function of scale. Specifically, on large scales we assume $\mathcal{E}$ to be constant, with a correlation length $\ell = 0.1\,h\,\mathrm{Mpc}^{-1}$. To model the small-scale noise we use $\mathcal{E} = [1 + 0.5\,\mathrm{erf}(k-2)]fS(k)$, where $f = 0.6\%$ for BAHAMAS, Cosmo-OWLS, EAGLE and Illustris-TNG300, $f = 0.8\%$ for OWLS and $f = 2\%$ for Illustris, with a longer correlation length $\ell = 0.5\,h\,\mathrm{Mpc}^{-1}$.

We should take particular care in the case of Horizon-AGN. The snapshots of the hydrodynamical run were taken at slightly different redshifts with respect to the GrO. We correct at first order this effect by rescaling the power spectra normalised by the growth factors at the correct expansion factors according to Eq. A2 of Chisari et al. (2018). However, even after this correction there is still a 1% disagreement on large scales, arguably given by a difference in the number of particle species with which the two simulations have been carried on (Angulo et al., 2013; Chisari et al., 2018; van Daalen et al., 2020). For this reason, we set the amplitude of the envelope functions for Horizon-AGN to 1%.

To fit the ratio measurements, $S(k)$, we first rescale our fiducial GrO simulation to match the cosmology of each of the seven simulations. We then compute the power spectra before and after applying our BCM. For this procedure we use a $64\,h^{-1}\mathrm{Mpc}$ simulation, avoiding to use its paired and the interpolation between snapshots described in §3.4. We show in Appendix D that this choice will not affect the final results, since we expect the suppression $S(k)$ to be converged at 1% level. We have furthermore tested that the small differences in redshift between target and rescaled power spectra is at first order canceled out in the ratio.

We recall that the BCM is fully specified by 4 parameters: $\vartheta = (M_1, M_c, \eta, \beta)$. The prior for these parameters are assumed to be flat in log space over the range: $\log M_1 \in [9, 13]\,h^{-1}\mathrm{M}_{\odot}$, $\log M_c \in [12, 16]\,h^{-1}\mathrm{M}_{\odot}$, $\log \eta \in [-1, 1]$, $\log \beta \in [-1, 1]$. We note that with this prior choice, the ejected radius of each halo is defined such that $r_{ej} \geq r_{200}$.

We define our likelihood as

$$\mathcal{L}(\vartheta|\mathcal{D}) \propto \exp\left[-\frac{1}{2}\sum_{k}\left(\frac{S(k)_{\mathcal{D}} - S(k)_{\vartheta}}{\Sigma_{S(k)}}\right)^2\right], \tag{3.3}$$

where the subscripts $\mathcal{D}$ and ϑ refer to data and theoretical model, respectively, and $\Sigma_{S(k)}$ is the diagonal of $\mathcal{C}_{S,ij}$ defined in Eq.3.2. We sample the posterior probability with the affine invariant MCMC algorithm `emcee` (Foreman-Mackey et al., 2013), employing 8 walkers initialised with a latin-hypercube to optimise the hyper-volume spanned. Each walker has 2500 steps with a burn-in phase of 1000. We highlight that thanks to the heavy optimizations of all the codes involved, a chain step can be carried out in less than 6 seconds on a common laptop.

3.5.2 Best-fitting parameters

We now present the best fits and constraints on the BCM parameters as estimated from various hydrodynamical simulations.

Fig. 3.6 compares the measured suppression $S(k)$ with that predicted by our method evaluated with the best-fitting parameters. Remarkably, we can see that the BCM is an excellent description of the data at all scales considered. This is quantified in the bottom panel, which displays the difference between the data and the best fit model, thus can be

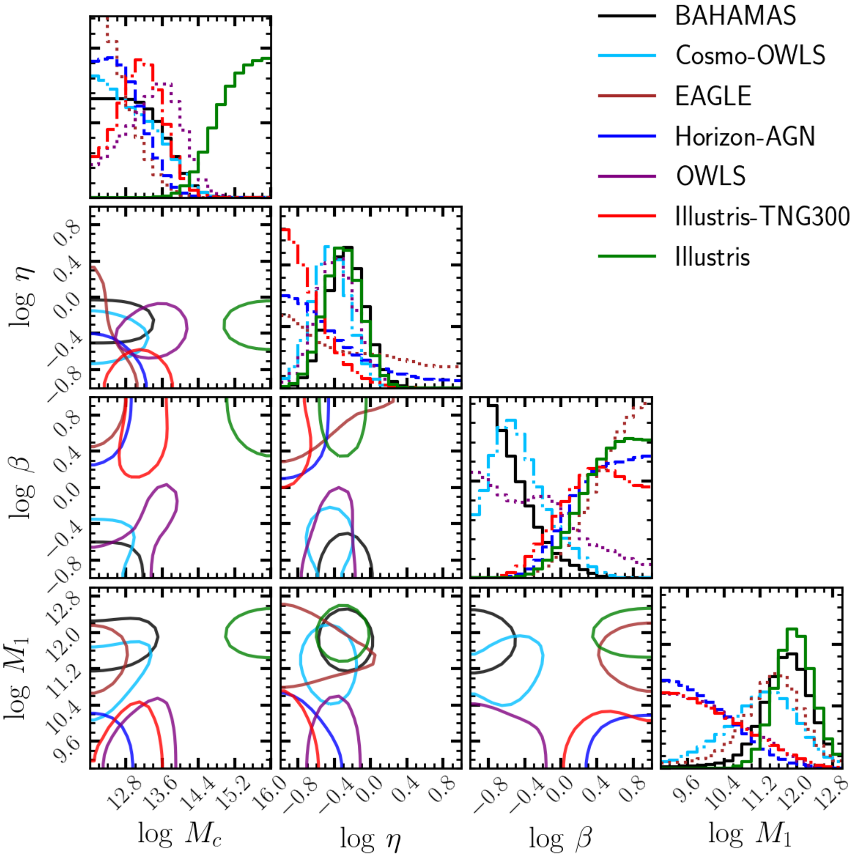

Figure 3.7: 1σ credibility levels of the free parameters of our Baryonic Correction Model, obtained by fitting the suppression in the power spectrum at $z = 0$ for EAGLE (brown), Horizon-AGN (blue), Illustris (green), Illustris-TNG (red), OWLS (purple), Cosmo-OWLS (light-blue) and BAHAMAS (black). The upper subplots show the marginalised posterior PDF of the baryonic parameters. The best-fitting models are shown in Fig. 3.6.

interpreted as the fractional accuracy of the model in predicting the full power spectrum. For all simulations and scales, this is better than 1%.

In Fig. 3.7 we show the 1σ credibility levels and the marginalised posterior probability density functions (PDFs) of the BCM parameters. The best-fitting values, together with the means and modes of the marginalised posteriors, are provided in Table 3.2.

We can see that there is a broad agreement between the preferred values for some parameters and between a subset of simulations, however, in general different hydrodynamical simulations lie on different regions of the BCM parameter space, as a consequence of the very different predictions for the suppression $S(k)$ owing to the differences in their physics implementation.

The Illustris simulation (Vogelsberger et al., 2014b) displays the largest suppression, $\approx$ 35 % at $k \approx 6\,h\,\mathrm{Mpc}^{-1}$, whereas the EAGLE run presents the weakest, 2% on the same scale. Other simulations fall in between, with Illustris-TNG and Horizon-AGN providing almost identical suppressions, as well as Cosmo-OWLS and BAHAMAS, at least on the scales considered.

Consistent with this picture, the expected value of M_c is the largest for Illustris and the smallest for EAGLE: $\approx 10^{15}$ and $\approx 10^{12}\,h\,\mathrm{Mpc}^{-1}$, respectively, with the other simulations in between. Interestingly, Illustris, BAHAMAS, Cosmo-OWLS and OWLS prefer roughly the same value of $\eta \approx 0.5$, whereas Illustris-TNG300, Horizon-AGN and EAGLE are consistent with each other and prefer much smaller values, $\eta \approx 0.15$, consistent with almost no ejected gas to large distances. BAHAMAS, Cosmo-OWLS and OWLS prefer small β values, $\beta \lesssim 0.5$, in contrast with the other simulations, which have rather larger values, $\beta \gtrsim 2.5$. The expected values of M_1 for Horizon-AGN, Illustris-TNG and OWLS are $\lesssim 10^{10}\,h^{-1}\mathrm{M}_{\odot}$, whereas for all the others $M_1 \gtrsim 10^{11}\,h^{-1}\mathrm{M}_{\odot}$.

Finally, we note that there are rather weak degeneracies among parameters, which supports the idea that the BCM is a general and minimal modelling of baryonic effects in simulations, meaning that it can reproduce arbitrary matter power spectra with a minimum set of free parameters. It is also clear that there is no consensus on the magnitude of baryonic corrections, and thus the need for a flexible modelling for cosmological data analysis.

3.5.3 Relation to the baryon fraction in clusters

Although hydrodynamical simulations are calibrated to reproduce several observables, they make specific choices for various processes of their sub-grid physics.

Recently, van Daalen et al. (2020) analysed a suite of simulations from the BAHAMAS, OWLS, and Cosmo-OWLS projects to study how the initial mass function, supernovae and AGN feedback, and metal enrichment recipes impact the power spectrum. Regardless of

Simulation	$M_c\,[10^{14}\,h^{-1}\mathrm{M}_\odot]$	η	β	$M_1\,[10^{11}\,h^{-1}\mathrm{M}_\odot]$
BAHAMAS	(0.38, 0.33, 0.08)	(0.53, 0.54, 0.53)	(0.47, 0.12, 0.22)	(10.85, 8.63, 5.63)
Cosmo-OWLS	(0.04, 0.01, 0.07)	(0.35, 0.35, 0.36)	(0.25, 0.22, 0.34)	(1.61, 2.09, 1.54)
OWLS	(0.4, 0.45, 0.24)	(0.46, 0.43, 0.41)	(0.67, 0.8, 0.45)	(0.01, 0.04, 0.14)
Horizon-AGN	(0.12, 0.05, 0.04)	(0.15, 0.17, 0.35)	(6.38, 8.31, 3.15)	(0.07, 0.02, 0.09)
Illustris-TNG300	(0.23, 0.19, 0.12)	(0.14, 0.15, 0.18)	(4.09, 2.56, 2.56)	(0.22, 0.03, 0.14)
Illustris	(66.48, 91.03, 22.1)	(0.49, 0.5, 0.5)	(6.36, 5.42, 3.66)	(9.44, 9.65, 8.85)
EAGLE	(0.18, 0.01, 0.03)	(0.14, 0.11, 0.58)	(9.65, 6.23, 4.23)	(11.15, 4.2, 2.52)

Table 3.2: For each BCM parameter we tabulate the best-fit, the mode and the mean values of the marginalised posterior PDF. See §3.3 for details on the baryonic model, and §3.5 for details on how the values were found.

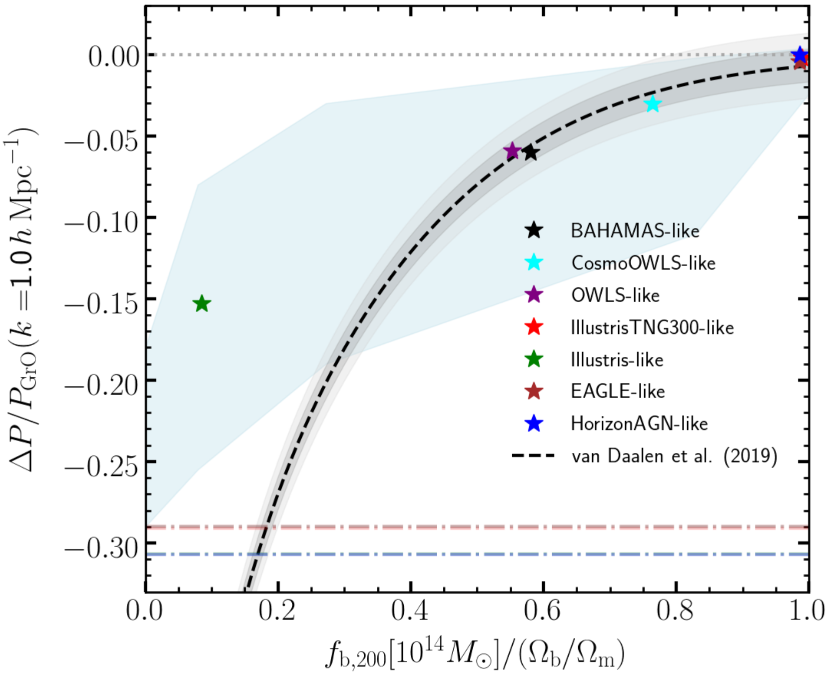

Figure 3.8: Baryonic impact on the matter power spectrum at $k = 1\,h\,\mathrm{Mpc}^{-1}$, defined as $\Delta P(k)/P(k)$ as a function of the halo baryon fraction for haloes of $10^{14}\,\mathrm{M}_\odot$. The star symbols correspond to the quantity measured in our simulation using a feedback model that resemble the hydrodynamical simulations specified in the legend, in halo mass interval of $[6\times10^{13}$,$2\times10^{14}]$ $\mathrm{M}_\odot$. The light blue shaded area marks the region allowed by the BCM, varying the parameters within the priors in logarithmic space $\log M_1 \in [9, 13]$, $\log M_c \in [12, 16]$, $\log\eta \in [-1, 1]$, $\log\beta \in [-1, 1]$. The dashed-dotted lines represents the maximum theoretical suppression given by $(1-\Omega_b/\Omega_m)^2-1$, the different colors being referred to the simulation cosmology according to the legend. The black dashed line is the fit provided by van Daalen et al. (2020), being the grey and light grey shaded areas the 1% and 2% deviations, respectively.

these choices, they found a tight correlation ($\approx$1%) between the mean baryon fraction inside haloes and the power spectrum suppression. These relations also held for the EAGLE, Illustris, Illustris TNG and Horizon-AGN simulations. We now test whether our BCM implementation is able to recover such correlation.

In Fig. 3.8 we show all possible power spectrum suppressions (within our prior parameter space) at $k = 1h\,\mathrm{Mpc}^{-1}$ predicted by our model at a fixed baryon fraction. For comparison, stars show the mean BCM values found in the previous section for various hydrodynamical simulations. Also for comparison, dashed lines indicate an estimate for the largest possible suppression expected for a given baryon fraction, i.e. assuming haloes expel all their gas to infinity. Decomposing the power spectrum in dark matter and baryonic contribution, it is easy to show this is given by:

$$\max\left[S(k)\right] = \left(1 - \frac{\Omega_b}{\Omega_m}\right)^2 . \tag{3.4}$$

Firstly, we see that the BCM predicts a clear relation between $S(k)$ and the baryon content of clusters, including the relation reported in van Daalen et al. (2020) down to a baryon fraction $f_b \approx 0.3$. For smaller baryon fractions, the predictions disagree. However, we note that in that regime van Daalen et al. (2020) relies on an extrapolation and indeed for $f_b \lesssim 0.2$ predicts a larger suppression than the maximum expected.

We note that our relation is significantly looser than that of van Daalen et al. (2020) – it is interesting to speculate the reasons behind this. On one hand, this could imply that there are fundamental relationships between the free parameters of the BCM, or that the functional forms provide more freedom than required. This could imply that a more deterministic model could be found in the future. On the other hand, many numerical simulations are calibrated to reproduce certain observables which might artificially limit the range of possible suppressions.

Very interestingly, the baryon fractions inferred by fitting the simulations (coloured stars) perfectly agree (< 1 %) with the fitting function provided by van Daalen et al. (2020), in all cases except for Illustris. This means that by only providing the clustering our model is able to correctly predict the amount of DM and baryons in simulated clusters. In the case of Illustris, on the other hand, our model indicates $f_b \approx 10$ % the cosmic value, whereas the measurement from the hydrodynamical simulation is $f_b \approx 35$ %. Extreme feedback models, such as the Illustris one, appears to be strong enough to perturb the gas outside the halo boundaries. In order to reproduce the clustering of these simulations within the assumption of the model, i.e. no particle is displaced outside haloes, more gas needs to be expelled from the halo, resulting in an underestimation of the halo baryon fraction.

To confirm this hypothesis, we have fit another simulation of the Cosmo-OWLS suite, run with the same sub-grid implementation but with higher minimum heating temperature for AGN feedback, $T = 10^{8.7}\mathrm{K}$. We have found that in this case the baryon fraction is underestimated by a factor of 2. Despite the fact that such strong feedback models are not preferred by observations, it will be interesting to explore further these aspects in the future, to refine the parametrisation and recipes of the BCM.

3.5.4 Redshift evolution of baryonic parameters

Up to this point, we have only considered the baryonic effects at redshift zero. None of the BCM free parameters has a clear theoretical redshift dependence, except for M_1, for which we give a parameterisation based on halo abundance matching in Appendix B. A naive approach would be to consider the other parameters constant, thus assuming that the evolution of the baryonic effects is only given by the evolution of the halo mass function. However, it has already been proven that this is not the case. The BCM fitting function parameters provided by Schneider and Teyssier (2015a) show in fact a clear redshift dependence, when applied to Horizon-AGN at different snapshots (Chisari et al., 2018). In this section, we extend Chisari et al. (2018) analysis by fitting the power spectrum suppression for BAHAMAS, Cosmo-OWLS, OWLS and Horizon-AGN at multiple redshifts between $0 \leq z \leq 2$. We perform the fit with the same setup used in the previous section for $z = 0$.

We display the measured $S(k)$ along with the best-fitting BCM predictions in Fig. 3.9. Firstly, we can see a clear evolution of $S(k)$, with an amplitude that is typically smaller at high z. This is comparable with the analysis of Chisari et al. (2018). Remarkably, our model provides an excellent fit for the data over all the scales and redshifts considered, achieveng a percent accuracy even in the most extreme cases.

In Fig. 3.10 we show the expectation values for M_c, η, β, and M_1 as a function of redshift. We find that BAHAMAS, Cosmo-OWLS and OWLS do not show a significant evolution of the AGN feedback range, having the η parameter roughly constant in time. On the contrary, Horizon-AGN shows a monotonic increase of η, in agreement with the finding of Chisari et al. (2018). The power spectrum suppression $S(k)$ of the hydrodynamical simulations in study roughly peaks around $z \approx 1$. Therefore, for the correlation shown in Fig. 3.8 we can expect the peak of the quantity of gas expelled from haloes around this redshift.

Indeed, we find that the mean values of M_c in all the simulations increase up to $z = 1$ and a slowly decrease afterwards, except for Horizon-AGN in which M_c monotonically increases. The characteristic host halo mass M_1 shows a similar trend, increasing at low redshifts and staying somewhat constant after $z \approx 0.5$. Finally, it appears that for OWLS, Cosmo-OWLS and BAHAMAS steeper transitions in mass from gas-rich to gas-poor haloes are preferred at higher redshifts. At odds with this trend, Horizon-AGN mean values of β monotonically

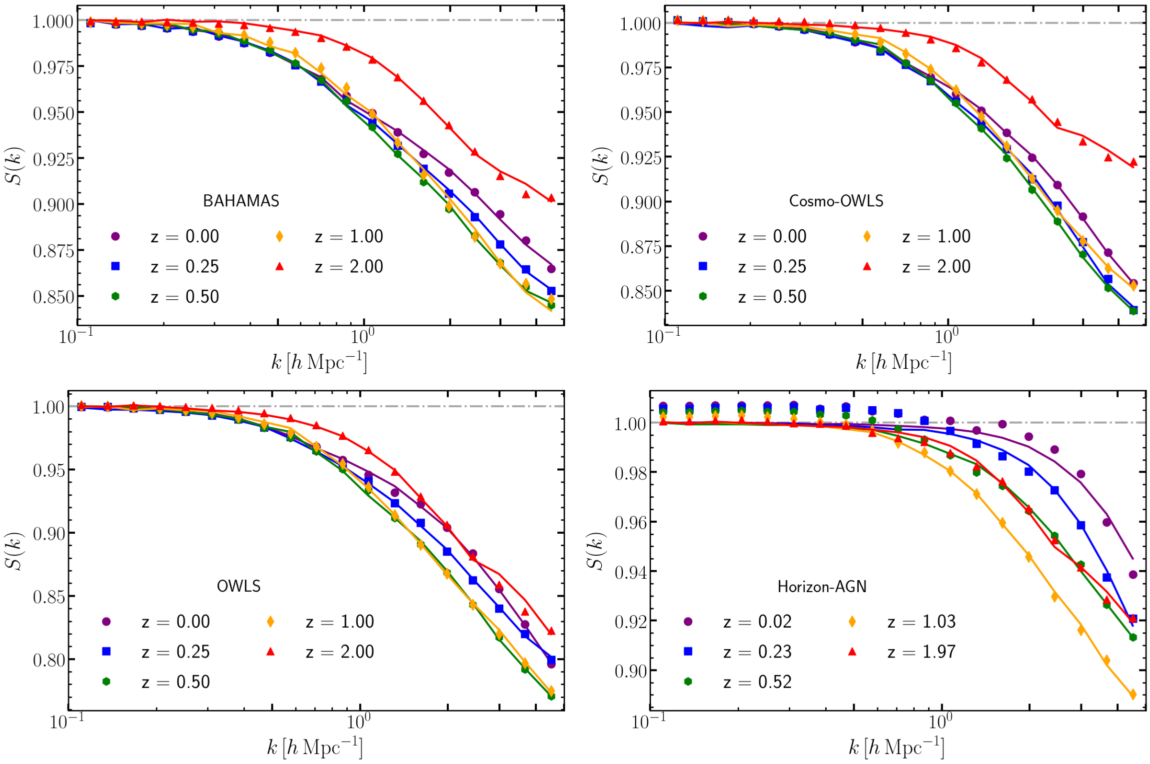

Figure 3.9: The impact of baryons on the power spectrum, $S(k) \equiv P/P_{GrO}$ as measured in the BAHAMAS (top left), Cosmo-OWLS (top right), OWLS (bottom left), and Horizon-AGN (bottom right) simulations at redshifts 0, 0.25, 0.5, 1, 2, as indicated by the legend. We do not show all the redshifts available for display reasons. Solid lines represent the best-fitting model.

decrease from $z = 0$ to $z = 1$.

In conclusion, it is clear that it is required a large BCM parameter space in order to describe different state-of-the-art hydrodynamical simulations. The redshift evolution of the parameters shows some similarities but it is not always consistent among the simulations. All this emphasises the importance of having flexible and general recipes in the BCM, at the risk of biasing parameter estimates.

3.6 Information analysis: baryon-cosmology degeneracies

In the previous sections we have shown that our framework can simultaneously model cosmology and astrophysics in the mass power spectrum. Now, we explore the degeneracies between them, and investigate how much cosmological information is lost after marginalising over the free parameters of the BCM.

3.6.1 Fisher Matrix

We employ a Fisher formalism to quantity the amount of information encoded in the mass power spectrum. Notice that we refrain from modelling the shear power spectrum (which would correspond to a convolution of the mass power spectrum with the relevant lensing kernel) to keep our study as general and independent of details of a particular experiment (e.g. the redshift distribution of background galaxies) as possible.

Using the power spectrum $P(k)$ as our observable, and assuming a multivariate Gaussian distribution, the Fisher matrix is defined as:

$$\mathcal{F}_{ij} \equiv \frac{\partial P}{\partial \vartheta_i} \mathcal{C}^{-1} \frac{\partial P^\dagger}{\partial \vartheta_j} + \frac{1}{2} tr \left[\mathcal{C}^{-1} \frac{\partial \mathcal{C}}{\partial \vartheta_i} \mathcal{C}^{-1} \frac{\partial \mathcal{C}}{\partial \vartheta_j} \right] \tag{3.5}$$

where $\mathcal{C}$ is the observable covariance matrix. We neglect the second term of Eq.3.5 to ensure the conservation of the information (Carron, 2013), noting however that $\mathcal{C}$ depends very weakly on cosmology and that term would be negligible (Kodwani et al., 2019).

Model parameters and priors

Our fiducial model will consist of a 8-parameter cosmology: five parameters describing a minimal model (Ω_m, Ω_b, h, n_s, A_s), one parameter describing the total neutrino mass ($\sum m_\nu$), and two parameters describing the dark energy equation of state, w_0 and w_a in the Chevallier-Polarski-Linder parametrisation, (Chevallier and Polarski, 2001; Linder, 2003). We assume fiducial values for these parameters consistent with the current constraints from CMB+BAO+Lensing (Planck Collaboration et al., 2018, hereafter Planck18). Specifically:

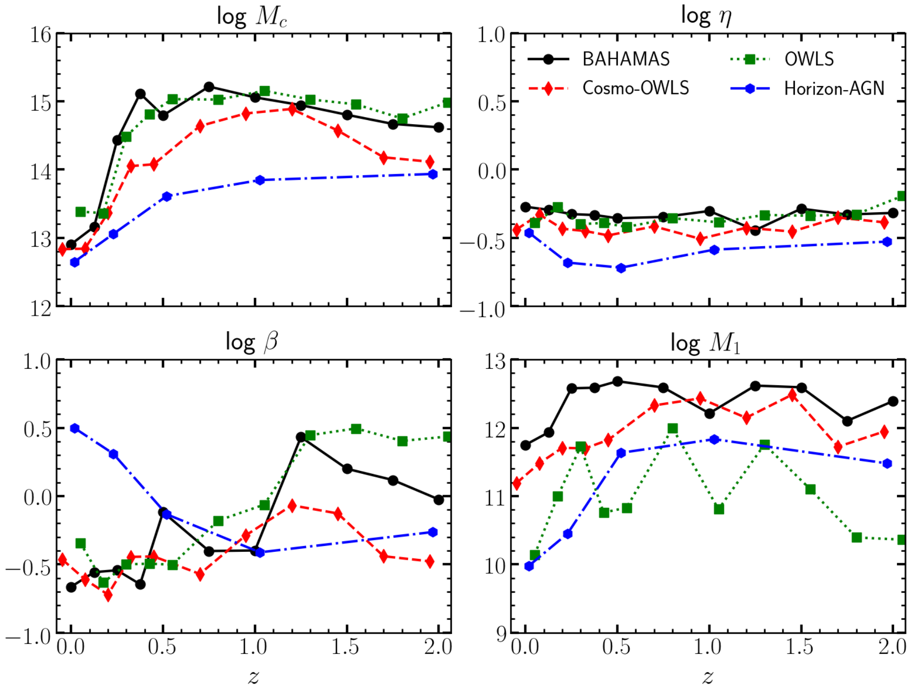

Figure 3.10: Marginalised values of the best-fitting BCM parameters for the BAHAMAS, Cosmo-OWLS, OWLS, and Horizon-AGN simulations at different redshifts $0 \geq z \geq 2$, as indicated by the legend. Note that the redshifts of the measurements are slightly shifted for display purposes.

$\Omega_{cdm} = 0.261$, $\Omega_b = 0.04897$, $\Omega_\Lambda = 0.69889$, $H_0 = 67.66\,\mathrm{km\,s^{-1}}h^{-1}\mathrm{Mpc}$, $n_s = 0.966$, $A_s = 2.105 \times 10^{-9}$, $w_0 = -1$, $w_a = 0$, $\sum m_\nu = 0.06$ eV.

We will also consider 4 additional baryonic parameters specifying the BCM. In particular, the best-fitting values of BAHAMAS found in §3.5: $M_c = 3.3 \times 10^{13}\ h^{-1}\mathrm{M}_\odot$, $\eta = 0.54$, $\beta = 0.12$, $M_1 = 8.63 \times 10^{11} h^{-1}\mathrm{M}_\odot$. This specific choice is justified by noticing that the BAHAMAS simulation have been specifically calibrated to match the observed baryon fraction in haloes, a quantity that is well correlated with baryonic clustering effects. Therefore, we expect its predictions to be more reliable for this analysis. Moreover, the cosmological framework of the simulation, which is given by Planck 2015 best-fitting values and includes massive neutrinos, is very similar to our fiducial one. We set the redshift of our analysis at $z = 0.25$, around which the lensing window of most of the current and forthcoming lensing surveys is peaked.

Covariance matrix

Very often, when computing the covariance matrix of the observable, $\mathcal{C}$, it is implicitly assumed a perfect theoretical model over the whole range of scales. This, however, is not correct in general. Specifically, for the case of nonlinear power spectrum, there are model uncertainties (arising from, for instance, how baryonic effects are described, the solution of the Vlassov-Poisson equations by N-body simulations, or emulation uncertainties) that should be taken into account. Therefore, we split our covariance matrix in two terms: $\mathcal{C} = \mathcal{C}_{\rm D} + \mathcal{C}_{\rm T}$, where $\mathcal{C}_{\rm D}$ describes the data covariance and $\mathcal{C}_{\rm T}$ the theory one. We employ a Gaussian data covariance which reads

$$\mathcal{C}_{{\rm D},ij} = \delta_{ij} \, \frac{2}{N_k} \left[P(k_i) + \frac{1}{\bar{n}} \right]^2 , \tag{3.6}$$

where N_k is the number of independent modes in each bin, approximated as $N_k = V_{\rm box} k^2 \Delta k / (2\pi)$ being Δk the bin width, and $1/\bar{n}$ is the shot noise term. The reference power spectrum $P(k)$ is computed with `halofit` (Takahashi et al., 2012) within the fiducial cosmology Planck18, and we consider for the shot noise term a total volume of $1\,h^{-3}{\rm Gpc}^3$ and a number density $\bar{n} = 5 \cdot 10^{-2}\ h^3$ Mpc^{-3}.

For $\mathcal{C}_{\rm T}$ we employ the same procedure used in §3.5.1, Eq. 3.2. We consider here as sources of model error the BCM and the cosmology rescaling. For the first, we assume $\mathcal{E}$ to be a constant with amplitude 1% of the reference power spectrum, and a correlation length $\ell = 1\,h\,{\rm Mpc}^{-1}$ which is motivated by our findings in Fig. 3.6.

For the term originating from the cosmology rescaling, $\mathcal{E}$ is a constant $P(k)/100$ that raises smoothly up to 2 % at $k \sim 1\,h\,{\rm Mpc}^{-1}$, $\mathcal{E} = [1.5 + 0.5\ {\rm erf}(k-1)]P(k)$, and same correlation length $\ell = 1\,h\,{\rm Mpc}^{-1}$, since typical deviations from the target simulation are similar on all scales (c.f. Fig. 3.5 and Contreras et al. 2020a). The theory covariance is simply given by the sum of the two contributions described above.

Numerical derivatives

The next ingredient for computing the Fisher matrix elements is the estimation of the partial derivatives $\partial P/\partial \vartheta_i$. We compute these using second-order-accurate central finite differences:

$$\frac{\partial P_\vartheta(k)}{\partial \vartheta} \approx \frac{P_{\vartheta+\epsilon}(k) - P_{\vartheta-\epsilon}(k)}{2\epsilon}. \tag{3.7}$$

We have checked that using the fourth-order approximation the results are practically identical. The parameter intervals, listed in Tab 3.3, are chosen to produce a 1 % effect in the matter power spectrum in the range $[0.01, 5]\ h\,{\rm Mpc}^{-1}$. We have carefully checked that these intervals are sufficiently small so that the power spectrum response is still linear but large enough so numerical noise is reduced.

Operationally, we rescale the cosmology of our simulation to the required parameter set, apply the BCM, and then measure the power spectra. In this analysis we use a set of paired simulations run with 768^3 particles and a box size of $256 h^{-1}{\rm Mpc}$ described in §3.2. To increase the precision of the scaling, we furthermore apply the interpolation between snapshots discussed in section §3.4. Therefore, for each point in the parameter space we

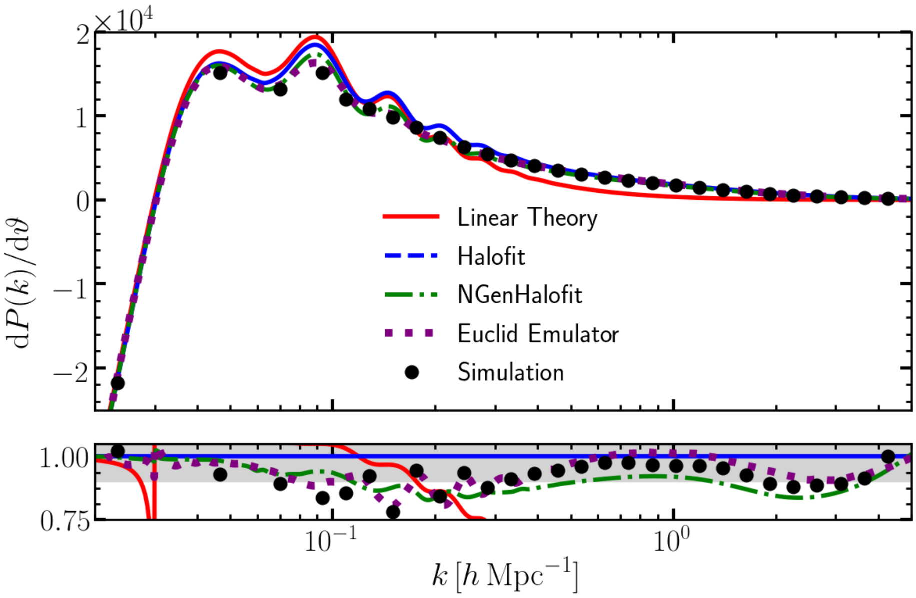

Figure 3.11: *Upper panel:* derivatives of the matter power spectrum at $z = 0.25$ with respect to Ω_{cdm}, evaluated for a Planck18 (with $\sum m_\nu = 0\,\mathrm{eV}$) cosmology and a BAHAMAS-like baryonic model. The black symbols indicate the results obtained using our cosmology scaling technique, which we compare against linear theory (red), `halofit` (blue), `NGenHalofit`(green) and `EuclidEmulator` (purple). *Lower panel:* ratio over `halofit` of the derivatives shown in the upper panel.

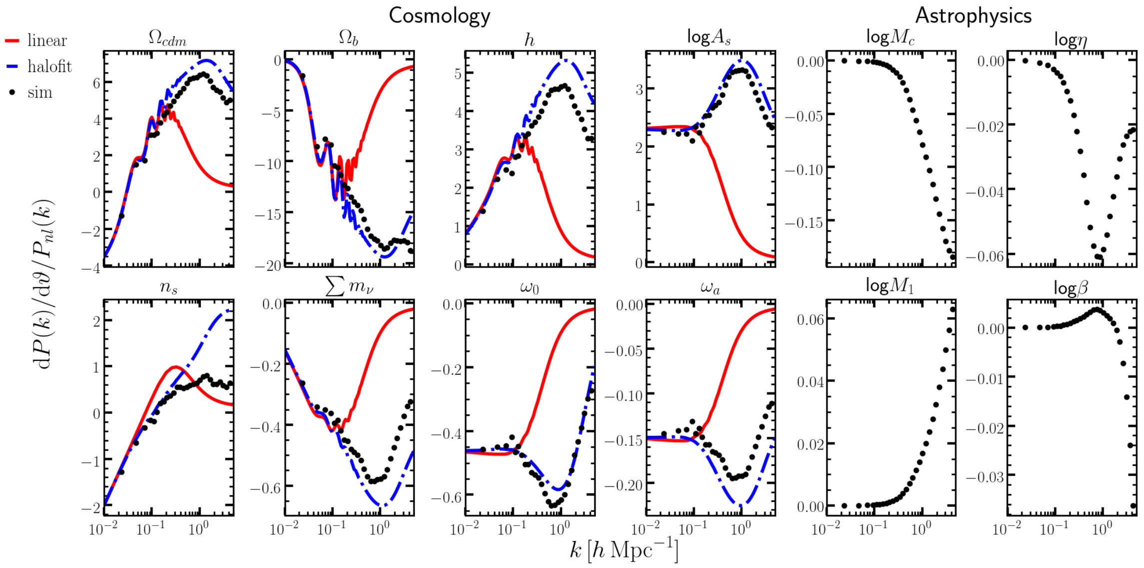

Figure 3.12: Derivatives of the matter power spectrum around the cosmology preferred by (Planck Collaboration et al., 2018) at $z = 0.25$. Symbols display the results computed with rescaled N-body simulations, whereas blue and red solid lines do so for `halofit` and linear perturbation theory, respectively.

scale the cosmology of four snapshots (two paired), and apply the BCM four times. In this case, we measure the power spectrum in bins which are multiples of the fundamental mode.

To achieve the extremely high precision required by the Fisher matrix calculation (e.g. numerical stability of the matrix inversion) we make a regression of our data in logarithmic bins for $k > 0.1h\,\mathrm{Mpc}^{-1}$, using the Gaussian processes framework `Gpy` (GPy, 2012), and furthermore applying a gaussian smoothing to remove any residual small-scale noise.

To test the accuracy of our results we compare our derivatives against those predicted by linear theory given by the Boltzmann solver `CLASS` (Lesgourgues, 2011a), `halofit` (Takahashi et al., 2012), `EuclidEmulator` (Knabenhans et al., 2019) and `NGenHalofit` (Smith and Angulo, 2019). The `EuclidEmulator` is built using a suite of 100 simulations run with different cosmologies, with a nominal absolute accuracy of 1%, whereas `NGenHalofit` is a 3%-accurate extension of `halofit` obtained by calibrating against the Däemmerung suite of simulations. Since none of these two codes support massive neutrino cosmologies, we perform the comparison assuming $\sum m_\nu = 0\,\mathrm{eV}$ and furthermore neglect baryonic effects.

In Fig. 3.11 we show our results for $\vartheta = \Omega_{cdm}$. On the largest scales considered, `halofit`, `NGenHalofit`, `EuclidEmulator` and our cosmology scaling technique all perfectly agree. On intermediate scales ($k > 0.1\,h\,\mathrm{Mpc}^{-1}$) the methods start to disagree at the 20% level. Specifically, our method, `EuclidEmulator` and `NGenHalofit` are in very good agreement but are systematically different from linear theory and `halofit`.

It is also interesting to note that BAO oscillations in `NGenHalofit` are damped more efficiently with respect to `halofit` and linear theory, but not as much as in `EuclidEmulator`. On small scales, `EuclidEmulator` predictions depart from those of `NGenHalofit`, providing again similar results around $k \approx 4\,h^{-1}\mathrm{Mpc}$. The cosmology scaling algorithm predicts power spectra which match the ones from `EuclidEmulator` within 1%, and accordingly the derivatives appear to be at the same accuracy level, supporting the validity of our approach. Although not shown here, we have checked that we obtain similar conclusions when considering other cosmological parameters in our set. It is also worth to highlight that we have obtained our results with only two relatively small simulations, $L = 256h\,\mathrm{Mpc}^{-1}$.

Having tested our implementation against other nonlinear models, we now consider our entire parameter space including massive neutrino and dynamical dark energy. In Fig. 3.12 we show the measured partial derivatives with respect to each of our 12 parameters. Linear theory and `halofit` predictions are overplotted for reference in the case cosmological parameters.

Cosmological derivatives provided by the three methods agree on large scales but differ on smaller scales ($k > 0.1h\,\mathrm{Mpc}^{-1}$). The good agreement between our approach with `NGenHalofit` and `EuclidEmulator` shown in Fig. 3.11 suggests the differences arise from inaccuracies in `halofit` rather than in the cosmology rescaling.

The dependence of the power spectrum with BCM parameters is consistent with that

parameter (ϑ)	interval (ϵ)
Ω_{cdm}	2.6×10^{-3}
Ω_b	7.0×10^{-4}
H_0 $[\mathrm{Km\,s^{-1}Mpc^{-1}}]$	1.6×10^{-3}
n_s	3.5×10^{-3}
$\log A_s$	2.7×10^{-3}
w_0	5.1×10^{-2}
w_a	5.2×10^{-2}
$\sum m_\nu$ [eV]	2.0×10^{-2}
M_c $[h^{-1}\mathrm{M}_\odot]$	1.2×10^{-1}
M_1 $[h^{-1}\mathrm{M}_\odot]$	3.5×10^{-1}
η	1.3×10^{-1}
β	1.4×10^{-1}

Table 3.3: Parameter intervals used to compute numerically the derivatives of the power spectrum. The values were chosen to cause 1% change in the nonlinear matter power spectrum over the range $k \in [0.01 - 5]\,h\,\mathrm{Mpc}^{-1}$.

shown in Fig. 3.4, being the range of the AGN feedback parametrised by η the one impacting the power spectrum on larger scales, while the galaxy formation parametrised by M_1 causes an enhancement of power on small scales.

3.6.2 Information in the mass power spectrum

In the Gaussian approximation, the total amount of information that we can extract up to a given scale is proportional to the number of independent modes contained in that scale. Since the number of independent modes N_k goes as $N_k \propto k^3$, it is evident that even a modest increase of the smallest scale modelled can unlock a big amount of information. Small scales, on the other hand, are more affected by baryonic physics. In this subsection we will explore this interplay.

In Fig. 3.13 we show the 1σ credibility regions of baryonic and cosmological parameters, employing as minimum scales wavenumbers from $2\,h\,\mathrm{Mpc}^{-1}$ to $5\,h\,\mathrm{Mpc}^{-1}$. The baryonic parameters show many degeneracies, both between each other and the cosmological parameters. In particular, for large M_c the model prefers low η and h, and large values of w_0, A_s, Ω_{cdm} . The β parameter is degenerate with M_1, and for large values of η are preferred large M_1. Moreover, η is degenerate with the dark energy equation-of-state parameters, preferring large values for low w_0 and high w_a.

As we consider smaller scales, constraints improve and some of the degeneracies flip direction or are completely broken. For example, large values of h seem to prefer high M_1 considering only scales up to $k = 3\,h\,\mathrm{Mpc}^{-1}$, but low M_1 extending the analysis to smaller scales. The degeneracy between h and Ω_b is broken including scales $k \geq 4\,h\,\mathrm{Mpc}^{-1}$. At large scales, the sum of neutrino masses $\sum m_\nu$ shows an anticorrelation with M_c, a result

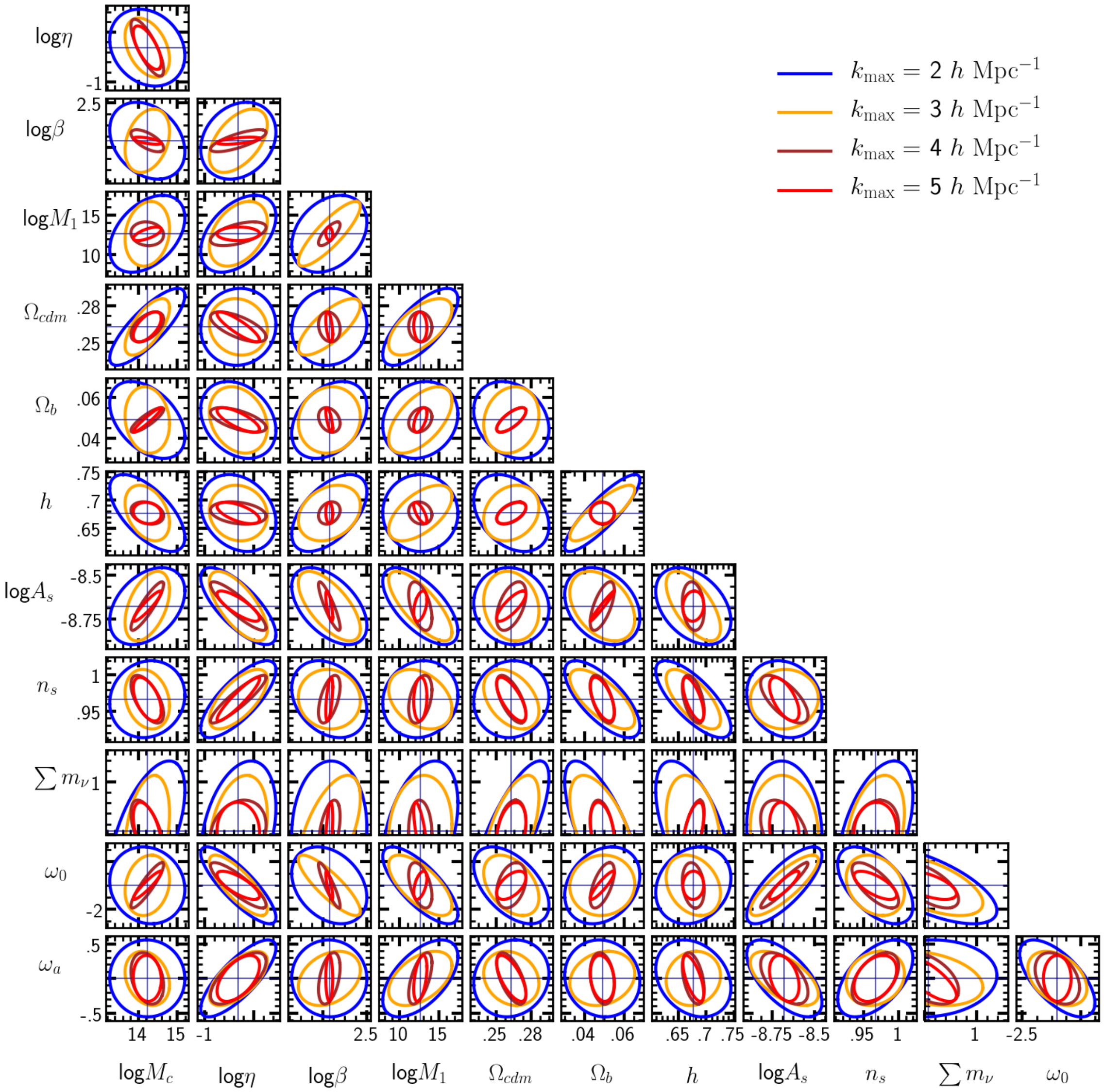

Figure 3.13: 1σ ellipses computed considering as maximum wavenumber of the analysis k_{max}=2,3,4 and 5 $h\,\mathrm{Mpc}^{-1}$ (blue, orange, brown and red solid lines, respectively). These Fisher forecasts have been computed using a $256\,h^{-1}\mathrm{Mpc}$ simulation, scaled to Planck18 cosmology and employing a BAHAMAS-like baryonic feedback at redshift $z = 0.25$. Notice that we are not considering the theoretical contribution to the covariance matrix to show the dependence of the parameter degeneracies with the minimum scale.

similar to what found by Parimbelli et al. (2019), using `halofit` combined with BCM fitting function up to $k \leq 0.5\, h\, \mathrm{Mpc}^{-1}$ in weak lensing forecasts. We note that, however, including the small scales the situation changes, and for large neutrino masses are preferred high values of M_c.

In principle, it is possible to constrain the BCM parameters through observations, e.g. the halo baryonic fraction and stellar-to-halo mass relation through X-ray, thermal Sunyaev-Zeldovich effect or weak-lensing data. In practice, however, the actual constraints on the BCM parameters are loose because of both observational and modelling uncertainties (e.g. hydrostatic mass bias, see Schneider et al., 2019).

A viable alternative can be the marginalisation over the baryonic parameters to avoid biased results in the estimation of the cosmological parameters, at the price of loosing constraining power. In Fig. 3.14 we show the 1σ credibility regions obtained by ignoring, fixing and marginalising over the baryonic physics. Interestingly, the degeneracies of the cosmological parameters slightly change if we consider or not the baryonic effects, even if we do not marginalise over them. Notice that by construction the ellipses are centred about the true values of the parameters, therefore the plot is not meant to show the possible biases of the parameters estimation. It is also important to note that, despite the use of a state-of-the-art modelling within high resolution N-body simulations, the theoretical errors of the model are still the main uncertainties on the constraints, and must be incorporated in each pipeline to avoid bias in parameter estimations. On the other hand, we find that the marginalisation over the baryonic parameters have a quite different impact on the constraining power for different parameters.

In Fig. 3.15 we display the expected marginalised 1σ constraints in the parameters employing the information up to varying wavelengths. We display a case where we assume perfect knowledge of the astrophysical processes (solid lines) and where we marginalise over the baryonic parameters (dashed lines). It is evident that the impact of the marginalisation is scale-dependent, and generally larger on large scales. The constraints obtained at $k = 5\, h\, \mathrm{Mpc}^{-1}$ for $\sum m_\nu$, Ω_b and w_a are factors of ~ 2 larger after the marginalisation. On the contrary, h, A_s and w_0 have a factor of $\sim 4-5$ weaker constraints, with the other parameters falling in between.

Recently, Schneider et al. (2020) have performed a similar study, fitting the shear power spectrum using a model which combines the predictions of `halofit` with an emulator built upon a baryon correction model. They find that constraints in n_s are more than a factor of 2 weaker after the marginalisation, whereas h and Ω_m less than 50%. These results are in broad agreement with our findings, even if a more direct comparison is not possible because of the different assumptions in the BCM setup, the characteristics of the target survey and the observable used in the analysis.

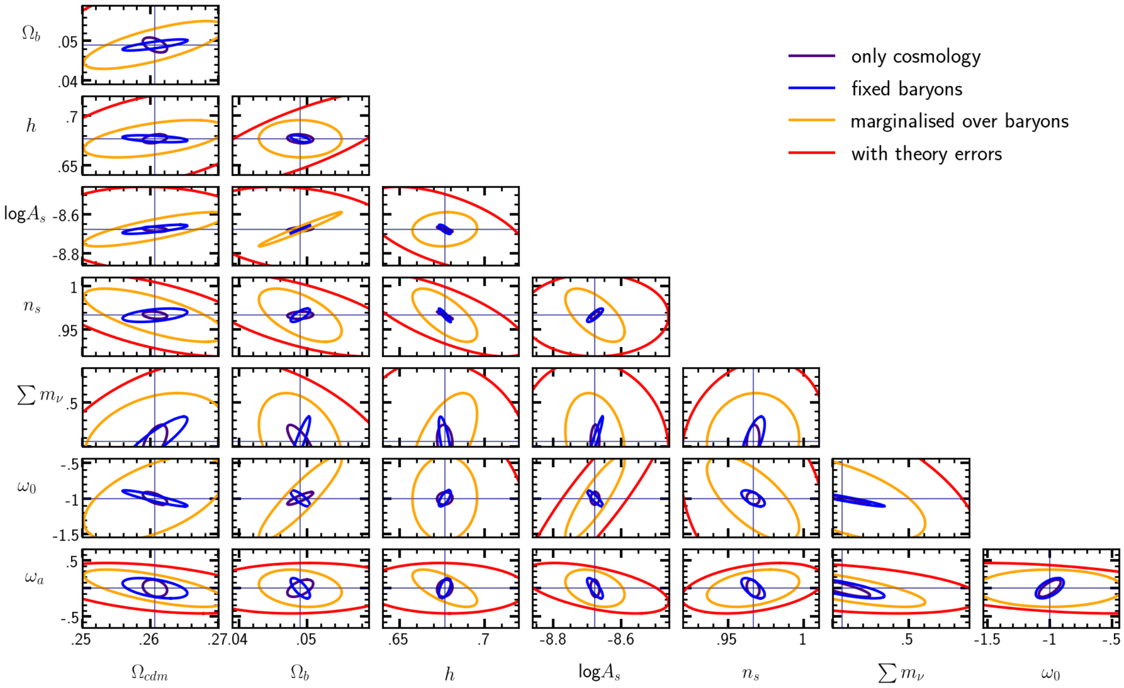

Figure 3.14: 1σ Fisher contours of the matter power spectrum measured at scales $k \leq 5\,h\,\mathrm{Mpc}^{-1}$, considering only cosmology (purple line), an exact baryon modelling (blue), marginalising over the baryonic parameters (orange), and including in the marginalisation the theory errors (red).

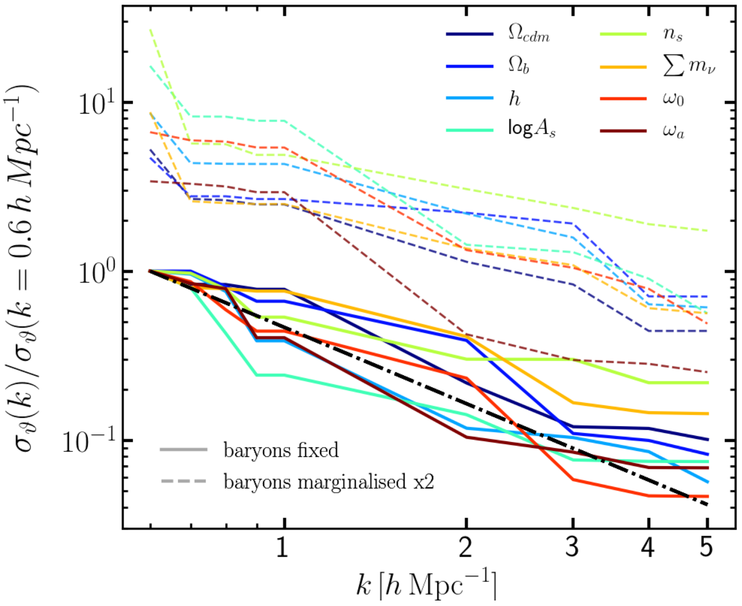

Figure 3.15: Expected accuracy in cosmological parameters constraints as a function of the maximum wavenumber k used in the analysis. Different colours display the results for different parameters, as indicated by the legend. Dashed and solid lines show the ratio between results obtained marginalising and fixing baryonic parameters, respectively. Note the former are multiplied by a factor of two for display purposes. The dashed-dotted line represents the ideal scaling expected for Gaussian fields, $\propto k^{-3/2}$.

3.7 Discussion and Conclusions

Cosmological observations are entering an age where uncertainties in data models are significantly limiting the inferred parameter constraints. In particular, for weak gravitational lensing, not only the nonlinear evolution of density fluctuations but also details of galaxy formation theory and the evolution of cosmic gas become important for correctly interpreting future measurements.

Jointly modelling cosmology and astrophysics via hydrodynamical simulations requires a huge computational effort because of the large dynamical range and number of (still uncertain) astrophysical processes involved. In addition, hydrodynamical simulations make specific choices about the physics included, hydrodynamical solver, and the free parameters of each sub-grid recipe. To consistently and systematically explore different models of both cosmology and astrophysics appears simply unfeasible with the current computational power without making multiple assumptions.

In this context, baryonic correction and cosmology rescaling methods appear to provide a fast and flexible approach to capture the effects of astrophysics and cosmology on the full density field. The main idea is to model the impact of baryonic physics with a minimal set of recipes (motivated by observations and numerical simulations), which are applied in post-processing to a gravity-only simulation with varying cosmologies, as provided by cosmology-rescaling methods. In this way, observations such as weak-lensing and Sunyaev-Zeldovich could simultaneously constrain cosmological and astrophysical parameters.

Key points of this method are the dispensable use of a full set of N-body simulations, the relatively easy incorporation of extensions to ΛCDM, the large parameter space covered, and the possibility of carrying out larger and more accurate simulations to achieve a higher precision in the matter clustering measurements. We recall moreover that for each of the baryon-cosmology set we obtain a full 3D prediction for the galaxy, gas, and star distributions, opening up interesting possibilities of predicting the cross-correlations of different observables.

In this chapter we have discussed one possible implementation of such baryonic correction models applied on one paired N-body simulation rescaled to different cosmologies. Below we summarise the main findings:

- Our specific Baryon Correction Model (BCM) is able to describe the mass matter power spectrum up to $k = 5h\,\mathrm{Mpc}^{-1}$ at $z = 0$, achieving an accuracy of $< 1\%$ for all 7 state-of-the art hydrodynamical simulations here considered (Fig. 3.6).

- By only fitting the mass clustering, we are able to recover the correct halo baryon fraction in most of the cases, except for extreme feedback models (e.g. Illustris, Fig. 3.8).

- Different hydrodynamical simulations prefer different values and redshift evolution for the free parameters of the BCM (Fig. 3.7). Despite this, there is a relatively tight correlation between the baryon fraction in clusters and the baryon-induced power spectrum suppression (Fig. 3.10).
- Applying our BCM to cosmology-rescaled simulations adds only $< 1\%$ uncertainty to the whole approach (Fig. 3.5).
- Using a Fisher matrix formalism we explore the impact of baryons on the information available in the mass power spectrum up to $k \sim 5h\,\mathrm{Mpc}^{-1}$ (Fig. 3.12). We find baryons change the sensitivity of $P(k)$ to cosmology, altering the degeneracy among parameters.
- After a marginalisation over the free parameters of the BCM, there is a moderate degradation of constraining power (see Fig. 3.15). Specifically, constraints decrease by factors of 2-4 depending on the parameter considered. Naturally, these values will depend on the specific setup of a given survey.
- Errors and uncertainties in any data model exist and cannot be neglected. We estimate the magnitude of such uncertainty for our approach to be of about $\sim 2\%$. We incorporate these errors in our Fisher analysis and find that it degrades cosmological information further than a marginalization of the BCM free parameters (red contours, Fig 3.14) for the setup considered here.

In conclusion, the combination of BCM and cosmology rescaling provides a powerful framework for simultaneously model cosmology and baryonic physics for large scale structure, and weak gravitational lensing in particular. There are some aspects that are important to highlight in the context of future data analyses.

First, it is crucial to understand and quantify all sources of uncertainties in data models. This can be achieved, for instance, by analysing mock lensing surveys constructed from state-of-the-art hydrodynamical simulations and realistic conditions. Naturally, the exact impact of theory errors depend on the specifics of the target observational setup and the model employed, but we emphasise the need of more flexible rather than more deterministic models for baryonic effects.

Second, it is important to guarantee that the BCM is both minimal and flexible enough so that derived constraints are as tight as possible, but also that they do not make strong assumptions regarding the underlying baryonic physics. This is crucial to ensure robust constraints on, for instance, neutrino masses. Thanks to the clear physical meaning of each component and the free parameters of the BCM, the assumptions, functional form and values can be directly compared with hydrodynamical simulations under extreme physics implementations.

Third, the accuracy of the BCM, the cosmology rescaling, and numerical simulations as a whole can be improved further. For instance, better concentration-mass relation models and the joint use of various simulations can improve the accuracy of cosmology-rescaling; systematic comparison among different N-body codes as a function of force and time-integration accuracy; and direct testing of the recipes within the BCM.

An interesting path is to extend the BCM to other gas properties. This would pave the way for joint analysis of multiple observables. For instance, the extent of the expelled gas should not only affect lensing observables, but also the amount of gas detectable via Sunyaev-Zeldovich effect. Similarly, the amount of galaxies and their mass affects the lensing signal on small scales, but also affects the galaxy correlation function on small scales. The use of high-resolution simulations enabled by the cosmology-rescaling should also allow for more sophisticated and realistic modelling of the galaxy-halo connection, which should ultimately improve the performance of the BCM and reduce free parameters. We plan to explore all this in future works.

Chapter 4

Baryonification and bispectrum: going to higher orders

In this chapter, adapted from “Simultaneous modelling of matter power spectrum and bispectrum in the presence of baryons” (Aricò et al., 2021a), we demonstrate that baryonification algorithms, which displace particles in gravity-only simulations according to physically-motivated prescriptions, can simultaneously capture the impact of baryonic physics on the 2 and 3-point statistics of matter. Specifically, we show that our implementation of a baryonification algorithm jointly fits the changes induced by baryons on the power spectrum and equilateral bispectrum on scales up to $k = 5h\,\mathrm{Mpc}^{-1}$ and redshifts $0 \leq z \leq 2$, as measured in six different cosmological hydrodynamical simulations. The accuracy of our fits is typically $\sim 1\%$ for the power spectrum, and for the equilateral and squeezed bispectra, which somewhat degrades to $\sim 3\%$ for simulations with extreme feedback prescriptions. Our results support the physical assumptions underlying baryonification approaches and encourage their use in interpreting weak gravitational lensing and other cosmological observables.

4.1 Introduction

Despite large efforts of the scientific community, the nature of dark energy and dark matter remains elusive. Even if the standard ΛCDM model has successfully passed many independent tests in the last decades, recent tensions in the estimated values of the Hubble constant and in the amplitude of the linear fluctuation have been pointed out as a possible window to physics beyond ΛCDM (e.g. Verde et al., 2019; Wong et al., 2020). To successfully solve these tensions, it is paramount that current and upcoming cosmological surveys extract the maximum amount of cosmological information at the low redshifts, where dark energy and dark matter are more accessible (Planck Collaboration et al., 2018; Troxel et al., 2018; Benitez et al., 2014; Laureijs et al., 2011; DESI Collaboration et al., 2016; Aihara et al., 2018). For many observables and statistics, the limiting factor will be the predictability and accuracy of theoretical models employed to analyse the data.

For the case of next-generation weak lensing surveys, the largest theoretical uncertainty is given by baryonic physics – gas cooling, star formation, and feedback, for instance, modify significantly the total mass distribution in the universe in a way that is not possible to accurately predict from first principles. On the other hand, if these baryonic processes are modelled appropriately, then we could extract more cosmological information, and possibly also constrain astrophysical processes.

A promising approach to incorporate the baryonic effects in models for the cosmic density field is *baryonification* (Schneider and Teyssier, 2015a; Schneider et al., 2019; Aricò et al., 2020b). Briefly, these algorithms displace particles in gravity-only simulations according to physically-motivated recipes designed to mimic the effects produced by baryons in the Large Scale Structure (LSS) of the universe. This method has been extensively tested against many hydrodynamical simulations, and it is shown to be very accurate in capturing the changes induced by baryons on the power spectrum (Schneider et al., 2020; Aricò et al., 2020b).

In general, baryons are expected to modify the full density field and thus the whole hierarchy of N-point functions, not only the power spectrum. Indeed, hydrodynamical simulations predict a non-zero impact of the astrophysical processes on the bispectrum (i.e. the Fourier-space 3-point correlation function), and a difference dependence of baryon physics on power spectrum and bispectrum (Semboloni et al., 2013; Foreman et al., 2020). A joint analysis of power spectrum and bispectrum thus could potentially help to break degeneracies among different baryonic feedbacks. Moreover, the bispectrum is expected to add significant cosmological information in the analysis of ongoing and future weak lensing surveys (Kilbinger and Schneider, 2005; Bergé et al., 2010; Semboloni et al., 2013), especially when self-calibrating the measurements taking advantage of the different redshift dependences of the two statistics (Huterer et al., 2006). The exploitation of the extra information provided by the bispectrum is limited by the accuracy and computational cost of the bispectrum models, as well as the unknown impact of systematics e.g. baryon physics and intrinsic alignment. Big steps foward have been done in the last years, and the development of efficient, publicly available codes (e.g. `bskit` (Foreman et al., 2020)) to measure the bispectrum in simulations, techniques as the folding of particle distribution (see Appendix F), and the common use of emulators to efficiently explore the parameter space of expensive functions (e.g. Heitmann et al., 2014; Knabenhans et al., 2019; Winther et al., 2019; McClintock and Rozo, 2019; Pellejero-Ibañez et al., 2020; Angulo et al., 2020; Euclid Collaboration et al., 2020; Aricò et al., 2020a; Zennaro et al., 2021), pave the way to the incorporation of the bispectrum in the analalysis of upcoming surveys.

Motivated by these findings, in this chapter we extend the analysis of the baryonification algorithm presented in Aricò et al. (2020b) (hearafter A20) to the bispectrum. We note that exploring the predictions of baryonification for the bispectrum is also important since it could highlight the pitfalls of the method or, instead, could support the correctness of the whole approach. Additionally, this comparison would represent an independent test of the method since higher-order statistics were never employed in the formulation of the baryonification algorithm. Given the simplifications and assumptions of baryonification methods – e.g. spherically symmetric displacements, dependences on halo mass, and neglected physical processes – it is unclear whether they would be able to consistently model baryonic effects on the power spectrum and bispectrum.

First, we extend the model to account for gas that has been reaccreted by halos, and then show how different model parameters change the power spectrum and bispectrum. Then, we show that our baryonification implementation can simultaneously reproduce, to better than 3%, the power spectrum and bispectrum measured in six state-of-the-art hydrodynamical simulations at $k \leq 5h\,\mathrm{Mpc}^{-1}$ and at $z \leq 2$. These range of scales and redshifts are suited to optimally extract information from *stage IV* surveys, where the signal is expected to peak at $z \approx 1$ and $k \approx 1h\,\mathrm{Mpc}^{-1}$ (Taylor et al., 2018b,a, 2020). We furthermore explore the impact that the different components of the model, e.g. central galaxy, ejected gas and back-reaction onto dark matter, have on the matter bispectrum.

This chapter is structured as follow: in §4.2 we describe our numerical simulations, while in §4.3 we present our methodologies for baryonic and cosmology modelling of the density field. In §4.4 we discuss the impact of baryons in the bispectrum, whereas in §4.5 we show our fits to the hydrodinamical simulations. We give our conclusions in §4.6.

4.2 Numerical simulations

In this work we use the same suite of N-body simulations used in A20. We refer the reader to it for further details, and here we only provide a brief description.

Our gravity-only simulations were carried out with `l-gadget-3` (Angulo et al., 2012), a modified version of `gadget` (Springel, 2005). We employ simulations of box sizes: L=64, 128, and 256 $h^{-1}\mathrm{Mpc}$ containing 192^3, 384^3, 768^3 particles, respectively. We adopt the *Nenya* cosmology, as defined by Contreras et al. (2020a): $\Omega_{\mathrm{cdm}} = 0.265$, $\Omega_{\mathrm{b}} = 0.050$, $\Omega_\Lambda = 0.685$, $H_0 = 60\ \mathrm{km}\,s^{-1}\,\mathrm{Mpc}^{-1}$, $n_s = 1.010$, $\sigma_8 = 0.90$, $\tau = 0.0952$, $\sum m_\nu = 0$, $w_0 = -1$, and $w_a = 0$. These parameters are optimal to rescale them to a large range of cosmologies (Contreras et al., 2020a; Angulo et al., 2020). To test the accuracy of this rescaling, we will consider two additional simulations of $512\,h^{-1}\mathrm{Mpc}$ and 1536^3 particles: one adopting the *Nenya* cosmology, and the other a massless neutrino *Planck* cosmology

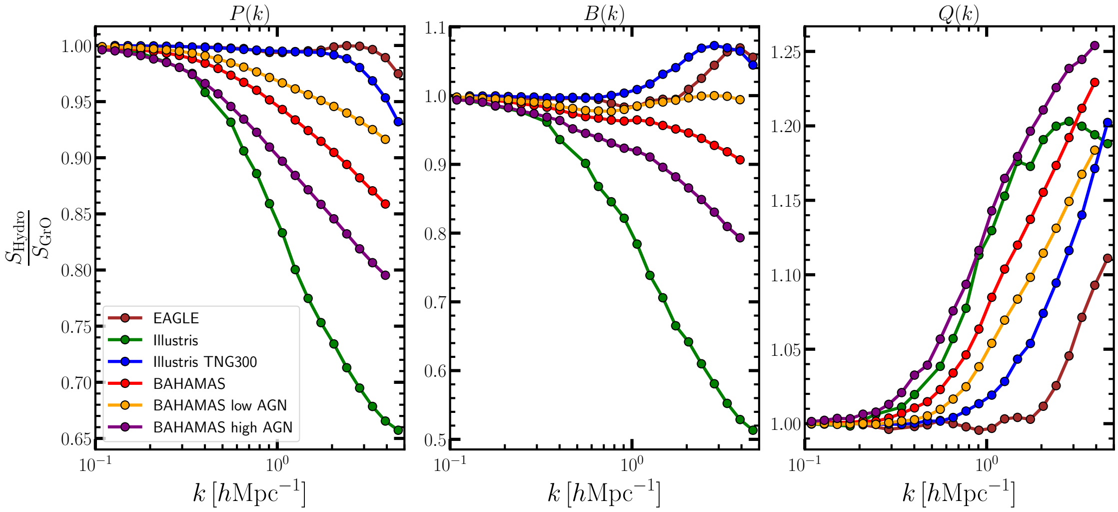

Figure 4.1: Baryonic effects at $z = 0$ on the power spectrum (left panel), equilateral bispectrum (central panel) and reduced bispectrum (right panel), measured in 6 hydrodynamical simulations: BAHAMAS (standard, low and high AGN), EAGLE, Illustris and Ilustris TNG-300. We display the ratio of $S = \{P, B, Q\}$ estimated in the full hydrodynamical simulation to that in their respective gravity-only counterpart.

(Planck Collaboration et al., 2018) [1]. To compute the statistics of the density field, we use catalogue of simulation particles, selected homogeneously, diluted by a factor of 4^3. The initial conditions of all our simulations were computed with the "fixed and paired" technique described in Angulo and Pontzen (2016), thus their cosmic variance is heavily suppressed. In Appendix E we show the impact that the "fixed and paired" technique has on the power spectrum and bispectrum in simulations with different box sizes. The cosmic variance in the bispectrum has an amplitude of $\approx 3\%$ in our $64\,h^{-1}\mathrm{Mpc}$ simulation, and less than 2% in our $256\,h^{-1}\mathrm{Mpc}$, whereas in the power spectrum is always below 1%. Thus, if not specified otherwise, our results will be computed with the L=$256\,h^{-1}\mathrm{Mpc}$ simulation, with which we expect our results to be converged to about 2% for both bispectrum and power spectrum.

4.2.1 Measurement of power spectra and bispectra

Considering an overdensity field in Fourier space $\delta(\mathbf{k})$, we define the power spectrum as

$$\langle \delta(\mathbf{k_1})\delta(\mathbf{k_2})\rangle \equiv (2\pi)^3\delta^D(\mathbf{k_1}+\mathbf{k_2})P(k_1) \tag{4.1}$$

and the bispectrum as

$$\langle \delta(\mathbf{k_1})\delta(\mathbf{k_2})\delta(\mathbf{k_3})\rangle \equiv (2\pi)^3\delta^D(\mathbf{k_1}+\mathbf{k_2}+\mathbf{k_3})B(k_1,k_2,k_3), \tag{4.2}$$

---

[1] $\Omega_{\rm cdm} = 0.261$, $\Omega_{\rm b} = 0.049$, $\Omega_\Lambda = 0.699$, $H_0 = 67.66\ \mathrm{km\,s^{-1}\,Mpc^{-1}}$, $n_s = 0.966$, $\sigma_8 = 0.81$, $\tau = 0.0561$, $\sum m_\nu = 0$, $w_0 = -1$, $w_a = 0$.

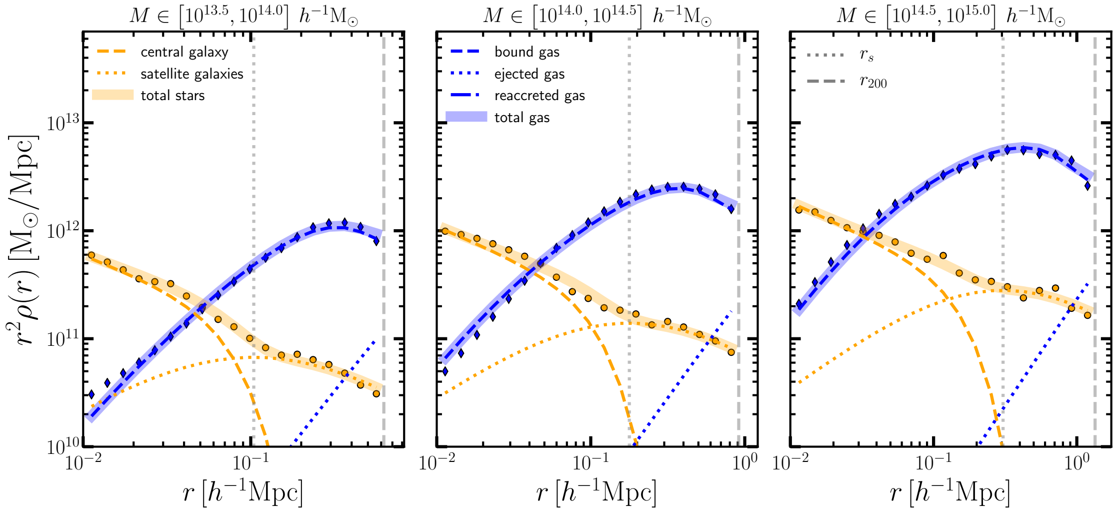

Figure 4.2: Density profiles of gas (blue diamonds) and stars (orange circles) as measured in the Illustris TNG-300 simulation, at $z = 0$. Each panel shows a different mass bin: $10^{13.5} - 10^{14}\,h^{-1}\mathrm{M}_\odot$ (left panel), $10^{14} - 10^{14.5}\,h^{-1}\mathrm{M}_\odot$ (central panel), and $10^{14.5} - 10^{15}\,h^{-1}\mathrm{M}_\odot$ (right panel). The baryonification model that best fits simultaneously the three density profiles is shown as blue and orange shaded bands for gas and stars, respectively. The different gas and stellar subcomponents are displayed with different line styles, according to the legend. Note that the reaccreted gas density is consistent with zero, thus not appearing in the plot.

where $\langle ... \rangle$ denotes the ensemble average and δ^D is the Dirac's delta. To reduce the dependence of the bispectrum on the power spectrum and cosmology, we will mostly consider the *reduced bispectrum* (Scoccimarro, 2000; Sefusatti and Komatsu, 2007), defined as

$$Q(k_1, k_2, k_3) \equiv \frac{B(k_1, k_2, k_3)}{P(k_1)P(k_2) + P(k_2)P(k_3) + P(k_1)P(k_3)}. \tag{4.3}$$

We will mostly focus on the equilateral configuration, $k_1 = k_2 = k_3$, since it is expected to contain the most independent information from the power spectrum. Indeed, in the extreme triangle configurations, the "squeezed" limit can be seen as "conditional" power spectra, and thus they are expected to present similar baryonic effects to the power spectrum (see e.g. Barreira et al., 2019); whereas the "squashed" limit generally track the equilateral one (Foreman et al., 2020). We focus on the equilateral configuration also because it is sensitive to anisotropies of the density field, of particular interest in our case, to test the spherical symmetry assumption in the modelling of baryons. In this case, Eq. 4.3 is reduced to:

$$Q(\mathtt{k}) = \frac{B(\mathtt{k})}{3P(k)^2}. \tag{4.4}$$

We measure the bispectrum using `bskit` (Foreman et al., 2020)[2], an extension of `nbodykit` (Hand et al., 2018) which uses a Fast Fourier Transform (FFT)-based bispectrum estimator (Scoccimarro, 2000). Both the bispectrum and the power spectrum are measured

---

[2] `https://github.com/sjforeman/bskit`

in two interlaced grids (Sefusatti et al., 2016) employing a *triangular shaped cloud* mass assignment scheme. The shot noise contribution is estimated as $1/\bar{n}$ for the power spectrum, and as $1/\bar{n}^2 + 1/\bar{n}[P(k_1) + P(k_2) + P(k_3)]$ for the bispectrum, and subtracted. Finally, we have rebinned all the measurements in 25 logarithmic bins over the interval $[0.1, 5.0]\,h\,\mathrm{Mpc}^{-1}$. Additionally, when measuring the clustering on small scales, we use the "folding" technique (Jenkins et al., 1998; Colombi et al., 2009), described in Appendix F, which reduces CPU and memory usage.

We will compare our results against the power spectra and bispectra from a number of cosmological hydrodynamical simulations, as measured by Foreman et al. (2020)[3]. Specifically, we use four state-of-the-art hydrodynamical simulations: BAHAMAS [4] (McCarthy et al., 2017, 2018), EAGLE [5] (Schaye et al., 2015; Crain et al., 2015; McAlpine et al., 2016; Hellwing et al., 2016; The EAGLE team, 2017), Illustris [6] (Vogelsberger et al., 2013, 2014b,a; Sijacki et al., 2015), and Illustris TNG-300 [7] (Springel et al., 2018; Pillepich et al., 2018; Nelson et al., 2018; Naiman et al., 2018; Marinacci et al., 2018; Nelson et al., 2019). In the case of BAHAMAS, we consider two additional AGN feedback calibrations, dubbed as "low-AGN" and "high-AGN": in the first one the temperature at which the AGN is activated is lower and thus the AGN feedback is weaker; whereas in the latter AGN feedback is stronger with respect to the standard run.

In Fig. 4.1 we show the baryonic effects on the power spectrum, bispectrum, and reduced bispectrum. We display the ratio of the clustering measured in the full hydrodynamical simulations to that in their gravity-only counterparts. Different colours show the results for different simulations, as indicated by the legend.

We see that the amplitude of baryonic effects considerably varies among simulations, in both power spectra and bispectra. In particular, Illustris and Bahamas high-AGN show the strongest suppression in both these statistics, likely due to their strong Supernovae and AGN feedback. On the contrary, EAGLE and Illustris TNG-300 show the smallest baryonic effects also likely related to their comparatively weak feedback in massive halos. We highlight that both of these simulations display an enhancement of the bispectrum at $k \approx 2 - 3\,h\,\mathrm{Mpc}^{-1}$, which has been linked to the presence of late-time reaccreted gas by Foreman et al. (2020). We will test this hypothesis with our baryonification framework later on.

Interestingly, whereas baryons can either suppress or enhance the gravity-only bispectrum, they appear simpler in the reduced bispectrum: baryons always enhance $Q(k)$ on small scales. Qualitatively, there seems to be a clear correlation between the baryonic effects in the power

---

[3] `https://github.com/sjforeman/hydro_bispectrum`

[4] `http://www.astro.ljmu.ac.uk/~igm/BAHAMAS/`

[5] `http://icc.dur.ac.uk/Eagle/`

[6] `https://www.illustris-project.org/`

[7] `https://www.tng-project.org`

spectrum and bispectrum. However, this correlation is not perfect: Illustris and BAHAMAS high-AGN show similar effects on the reduced bispectrum, but the effects on the power spectrum are clearly different [8]. In the next sections we will explore whether baryonification methods can successfully describe all these features at high precision.

4.3 Modelling of the density field

Given a particle field in a Gravity Only (GrO) N-body simulation, we can obtain the mass field in arbitrary cosmologies and baryonic scenarios by manipulating the positions and masses of the particles. To do so, we use the framework described in A20, which we recap next.

We first apply a "cosmology rescaling" to obtain a simulation at a desired cosmological parameter set (Angulo and White, 2010). For this, we scale the lengths, masses and time (by selecting different snapshots) of our simulation in order to match the amplitude of the linear density fluctuation of another cosmology. This technique has been extensively tested (Ruiz et al., 2011; Renneby et al., 2018; Mead and Peacock, 2014a,b; Mead et al., 2015; Angulo and Hilbert, 2015; Zennaro et al., 2019; Contreras et al., 2020a), and it has been recently extended to take into account the non-universality of the halo mass function (Ondaro-Mallea et al., 2021). The cosmology rescaling has a $< 3\%$ accuracy in the matter power spectrum and 5% in the matter bispectrum up to $k \sim 5h^{-1}\mathrm{Mpc}$ (Contreras et al., 2020a, Zennaro et al. in prep), over a broad range of cosmologies, even beyond-ΛCDM. Note we expect a higher accuracy for the ratio of baryonified over gravity-only outputs, as we will show later.

We then apply a "baryonification" algorithm to further displace the particles of the simulation, and mimic the effect of different baryonic components. In A20, each halo was assumed to have four components: dark matter, a central galaxy, bound gas, and expelled gas. In this work, we additionally model satellite galaxies and late-time reaccreted gas, which we describe in detail in the next subsection. The density profiles of all these components are parametrised with physically motivated functional forms, whereas the GrO halo density profile is modelled with as a NFW profile (Navarro et al., 1997). Once we have the initial and the "baryonic" density profiles, we compute a displacement field which, applied to the halo particles, distorts their distributions accordingly.

4.3.1 Updates of the baryon correction model

One of the main advantages of the *baryon correction model* is its extreme flexibility, which allows us to make modifications or include new physics according to various possible

---

[8] However, note that Illustris simulates a box less than $75\,h^{-1}\mathrm{Mpc}$, thus their results could be affected by cosmic variance and lack of long wavemodes. As showed in Appendix E, massive haloes contribute to baryonic effects more in the bispectrum than in the power spectrum. As a consequence, the reduced bispectrum measured in relatively small boxes is suppressed at small scales with respect to larger boxes.

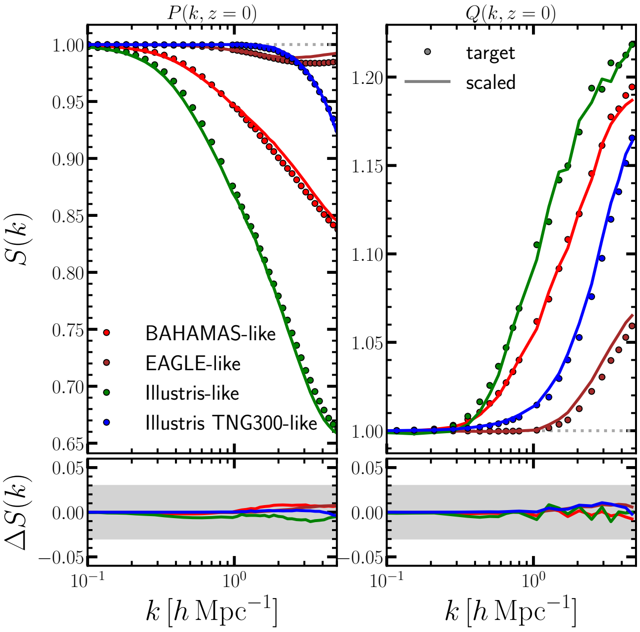

Figure 4.3: Accuracy of the cosmology-rescaling algorithm when used with a baryonification procedure. [*Upper panel:*] Ratio of the baryonified and gravity-only mass power spectra and reduced bispectra at $z = 0$. Symbols show the results using a simulation adopting the *Planck* cosmology, whereas lines indicate the results using a simulation *rescaled* to the same *Planck* cosmology. We provide results for 4 baryonification models roughly consistent with the effects expected in BAHAMAS (red), EAGLE (brown), Illustris (green) and Illustris TNG-300 (blue) models. [*Lower panel:*] Difference between the baryonic effects measured in the target and scaled simulation shown in the upper panels. The grey shaded band marks a discrepancy of 3%.

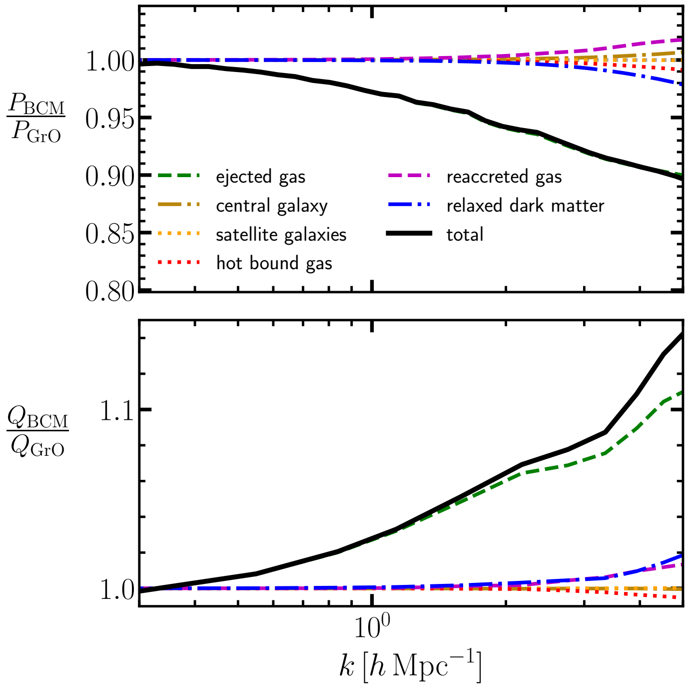

Figure 4.4: Modifications to the matter power spectrum (upper panels), and reduced bispectrum (lower panels) at $z = 0$ caused by baryons, as predicted by our baryonification algorithm with parameters mimicking the effects expected in the Illustris TNG-300 simulations. The total baryonic effect is decomposed into the contribution of each component, namely ejected gas, galaxies, hot bound gas, reaccreted gas, and dark matter, according to the legend.

scenarios. In this work, we have implemented in the model of A20 the following four main updates:

- The adoption of a more flexible functional form for the bound gas;
- The inner slope of the power-law in the central galaxy is a new free parameter;
- The modelling of a satellite galaxies component;
- The inclusion of a late-time reaccreted gas component;

We find that the parametrisation of the bound gas density shape used in Schneider and Teyssier (2015a); Aricò et al. (2020b) is not flexible enough to match the profiles measured in a wide range of halo masses of hydrodynamical simulations. We therefore use here a more flexible shape, with an explicit dependence on the halo mass. The shape of the bound gas now reads:

$$\rho_{\rm BG}(r) = \frac{y_0}{(1+r/r_{\rm inn})^{\beta_i}} \frac{1}{(1+(r/r_{\rm out})^2)^2} \tag{4.5}$$

where y_0 is a normalisation factor, obtained by imposing $\int_0^{r_{200}} {\rm d}r 4\pi r^2 \rho_{\rm BG}(r) = f_{\rm BG} M_{200}$. The profile is a double power-law with two characteristic scales, $r_{\rm inn}$ and $r_{\rm out}$, defining where the slope changes at small and large radii, respectively. We define the inner radius $r_{\rm inn} = \theta_{\rm inn} \times r_{200}$ and $r_{\rm out} = \theta_{\rm out} \times r_{200}$, with $\theta_{\rm inn}$ and $\theta_{\rm out}$ being free parameters of the model. The gas inner slope explicitly depends on halo mass as $\beta_i = 3 - (M_{\rm inn}/M_{200})^{\mu_i}$, with the characteristic mass $M_{\rm inn}$ and μ_i as free parameters. After checking the small impact that μ_i has on both power spectrum and bispectrum, we have fixed its value to $\mu_i = 0.31$, in agreement to the Model A-avrg in Schneider et al. (2019).

This profile is similar to that in Schneider et al. (2019), with the main difference being that in our model the bound gas perfectly traces the dark matter on scales beyond $r_{\rm out}$ and the ejected gas decay exponentially, whereas Schneider et al. (2019) models a single gas component, with the slope at large radii as a free parameter.

The central galaxy density profile is given by

$$\rho_{\rm CG}(r) = \frac{y_0}{R_h r^{\alpha_g}} \exp\left[-\left(\frac{r}{2R_h}\right)^2\right], \tag{4.6}$$

where y_0 is found imposing $\int_0^{r200} \rm d^3\rho_{\rm CG}(r) = f_{CG} M_{200}$, the half-mass radius is $R_h = 0.015 \times r_{200}$ and α_g, the inner slope of the central galaxy, is a free parameter of the model, with a fiducial value $\alpha_g = 2$.

In addition to the central galaxy, we add the stellar component of satellite galaxies. Stellar mass is, to a good approximation, collisionless and thus a good tracer of dark matter. For this reason we model the contribution of satellite galaxies as the dark matter. The dark matter back-reacts to the baryonic potential well, and therefore the satellite galaxies, being a linearly biased tracer of the dark matter, are quasi-adiabatically relaxed. We refer the reader to A20 for the details of the implementation of the back-reaction mechanism.

Motivated by the hypothesis of Foreman et al. (2020), who suggested the presence of an overdensity of gas reaccreted at late times to explain the maximum in the bispectrum around $k \approx 2.5h\,\rm Mpc^{-1}$ in the Illustris TNG-300 simulation, we added to our model a new gas component, which mimics such gas overdensity. We assume this new component to be Gaussian shaped:

$$\rho_{\rm RG}(r) = \frac{y_0}{\sqrt{2\pi}\sigma_r} \exp\left[-\frac{(r-\mu_r)^2}{(2\sigma_r)^2}\right], \tag{4.7}$$

where $y_0 = f_{\rm RG} M_{200} / \int_0^{r200} 4\pi r^2 \rho_{\rm RG}(r) dr$.

For simplicity, we assume the gas overdensity to have a fixed spatial distribution in terms of the halo virial radius, $\mu_r = 0.3 \times r_{200}$ and $\sigma_r = 0.1 \times r_{200}$, and after checking that our main results are not affected by this choice. We let free instead the mass fraction, $f_{\rm RG}$, as explained in what follows.

All the density profiles of the baryon correction model are normalised to M_{200}, with the abundance of each component determined by its respective mass fraction. The dark matter

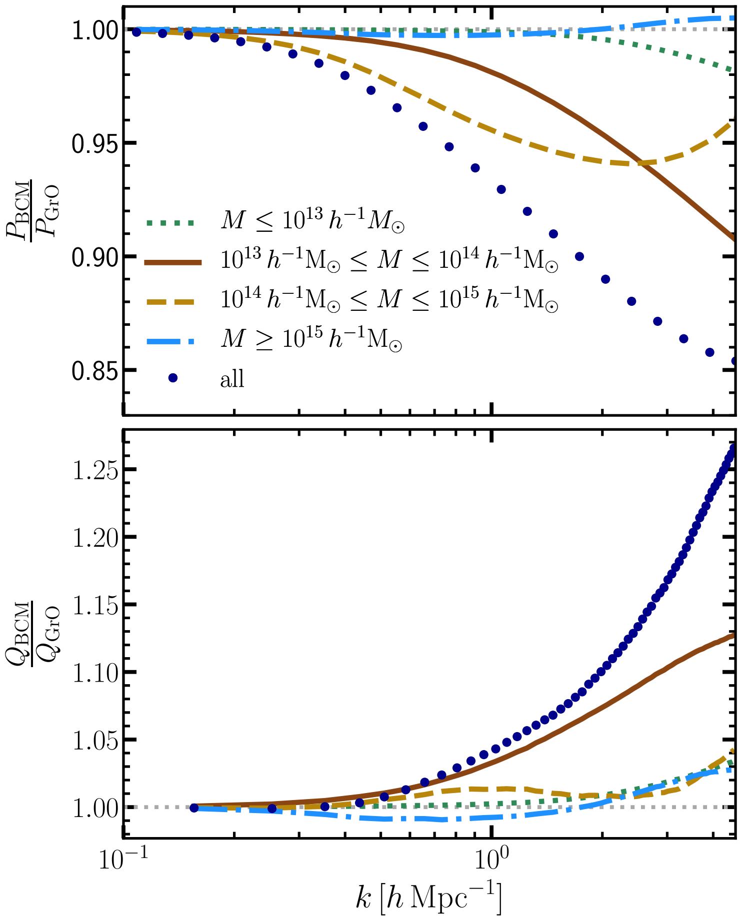

Figure 4.5: *Upper panel:* Baryon suppression of the matter power spectrum at $z = 0$, when applying the baryon correction model to haloes smaller than $10^{13}h^{-1}{\rm M}_{\odot}$ (green dotted line), between $10^{13} - 10^{14}h^{-1}{\rm M}_{\odot}$ (brown solid line), $10^{14} - 10^{15}h^{-1}{\rm M}_{\odot}$ (golden dashed line) and to all the haloes (blue dots) of our $512\,h^{-1}{\rm Mpc}$ simulation. *Lower panel:* Same as the upper panel, but for the ratios between baryonic and gravity-only results in the reduced bispectrum.

fraction is fixed by cosmology, $f_{\rm DM} = 1 - \Omega_{\rm b}/\Omega_{\rm m}$.

The central galaxy fraction is given by an abundance-matching parametrisation (Behroozi et al., 2013):

$$f_{\rm CG}(M_{200}) = \epsilon \left(\frac{M_1}{M_{200}}\right) 10^{g(\log_{10}(M_{200}/M_1))-g(0)}, \tag{4.8}$$

$$g(x) = -\log_{10}(10^{\alpha x} + 1) + \delta \frac{(\log_{10}(1 + \exp(x)))^{\gamma}}{1 + \exp(10^{-x})}. \tag{4.9}$$

We use the best-fitting parameters at $z = 0$ given by Kravtsov et al. (2018), along with the redshift dependence given by Behroozi et al. (2013), both reported in Appendix A of A20 and not included here for the sake of brevity.

Satellite and central mass fractions have the same parametric form, and their parameters are assumed to be linearly dependent e.g. $M_{1,\rm sat}(z = 0) = \alpha_{\rm sat} M_{1,\rm cen}(z = 0)$, with $\alpha_{\rm sat}$ as a free parameter of the model, similar to the approach of Watson and Conroy (2013).

The halo gas mass fraction, defined as the sum of the bound gas and the reaccreted gas, is

$$f_{\rm HG}(M_{200}) = f_{\rm BG} + f_{\rm RG} = \frac{\Omega_b/\Omega_m - f_{\rm CG} - f_{\rm SG}}{1 + (M_c/M_{200})^{\beta}}, \tag{4.10}$$

with M_c and β free parameters, and $f_{\rm CG}$, $f_{\rm SG}$, the central and satellite galaxy mass fractions, respectively. The reaccreted gas mass fraction is

$$f_{\rm RG}(M_{200}) = \frac{\Omega_b/\Omega_m - f_{\rm CG} - f_{\rm SG} - f_{\rm HG}}{1 + (M_r/M_{200})^{\beta_r}} = f_{\rm HG} \frac{(M_c/M_{200})^{\beta}}{1 + (M_r/M_{200})^{\beta_r}}, \tag{4.11}$$

with M_r as a free parameter and β_r fixed for simplicity to $\beta_r = 2$.

Finally, the bound and ejected gas mass fractions are set by mass conservation:

$$f_{\rm BG} = f_{\rm HG} - f_{\rm RG}; \tag{4.12}$$

$$f_{\rm EG} = \Omega_b/\Omega_m - f_{\rm CG} - f_{\rm SG} - f_{\rm HG}. \tag{4.13}$$

As an example, we show in Fig. 4.2 how this updated model is able to reproduce at the same time the gas and stellar density profiles measured in three different halo mass bins of Illustris TNG-300, $[10^{13.5} - 10^{14}]\,h^{-1}{\rm M}_{\odot}$, $[10^{14}, 10^{14.5}]\,h^{-1}{\rm M}_{\odot}$ and $[10^{14.5}, 10^{15}]\,h^{-1}{\rm M}_{\odot}$. Note that here our reaccreted mass fractions are consistent with zero, thus not appearing in the plot. In summary, our baryonic model has a total of 8 free parameters: 2 regulating the amount of gas retained in haloes, 4 shaping the gas density profile, 1 for the galaxy mass and 1 for the amount of reaccreted gas.

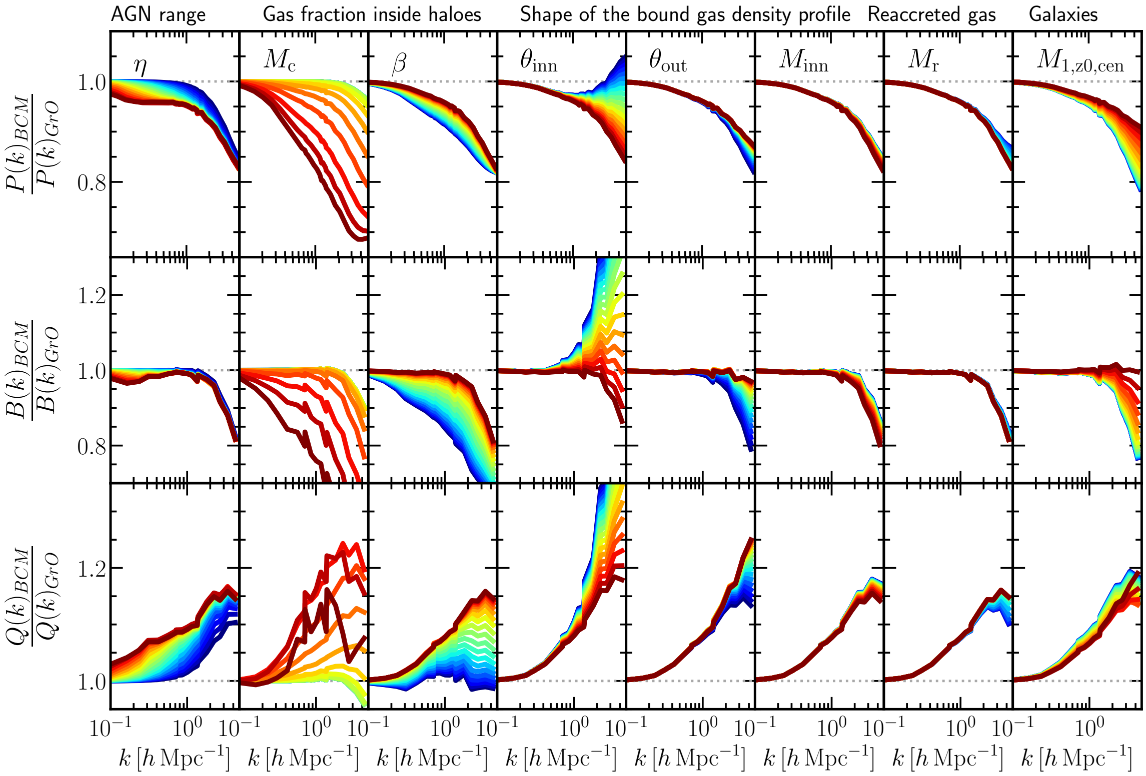

Figure 4.6: Modifications to the matter power spectrum (upper panels), bispectrum (central panels) and reduced bispectrum (lower panels) at $z = 0$ caused by baryons, according to our baryonification algorithm. Each column varies one of the free parameters of the model while keeping the others fixed at their fiducial value. Parameter ranges are $\log M_c \in [9, 15]$, $\log \eta \in [-0.7, 0.7]$, $\log \beta \in [-1, 0.7]$, $\log M_{\rm r} \in [12, 17]$, $\log M_{\rm 1,z0,cen} \in [9, 13]$, $\log \theta_{\rm inn} \in [-2, -0.5]$, $\log \theta_{\rm out} \in [-0.5, 0]$, $\log M_{\rm inn} \in [12, 16]$. Blue to red colors denote low to high parameter values.

4.3.2 Accuracy of cosmology rescaling and baryonification in the bispectrum

In A20 we showed that applying a baryonification algorithm together with a cosmology-rescaled simulation led to percent-accurate results in the power spectrum. We now perform an analogous test to validate the performance of the updated model and extend the analysis to the bispectrum.

In Fig. 4.3 we compare the baryonic effects on the power spectrum and reduced bispectrum as measured in a simulation carried out with a *Planck* cosmology and a simulation carried our with a *Nenya* cosmology and then rescaled to a *Planck* cosmology (c.f. §4.2). These two cases are denoted as target and scaled, respectively, and displayed by symbols and lines as indicated by the legend.

We display four different baryonification parameter sets, chosen to roughly reproduce the clustering of EAGLE, Illustris, Illustris TNG-300 and BAHAMAS. We can see that the difference between applying the BCM on top a rescaled or target simulation is less than 1% in the power spectrum and reduced bispectrum. We show these results only for $z = 0$, but we have explicitly checked that at higher redshifts we obtain similar outcomes.

We note that the initial conditions of the target simulation were not set to match that of the simulation we scale, nor its volume have been chosen to match the volume of the rescaled simulation (which could have increase the agreement further). Nevertheless, the errors we obtain are comparable to our target accuracies for reproducing the baryonic effects on the power spectrum and bispectrum.

4.4 Impact of baryons on the bispectrum

In this section we systematically explore the effects that the various baryonic components, and the free parameters associated to them, produce on the clustering.

We first isolate the effect of each baryonic component by selecting them one-by-one and considering all the others collisionless (thus behaving like dark matter). As shown in Fig. 4.4, we find that, in agreement with Schneider and Teyssier (2015a); Aricò et al. (2020b), the ejected gas largely dominates the suppression in the power spectrum, despite its low mass fraction. Interestingly, the ejected gas shows the largest effect also in the reduced bispectrum, but in this case it causes an enhancement of the power at all scales.

As an qualitative explanation, let us consider two overdensity fields, $\delta_{\rm BCM}$ and $\delta_{\rm GrO}$. Assuming that one is suppressed with respect to the other, $\delta_{\rm BCM} = (1-\alpha)\delta_{\rm GrO}$, it is easy to show that the ratios between their power spectra and equilateral bispectra are $P_{\rm BCM}/P_{\rm GrO} = (1-\alpha)^2$, and $B_{\rm BCM}/B_{\rm GrO} = (1-\alpha)^3$, respectively. Therefore, the reduced bispectrum ratio is $Q_{\rm BCM}/Q_{\rm GrO} = (1-\alpha)^{-1}$. In other words, we observe an enhancement of the reduced bispectrum because the suppression in the bispectrum is smaller than the squared suppression of the power spectrum. The other components are, in this particular setting of the BCM which roughly mimics the BAHAMAS simulation, subdominant, contributing to about 2% in the power spectrum and reduced bispectrum. The reaccreted gas, in particular, causes an enhancement at small scales in both the power spectrum and reduced bispectrum.

It is interesting to explore which halo masses contribute the most to the baryonic effects on clustering. In order to answer this question, we have split the halo catalogue of our simulation in different mass bins, and then we have applied our BCM separately to each of them. In Fig. 4.5 we show how haloes between $10^{13} - 10^{14} h^{-1}\mathrm{M}_{\odot}$ contribute for more than 50% of the effect on the power spectrum at small scales. Haloes of $10^{14} - 10^{15} h^{-1}\mathrm{M}_{\odot}$ are dominant at large scales in the power spectrum, whereas at the small scales, slightly smaller haloes contribute more. Haloes with $M < 10^{13} h^{-1}\mathrm{M}_{\odot}$ and $M > 10^{15} h^{-1}\mathrm{M}_{\odot}$ contribute for less than 2% percent, and only at small scales.

The relative contribution of halos of different mass slightly changes in the case of the reduced bispectrum. The dominant contribution is still from haloes of $10^{13} - 10^{14} h^{-1}\mathrm{M}_{\odot}$, but the relative impact of the most massive haloes in the simulation ($M > 10^{15} h^{-1}\mathrm{M}_{\odot}$) is not as small as for the power spectrum. The fact that the bispectrum is more sensitive to the largest haloes is not surprising (see e.g. Foreman et al., 2020), and has as a practical outcome the slower convergence of the bispectrum with simulated volume compared to that of power spectrum, which we investigate in Appendix E.

We quantify now the impact of the free parameters in the power spectrum and reduced bispectrum. To do so, we vary each parameter one by one, while keeping the others fixed to the value that best fits the BAHAMAS (standard AGN) simulation, described in §4.5. The intervals in which we vary parameters, in log_{10} units, are the following: $M_c/(h^{-1}\mathrm{M}_{\odot}) \in [9, 15]$, $\eta \in [-0.7, 0.7]$, $\beta \in [-1, 0.7]$, $M_r/(h^{-1}\mathrm{M}_{\odot}) \in [12, 17]$, $M_{1,z0,cen}/(h^{-1}\mathrm{M}_{\odot}) \in [9, 13]$, $\theta_{inn} \in [-2, -0.5]$, $\theta_{out} \in [-0.5, 0]$, $M_{inn}/(h^{-1}\mathrm{M}_{\odot}) \in [12, 16]$.

Note we do not show any free parameters for satellite galaxies, as they have a negligible impact on the matter clustering. In fact, they are a biased tracer of the dark matter, and additionally their mass fraction is very small. Given that the relaxation of the dark matter contributes only for a few percent in the matter clustering, it is easy to see why the baryonic effect caused by satellite galaxies is negligible. Thus, we fix their values to the best-fitting of the stellar profile of the Illustris TNG-300 simulation found in §4.3.1.

In Fig. 4.6 we display the mass power spectra, bispectra, and reduced bispectra obtained after applying the BCM to a GrO N-body simulation. Each panel varies a single parameter of the model while keeping the others fixed to their fiducial value. Bluer (redder) colors represent low (high) parameter values. We can see that almost all the parameter combinations predict a suppression in the power spectrum and an enhancement on the reduced bispectrum, at all the scales. Specifically, by increasing η (the parameter which set the maximum range of the AGN feedback), the suppression (enhancement) of the power spectrum (reduced bispectrum) is pushed, as expected, towards larger scales. The parameters M_c and β set the fraction of gas which is retained in haloes of a given mass, and thus also the mass of gas that is expelled. Therefore, is not surprising that these parameters have a big impact on both power spectrum and bispectrum, given that the ejected gas component is the dominant one. Varying M_c we span a 30% range in the clustering; in particular, higher values mean that increasingly larger haloes are free of gas, thus more ejected gas. In these cases we see, accordingly, a larger suppression in the power spectrum and enhancement in the reduced bispectrum.

Varying the shape of the bound gas through the parameters $\theta_{\rm inn}$, $\theta_{\rm out}$ and $M_{\rm inn}$ has an impact only on small scales. Specifically, the model seems very sensitive to $\theta_{\rm inn}$, for which we see a substantial enhancement of both power spectrum and reduced bispectrum when changing the inner gas slope at increasingly smaller radii. On the other hand, the dependence on $M_{\rm inn}$ looks negligible. As expected, increasing $M_{\rm 1,z0,cen}$, and thus having the peak of the star formation at higher halo masses, results in more power at small scales.

Finally, we see that the impact of the late-time reaccreted gas is very modest, despite we vary its mass fraction from practically zero to a limit value of $\approx 50\%$ for some halo masses. Arguably, the effect of this parameter in both power spectrum and reduced bispectrum, can be absorbed by a combination of the other parameters of the model, but might become more important on smaller scales.

We note that the models shown in Fig. 4.6 are just an illustrative example, and do not encompass all the possible modifications given by the BCM: even if the described trends would be likely similar, changing the underlying fiducial model would result in different amplitude and shapes of baryonic effects.

4.5 Fitting the hydrodynamical simulations

In this section, we explore whether the BCM is able to reproduce the impact of baryons in six different state-of-the-art hydrodynamical simulations, namely EAGLE, Illustris, Illustris TNG-300, and three different AGN implementations of BAHAMAS. We remind the reader that these simulations differ in cosmology, N-body code, sub-grid physics, box size, and observables with which they have been calibrated. They show a difference of 30% at $z = 0$ in the power spectrum and 15% in the reduced bispectrum, thus being a good benchmark for the flexibility and realism of our model.

We fit the power spectrum and the reduced bispectrum of each hydrodynamical simulation over the range $0.1 < k/(h\,{\rm Mpc}^{-1}) < 5$, both separately and jointly, varying seven free parameters: M_c, η, β, $M_{\rm 1,z0,cen}$, $\theta_{\rm inn}$, $\theta_{\rm out}$, $M_{\rm inn}$ within the priors shown in §4.4. We

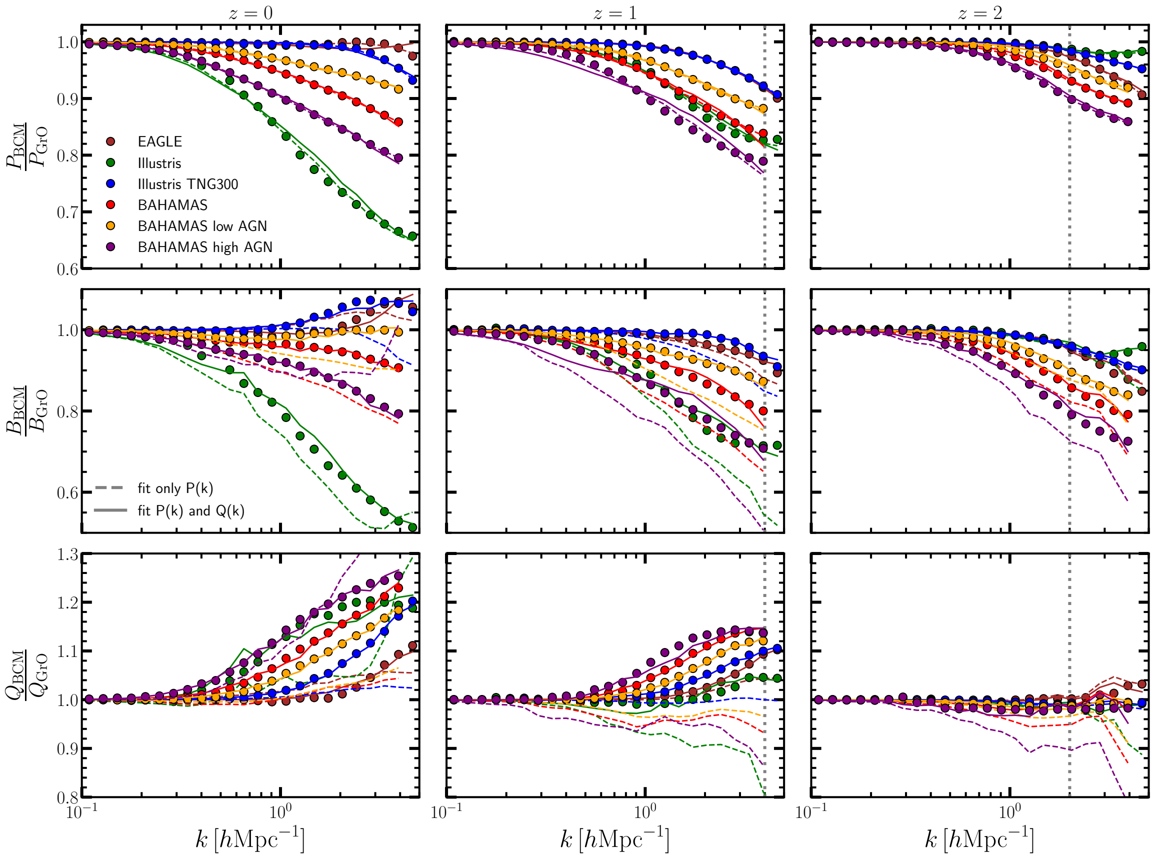

Figure 4.7: Measurements of the baryonic impact to the matter power spectrum, $S(k) \equiv P/P_{\rm GrO}$ (upper panels), equilateral bispectrum, $S(k) \equiv B/B_{\rm GrO}$ (central panels), and reduced equilateral bispectrum, $S(k) \equiv Q/Q_{\rm GrO}$ (bottom panels), in different hydrodynamical simulations according to the legend (symbols), at $z = 0$ (left), $z = 1$ (centre) and $z = 2$ (right). The best-fitting baryonification model constrained using only the power spectrum is displayed as dashed lines, whereas the best-fitting model constrained on both the power spectrum and reduced bispectrum shown with solid lines. Grey vertical dotted lines mark the scales where the estimated shotnoise contributes to $> 1/3$ of the clustering amplitude.

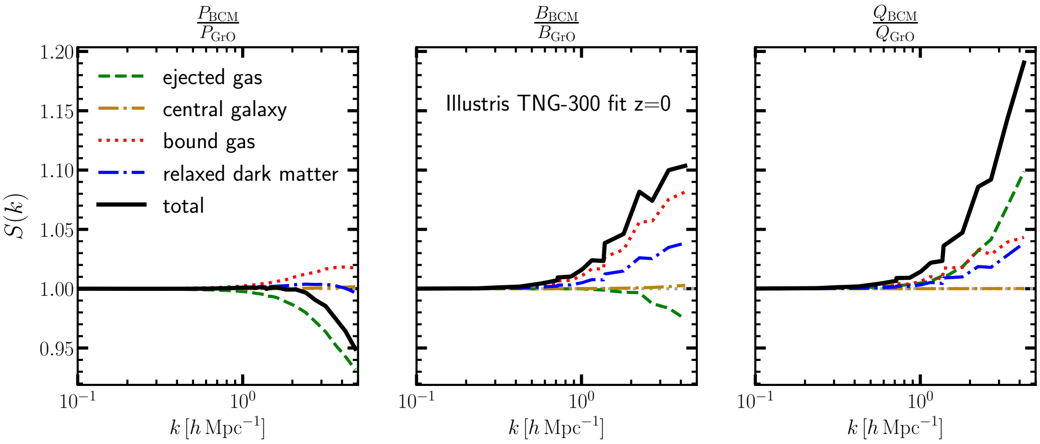

Figure 4.8: Best-fitting model to Illustris TNG-300 power spectrum and bispectrum, at $z = 0$. The contribution of the varyous baryon component are isolated in the power spectrum (left), equilaetral bispectrum (centre) and reduced bispectrum (right). Note that the bound gas, and the back-reaction to the dark matter, are the principale causes of the bump visible in the bispectrum at small scales.

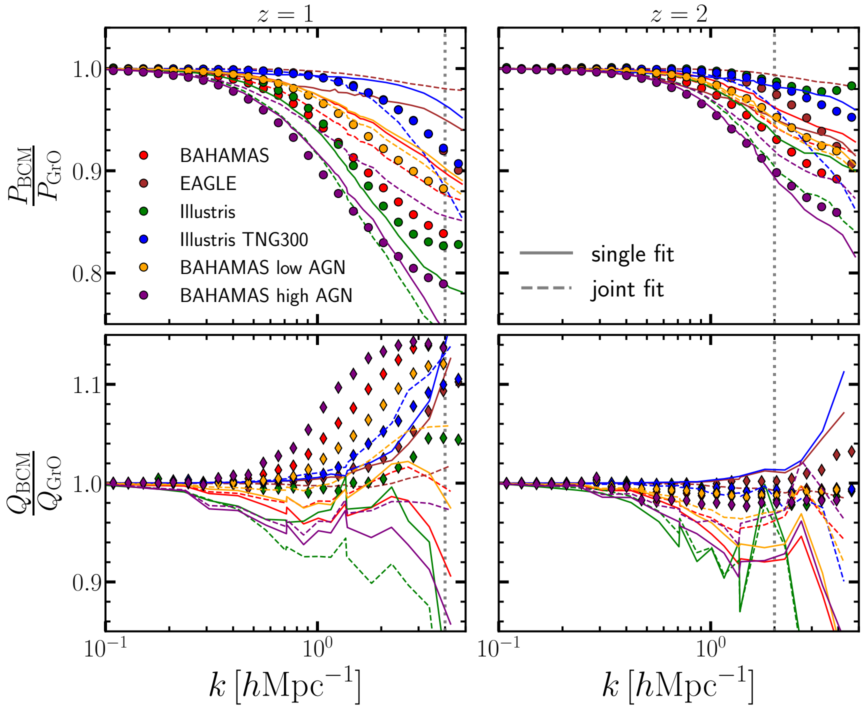

Figure 4.9: Impact of the redshifts evolution in the baryonic correction parameters. We have fitted the power spectra (upper panels) and reduced bispectra (lower panels) of the hydrodynamical simulations reported in the legend at $z = 0$, and then applied the same model at higher redshifts $z = 1, 2$, assuming our best-fitting parameters to be redshift independent.

assume no correlation among power spectrum and bispectrum nor among the measurements at different wavenumbers. Specifically, we use an empirical approach similarly to A20, where the covariance matrix is directly estimated by the intra-data variance, giving the same weights to power spectrum and bispectrum. We expect the errors associated to the bispectrum ratios to be larger than the one associated to the power spectrum (see for instance the errors measured by Foreman et al. (2020) by dividing the hydrodynamical simulation volume in subboxes). Nevertheless, being the purpose of this test to asses the accuracy of the joint fit of power spectrum and bispectrum, we avoid to give more weight to the former to not degrade the fit of the latter.

To perform the fit, we have implemented a *particle swarm optimisation* (PSO) algorithm (Kennedy and Eberhart, 1995). In this algorithm, a pack of particles efficiently searches the minimum of a function in a given parameter space. Each particle communicates with the others at each step, and they are attracted both to their local and the swarm global minima, with a relative strength that can be tuned. The velocity and position of the particles are updated in every step, depending solely on the swarm status in the previous step. Our Python PSO code is publicly available.[9] For our application, we use a swarm of 10 particles and 250 iterations, finding that an average of 100-150 steps are enough to converge to the global

---

[9] `https://github.com/hantke/pso_bacco`

minimum.

In Fig. 4.7 we present the main result of this chapter. We show the best BCM fits at three different redshifts, $z = 0$, 1, and 2. We have marked with a grey dotted line the scales where we estimate the shotnoise amplitude to be approximately 30% of the clustering amplitude: $k \approx 2\ h\,\mathrm{Mpc}^{-1}$ at $z = 2$, and $k \approx 4\ h\,\mathrm{Mpc}^{-1}$ at $z = 1$. We remind the reader that, in the cosmology rescaling process, the box of the simulations can vary of length, and so the shotnoise level can be slightly different. Due to the significant contribution of shotnoise, results at small scales and high redshifts should be interpreted carefully.

Dashed lines show the results when fitting only the power spectrum measurements. In this case, we recover the accuracy of 1% found in A20 in the power spectrum at all scales and redshifts. However, the baryonic impact on the bispectrum can be over- or under-estimated by up to 20%. In contrast, when fitting the power spectrum and bispectrum *together*, the accuracy of the power spectrum slightly degrades, but we obtain significantly better agreement with the bispectrum.

For all hydrodynamical simulations and at all the redshifts considered, we obtain joint fits that are $1 - 2\%$ accurate for the power spectrum and 3% for the bispectrum. We note that the worse performance is obtained for the simulations with the most extreme feedback e.g. Illustris and BAHAMAS high-AGN. In the case of BAHAMAS, which is arguably the most realistic simulation for our purposes, the fits describe simultaneously the baryonic effects on the power spectrum and bispectrum to better than 1%.

These results are achieved considering the late-time reaccreted gas fixed to zero. In particular, we note that the bump around $k \approx 2 - 3h\,\mathrm{Mpc}^{-1}$ in the bispectrum of Illustris TNG-300 and EAGLE are correctly reproduced by the model, despite the absence of the reaccreted gas component. To understand which BCM component causes this enhancement of the bispectrum at small scales, we isolate the impact of each baryon component to the clustering, similarly to what done in § 4.4. This analysis, reported in Fig. 4.8, clearly show that the bound gas causes an enhancement at small scales in both power spectrum and bispectrum. Furthermore, the back-reaction of the gas overdensity to the dark matter adds the necessary power to reproduce correctly the measurements of the Illustris TNG-300. We can conclude that, by simply assuming the gas as a double power-law, the model has enough flexibility (over the range of scales we considered) to explain the "bump" in the bispectrum measured in Illustris TNG-300 and EAGLE.

We have repeated the fits letting free the corresponding mass fraction, M_r, however, this did not result in noticeably improved fits. This finding is consistent with the hypothesis that, within the accuracy of our model and simulated data, and over the scales considered, the reaccreted gas is not necessary to reproduce the clustering of the hydrodynamical simulations analysed.

Finally, one could wonder what is the smallest number of free parameters necessary to produce accurate results. In A20 it is shown that with only 4 parameters it is possible to fit the power spectrum at 1%, and arguably the 7-8 parameters used here are degenerate, and effectively recastable into a model with a smaller parameter set. We leave the exploration of degeneracies between parameters and the finding of a minimal-model parameter set for a future work.

4.5.1 Redshift dependence of the baryon parameters

As already pointed out in previous works (Chisari et al., 2018; Aricò et al., 2020b), despite the baryonic parameters do not have a specific redshift dependence, when fitting the clustering at different redshifts they show a clear evolution. To quantify the inaccuracies obtained by fixing the baryonic parameters, we apply the baryonification algorithm to our simulation to snapshots that correspond to high redshifts ($z = 1, 2$), using the best-fitting parameters at $z = 0$ found in § 4.5.

In Fig. 4.9 we show the power spectra and reduced bispectra obtained. The error in the power spectrum is in most of the cases below 5%, for extreme models around 7-10%. On the other hand, the reduced bispectrum can be off of $10 - 20\%$. These errors must be taken into account when fixing at face value a set of baryonic parameters in multiple redshifts.

4.5.2 Baryonic effects on the squeezed bispectrum

We have so far analysed, for simplicity, only the equilateral configuration of the reduced bispectrum. In this section, we explore the baryonification performance for the "squeezed" configuration, which measures the correlation between points on isosceles triangles with one side much smaller than the other two in k-space, so that $k_1 \ll k_2 = k_3$. The squeezed bispectrum might be seen as a "conditional" two-point correlation which quantifies the dependence of small-scale nonlinearities on the large-scale background overdensity.

It has been shown that, in some cases, the baryonic effect on the squeezed bispectrum can be directly related to the power spectrum at small scales, when considering a k_1 long enough to not be affected by baryonic physics (Barreira et al., 2019; Foreman et al., 2020). Specifically, Barreira et al. (2019) have measured the "power spectrum response functions" in the Illustris TNG-300, using the separate universe approach, finding that they are largely unaffected by baryonic physics. This suggests that the information in the squeezed bispectrum is already contained in the power spectrum, and thus knowing the latter we can predict the former. However, as shown in Foreman et al. (2020), the analytical predictions given from the power spectrum response function are not always in agreement with the hydrodynamical simulations, e.g. BAHAMAS. This could be a hint that, in some cases, the response function

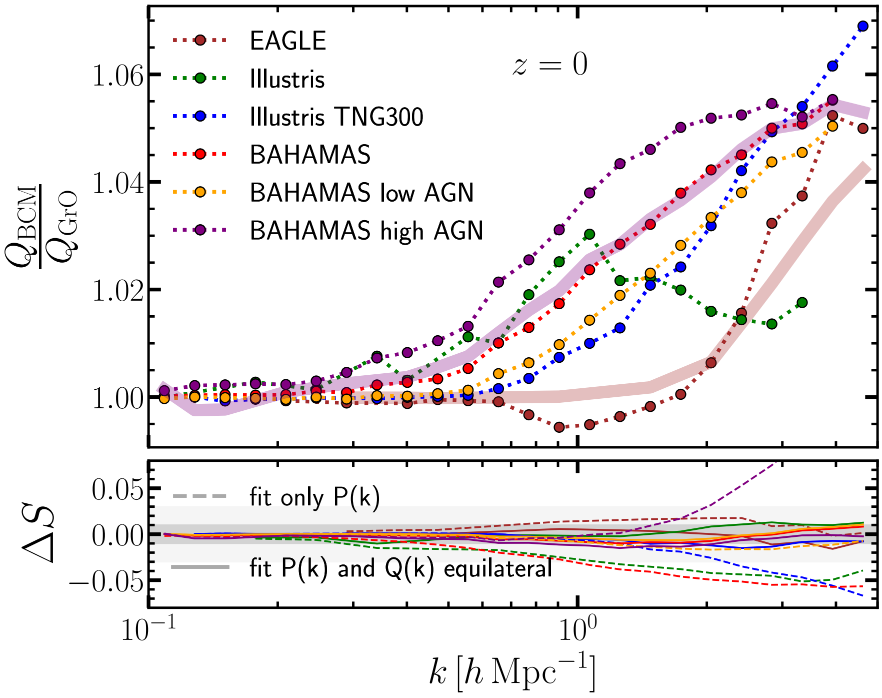

Figure 4.10: *Upper panel:* Measurements of the reduced squeezed bispectra at $z = 0$ in EAGLE, Illustris, Illustris TNG-300, BAHAMAS, Bahamas low-AGN and BAHAMAS high-AGN (symbols), according to the legend. The shaded band show our prediction obtained by fitting power spectrum and reduced equilateral bispectrum in the two most extreme models, EAGLE and BAHAMAS high-AGN. *Lower panel:* Difference between the ratios of reduced squeezed bispectra predicted by our baryon correction model and measured in the hydrodynamical simulations. The dashed lines show the model parameters fitting only the power spectra of the hydrodynamical simulations, whereas the solid lines show the model with parameters constrained by fitting both power spectra and equilateral reduced bispectrum.

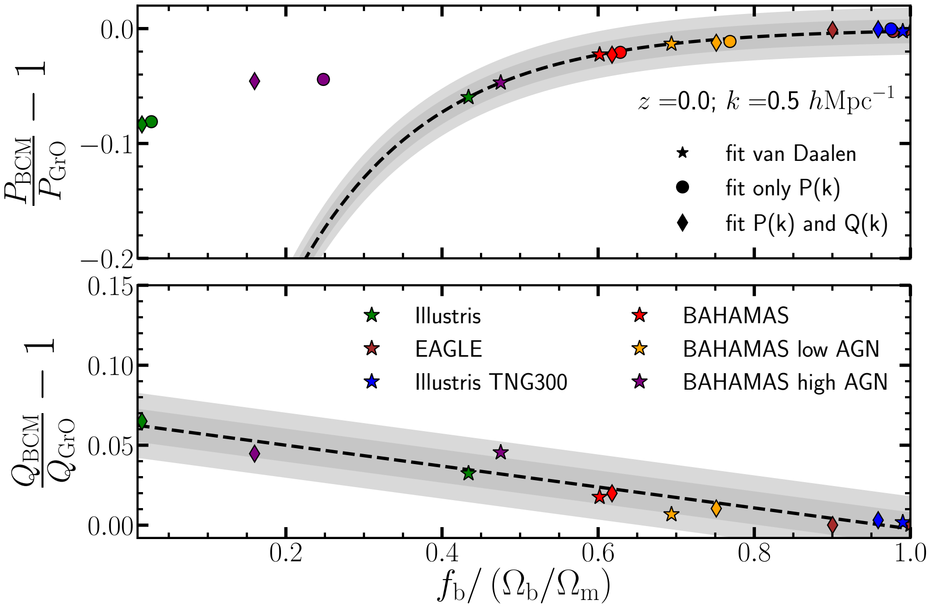

Figure 4.11: *Upper panel*: Relation between the baryonic impact on the power spectrum at $k = 1\,h\,\mathrm{Mpc}^{-1}$, defined as $\Delta P(k)/P(k)$, and the halo baryon fraction in haloes with a mass $[6\times10^{13}, 2\times10^{14}]$ $\mathrm{M}_{\odot}$. The black dashed line displays the fit provided by van Daalen et al. (2020), with the grey and light grey shaded bands marking a 1% and 2% deviation, respectively. For comparison, the colored stars emply the baryon fraction measured directly in the hydrodynamical simulations by van Daalen et al. (2020). The coloured symbols indicate the measurements of our baryonified simulations when using the best-fitting values calibrated against the power spectra (circles), and both power spectra and bispectra (diamonds). *Lower panel:* Same as the upper panel, but for the reduced bispectrum. In this case, the dashed line represents a simple linear regression of the symbols displayed.

are not fully specified by the power spectra.

Here, we take a somewhat agnostic approach, and test if we can predict correctly the squeezed bispectrum starting from the information contained in the power spectrum and the equilateral bispectrum. To do so, we apply to our gravity-only simulations a BCM with the parameters that reproduce both the power spectrum and reduced equilateral bispectrum for a given hydrodynamical simulations. Then, we measure the reduced squeezed bispectrum ($k_1 = k_2 > k_1 \sim 0.1\,h^{-1}\mathrm{Mpc}$) and compare it with those measured directly in the hydrodynamical simulations.

In Fig. 4.10 we show the results obtained at $z = 0$. First, we can notice that, as for the case of equilateral configurations, when considering baryon physics the reduced squeezed bispectrum is enhanced with respect to the gravity-only one. However, the baryonic effects in the squeezed bispectrum are smaller than those in the equilateral configuration – spanning a range of $2 - 7\%$, against a $10 - 25\%$ measured in the equilateral configuration.

We also see that our predictions for the squeezed reduced bispectrum agree very well with the simulation measurements, reaching a $\sim 1\%$ accuracy in all cases. This further supports the idea that the modifications to the density field in the barionification is accurately capturing the three-dimensional distortions induced by baryons, and not simply fitting an effective distortion in the power spectrum.

For comparison, we also display in Fig. 4.10 the predictions when tuning our model using only the power spectrum. As for the equilateral bispectrum, the impact of baryons is not captured very accurately, with discrepancies generally within 5% (EAGLE and BAHAMAS low-AGN $\leq 2\%$) to up to 10% (Bahamas high-AGN).

4.5.3 Baryon fractions in haloes

Recently, it has been shown that there is a tight correlation between baryonic effects on the power spectrum and the baryonic fraction inside haloes of $M \approx 10^{14} M_\odot$ (van Daalen et al., 2020). The best fits of the baryon correction model has been shown to be able to accurately recover such correlation, even if for large power spectrum suppression, which correspond to very strong AGN feedback, it tends to underestimate the baryon fraction measured in hydrodynamical simulation (Aricò et al., 2020b).

We now explore whether adding the information on the bispectrum the baryonic halo fractions become more constrained, and additionally, whether there is a relation between reduced bispectrum and baryon fraction, analogous to the one found for the power spectrum.

In Fig. 4.11 we show how, indeed, both the best-fitting parameter set can accurately reproduce the power spectra of the hydrodynamical simulations, but predict slightly different baryon parameters, and therefore different baryon fractions. This can be a hint of some degeneracies between parameters which is broken when including the bispectrum information. We note that in most of the cases, both of the predictions are in excellent agreement with the fitting function provided by van Daalen et al. (2020). For Illustris and BAHAMAS high-AGN, the opposite is true: both the predictions are off with respect to the fitting function, and including the bispectrum information does not improve the estimation of the gas fraction in clusters with respect to hydrodynamical simulations. This likely points to the fact that some of the baryonification assumptions somewhat break for extreme feedback scenarios. This could be related to gas fractions that are not monotonic with halo mass, or that these events affect gas beyond the boundaries of a halo (a process not included in our model). On the other hand, we note that the gas fractions in these simulations are in clear tension with observations which prefer values ≈ 0.6.

Regardless of the simulation, the bottom panel of Fig. 4.11 shows that the baryonic effects on the reduced equilateral bispectrum correlate with the baryonic fraction: the smaller the baryon fraction, the larger the bispectrum enhancement. Remarkably, the prediction from our model, when fitted with a simple linear regression, shows a trend as tight as the one found in the power spectrum (1%). To have an idea of the predictions from hydrodynamical simulations, we infer the baryon fractions from the power spectra measurements using the fitting function provided by van Daalen et al. (2020), and combine them to the measurement of the reduced bispectra enhancement. By doing so, we find that all the predictions are still within 1%, except for BAHAMAS high-AGN, which is slightly off but still well within 2%.

It would be very interesting to extend the analysis of van Daalen et al. (2020) to the bispectrum, to check if including a vast number of hydrodynamical simulations the relation still holds with a low scatter. Nevertheless, we stress that, a priori, the BCM does not predict a tight relation between baryon fraction and clustering. In A20 (Fig. 8) it was shown that the baryon fraction-clustering relation is more relaxed when considering the full BCM parameters ranges. Interestingly, it seems that the calibration and subgrid physics with which hydrodynamical simulations are run, translates into constraints and degeneracies of the BCM parameters, and thus constrain the baryon fraction.

4.6 Conclusions

In this chapter, we have used a combination of cosmology scaling and baryonification algorithms, to reproduce with a negligible computational time the density fields of various hydrodynamical simulations, up to very small and non-linear scales ($k = 5h\,\mathrm{Mpc}^{-1}$) and for two- and three-point statistics.

Below we summarise our main findings:

- Baryonic physics causes an enhancement in the reduced equilateral bispectrum at all the scales considered, roughly monotonically with the strength of the feedback mechanisms;

- It is possible to simultaneously reproduce the baryonic effects on the power spectrum and on reduced bispectrum (with 1% and $2-3\%$ precision, respectively), as measured in EAGLE, Illustris, Illustris TNG-300, and three different AGN implementations of BAHAMAS,
- In contrast, a baryon model tuned to only reproduce the power spectrum, can lead to up to $\sim 20\%$ discrepancies in the reduced bispectrum;
- We find that a double power-law gas density profile is flexible enough to reproduce the bump at small scales measured in the bispectrum of some hydrodynamical simulations (see Foreman et al., 2020). It appears thus that an additional modelling of gas overdensity at relatively small scales is superfluous.
- The model parameters that best fit the power spectrum and equilateral bispectrum also predict changes to the squeezed configurations at the $\sim 1\%$ level.
- The baryon parameters are not redshift independent; ignoring their time dependence results in a 5% inaccuracy in the power spectrum, and $10-20\%$ in the reduced bispectrum, up to $z=2$;
- Analysing the best-fitting models to the hydrodynamical simulations, we find a correlation between baryonic effects on the bispectrum and baryon fraction inside haloes, similar to the one for the power spectrum found in van Daalen et al. (2020),

Overall, our results support the physical soundness (as well as our specific numerical implementation) of baryonification algorithms. This also encourages its use not only in spherically-averaged 2-point statistics, but also in cross-correlations and in other statistics such as peak counts.

The next generation surveys will produce a huge amount of data, which is only partially interpretable with the current theoretical models. This work is a contribution to the effort to overpass models based on only gravitational interactions, and fully exploit the data up to higher-order statistics. We anticipate that our approach will be a valid tool for a fast production of mock density fields, accurate to very small scales and statistics of order higher than 2-point, useful for pipeline validation, blind comparisons or for direct exploitation of the data, e.g. marginalising over baryonic effects.

Chapter 5

Cosmology and baryons: a neural network emulator

In this chapter, adapted from the paper "The BACCO Simulation Project: A baryonification emulator with Neural Networks" (Aricò et al., 2020a), we present a neural-network emulator for baryonic effects in the non-linear matter power spectrum. We calibrate this emulator using more than $50,000$ measurements in a 15-dimensional parameters space, varying cosmology and baryonic physics. Baryonic physics is described through a baryonification algorithm, that has been shown to accurately capture the relevant effects on the power spectrum and bispectrum in state-of-the-art hydrodynamical simulations. Cosmological parameters are sampled using a cosmology-rescaling approach including massive neutrinos and dynamical dark energy. The specific quantity we emulate is the ratio between matter power spectrum with baryons and gravity-only, and we estimate the overall precision of the emulator to be $2-3\%$, at scales $k < 5\,h\,\mathrm{Mpc}^{-1}$, and redshifts $0 < z < 1.5$. We also obtain an accuracy of $1-2\%$, when testing the emulator against a collection of 74 different cosmological hydrodynamical simulations and their respective gravity-only counterparts. We show also that only one baryonic parameter, namely M_c, which sets the gas fraction retained per halo mass, is enough to have accurate predictions of most of the baryonic feedbacks at a given epoch. Our emulator is publicly available at `http://www.dipc.org/bacco`.

5.1 Introduction

Gravity is the dominant force that shapes the structure of the Universe on very large scales. On small scales, however, hydrodynamical forces and astrophysical processes such as cooling, star formation, supernovae and AGN feedback, become important and cosmic structure is the result of their joint co-evolution and interaction with gravity. Details of such processes are not fully understood nor sufficiently constrained by current observations to formulate a predictive theory of structure formation on all scales.

In fact, our limited knowledge about the baryonic physics is one of the main uncertainties in modelling, and cosmological interpretation, of ongoing weak gravitational lensing surveys, which map the distribution of density fluctuations in the Universe. For upcoming surveys, sources of statistical noise will be dramatically reduced and the relative importance of the baryonic uncertainties will increase. For instance, ignoring the impact of baryonic processes in a Euclid-like survey (Laureijs et al., 2011), would result in a $\approx 5\sigma$ bias on cosmological parameters constraints (Semboloni et al., 2011, 2013; Schneider et al., 2020).
An alternative to deal with this uncertainty is to restrict data analyses to scales large enough to be reasonably unaffected by baryons. However, this would imply discarding a huge amount of cosmological information, which could be crucial to distinguish between, for instance, competing theories for cosmic acceleration or the nature of the dark matter particle. Arguably, the most complete and complex method to evolve simultaneously gravity and baryon physics is currently given by magneto-hydrodynamical simulations. These implement a large number of different physical processes, and recently the optimisations of the algorithms and the increasing power of super computers have opened-up to simulations of relatively large cosmological boxes (Schaye et al., 2010; van Daalen et al., 2011; Le Brun et al., 2014; Vogelsberger et al., 2013; Dubois et al., 2014; Schaye et al., 2015; McCarthy et al., 2017; Springel et al., 2018). Unfortunately, these simulations are still too computationally expensive to be directly used in data analysis. Thus, over the last years, a number of different approaches have been proposed for fast modelling of baryons. A non-complete list is: extensions to the halo model (e.g. Semboloni et al., 2011; Mohammed et al., 2014; Fedeli, 2014; Mead et al., 2015; Debackere et al., 2020; Mead et al., 2020); Principal Component Analyses (Eifler et al., 2015; Huang et al., 2019); machine learning-based methods (Tröster et al., 2019; Villaescusa-Navarro et al., 2020); Effective Field Theory of Large-Scale Structure (Bragança et al., 2020). Among these, a promising method is the so-called *baryon correction model*, or *baryonification* (Schneider and Teyssier, 2015a; Schneider et al., 2019; Aricò et al., 2020b).

The main idea of baryonification is to modify the outputs of gravity-only simulations according to physically motivated recipes for the spatial distribution of baryons. As a result, the three-dimensional total matter density field can be predicted as a function of cosmology and baryonic physics (Aricò et al., 2021a). Some main advantages of this approach are that its free parameters have a clear physical interpretation, it does not rely on the correctness of any particular hydrodynamical simulation, it can be linked directly with observations, and that it predicts the full density field and not only specific correlation functions or power spectra.

The aforementioned advantages come at the price of a significant computational cost in comparison to e.g. the halo model and other analytic approaches. The computational cost of baryonification, in fact, roughly scales linearly with the number of haloes in a simulation and thus can be rather expensive for large simulations. For instance, to apply the heavily optimised baryonification algorithm of Aricò et al. (2020b, 2021a) on top of a $512\,h^{-1}\mathrm{Mpc}$-box simulation with 1536^3 particles takes approximately 10 CPU-minutes. Although this is a negligible time for many applications, for intensive parameter-space sampling where hundreds of thousands of evaluations might be required, the baryonification could make data analysis unfeasible.

To overcome this problem, we build and validate an emulator for the effects of baryonification on the density power spectrum. This emulator is able to provide very accurate predictions in a fraction of second. An additional advantage of the emulator over the full algorithm is its extreme flexibility: the emulator does not need to directly handle the outputs of N-body simulations, and thus can be easily incorporated to any lensing analysis pipeline. Recently, emulators have been increasingly popular in cosmology, as they provide a mean to exploit the statistical power of large numerical simulations with negligible computational memory and time requirements.

In the last years, emulators of different observables have been built, e.g. matter power spectrum (e.g. Heitmann et al., 2014; Knabenhans et al., 2019; Winther et al., 2019; Angulo et al., 2020; Euclid Collaboration et al., 2020; Aricò et al., 2021b; Mootoovaloo et al., 2021), mass function (e.g. McClintock et al., 2019; Bocquet et al., 2020), and including galaxy correlation function and Lyman$-\alpha$ Forest (Zhai et al., 2019; Bird et al., 2019; Zennaro et al., 2021). Alternatively, emulators of the Likelihood function have been proposed for cosmology inference (e.g. McClintock and Rozo, 2019; Pellejero-Ibañez et al., 2020). An emulator for the baryonic suppression has been presented by Schneider et al. (2020), based on the baryonification algorithm presented in Schneider et al. (2019) and the emulation setup of Knabenhans et al. (2019). Additionally to the baryon parameters, this emulator includes changes on cosmology through the baryon fraction $f_\mathrm{b} = \Omega_\mathrm{b}/\Omega_\mathrm{m}$, which was shown to be the dominant dependence of the model, but does not explicitly incorporate the effect of cosmology on the properties of the underlying mass field.

Here, we exploit the framework described in Aricò et al. (2020b, 2021a) and in Angulo et al. (2020), to build an emulator which encodes all the dependencies on 7 baryon parameters and also on 8 cosmological parameters, including massive neutrinos and dynamical dark energy. We train a feed-forward Neural Network with tens of thousands of different combinations of cosmology and baryonification parameters to learn the changes on the matter power spectrum induced by baryonic physics.

We will show that our emulation is accurate at a $\sim 1-2\%$ level over our whole 15-dimensional parameter space, which covers scales $0.01 \leq k \leq 5h\,\mathrm{Mpc}^{-1}$ and redshifts $0 \leq z \leq 1.5$. We note that the majority of statistical power of a *stage IV* survey is expected to be at $z \approx 1$ and $1 \leq k/(h/\mathrm{Mpc}) \leq 7$ (Taylor et al., 2018a), and therefore it should be fairly captured by our emulator. Nevertheless, we plan to keep updating the training set of our emulator, and expand its range in scale and redshift in the future.

We will validate the performance of our emulator against a library of 74 hydro-dynamical simulations and their respective gravity-only counterparts. In particular, we make use of BAHAMAS, Cosmo-OWLS, OWLS, EAGLE, Illustris, Illustris TNG, and Horizon simulations. We will show that we can accurately reproduce all of their power spectra, and subsequently will explore the minimal baryonic parameterisation that could be needed in future weak lensing data analyses.

This chapter is structured as follows: in §1.2.3 we describe the numerical techniques we employ; in §5.3 we present our baryonification emulator. In §5.4 we explore the baryonic effects dependencies on cosmology, and in §5.5 we discuss the model constraints obtained by fitting measurement from hydrodynamical simulations. We recap our main findings and conclude in §5.6.

5.2 Numerical methods

In this section we describe the main numerical methods we will employ throughout this chapter. We start by describing our cosmological N-body simulations (§5.2.1). We continue by recapping the algorithms with which we will model baryonic effects on these simulations (§5.2.2) and modify their cosmological parameters (§5.2.3). We then briefly discuss our power spectrum measurements (§5.2.4) and finish by performing tests to quantify the accuracy of our predictions (§5.2.5).

5.2.1 Numerical Simulations

In this work, we make use of two different suites of simulations. One, dubbed “main", is the suite we use to compute the models with which we train the Neural Network emulator. We employ another suite of simulations, dubbed “test‘", to assess the uncertainty of the model, by estimating the accuracy of baryonification and cosmology scaling algorithms.

Main suite

Our main suite of simulations is part of the “BACCO simulation" project – a set of simulations specially designed, in terms of cosmology and numerical parameters, to provide highly accurate predictions for cosmic structure as a function of cosmology.

Specifically, we employ a set of four gravity-only simulations with 1536^3 particles of mass $m_p \sim 3 \times 10^9 h^{-1}\mathrm{M}_\odot$ in a box of $L = 512\,h^{-1}\mathrm{Mpc}$ a side. The initial conditions

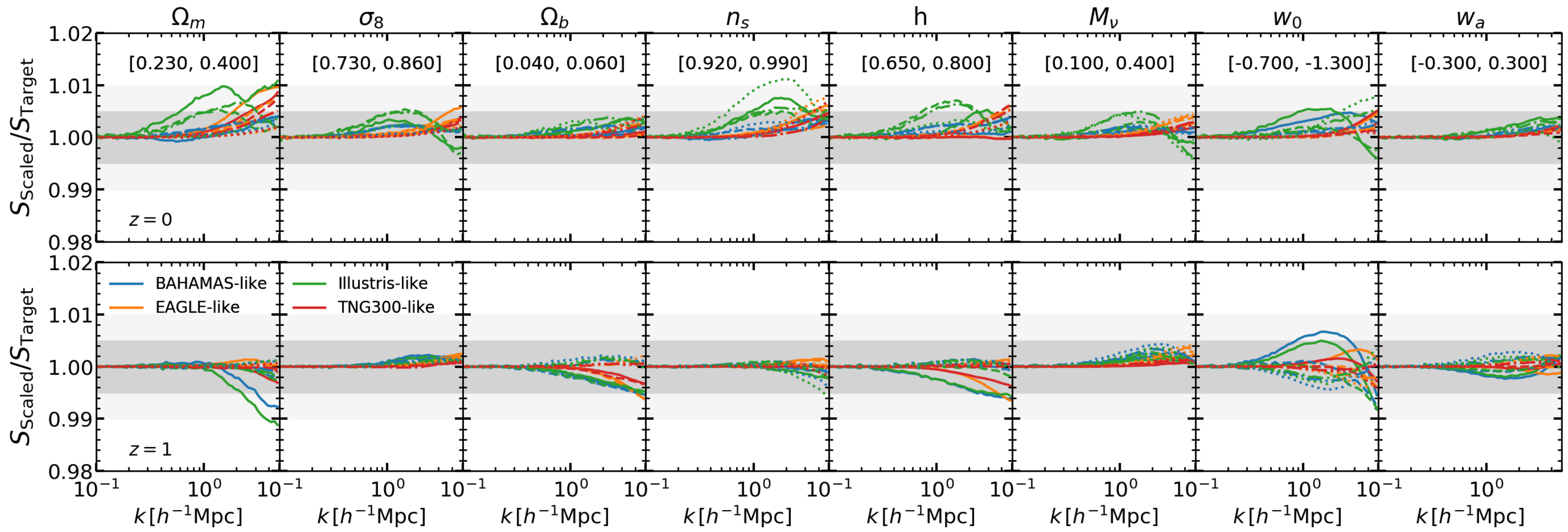

Figure 5.1: Accuracy of the cosmology rescaling algorithm with baryonification at $z = 0$ (upper panels) and $z = 1$ (bottom panels). We display the ratios of $S \equiv P_{\rm bcm}/P_{\rm GrO}$ estimated on a simulation whose cosmology has been rescaled ($S_{\rm scaled}$) over the same quantity but computed on a simulation carried out directly with the target cosmology $S_{\rm target}$. Each column shows variations on different cosmological parameters, shown in the titles, in a range specified in square brackets in the panels. Different line styles refer to different values of the cosmological parameter varied in the range displayed. Different colours show the results adopting 4 different baryonification parameter sets consistent with the modifications predicted by different hydrodynamical simulations. The grey bands highlight 0.5% and 1% accuracy in the resulting “baryonified” power spectrum.

Cosmology	$\Omega_{\rm cdm}$	$\Omega_{\rm b}$	h	$n_{\rm s}$
`nenya`	0.265	0.050	0.60	1.01
`narya`	0.310	0.050	0.70	1.01
`vilya`	0.210	0.060	0.65	0.92
`theone`	0.259	0.048	0.68	0.96

Table 5.1: Cosmological parameters set used in the BACCO simulation project. All the cosmologies assume a flat geometry, massless neutrinos ($M_\nu = 0$), a dark energy equation of state with $w_0 = -1$ and $w_a = 0$, an amplitude of matter fluctuations $\sigma_8 = 0.9$, and optical depth at recombination $\tau = 0.0952$.

were generated using 2LPT at $z = 49$, and the amplitude of Fourier modes were fixed to the ensemble average of the linear-theory power spectrum obtaining a significant cosmic variance suppression (Angulo and Pontzen, 2016). Gravitational evolution was computed using `L-Gadget3` (Springel, 2005; Angulo et al., 2012, 2020) with a Plummer-equivalent softening length of $\epsilon = 5\,h^{-1}{\rm kpc}$. We consider as our particle catalogue a down-sample of the full catalogue by a factor of 4^3.

We highlight that the force and mass resolution, as well as the numerical parameters controlling the accuracy of the force computation and time integration were chosen to provide results converged at the 1% level in the nonlinear power spectrum at $z = 0$. This numerical setup, for instance, was shown to perform extremely well in the Euclid Code Comparison project (Schneider et al., 2016), agreeing within 2% with most of other N-body codes up to $k \sim 10h^{-1}{\rm Mpc}$ (Angulo et al., 2020).

Each of these four simulations adopts a different set of cosmological parameters, carefully chosen so that together can efficiently cover a large region of cosmologies when combined with rescaling algorithms. In this work, we add a new cosmology to the three original ones described in Contreras et al. (2020a), thus improving the accuracy to better than 2% for ΛCDM parameters up to $k = 5h\,{\rm Mpc}^{-1}$, and to better than 3% when extended to massive neutrinos and dynamical dark energy. The parameters of these four cosmology are specified in Tab. 5.1. We will show how, thanks to this setup, we will achieve an accuracy of 1% in the scaling of the baryonic suppression.

We note that these simulations are identical to those of Angulo et al. (2020) but on a smaller volume, which significantly reduces the computational cost of our calculations while adding almost no additional noise (see Appendix G for a comparison on selected cases).

Testing suite

To quantify the uncertainty in the cosmology-dependence of our predictions, we will employ a set of 30 N-body simulations carried out with different cosmologies. These simulations, presented in Contreras et al. (2020a), feature the same mass and force resolution as our main suite, but on a smaller volume: each simulation has a side-length chosen to match the re-scaled box from a $L = 256h^{-1}\mathrm{Mpc}$ simulation.

The cosmological parameter sets of these simulations correspond to that of `nenya`simulation and then systematically varying one of the following parameters $\theta = \{\Omega_{\mathrm{m}},\, \Omega_{\mathrm{b}},\, \sigma_8,\, n_s,\, h,\, M_\nu, w_0,\, w_a\}$ over a range set by roughly 10 times the uncertainty given by recent CMB analyses combined with large-scale structure data (Planck Collaboration et al., 2018). We note that this range coincides with the parameter range we employ to construct our baryonification emulator (c.f. §5.3.1 and Eq. 5.1). In the test simulations, the density of massive neutrinos is followed in a mesh according to Ali-Haïmoud and Bird (2013).

In subsequent sections we will compare our baryonification algorithm when applied to a rescaled main simulation or when applied directly to one of these test simulations.

5.2.2 Baryonification algorithm

To model the impact of baryonic physics on the mass distribution, we employ the so-called “baryonification” algorithms (Schneider and Teyssier, 2015a; Schneider et al., 2019; Aricò et al., 2020b). In short, the approach uses a set of physically-motivated prescriptions for how different physics – star formation, gas cooling, AGN feedback, etc – are expected to modify the distribution of mass in the universe. These modifications are then applied to the output of gravity-only N-body simulations by perturbing accordingly the position of particles.

Given the uncertainties associated with baryonic physics, the baryonification approach has the huge advantage of being able to explore a large number of possible modifications to the matter power spectrum. The parameters of the model can be compared, and potentially constrained, with observations and/or results from hydrodynamical simulations.

Here, we employ the implementation described in Aricò et al. (2021a). Specifically, the model contains the following components:

- Gas bound in haloes, whose density is described by a double power law with a transition and slopes being free parameters;

- The ejected gas density, described as a constant with an exponential cut-off, set by a characteristic scale, η;

- Central galaxies with a mass profile given by an exponentially-decaying power law, here fixed to r^{-2}.

- Satellite galaxies are assumed to follow dark matter and to be 20% of the mass of the central galaxy[1].

---

[1] This somewhat arbitrary satellite-galaxy mass fraction is not expected to impact our results, see Aricò et al. (2021a) for more details.

- Dark matter. The model accounts for the back-reaction of the baryonic mass components onto the dark matter, which is assumed to quasi-adiabatically relax in response to the modified gravitational potential.

The mass fractions of the bound and ejected gas are given by parametric functions of the host halo mass, whereas that of the central galaxies is derived from abundance matching. The sum of stellar and gas mass fractions, included the ejected gas, is by construction equivalent to the cosmic baryon fraction $\Omega_{\rm b}/\Omega_{\rm m}$. For further details on the implementation, we refer the reader to Aricò et al. (2021a, 2020b).

5.2.3 Cosmology Rescaling

To model the cosmology dependence of baryonification, we have employed cosmology-rescaling algorithms (Angulo and White, 2010). The main idea behind these is that the outputs of a given simulation can be manipulated so that they represent nonlinear structure on a cosmology different to that originally adopted to run the simulation. The target cosmology can be any parameter in ΛCDM, and has recently been extended to include the effects of massive neutrinos and dynamical dark energy (Zennaro et al., 2019).

Here, we employ the latest version of the rescaling algorithm (Contreras et al., 2020a; Angulo et al., 2020), which considers the effect of large-scale flows through 2nd order Lagrangian perturbation theory, and the cosmology dependence of the concentration-mass relation. In this work, the halo masses are additionally corrected to take into account the non-universality of the mass function (Ondaro-Mallea et al., 2021). Overall, the algorithm is extremely fast – usually taking a few minutes per target cosmological model – which allows to densely sample a given target cosmological parameter space.

5.2.4 Power Spectrum Measurements

We compute the power spectrum of our mass fields with Fast Fourier Transforms and combining two interlaced grids (Sefusatti et al., 2016) with 384^3 points and a Cloud-in-Cell mass assignment scheme. Since our box sizes are typically $\sim 500h^{-1}{\rm Mpc}$, the Nyquist frequency is $\sim 1h^{-1}{\rm Mpc}$. Thus, to compute our predictions down to smaller scales, we repeat the procedure after "folding" the density field 4 times in each coordinate direction (Jenkins et al., 1998).

We measure the power spectrum on 50 logarithmically-spaced bins over the range $0.01 < k/(h\,{\rm Mpc}^{-1}) < 5$, with $k' = \pi N/(2L)$, where L is the simulation boxsize and N is the cubic root of the grid points, as the transition scale between the original and folded measurements. Finally, we estimate and subtract the shot-noise following Angulo et al. (2020) by comparing the power spectrum measurements of the unscaled simulations using the full simulation particle set.

For each simulated or rescaled simulations we obtain power spectrum measurements for the mass density field with and without modelling the baryonic effects. We refer to these as gravity only and baryonified outputs, and employ the acronyms GrO and BCM, respectively.

5.2.5 Validation

The cosmology rescaling algorithm has been validated by multiple studies (Ruiz et al., 2011; Angulo and Hilbert, 2015; Renneby et al., 2018). Specifically, Contreras et al. (2020a) showed that the nonlinear power spectrum can be recovered better than 1% up to $k \sim 1h^{-1}\mathrm{Mpc}$ and better than 3% up to $k \sim 5h^{-1}\mathrm{Mpc}$; whereas Ondaro-Mallea et al. (2021) show that the halo mass function is obtained to better than 2%, over the whole parameter space considered here.

Likewise, the baryonification procedure has been validated by comparing their predictions to state-of-the-art cosmological hydrodynamical simulations (Schneider et al., 2019, 2020; Aricò et al., 2020b). Our particular implementation has been tested in Aricò et al. (2020b) and Aricò et al. (2021a), where we showed baryonic effects in the mass power spectrum and bispectrum can be *simultaneously* reproduced to about 1 and 3%, respectively. This over the scales up to $k \sim 5h\,\mathrm{Mpc}^{-1}$ and for the Illustris, Illustris-TNG, EAGLE, and BAHAMAS (standard, low-AGN, and high-AGN versions) hydrodynamical simulations.

Here, we focus on exploring the accuracy of the predictions when both algorithms are employed together. For this, we have first rescaled our main simulations to each of the 30 cosmologies in our suite of "test" simulations. Then, we applied our baryonification algorithm employing 5 different set of parameters, consistent with various hydrodynamical simulations. We compare our measurements against the same baryonification models but applied directly on our test simulations.

We present our results in Fig. 5.1, where each panel shows variations on different cosmological parameters, and for different baryonic scenarios, as indicated by the legend. Note we display the ratio between $S(k)$s, which can be directly interpreted as the fractional error on a baryonified power spectrum considering a perfect knowledge of the gravity-only power spectrum: $P_{\mathrm{BCM}}(k) = S(k)P_{\mathrm{GrO}}(k)$.

We can see that the cosmology rescaling indeed allows to obtain very accurate predictions for the cosmological dependence of baryonification. On scales larger than $k \sim 1h\,\mathrm{Mpc}^{-1}$, $S(k)$ is almost identical regardless whether it is obtained from a direct or rescaled N-body simulation, with differences being typically less than 0.005. On smaller scales at $z = 0$, the error somewhat increases, however, in all cases it remains below 0.01, which implies that the full nonlinear power spectrum is predicted to better than 1%. At $z = 1$, the overall accuracy increases, being in most of the cases better than 0.5%. In Appendix H we show that by varying simultaneously all parameters we recover similar accuracy.

5.3 Baryonification Emulator

In this section we will use the cosmology rescaling and baryonification techniques to build a Neural Network emulator, and quantify its accuracy and precision. This section is organised as follows: in § 5.3.1 we define the emulator parameter space and training dataset; in § 5.3.2 we describe the treatement we apply to the dataset prior to the emulation to improve its stability, and in § 5.3.3 we delineate the specifics of the Neural Network we employ to perform the emulation.

5.3.1 Parameter Space

We consider a cosmological parameter space given by the main ΛCDM model, extended with massive neutrinos and dynamical dark energy, over the following range:

$$\begin{aligned} \sigma_8 &\in [0.73, 0.9] \\ \Omega_{\rm m} &\in [0.23, 0.4] \\ \Omega_{\rm b} &\in [0.04, 0.06] \\ n_{\rm s} &\in [0.92, 1.01] \\ h &\in [0.6, 0.8] \\ M_\nu\,[\mathrm{eV}] &\in [0.0, 0.4] \\ w_0 &\in [-1.15, -0.85] \\ w_{\rm a} &\in [-0.3, 0.3] \end{aligned} \tag{5.1}$$

where σ_8 is the *cold* mass linear mass variance in $8\,h^{-1}\mathrm{Mpc}$ spheres; $\Omega_{\rm m}$ and $\Omega_{\rm b}$ are the density of cold matter and baryons in units of the critical density of the Universe; $n_{\rm s}$ is the primordial spectral index; h is the dimensionless Hubble parameter $h = H_0/(100\,\mathrm{km\,s^{-1}Mpc^{-1}})$; M_ν is the mass of neutrinos in units of eV; and w_0 and $w_{\rm a}$ are parameters describing the time-evolving dark energy equation of state via $w(z) = w_0 + (1-a)\,w_{\rm a}$. We note that these are the same parameter ranges used in Angulo et al. (2020), chosen to be roughly 10σ around Planck2018 best-fitting model (Planck Collaboration et al., 2018).

Additionally, we consider 7 parameters describing the baryonic physics according to our baryonification algorithm:

$$
\begin{aligned}
\log M_{\mathrm{c}}/(h^{-1}\mathrm{M}_{\odot}) &\in [9.0, 15.0] \\
\log \eta &\in [-0.7, 0.7] \\
\log \beta &\in [-1, 0.7] \\
\log M_{1,\mathrm{z0,cen}}/(h^{-1}\mathrm{M}_{\odot}) &\in [9, 13] \\
\log M_{\mathrm{inn}}/(h^{-1}\mathrm{M}_{\odot}) &\in [9, 13.5] \\
\log \theta_{\mathrm{inn}} &\in [-2, -0.5] \\
\log \theta_{\mathrm{out}} &\in [-0.5, 0]
\end{aligned}
\tag{5.2}
$$

where η parameterises the extent of the ejected gas; $\{\theta_{\mathrm{inn}}, M_{\mathrm{inn}}, \theta_{\mathrm{out}}\}$ describe the density profiles of hot gas in haloes and $\{M_{\mathrm{c}}, \beta\}$ its mass fraction; and $\{M_{1,\mathrm{z0,cen}}\}$ is the characteristic halo mass scale for central galaxies (see §5.2.2 and Aricò et al. 2021a for further details). These parameter ranges are very similar to the ones used in Aricò et al. (2021a), where they were shown to be wide enough to correctly reproduce the clustering of several hydrodynamical simulations. They are chosen taken into account the specifics of the gravity-only simulations where the baryonification is applied to, other than broad astrophysical constraints.

To optimally sample the hypervolume, we create a $10,000$-point Latin hypercube on this 15-dimensional parameter space. For each point in this set, we first rescale one of our main simulations to the corresponding cosmology and then apply our baryonification algorithm with the corresponding parameters. The simulation used for a given target cosmology is given by a Neural Network trained to minimise the error in the cosmology scaling process, as described in Contreras et al. (2020a).

We repeat this for ~ 10 simulation snapshot times over the range $0 \leq z \leq 1.5$, and measure the power spectrum of the gravity-only and baryonified outputs, as described in §5.2.4. We have heavily optimised all of our codes involved, and this procedure takes approximately 3 minutes on 12 cores per parameter set, and employed $36,000$ CPU hours as a whole.

5.3.2 Power Spectrum Data

Overall, we have computed $S(k) \equiv P_{\mathrm{bcm}}/P_{\mathrm{GrO}}$ using the power spectrum of the gravity-only and baryonified field for roughly $50,000$ cases. This constitutes our primary dataset.

To reduce the dimensionality of our problem, and the significant trends present in our data (which could, for instance, lead to overfitting problems in our Neural Network training), we filter out small scale noise. First, we apply a Savitzky-Golay filter of order 5 and 11 points to each of our measured $S(k)$. We then perform a Principal Component Analysis (PCA) with mean subtraction, and keep in our data only the 6 vectors with the highest eigenvalues.

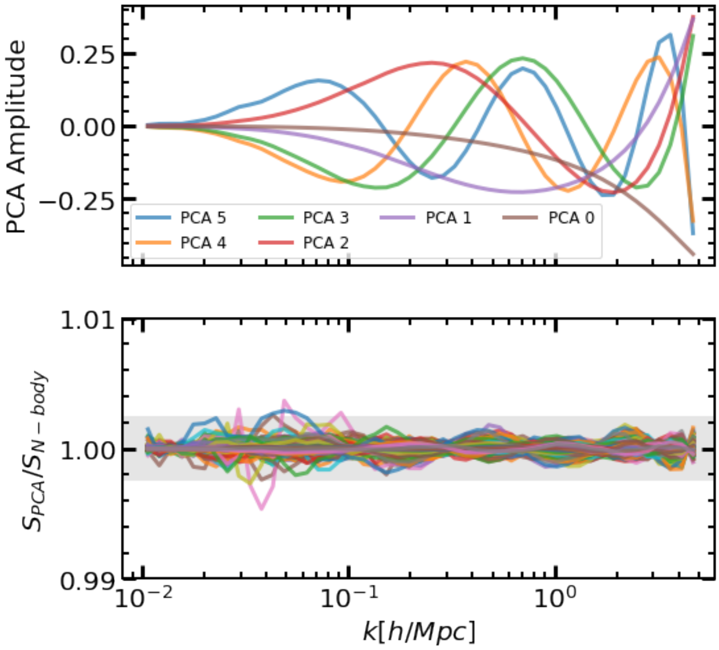

Figure 5.2: Principal Analysis Decomposition of our set of baryonified power spectra. In the top panel we display the first 6 eigenvectors of our Principal Component Analysis. In the bottom panel we show the ratio of $S \equiv P_{\rm BCM}/P_{\rm GrO}$ as estimated using the aforementioned 6 PCs, $S_{\rm PCA}$, over the same quantity without any decomposition, $S_{N-{\rm body}}$.

In the upper panel of Fig. 5.2 we display these 6 PC vectors as a function of wavenumber. We can see that the most important feature, shown as a purple line, is a smooth suppression of the power spectrum starting at $k \sim 0.5h\,{\rm Mpc}^{-1}$, which can be related to the effect of gas ejection in haloes. The second most important vector describes an increase in the power on small scales, linked to gas condensation and the presence of stars at the centre of haloes.

In the bottom panel we show the ratio of $S(k)$ reconstructed using the first 6 PCs over the full $S(k)$ vector. We show the results for a random 10% of our data. We can appreciate that the residuals are almost always smaller than 0.5%, indicated by the grey region, which confirms the accuracy of our PC decomposition. We note that the residuals increase to 1.5%, and 1% when only the first 3 and 5 PCs are considered, respectively.

It is interesting to note that our PC decomposition indicates that only 6 numbers are sufficient to accurately describe all possible values of S(k) allowed by our framework, including variations of both cosmological and baryonic parameters. In § 5.5 we will explore this issue further and seek for a minimal parameterisation that is able to describe a large variety of hydrodynamical simulations.

Finally, we note that these 6 PCs could be considered as an optimal and adequate basis functions for a purely data-driven modelling of baryonic effects on the power spectrum.

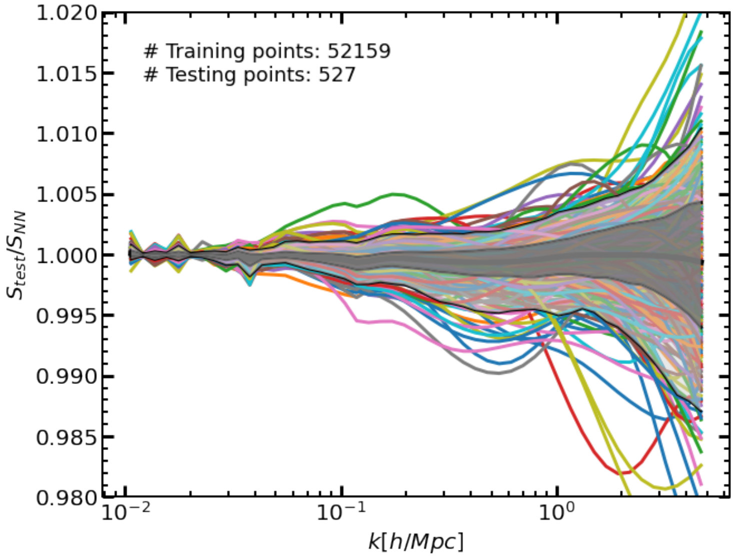

Figure 5.3: Ratio between the predictions of our Neural Network emulator for $S \equiv P_{\mathrm{bcm}}/P_{\mathrm{GrO}}$ over the corresponding measurement on our baryonified simulations, S_{test}. Coloured lines show the results for a set of 60 combinations of cosmology and baryonic physics, not included in our training sample. The shaded regions enclose 68% and 95% of the measurements and the mean is marked by the think grey line.

5.3.3 Neural Network Emulator

We employ a feed-forward Neural Network to predict the baryonic effects on the power spectrum, $S(k) \equiv P_{\mathrm{BCM}}/P_{\mathrm{GrO}}$ for a given set of cosmological and baryonic parameters. Our network architecture consists on two fully-connected hidden layers with 400 neurons each, and a Rectified Linear Unit as an activation function.

We randomly select 99% of our data as a training set and the remaining 1% as a validation sample ($\sim 52,000$ and ~ 500 power spectrum measurements, respectively).

We construct our Neural Network using the Keras library together with the TensorFlow back-end (Chollet et al., 2015; Abadi et al., 2016). We use the adaptive stochastic optimization algorithm Adam with a learning rate 10^{-3}, and define the mean squared error as the loss function. For the training we employ $20,000$ epochs, which takes approximately 20 hours on a single GPU to complete. We note that we have experimented with the inclusion of batch normalization and dropouts, finding no significant improvements in the accuracy nor in the degree of overfitting of our network.

5.3.4 Performance Test

To estimate the accuracy of our Neural Network emulator, we have compared its predictions for $S(k)$ against the value directly measured in our training sample. We display the results in Fig. 5.3 with coloured lines showing the measurement for each of the individual parameter sets in our testing sample, and the thick line and shaded grey areas indicating the average and

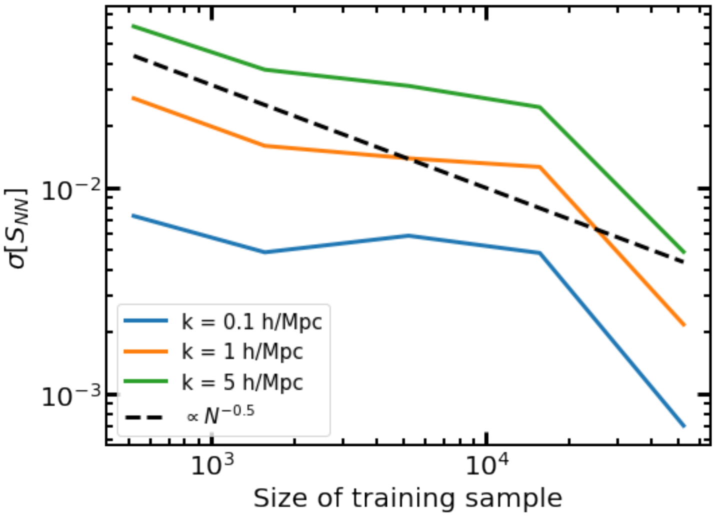

Figure 5.4: Dependence of the accuracy of our Neural Network emulator on the number of training points. Blue, orange, and green lines show the results measured at three wavenumbers: 0.1, 1, and $5\,h\,\mathrm{Mpc}^{-1}$, respectively.

regions containing 68% and 95% of the data, respectively.

Firstly, we see that our emulator is unbiased at the 0.1% level, and has a very high precision up to $k \sim 1h\,\mathrm{Mpc}^{-1}$ where deviations are typically less than 0.2%. On smaller scales the precision somewhat degrades but it is typically within 1% up to $k = 5h\,\mathrm{Mpc}^{-1}$ with only 2 cases deviating more than 3%. We have tried different combinations of the Neural Network finding that these results are fairly insensitive to architecture details and are limited by a finite number of training points, as we will discuss next.

In Fig. 5.4 we display the typical precision of our Neural Network as a function of the number of points in the training set. To do this, we retrain our emulator employing a random selection of points in our training set. For a fair comparison, we estimate the uncertainty using always the same 500 testing cosmologies. The precision of the emulation scales roughly as ${N_{\mathrm{T}}}^{-0.5}$, where N_{T} is the number of points in the training set. In this work, we feed our emulator with a number of power spectra such that the uncertainty in the emulation is of the same order as our model error, i.e. 1%. Thus, the overall expected precision is conservatively of $2-3\%$.

We note that, however, in principle the emulation precision can be improved further by adding extra training points. We plan to constantly update our public emulator, until the uncertainty in the interpolation is negligible compared to the other sources of errors.

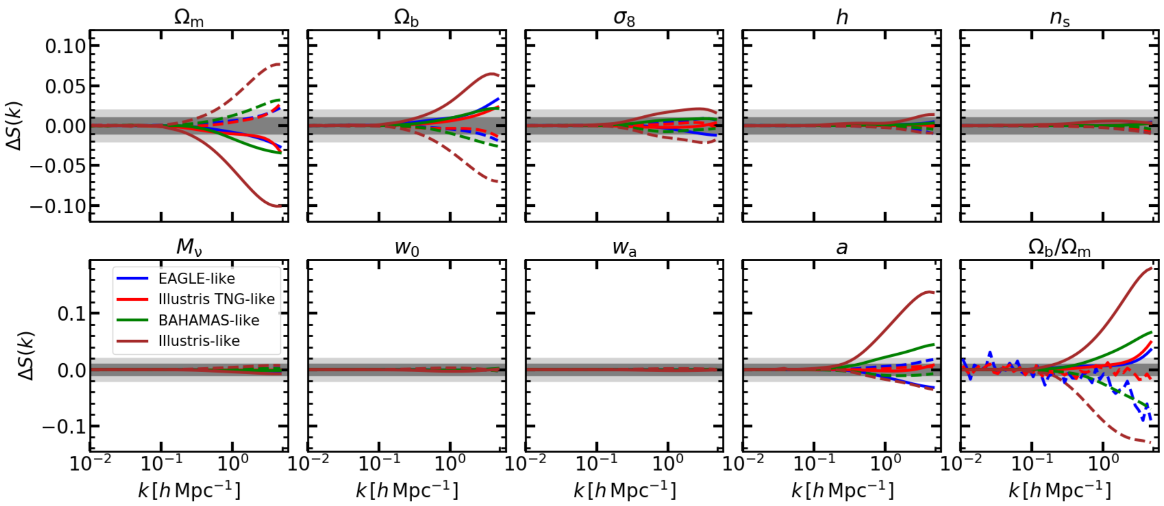

Figure 5.5: Cosmology dependence of the baryonic effects on the non-linear mass power spectrum. We display $\Delta S(k) = S(k,\hat{\theta}) - S(k,\bar{\theta})$, where $S(k) = P_\mathrm{bcm}/P_\mathrm{GrO}$, $\hat{\theta}$ are the extreme values in our parameter range consider and $\bar{\theta}$ is the centre of that range (c.f. Eq. 5.1). Solid and dashed lines represent left and right differences, respectively Different panels show the results for $\theta = \{\Omega_\mathrm{m}, \sigma_8, \Omega_\mathrm{b}, n_s, h, M_\nu, w_0, w_\mathrm{a}, a, \Omega_\mathrm{b}/\Omega_\mathrm{m}\}$, as estimated from our Neural Network emulator by using baryonic parameters consistent with different hydrodynamical simulations, as indicated in the legend. Grey shaded regions denote a 1% and 2% change in $S(k)$ over the parameter range we consider in our emulator.

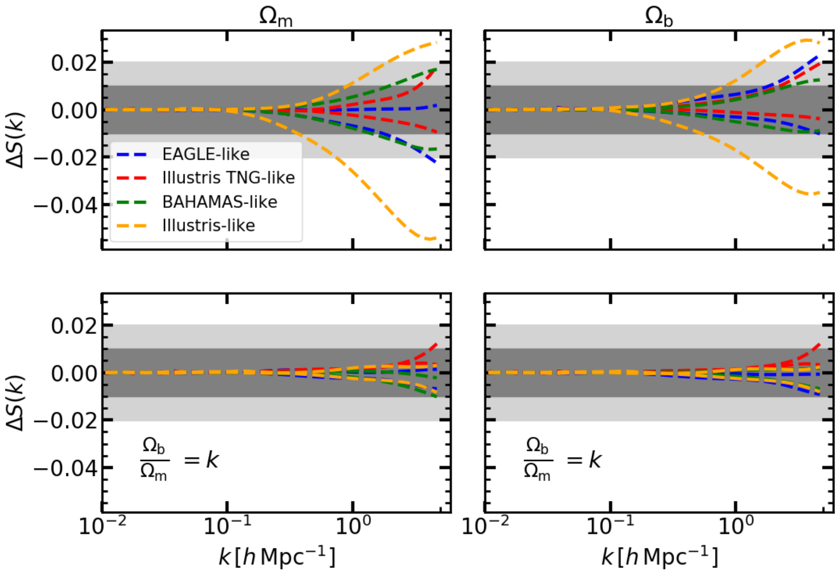

Figure 5.6: Same as Fig. 5.5 for Ω_m and Ω_b (but considering a smaller $\Delta\theta$ range), with free (upper panels) and fixed to 0.13 (lower panels) cosmic baryon fraction $\Omega_\mathrm{b}/\Omega_\mathrm{m}$.

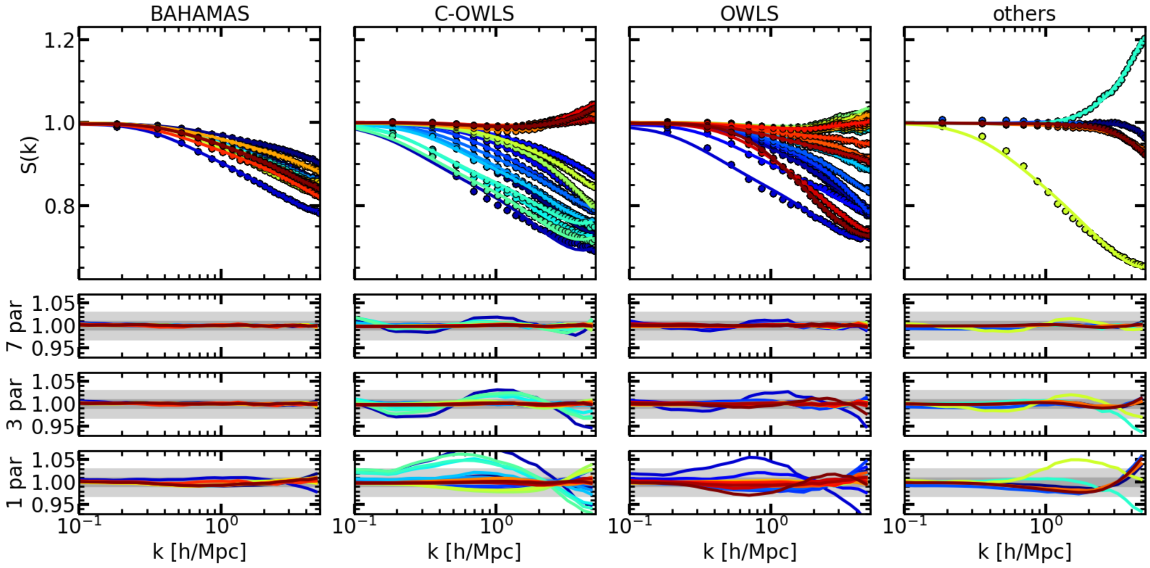

Figure 5.7: *Upper panels:* The symbols show the baryonic impact on the matter power spectrum at $z = 0$, defined as $S(k) = P_{\rm Hydro}/P_{\rm Gro}$, as measaured in BAHAMAS (first column), Cosmo-OWLS (second column), OWLS (third column), and EAGLE, Illustris, Illustris TNG, and Horizon hydrodynamical simulations. The solid line represents the best-fitting models obtained with our emulator. *Lower panels:* ratio between the measurements of the suppression in the power spectrum induced by baryons, as measured in the hydrodynamical simulations and in our best-fitting model, considering 7 (top), 3 (middle), and 1 (bottom) free parameters.

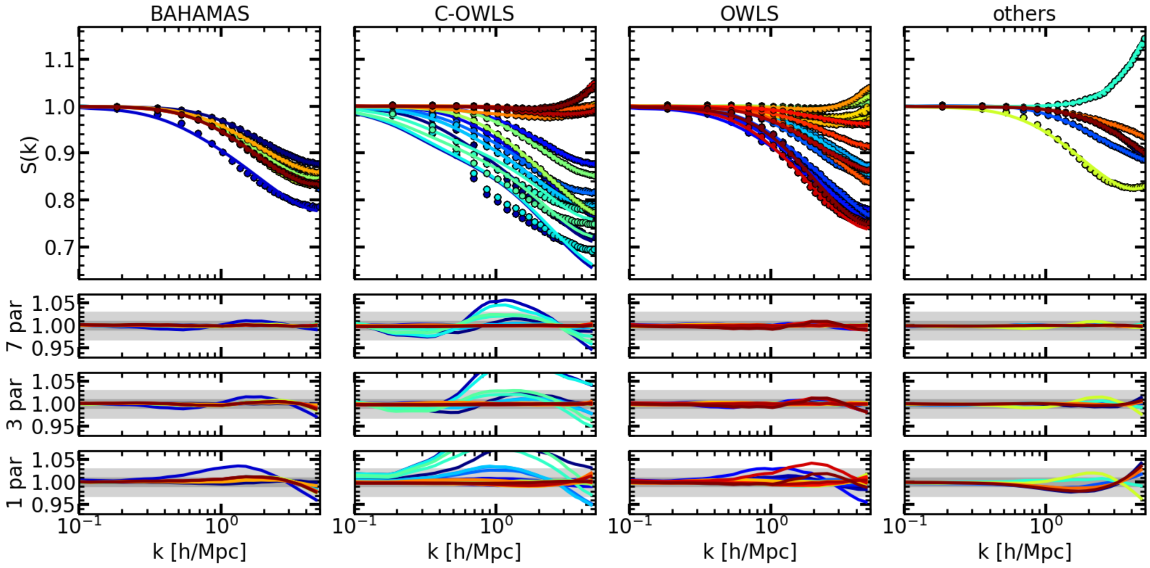

Figure 5.8: Same as Fig. 5.7 but at $z = 1$.

5.4 The cosmology dependence of baryonic effects on the power spectrum

It is sometimes assumed that the effects of baryonic physics and galaxy formations are independent of most, if not all, cosmological parameters. For instance, van Daalen et al. (2011) shows that the suppression of the power spectrum is very similar among hydrodynamical simulations assuming parameters consistent with the analysis of 3rd and 7th-year WMAP data. On the other hand, van Daalen et al. (2020) find small but significant differences in a more recent analysis employing larger simulations but considering similar changes in cosmology.

In Fig. 5.5 we explore the cosmological dependence expected in our baryonification algorithm. In each panel we display the difference in $S(k)$ obtained with the maximum change allowed by the cosmological parameter range in our emulator. Note we also display the expansion factor, a, and the cosmic baryon fraction, $\Omega_{\mathrm{b}}/\Omega_{\mathrm{m}}$. We show results for different baryonification parameter sets consistent with BAHAMAS, EAGLE, Illustris, or Illustris-TNG.

We can see that in general baryonic physics and cosmology are not independent. The strength on the dependence varies with baryonic physics and the cosmological parameter considered. The main dependence appears to be with respect to Ω_{m} and Ω_{b}, followed by σ_8. The other parameters show variations within 1%, consistent with the emulator precision.

In our model, cosmological dependence can appear only through three channels: the halo mass function, which modulates the contribution of baryonic effects in haloes of different mass; the baryon fraction, which sets the overall importance of baryonic effects; and the concentration-mass relation, which regulate the displacement field on small-scales. We will explore these next.

To investigate the role of baryon fraction, we have computed the variation in the baryonic suppression by varying Ω_{m} and Ω_{b}, but keeping fixed their ratio to $\Omega_{\mathrm{b}}/\Omega_{\mathrm{m}} = 0.13$. We display our results in Fig. 5.6 for variations in Ω_m and Ω_b, since these are the only two parameters that can be affected. We can appreciate that now baryonic suppression and cosmology become largely independent of each other.

Since w_0 and w_a only affect the cosmic growth history – leaving intact the linear power spectrum and the baryon fraction, we can employ variations with respect to them to estimate the role of the cosmology-dependence of the concentration-mass relation. Indeed, over the parameter range we consider, the concentration of $10^{13}h^{-1}\mathrm{M}_{\odot}$ haloes varies from 4 to 8, but the value of $S(k)$ barely changes. This points to a very minor role of the concentration-mass relation for realistic cosmological variations.

Conversely, variations with respect to σ_8 change primarily the halo mass function, and in this case, we observe small but non-negligible variation in the baryonic effects, of $2-3\%$ in our entire parameter range.

In summary, our model for baryonic physics shows clear dependence with cosmology. The primary correlations are induced by variations on the baryon fraction, whereas remaining correlations can be explained by variations in the underlying halo mass function. The concentration-mass relation introduces a very minor effect. These results can serve as a guide to, for instance, simulations campaigns that seek to explore the cosmological dependence of the baryonic effects with hydro-dynamical calculations.

5.5 Constraints on the baryon parameter space

We test the accuracy of our emulator with a large collection of gravity-only and hydrodynamical simulations. Specifically, we use 16 BAHAMAS simulations[2] (McCarthy et al., 2017, 2018), 23 Cosmo-OWLS (Le Brun et al., 2014), 29 OWLS (Schaye et al., 2010; van Daalen et al., 2011), EAGLE[3] (Schaye et al., 2015; Crain et al., 2015; McAlpine et al., 2016; Hellwing et al., 2016; The EAGLE team, 2017), Illustris[4] (Vogelsberger et al., 2013, 2014b,a; Sijacki et al., 2015), 2 Illustris TNG (100 Mpc and 300 Mpc)[5] (Springel et al., 2018; Pillepich et al., 2018; Nelson et al., 2018; Naiman et al., 2018; Marinacci et al., 2018; Nelson et al., 2019), and 2 Horizon (with and without AGN)[6] (Dubois et al., 2014). We note that a large part of this dataset, specifically the power spectra from OWLS, Cosmo-OWLS and BAHAMAS, have been collected and published by van Daalen et al. (2020)[7].

The simulations considered implement a wide range of different physical processes. Among others, AGN feedback, supernovae feedback, mass loss from Asymptotic Giant Branch stars, radiative cooling, stellar winds, and stellar initial mass function are varied. Furthermore, the simulations have different mass resolutions and box sizes, and this can mildly impact the expected suppression given by baryons. However, as pointed out in van Daalen et al. (2020), the main driver of the differences in hydrodynamical simulations predictions is the calibration of the subgrid processes. In fact, the hydrodynamical simulations are usually calibrated to reproduce one or more observables, even though their agreement with non-calibrated observables might be rather poor.

The most important quantity for determining the impact of baryonic physics on the power spectrum is how much gas has been retained in group-size haloes. Considering this specific observable, we choose BAHAMAS as our main test suite of simulations, whose

---

[2] `http://www.astro.ljmu.ac.uk/~igm/BAHAMAS/`

[3] `http://icc.dur.ac.uk/Eagle/`

[4] `https://www.illustris-project.org/`

[5] `https://www.tng-project.org`

[6] `https://www.horizon-simulation.org/`

[7] `http://powerlib.strw.leidenuniv.nl`

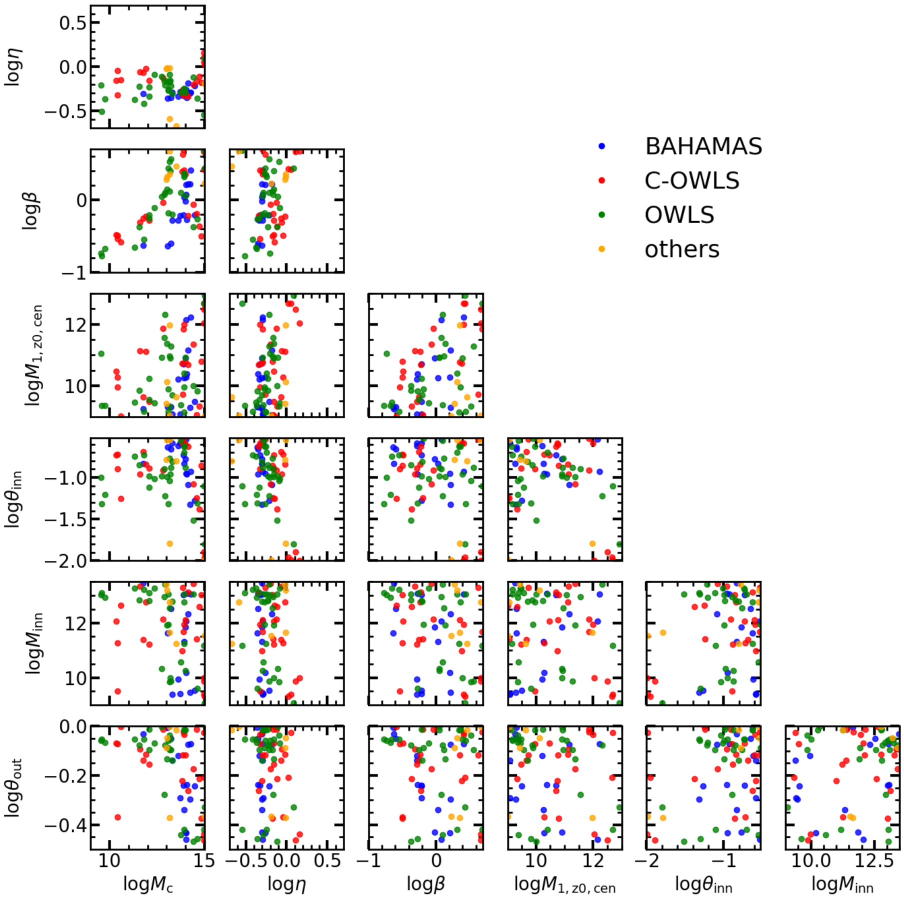

Figure 5.9: Best-fitting parameters obtained by fitting the hydrodynamical simulations BAHAMAS (blue), C-OWLS (red), OWLS (green), and EAGLE, Illustris, Illustris TNG, Horizon (orange).

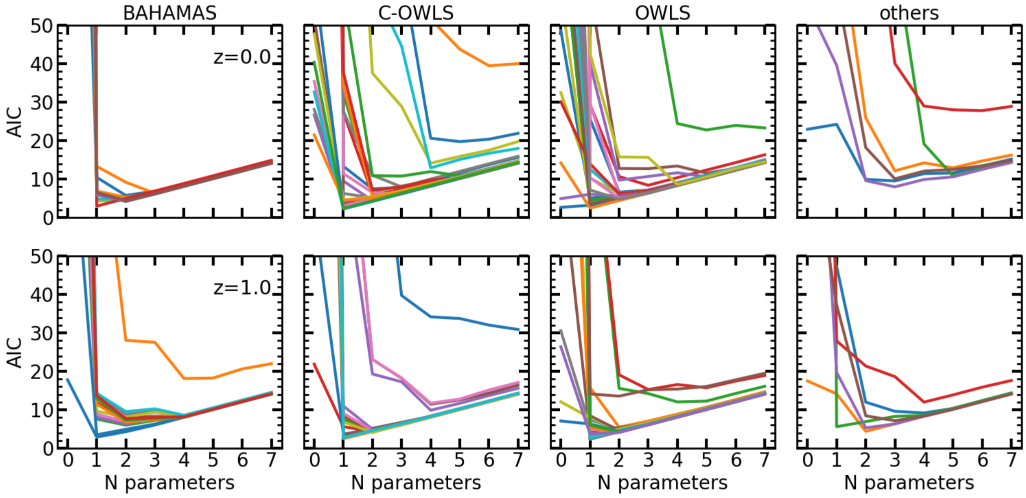

Figure 5.10: Akaike Information Creterion (AIC) computed by using a baryonic model which use from 0 to 7 free parameters, at $z = 0$ (top panels) and $z = 1$ (bottom panels). We consider as data the hydro/gravity-only power spectra ratios measured in BAHAMAS (first column), Cosmo-OWLS (second column), OWLS (third column), and Illustris-TNG, EAGLE, Illustris and Horizon (fourth column). Each different color refer to a single simulation run.

sub-grid recipes were calibrated using the observed stellar and gas fractions in clusters.[8] Nevertheless, we include all the power spectra in our analysis, as we expect their diversity to be an excellent benchmark for the flexibility of our emulator.

5.5.1 Baryonification Parameter Constraints

We use our emulator to fit the measured power spectrum ratio $S(k)$ in the 74 different hydrodynamical simulations and their respective gravity-only counterparts, at two different redshifts, $z = 0$ and $z = 1$.[9]. We note that the various models span a range of effects which goes from a 30% suppression to a 20% enhancement.

In each case, we first fix the value of cosmological parameters to those used in each simulation and then constrain the values of the free baryonification parameters. We sample the posterior distribution function using the public code `emcee` (Foreman-Mackey et al., 2013) with 14 walkers of 5000 points, removing as a burn-in phase the first 3000 points of each walker. To homogenise the different measurements, we rebin all the power spectra in 30 linear bins over the range $k \in [0.1, 5]\, h\,\mathrm{Mpc}^{-1}$.

We estimate covariance matrix empirically following Aricò et al. (2020b):

$$\mathcal{C}_{S,ij} = \mathcal{E}(k_i)\mathcal{K}(k_j, k_i)\mathcal{E}_j^T(k_j), \tag{5.3}$$

where $\mathcal{E}$ is an "envelope" function that describes the typical amplitude of the uncertainty as a function of wavenumber, and $\mathcal{K}(k)$ the correlation of this uncertainty, which we model as a Gaussian distributed random variable $\mathcal{K} = \mathcal{N}(|k_i - k_j|, \ell)$. For all the models, we assume at large scales $\mathcal{E}$ to be a constant $fS(k)$ with $f = 1\%$, and a correlation length $\ell = 1\, h\,\mathrm{Mpc}^{-1}$. To model the small-scale noise we use $\mathcal{E} = [1 + 0.5\ \mathrm{erf}(k - 2)]fS(k)$, where $f = 2\%$.

We note that we do not expect this covariance matrix to provide a fair description of all possible uncertainties associated to $S(k)$ in all the simulations considered. The simulations, in fact, have box sizes ranging from $\approx 60\, h^{-1}\mathrm{Mpc}$ to $\approx 400\, h^{-1}\mathrm{Mpc}$, different mass resolutions, different implementation of sub-grid physics, and have even been carried out with different simulation codes, whose impact we do not model in our covariance matrices. Therefore, accurately describing the measured $S(k)$ will be an even more stringent test of the flexibility of our emulator. We note, however, that a more careful estimation of the covariance matrix is required in case, for instance, of cosmological parameters estimation.

In Figs. 5.7 and 5.8 we show the best-fitting models for all the 74 hydrodynamical simulations at $z = 0$ and $z = 1$, respectively. We see that the emulator is able to reproduce remarkably well the very diverse set of baryonic effects here considered. In particular, the

---

[8] These simulations have also box sides of $400\, h^{-1}\mathrm{Mpc}$, and therefore we expect the ratio $S(k)$ to be little affected by cosmic variance and finite-volume effects.

[9] For some simulations, the power spectrum at $z = 1$ is not available.

BAHAMAS suite – arguably the most realistic set of simulations for estimating baryonic effects – is particularly well reproduced, with differences being less than 1% at both $z = 0$ and $z = 1$. The OWLS suite is also very well fitted by our emulator, with an accuracy comparable to that in BAHAMAS. On the other hand, although most of the simulations in the C-OWLS suite are also accurately reproduced, specially at $z = 0$, few simulations featuring very strong AGN feeback at $z = 1$ are not captured very accurately. This specific simulations (cyan and blue symbols in the second column) display a step-like suppression at $k \sim 0.8h\,\mathrm{Mpc}^{-1}$ not seen in any other simulation. Elucidating the origin of such feature is beyond the scope of this thesis, and here we simply highlight that even in this very extreme case, the measurements are reproduced at the 5% level with our emulator.

The value of the $z = 0$ best-fitting parameters for all the simulations are shown in Fig. 5.9. Most of the simulations prefer a value of the AGN range $\eta \approx 0.5$, which suggest this is set by gravitational, rather than sub-grid, physics. We also see a correlation between M_c and β: low values of M_c compensate for low values of β such that the gas fraction retained in the halo is preserved, which is expected to be the main quantity determining $S(k)$ on intermediate scales. Finally, relatively large values of θ_inn are preferred, which disfavours steep inner gas profiles. Although not shown here, similar trends are found at $z = 1$, with a consistent shift of η to smaller values.

On the other hand, the values for $M_\mathrm{1,z0,cen}$, θ_out, and M_out do not show any clear common trend among the hydrodynamical simulations. By inspecting one by one the marginalised posteriors of single hydrodynamical simulations, we notice that in many cases these parameters are actually unconstrained by our simulated data.

The results of this section suggest that, in most cases, hydrodynamical simulations can be modelled by a subset of the baryonic parameters. We explore this further in the next subsection.

5.5.2 A minimal parameterisation for baryonification

Our default baryonic model includes seven free parameters describing multiple galaxy formation and baryonic physics. Arguably, some of these parameters present degeneracies among them and/or do not significantly change the power spectrum over the range of scales and redshifts we seek to model. For instance, in §5.3.2 we showed that only 5 PCs are needed to describe at 1% the full range of power spectrum suppression that our model allows. Moreover, by fitting our set of 74 hydrodynamical simulations, we found that three parameters – $M_\mathrm{1,z0,cen}$, θ_out, and M_out – are unconstrained in most cases.

We now focus on the question of how many free parameters are needed to fit the power spectrum suppression measured in the set of hydrodynamical simulations described above.

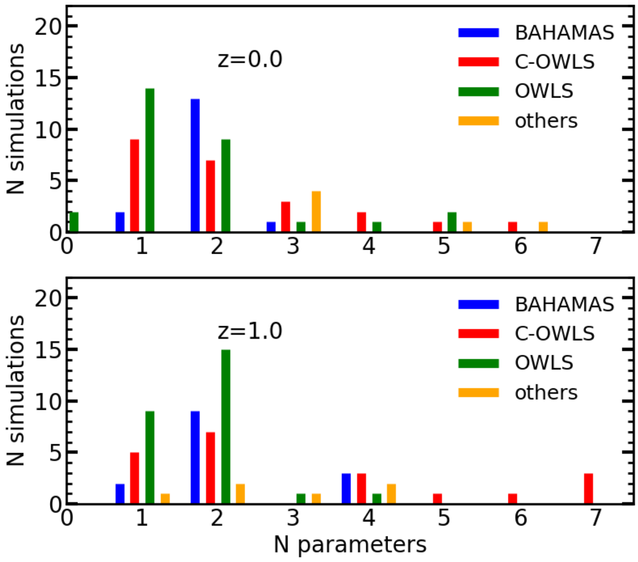

Figure 5.11: Number of hydrodynamical simulations which prefer a model with a given number of free parameters according to the Akaike Information Criterion. The simulations used are from BAHAMAS (blue), Cosmo-OWLS (red), OWLS (green), and Illustris-TNG, EAGLE, Illustris and Horizon (orange), at $z = 0$ (top panel) and $z = 1$ (bottom panel).

In addition to the full model discussed in the previous subsection, we consider seven stripped down versions, which we fit to the same library of power spectra.

We consider a baseline model with no free parameters, where we fix the baryonic parameters to the mean of the best-fitting values of all the hydrodynamical simulations used in §5.5. Following, we free an increasing number of parameters while keeping fixed the others to the same values as in the baseline model. In a second model, we vary only the parameter $M_{\rm c}$, and thus the gas fraction in haloes; a third model additionally varies the AGN range, η, and a forth one includes further the slope of the halo mass-bound gas relation, β. We consider also a 4-parameter model which includes the central galaxy mass $M_{1,\rm z0,cen}$, and 5 and 6 parameter models which consider also the gas shape parameters $\theta_{\rm inn}$ and $M_{\rm inn}$, respectively.

We show the fits using the 1, 3, and full 7-parameter models in the bottom panels of Fig. 5.7 at $z = 0$, and in Fig. 5.8 at $z = 1$. The emulator performs surprisingly well even when considering just a single free parameter. Considering the BAHAMAS simulations, the 1-parameter model fits at the 1% level most of the data at $z = 0$ and $z = 1$. The accuracy of the simulation that features the strongest AGN feedback somewhat degrades to $\sim 3\%$. The bulk of the the other simulations is reproduced at $2 - 3\%$, with few extreme cases exceeding 6%.

We compare the relative performance of these models using the Akaike Information Creterion (AIC) (Akaike, 1974). This criterion maximises the information entropy or, in other words, minimises the information loss of a model given some data. In practice, the AIC has one term which rewards the goodness of the fit, and one term that discourages large number of parameters to avoid overfitting.

For each model and target power spectrum ratio, we compute the AIC as:

$$\mathrm{AIC} \equiv -2 \log P(d_i|\hat{\theta}) + 2N_\theta, \tag{5.4}$$

where $P(d_i|\hat{\theta})$ is the maximum likelihood estimate, and N_θ the number of free parameters of the model. Thus, models which minimise the AIC are considered preferred by the data.

In Fig. 5.10 we compare the distribution of the AIC values for all of our models and hydrodynamical simulations. Each panel shows results for a given simulation suite and redshift, as indicated by the figure legend. In most of the cases, the AIC values go from ≈ 0 in the 1-parameter model, to ≈ 15 in the 7-parameter model. For some simulations, the AIC is systematically higher, $\mathrm{AIC} > 30$. In these cases, where the fit to the data is somewhat poorer, the minima are consistently shifted toward a larger number of free parameters. The baseline model, which feature no free parameters, has AIC values tipically 1-3 orders of magnitude larger than the other models. This means that the emulator is generally not able to describe properly the hydrodynamical simulations, when fixing all its parameters to their averaged best-fitting values. Finally, we note that the results at $z = 0$ and $z = 1$ are qualitatively similar.

We show in Fig. 5.11 a histogram of the number of hydrodynamical simulations that prefer a model with a given number of free parameters. At both $z = 0$ and $z = 1$, most of the simulations are best described by models with 1 or 2 free parameters, whereas models with larger number of parameters are needed only in a few cases. In some of the OWLS and Cosmo-OWLS suites, where the subgrid processes are varied more aggressively compared to a standard BAHAMAS simulation, a 3 or 4 parameter model is preferred. When fitting very extreme scenarios, such as Illustris or Horizon no-AGN, a model with at least 4 parameters is required. Most of the BAHAMAS simulations, our fiducial suite, seem to prefer a 2-parameters model, where both the gas fraction retained in haloes, M_{c}, and the AGN feedback range, η, are varied. However, the η best-fitting values for the BAHAMAS are broadly consistent between the different simulations of the suite, being their mean and standard deviation $\bar{\eta}(z = 0) = 0.51 \pm 0.06$ and $\bar{\eta}(z = 1) = 0.38 \pm 0.09$, whereas taking into account all the 74 hydrodynamical simulations we obtain $\bar{\eta}(z = 0) = 0.63 \pm 0.23$ and $\bar{\eta}(z = 1) = 0.47 \pm 0.42$. Therefore, it is possible that a 2-parameter model is favoured because in the 1-parameter model we have fixed η to a large value, incompatible with the BAHAMAS suite. We confirm this hypothesis by running again our MCMC chains, this time using in the baseline model the mean of the best-fitting parameters in the BAHAMAS simulations. As expected, in this case, the AIC for the BAHAMAS suite largely favours the 1-parameter model, where only $M_{\rm c}$ is varied. Specifically, only two simulations prefer a model with more than 1 free parameters on a total of 16.[10] We note that by varying just one parameter, the baryonic suppression measured in all the BAHAMAS simulations is reproduced at 1%, except for the case that features the most extreme AGN feedback, BAHAMAS high-AGN, which has an accuracy of 3%. We conclude that, considering only our fiducial suite of simulations, the BAHAMAS, only one free parameter is enough to fairly describe the baryonic effects on the power spectrum at a given redshift. However, by adding an additional parameter we can accurately reproduce most of the 74 hydrodynamical simulations here considered, whereas in a few extreme cases more parameters are required. This finding is particularly interesting, since with upcoming observations of the gas distribution, from e.g. SZ or X datasets, it will be likely possible to put tighter constraints on baryonic parameters such as $M_{\rm c}$ or η.

5.6 Summary and Conclusions

In this chapter, we have built and validated a 15-dimensional emulator of the baryonic "boost factor", that is the baryonic to gravity-only ratio in the non-linear matter power spectrum, for scales $0.01 < k < 5h\,{\rm Mpc}^{-1}$, and redshifts $0 < z < 1.5$.

Specifically, we considered 8 cosmological parameters – 5 standard ΛCDM parameters plus massive neutrinos and dynamical dark energy – and 7 baryonic parameters. The baryonic parameters are physically motivated and describe the gas fraction retained in haloes, AGN feedback strength, characteristic galaxy mass and the dependence of gas fractions on halo mass. In our approach, cosmology and baryon physics are consistently treated, by exploiting a combination of cosmology rescaling and baryonification algorithms, within the framework described in Aricò et al. (2020b, 2021a).

The range in cosmological and baryonic parameters employed by our emulator is set to cover values currently allowed by observations and hydrodynamical simulations. The emulator, a feed-forward Neural Network composed by two hidden layers of 400 neurons each, is trained with $50,000$ power spectra which yields a nominal precision of 2-3$\%$ ($1-2\%$ from the baryonification plus cosmology rescaling and 1% from the emulation). This level of uncertainty, however, can decrease in future by adding further training spectra. We note that, when combined with the emulator of the non-linear matter power spectrum presented in Angulo et al. (2020), the two joined emulators are expected to deliver predictions accurate at $4-5\%$ level.

We have assessed the accuracy of our emulator by using a large suite of 74 state-of-the-art hydrodynamical simulations and their gravity-only corresponding counterparts, taken from

---

[10] One simulation prefers a 2-parameters model, but the difference in AIC with the 1-parameter model is only ≈ 2.

the BAHAMAS, Cosmo-OWLS, OWLS, Illustris-TNG, EAGLE, Illustris, and Horizon suites. It is noteworthy that all (but the two most-extreme C-OWLS simulations) data at $z = 0$ and $z = 1$ are reproduced within the accuracy of the emulator precision.

By using our emulator, we have shown that cosmology impacts the baryonic processes mainly through the cosmic baryon fraction, $\Omega_\mathrm{b}/\Omega_\mathrm{m}$, in agreement with Schneider et al. (2020). Additionally, we have found secondary dependences caused by modifications to the halo mass function, given for instance by the overall normalisation of the matter fluctuations amplitude, while the internal concentration of haloes, which are caused for example by different dark energy models, are negligible.

Finally, we have searched for a minimal set of free baryonification parameters. To do that, we have compared the ability of models with a different number of free parameters to reproduce the simulation power spectrum ratios. At a given redshift, just one parameter is enough to accurately span all the range of feedback predicted by the BAHAMAS simulations. This parameter, namely M_c, makes the trade-off between the quantity of gas retained in haloes and expelled by the AGN. We note that our approach naturally takes into account the redshift evolution of the halo mass function and concentration-mass relation. However, only the stellar parameters are redshift dependent, while the gas parameters, M_c included, are currently not. If not properly taken into account, this is expected to have a mild repercussion on the accuracy of the predictions across different redshifts.

Although the BAHAMAS suite is arguably the best proxy for baryonic effects in the real universe, as it was specifically calibrated using observed stellar and gas fractions in clusters, other simulation suites are also described relatively well with a single free parameter, although they prefer more complicated models.

We anticipate that this emulator will be a valuable tool in the exploitation of current and forthcoming weak lensing surveys.

Summary and Conclusions

In this thesis, we have developed an accurate and fast framework to model the three-dimensional distribution of the cosmic matter density field and its time evolution. We have run N-body simulations to reach the widest dynamical range allowed by modern supercomputers, and employed a state-of-the-art cosmology rescaling algorithm, to capture the cosmological dependence of the matter density field. Motivated by the systematic uncertainties which heavily affect ongoing weak lensing surveys, particular care has been devoted to gain physical insight on how different astrophysical processes impact the Large Scale Structure. To do so, we have implemented a baryon correction model, a hybrid technique that couples analytical prescriptions based on theoretical assumptions with numerical predictions given by simulations. To make our model fast enough to be directly used in parameter inference, we have used machine learning and built emulators of the power spectra measured in our simulations.

In §2, we have presented our main set of N-body simulations, constituted by 6 simulations of ≈ 2 Gpc and 3440^3 (≈ 80 billion) particles, run with 3 different cosmologies and "pair and fixed" initial conditions to suppress cosmic variance (Angulo and Pontzen, 2016). The cosmologies of the simulations have been chosen to minimise the error of the rescaling algorithm in a broad parameter range. The original cosmology rescaling algorithm (Angulo and White, 2010) has been updated to take into account of concentration-mass relation and non-universality of halo the mass function (Contreras et al., 2020a; Ondaro-Mallea et al., 2021), and extended to dynamical dark energy and massive neutrinos (Contreras et al., 2020a; Zennaro et al., 2019). In this way, the power spectrum of (gravitational-only) matter, haloes, and sub-haloes can be recovered at better than 2% accuracy within ΛCDM and 3% considering the extensions to massive neutrinos and dynamical dark energy, up to $k = 5\,h\,\mathrm{Mpc}^{-1}$, and the halo mass function at better than 2% up to $M = 5 \cdot 10^{14}\,h^{-1}\mathrm{M}_{\odot}$.

In §3 we have described our implementation of the Baryon Correction Model (BCM) algorithm (Schneider and Teyssier, 2015a). The idea is to displace the particles of a gravity-only N-body simulation, to take into account the non-gravitational effects that reshape the spatial distribution of different baryonic components. In our full model, these components are, specifically, central and satellite galaxies, and bound, ejected, and re-accreted gas onto haloes. Also the back-reaction on the dark matter caused by the baryon gravitational potential is taken into account. Once the density profiles of all these components are computed, the particles of the simulations are moved accordingly to the analytical predictions. The free parameters of our model (up to 8) can be constrained by observations or hydrodynamical simulations, and we have checked that our implementation is flexible enough to fit the density profiles of hydrodynamical simulations, e.g. the Illustris TNG.

Our numerical implementation is highly optimised, and one of the main speed-up factors is obtained neglecting the displacement fields of the particles initially outside of haloes, which follow closely the dark matter distribution.

We have tested our BCM against several state-of-the-art simulations: the baryonification is able to recover their power spectra within percent accuracy (Aricò et al., 2020b). When fitting the power spectrum, we recover the same anti-correlation between the fraction of baryons retained in haloes and the suppression in the power spectrum found in different hydrodynamical simulations (van Daalen et al., 2020). This is a hint that our model is correctly capturing the net mass flow induced by baryonic processes. Overall, our model suggests that galaxy formation increases the power at small scales, due to the presence of the bright central galaxies, whereas the contribution of satellite galaxies is negligible. The gas ejected by the accreting supermassive black holes at the center of galaxies can cause significant suppression of power up to large scales. The hot gas inside haloes has a modest impact on the clustering, whereas the dark matter is more concentrated at the center and flatter in the outskirts of the halo, due to the back-reaction caused by the central galaxy and ejected gas, respectively.

By using a Fisher matrix formalism, we have shown that there is a wealth of cosmological information lying on small scales ($k \geq 1h\,\mathrm{Mpc}^{-1}$) in the power spectrum. Unfortunately, by marginalising over the baryonic parameters, we expect a mild degradation of the constraining power in cosmology, up to a factor of 4, depending on the parameter considered.

To maximise the information that can be extracted, we can go to higher-order statistics than 2-point. In fact, baryonic processes impact differently the 2-point and 3-point statistics, and thus going to higher-order can help to break degeneracies between parameters (Semboloni et al., 2013). Motivated by this, in §4 we have studied the predictions of the bispectrum made by baryonification. We have found that baryonification can reproduce the power spectrum and bispectrum of several state-of-the-art cosmological hydrodynamical simulations at better than 3% up to $k = 5\,h\,\mathrm{Mpc}^{-1}$. Interestingly, we find a tight anti-correlation between baryon fractions inside haloes and baryonic effects on the bispectrum, similarly to what was previously found with power spectra. Finding such correlations, which link a direct observable to the matter clustering, paves the way to minimal phenomenological models which could be used up to higher-order statistics.

Thanks to the heavy optimisations involved, the process of scaling cosmology, baryonification, and measurement of the power spectrum of a simulation takes only up to few minutes, depending on the size of the simulation. Nevertheless, this could be the main limitation when doing parameter inference analysis: a standard MCMC can require hundreds of thousands of evaluations of a model, depending on the number of free parameters.

To get around the computational cost of the model, we have used emulators, which are interpolators of a (costly) function defined in a given hyper-parameter space. By evaluating the function in such a way to cover evenly the hyper-volume, the emulator provides quick and accurate predictions in the whole parameter space. A possible approach could be, for instance, to emulate the likelihood function, which in cosmology applications is usually Gaussian, and thus well captured by Gaussian Processes (see e.g. Pellejero-Ibañez et al., 2020). Here, we have followed a more flexible approach, emulating directly the model predictions, to be able to apply the same emulators to different data sets. The emulation has been performed by using machine learning, and specifically Gaussian Processes and artificial neural networks. We have found that the latter ones should be preferred when using large training sets, given their computational and memory requirements.

In this way, the hundreds of Terabytes contained in our simulations data are compressed in a model of only a few Megabytes, that can be downloaded and used in a couple of lines in Python. Moreover, the artificial neural network scheme that we have used to build our emulators allows evaluating multiples models in the order of a millisecond, when running on a single core of a common laptop. Overall, the error introduced in the emulation is subdominant compared to other sources of errors in the modelling.

For convenience, we have split the full power spectrum measured in our post-processed simulations into three different parts: linear, non-linear, and baryonic contributions.

In §1 we have used about 160,000 spectra computed with the Boltzmann code `CLASS` (Lesgourgues, 2011a), to build a neural network emulator for the linear matter power spectrum. We have shown that its accuracy is better than 0.3% and that it is compatible with the statistical requirements of stage IV weak lensing surveys (Aricò et al., 2021b);

In §2 we have presented our Gaussian Process emulator of the non-linear matter power spectrum "boost factor", that is the non-linear to linear ratio. We obtained it by scaling the cosmology of our main simulations to 800 different cosmologies, finding a percent level accuracy (Angulo et al., 2020) in the emulation. We have also built a version of this emulator with artificial neural networks.

In §5 we have built a neural network emulator of the baryonic boost factor, that is the baryonic to non-linear ratio. This emulator depends on 15 parameters, 8 relative to cosmology (included massive neutrinos and dynamical dark energy) and 7 to astrophysical processes. We have tested our emulator against 74 different state-of-the-art cosmological hydrodynamical simulations, including OWLS, Illustris, Horizon, Cosmo-OWLS, EAGLE, BAHAMAS, Illustris-TNG, presented in Schaye et al. (2010); Vogelsberger et al. (2014b); Dubois et al. (2014); Le Brun et al. (2014); Schaye et al. (2015); McCarthy et al. (2017); Pillepich et al. (2018). These simulations are very different for hydrodynamical solvers, sub-grid physics implementations, cosmology, and initial conditions. Nonetheless, our emulator is able to fit all their baryonic boost factors at percent accuracy, while providing predictions in a few milliseconds (Aricò et al., 2020a). Exploiting the speed and flexibility of this emulator, we have shown that cosmology impacts the baryonic processes mainly through the cosmic baryon fraction, $\Omega_{\rm b}/\Omega_{\rm m}$, in agreement with what was found in Schneider et al. (2020). Additionally, we have found secondary dependencies caused by modifications to the halo mass function, given e.g. by the overall normalisation of the matter fluctuations amplitude. On the contrary, the internal concentration of haloes, which are caused for example by different dark energy models, are negligible.

Finally, we have searched for a minimal set of free baryonification parameters. To do that, we have compared the ability of models with a different number of free parameters to reproduce the predictions from hydrodynamical simulations, using the Akaike Information Creterion (AIC). This criterion minimises the information loss of a model given some data. We have found that, at a given redshift, just one free parameter is enough to accurately span all the range of feedback predicted by the BAHAMAS simulations. This parameter, namely $M_{\rm c}$, makes the trade-off between the quantity of gas retained in haloes and expelled by feedback processes e.g. supernovae and accretion onto supermassive black holes.

In the upcoming years, missions e.g. Euclid[11], LSST[12], and the Roman Space Telescope[13], plan to shed light on some of the biggest mysteries in modern physics, the nature of dark energy and dark matter. Among the cosmological probes included in these experiments, e.g. supernovae and Baryonic Acoustic Oscillations (BAO), weak gravitational lensing will have a key role, because of its unique sensitivity to the dark matter field and growth of structures. In this context, we expect the techniques and results presented here to be highly valuable. In fact, including astrophysical and hydrodynamical processes will be paramount for a correct interpretation of the data, and to avoid a biased inference of the relevant

---

[11] `https://www.euclid-ec.org/`

[12] `https://www.lsst.org/`

[13] `https://roman.gsfc.nasa.gov/`

cosmological parameters. Additionally, it could provide precious information on poorly understood baryonic physics, for example on the feedback from supermassive black holes accreting gas at the center of galaxies.

The framework developed in this thesis provides a powerful tool for the exploitation of ongoing and future LSS surveys, because of its accuracy, speed, range of validity, and flexibility. The three-dimensional nature of our approach opens up to analyses of different statistics, including cosmological and baryonic dependencies. For instance, one could investigate how astrophysical processes impact the halo mass function, and therefore the galaxy clusters count, or build lightcones to have convergence maps varying different baryonic scenarios.
We have made publicly available at this url[14] three emulators with the linear, non-linear, and baryonic contribution to the matter power spectrum, indispensable to compute the cosmic shear and galaxy-galaxy lensing correlation functions. When combined all together, our emulators can provide predictions accurate at better than 5%, in a large cosmological parameter space, about 10σ around Planck best-fitting parameters (Contreras et al., 2020a; Planck Collaboration et al., 2018), on scales of $0.001 \leq k/(h\,\mathrm{Mpc}^{-1}) \leq 5$ and redshifts $z \leq 1.5$. We note that the majority of statistical power of a stage IV survey is expected to be at $z \approx 1$ and $1 \leq k/(h\,\mathrm{Mpc}^{-1}) \leq 7$ (Taylor et al., 2018b), and therefore it should be fairly captured by our emulators. Nevertheless, we plan to keep updating the training set of our emulators, to increase their accuracy and expand their scale and redshift ranges.

The work done so far opens up to many different applications and follow-up projects:

- Applying the neural network emulators to current weak lensing data. A dataset e.g. DES Collaboration et al. (2021), covering 5,000 square degrees of the sky, has potentially the statistical power to constrain astrophysical processes e.g. AGN feedback from supermassive black holes;

- Joining Sub-Halo Abundance Matching (SHAM) methods with baryonification and cosmology rescaling algorithms. A self-consistent modelling of galaxy and gas distributions, where the BCM is informed by the SHAM, would provide an accurate method for cross-correlations up to small scales. This would benefits analyses like the 3x2pt, i.e. cosmic shear, galaxy clustering and galaxy-galaxy lensing;

- Extending the baryonification to other hydrodynamical properties than density, e.g. pressure (thermal and non-thermal) and temperature. By doing so, it would be possible to predict thermal Sunyaev-Zel'dovich power spectra, and including to generate fast Compton-y and X-rays maps.

---

[14] `https://bitbucket.org/rangulo/baccoemu/`

- Extending the rescaling algorithm to modified gravity models, and investigate the interplay with baryonic effects;
- Studying the degeneracy between the effects of baryons and massive neutrinos on the LSS clustering;
- Investigating the time dependence of the baryonic effects, seeking for a physically-motivated parametrisation;
- Investigating and modelling the baryonic effects on the LSS velocity field. Such studies can be helpful to model the kinetic Sunyaev-Zel'dovich effect;

Future extensions of this framework could constrain simultaneously cosmology and astrophysics, by using cross-correlations of different fields, from galaxy to matter (given by the cosmic shear) and gas pressure (given by the thermal Sunyaev-Zel'dovich), while being robust to the systematics relative to each individual field. As the accuracy of the observations increases, so should our theoretical modelling, while being physically interpretable and flexible enough to explore all the viable scenarios.

Resumen y Conclusiones

En esta tesis, hemos desarrollado un marco preciso y rápido para modelar la distribución tridimensional del campo de densidad de la materia cósmica y su evolución temporal. Hemos realizado simulaciones de N-cuerpos para alcanzar el rango dinámico más amplio que permiten los superordenadores modernos, y hemos empleado un algoritmo de reescalado cosmológico de última generación, para capturar la dependencia cosmológica del campo de densidad de la materia. Motivado por las incertidumbres sistemáticas que afectan en gran medida a los estudios de lentes débiles en curso, se ha prestado especial atención a obtener una visión física sobre cómo los diferentes procesos astrofísicos afectan a la Estructura a Gran Escala. Para ello, hemos implementado un modelo de corrección bariónica, una técnica híbrida que combina prescripciones analíticas basadas en teóricas con predicciones numéricas dadas por las simulaciones. Para que nuestro modelo sea lo suficientemente rápido como para ser utilizado directamente en la inferencia de parámetros, hemos utilizado el aprendizaje automático y hemos construido emuladores de los espectros de potencia medidos en nuestras simulaciones.

En §2, hemos presentado nuestro conjunto principal de simulaciones de N-cuerpos, constituido por 6 simulaciones de $\approx$ 2 Gpc y 3440^3 (≈ 80 miles de millones) de partículas, ejecutadas con 3 cosmologías diferentes y " *paired and fixed*" condiciones iniciales para suprimir la varianza cósmica (Angulo and Pontzen, 2016). Las cosmologías de las simulaciones se han elegido para minimizar el error del algoritmo de reescalado en un amplio rango de parámetros. El algoritmo original de reescalado cosmológico (Angulo and White, 2010) se ha actualizado para tener en cuenta la relación concentración-masa y la no universalidad de la función de masa de los halos (Contreras et al., 2020a; Ondaro-Mallea et al., 2021), y se ha extendido a la energía oscura dinámica y a los neutrinos masivos (Contreras et al., 2020a; Zennaro et al., 2019). De este modo, el espectro de potencia de la materia (sólo gravitacional), de los halos y de los subhalos puede recuperarse con una precisión mejor del 2% dentro de ΛCDM y del 3% considerando las extensiones a los neutrinos masivos y a la energía oscura dinámica, hasta $k = 5h\,\mathrm{Mpc}^{-1}$, y la función de masa del halo con una precisión mejor del 2% hasta $M = 5 \cdot 10^{14} h^{-1}\mathrm{M}_{\odot}$.

En §3 hemos descrito nuestra implementación del algoritmo de corrección barionica (BCM) (Schneider and Teyssier, 2015a). La idea es desplazar las partículas de una simulación de N-cuerpos sólo gravitacional, para tener en cuenta los efectos no gravitacionales que remodelan la distribución espacial de los diferentes componentes bariónicos. En nuestro modelo completo, estos componentes son, en concreto, las galaxias centrales y satélites, y el gas vinculado, expulsado y re-acreditado en los halos. También se tiene en cuenta la reacción a posteriori de la materia oscura causada por el potencial gravitatorio de los bariones. Una vez calculados los perfiles de densidad de todos estos componentes, las partículas de las simulaciones se desplazan de acuerdo con las predicciones analíticas. Los parámetros libres de nuestro modelo (hasta 8) pueden ser restringidos por observaciones o simulaciones hidrodinámicas, y hemos comprobado que nuestra implementación es lo suficientemente flexible como para ajustarse a los perfiles de densidad de las simulaciones hidrodinámicas, por ejemplo el Illustris-TNG.

Nuestra implementación numérica está altamente optimizada, y uno de los principales factores de aceleración se obtiene no considerando los campos de desplazamiento de las partículas inicialmente fuera de los halos, que siguen de cerca la distribución de la materia oscura.

Hemos comparado nuestro BCM con varias simulaciones del estado del arte: la barionificación es capaz de recuperar sus espectros de potencia con una precisión porcentual (Aricò et al., 2020b). Al ajustar el espectro de potencia, recuperamos la misma anticorrelación entre la fracción de bariones retenidos en los halos y la supresión en el espectro de potencia encontrada en diferentes simulaciones hidrodinámicas (van Daalen et al., 2020). Esto es un indicio de que nuestro modelo capta correctamente el flujo de masa neto inducido por los procesos bariónicos. En general, nuestro modelo sugiere que la formación de galaxias aumenta la potencia a escalas pequeñas, debido a la presencia de las galaxias centrales, mientras que la contribución de las galaxias satélites es insignificante. El gas expulsado por los agujeros negros supermasivos en acreción en el centro de las galaxias puede causar una supresión significativa de la potencia hasta escalas grandes. El gas caliente en el interior de los halos tiene un impacto modesto en la agrupación, mientras que la materia oscura está más concentrada en el centro y más plana en las afueras del halo, debido a la reacción a posteriori causada por la galaxia central y el gas expulsado, respectivamente.

Utilizando un formalismo matricial de Fisher, hemos demostrado que existe una gran cantidad de información cosmológica en escalas pequeñas ($k \geq 1h\,\mathrm{Mpc}^{-1}$) en el espectro de potencia. Desafortunadamente, al marginar sobre los parámetros bariónicos, esperamos una leve degradación del poder de restricción en cosmología, hasta un factor de 4, dependiendo del parámetro considerado.

Para maximizar la información que se puede extraer, podemos ir a estadísticas de orden más alto que las de 2 puntos. De hecho, los procesos bariónicos impactan de forma diferente en las estadísticas de 2 puntos y 3 puntos, por lo que ir a un orden superior puede ayudar a romper las degeneraciones entre parámetros (Semboloni et al., 2013). Motivados por esto, en §4 hemos estudiado las predicciones del biespectro realizadas por barionificación. Hemos encontrado que la barionificación puede reproducir el espectro de potencia y el biespectro de varias simulaciones hidrodinámicas cosmológicas de última generación a un nivel mejor que 3% hasta $k = 5h\,\mathrm{Mpc}^{-1}$. Curiosamente, encontramos una estrecha anticorrelación entre las fracciones de bariones en el interior de los halos y los efectos bariónicos en el biespectro, de forma similar a lo encontrado anteriormente con los espectros de potencia. El hallazgo de tales correlaciones, que vinculan un observable directo con la agrupación de la materia, allana el camino hacia modelos fenomenológicos mínimos que podrían utilizarse hasta estadísticas de orden superior.

Gracias a las optimizaciones implicadas, el proceso de escalado de la cosmología, la barionización y la medición del espectro de potencia de una simulación sólo lleva unos minutos, dependiendo del tamaño de la simulación. Sin embargo, esta podría ser la principal limitación a la hora de realizar el análisis de inferencia de parámetros: un MCMC estándar puede requerir cientos de miles de evaluaciones de un modelo, dependiendo del número de parámetros libres.

Para sortear el coste computacional del modelo, hemos utilizado emuladores, que son interpoladores de una función (costosa) definida en un espacio hiperparamétrico dado. Evaluando la función de forma que cubra uniformemente el hipervolumen, el emulador proporciona predicciones rápidas y precisas en todo el espacio de parámetros. Un posible enfoque podría ser, por ejemplo, emular la función de verosimilitud, que en las aplicaciones de cosmología suele ser gaussiana, y por tanto bien capturada por los procesos gaussianos (véase por ejemplo Pellejero-Ibañez et al., 2020). Aquí hemos seguido un enfoque más flexible, emulando directamente las predicciones del modelo, para poder aplicar los mismos emuladores a diferentes conjuntos de datos. La emulación se ha realizado utilizando el aprendizaje automático, y en concreto los procesos gaussianos y las redes neuronales artificiales. Hemos comprobado que estas últimas son preferibles cuando se utilizan grandes conjuntos de entrenamiento, dados sus requerimientos computacionales y de memoria.

De este modo, los cientos de Terabytes que contienen los datos de nuestras simulaciones se comprimen en un modelo de sólo unos pocos Megabytes, que puede ser descargado y utilizado en un par de líneas en Python. Además, el esquema de red neuronal artificial que hemos utilizado para construir nuestros emuladores permite evaluar múltiples modelos en el orden de un milisegundo, cuando se ejecuta en un solo núcleo de un ordenador portátil común. En general, el error introducido en la emulación es subdominante en comparación con otras fuentes de error en la modelización.

Por comodidad, hemos dividido el espectro de potencia completo medido en nuestras simulaciones posprocesadas en tres partes diferentes: contribuciones lineales, no lineales y bariónicas.

En §1 hemos utilizado unos 160.000 espectros calculados con el código Boltzmann `CLASS` (Lesgourgues, 2011a), para construir un emulador de red neuronal para el espectro de potencia de la materia lineal. Hemos demostrado que su precisión es mejor que 0,3% y que es compatible con los requisitos estadísticos de los estudios de lentes débiles de la fase IV (Aricò et al., 2021b);

En §2 hemos presentado nuestro emulador de Proceso Gaussiano del espectro de potencia de la materia, y específicamente la fracción entre esoectro no lineal y lineal. Lo hemos obtenido escalando la cosmología de nuestras simulaciones principales a 800 cosmologías diferentes, encontrando una precisión de nivel porcentual (Angulo et al., 2020) en la emulación. También hemos construido una versión de este emulador con redes neuronales artificiales.

En §5 hemos construido un emulador con redes neuronales del factor bariónico, es decir, la fracción entre espectro con efectos bariónicos y no lineal. Este emulador depende de 15 parámetros, 8 relativos a la cosmología (incluyendo neutrinos masivos y energía oscura dinámica) y 7 a procesos astrofísicos. Hemos probado nuestro emulador contra 74 simulaciones hidrodinámicas cosmológicas diferentes, incluyendo OWLS, Illustris, Horizon, Cosmo-OWLS, EAGLE, BAHAMAS, Illustris-TNG, presentadas en Schaye et al. (2010); Vogelsberger et al. (2014b); Dubois et al. (2014); Le Brun et al. (2014); Schaye et al. (2015); McCarthy et al. (2017); Pillepich et al. (2018). Estas simulaciones son muy diferentes en lo que respecta a los solucionadores hidrodinámicos, las implementaciones de la física de subgrilla, la cosmología y las condiciones iniciales. Sin embargo, nuestro emulador es capaz de ajustarse a todos sus factores bariónicos con un porcentaje de precisión, mientras que proporciona predicciones en unos pocos milisegundos (Aricò et al., 2020a).

Aprovechando la velocidad y la flexibilidad de este emulador, hemos demostrado que la cosmología afecta a los procesos bariónicos principalmente a través de la fracción cósmica de bariones, $\Omega_{\rm b}/\Omega_{\rm m}$, de acuerdo con lo encontrado en Schneider et al. (2020). Además, hemos encontrado dependencias secundarias causadas por modificaciones en la función de masa de los halos, dadas, por ejemplo, por la normalización global de la amplitud de las fluctuaciones de la materia. Por el contrario, la concentración interna de los halos, causada por ejemplo por diferentes modelos de energía oscura, es inapreciable.

Por último, hemos buscado un conjunto mínimo de parámetros libres de la barionización.

Para ello, hemos comparado la capacidad de los modelos con un número diferente de parámetros libres para reproducir las predicciones de las simulaciones hidrodinámicas, utilizando el criterio Akaike Information Creterion (AIC). Este criterio minimiza la pérdida de información de un modelo dados unos datos. Hemos descubierto que, a un desplazamiento al rojo determinado, basta con un solo parámetro libre para abarcar con precisión todo el rango de retroalimentación predicho por las simulaciones de BAHAMAS. Este parámetro, M_c, hace que el compromiso entre la cantidad de gas retenida en los halos y la expulsada por los procesos de retroalimentación, como las supernovas y la acreción a los agujeros negros supermasivos.

En los próximos años, misiones e.g. Euclid[15], LSST[16], y Roman Space Telescope[17], planean descubrimientos sobre algunos de los mayores misterios de la física moderna, la naturaleza de la energía oscura y la materia oscura. Entre las sondas cosmológicas incluidas en estos experimentos, por ejemplo las supernovas y las BAO, las lentes gravitacionales débiles tendrán un papel clave, debido a su sensibilidad única al campo de la materia oscura y al crecimiento de las estructuras. En este contexto, nos esperamos que las técnicas y los resultados presentados aquí sean muy valiosos. De hecho, incluir los procesos astrofísicos e hidrodinámicos será muy importante para una correcta interpretación de los datos, y para evitar una inferencia incorrecta de los parámetros cosmológicos relevantes. Además, podría proporcionar información valiosa sobre la poco conocida física bariónica, por ejemplo, sobre la retroalimentación de los agujeros negros supermasivos que acrecionan gas en el centro de las galaxias.

El marco desarrollado en esta tesis proporciona una poderosa herramienta para la explotación de los estudios actuales y futuros, debido a su precisión, velocidad, rango de validez y flexibilidad. La naturaleza tridimensional de nuestro enfoque se abre a los análisis de diferentes estadísticas, incluyendo las dependencias cosmológicas y bariónicas. Por ejemplo, se podría investigar cómo los procesos astrofísicos afectan a la función de masa del halo y, por tanto, al recuento de cúmulos de galaxias, o construir conos de luz para tener mapas de convergencia que varíen diferentes escenarios bariónicos.

Hemos puesto a disposición del público en esta url[18] tres emuladores con la contribución lineal, no lineal y bariónica al espectro de potencia de la materia, indispensables para calcular las funciones de correlación de esquilado cósmico y de lentes galaxia-galaxia. Cuando se combinan todos juntos, nuestros emuladores pueden proporcionar predicciones precisas con

---

[15] `https://www.euclid-ec.org/`

[16] `https://www.lsst.org/`

[17] `https://roman.gsfc.nasa.gov/`

[18] `https://bitbucket.org/rangulo/baccoemu/`

más del 5%, en un gran espacio de parámetros cosmológicos, alrededor de 10σ alrededor de los parámetros de mejor ajuste de Planck (Contreras et al., 2020a; Planck Collaboration et al., 2018), en escalas de $0.001 \leq k/(ihMpc) \leq 5$ y corrimientos al rojo $z \leq 1.5$. Observamos que la mayor parte de la potencia estadística de un sondeo de fase IV se espera que esté en $z \approx 1$ y $1 \leq k/(h\,\mathrm{Mpc}^{-1}) \leq 7$ (Taylor et al., 2018b), y por lo tanto debería ser bastante captada por nuestros emuladores. No obstante, tenemos previsto seguir actualizando el conjunto de entrenamiento de nuestros emuladores, para aumentar su precisión y ampliar sus rangos de escala y desplazamiento al rojo.

El trabajo realizado hasta ahora se abre a muchas aplicaciones diferentes y proyectos de seguimiento:

- Aplicar los emuladores de redes neuronales a los datos actuales de lentes débiles. Un conjunto de datos, por ejemplo, DES Collaboration et al. (2021), que cubre 5.000 grados cuadrados del cielo, tiene potencialmente el poder estadístico para restringir los procesos astrofísicos, por ejemplo AGN la retroalimentación de los agujeros negros supermasivos;

- La unión de los métodos de Sub-Halo Abundance Matching (SHAM) con los algoritmos de barionificación y reescalado de la cosmología. Una modelización autoconsistente de las distribuciones de galaxias y de gas, en la que el BCM es informado por el SHAM, proporcionaría un método preciso para las correlaciones cruzadas hasta escalas pequeñas. Esto beneficiaría a análisis como el 3x2pt, es decir, la cizalla cósmica, la agrupación de galaxias y las lentes galaxia-galaxia;

- Ampliar la barionización a otras propiedades hidrodinámicas distintas de la densidad, por ejemplo, la presión (térmica y no térmica) y la temperatura.

  Al hacerlo, sería posible predecir los espectros de potencia de Sunyaev-Zel'dovich térmico, e incluso generar mapas rápidos de Compton-y y rayos X.

- Extender el algoritmo de reescalado a los modelos de gravedad modificados, e investigar la interacción con los efectos bariónicos;

- Estudiar la degeneración entre los efectos de los bariones y los neutrinos masivos;

- Investigar la dependencia temporal de los efectos bariónicos, buscando una parametrización motivada físicamente;

- Investigar y modelar los efectos bariónicos en el campo de velocidad. Estos estudios pueden ser útiles para modelar el efecto Sunyaev-Zel'dovich cinético;

Las futuras extensiones de este marco podrían restringir simultáneamente la cosmología y la astrofísica, mediante el uso de correlaciones cruzadas de diferentes campos, desde la galaxia hasta la materia (dada por el esquilado cósmico) y la presión del gas (dada por el Sunyaev-Zel'dovich térmico), siendo al mismo tiempo robustos a la sistemática relativa a cada campo individual. A medida que aumente la precisión de las observaciones, también debería hacerlo nuestro modelo teórico, siendo al mismo tiempo físicamente interpretable y lo suficientemente flexible como para explorar todos los escenarios viables.

Data Availability

All our Neural Network emulators are publicly available at `http://www.dipc.org/bacco`, or equivantly at the `github` repository `https://bitbucket.org/rangulo/baccoemu/`.

Our Particle Swarm Optimisation algorithm is publicly available at `https://github.com/hantke/pso_bacco`.

The Boltmann solver we have used, `CLASS` (Lesgourgues, 2011a), is available at `https://lesgourg.github.io/class_public/class.html`.

The code we have used to measure the bispectrum in our simulations, `bskit` (Foreman et al., 2020), is available at `https://github.com/sjforeman/bskit`.

The measurements of the power spectra and bispectra of the BAHAMAS, EAGLE, Illustris, and Illustris TNG simulations are available at `https://github.com/sjforeman/hydro_bispectrum` (Foreman et al., 2020).

The measurements of the power spectra of the hydrodynamical and gravity-only runs of the BAHAMAS, Cosmo-OWLS and OWLS simulations are available at `http://powerlib.strw.leidenuniv.nl/` (van Daalen et al., 2020).

Other data underlying this thesis will be shared on reasonable request.

Acknowledgements

We acknowledge the support of the E.R.C. starting grant 716151 (BACCO), and the computer resources at MareNostrum and the technical support provided by Barcelona Supercomputing Center (RES-AECT-2019-2-0012, RES-AECT-2020-3-0014).

We thank Elisa Chisari, Wojtek Hellwing, Volker Springel, Marcel van Daalen, Mark Vogelsberger, and Simon Foreman, for kindly making various simulation data available to us. We acknowledge the Illustris, Illustris TNG, BAHAMAS, OWLS, Cosmo-OWLS, Horizon, and EAGLE teams, for providing/making public the data of their hydrodynamical simulations.

We thank Björn Malte-Schaefer, Marcel van Daalen, Wojtek Hellwing, Alex Barreira, Simon Foreman, Jonás Chaves-Montero, Angela Chen, Dragan Huterer, Ian McCarthy, and the anonymous referees of the papers upon which this thesis is based, for the careful reading and the useful comments they provided on our manuscripts. We acknowledge the hospitality of the Max Planck Institute for Astrophysics in Garching, where the final part of this work was carried out, and Louis Legrand for pointing out a useful function in the Fisher analysis.

This thesis would not exists without the paramount contributions of my colleagues and coauthors: Raul Angulo, Carlos Hernández-Monteagudo, Matteo Zennaro, Sergio Contreras, Marcos Pellejero Ibañez, Lurdes Ondaro Mallea, Yetli Rosas-Guevara, and Jens Stücker.

I specially thank my supervisors, Raul Angulo and Carlos Hernández-Monteagudo, for guiding me in these four years of research, and my tutor, Theopisti Dafni, for being a great reference at the University of Zaragoza.

I warmly thank Silvia Bonoli, Elisa Chisari, Martin Crocce, Joachim Harnois-Deraps, and Ian McCarthy, to kindly accept to be members of my PhD Committee.

Thanks a lot to David Izquierdo-Villalba, Daniele Spinoso, and Rafael Logroño-García, UniZar fellows without whom I probably would have not get a single deadline of the university.

Finally, I would like to thank my colleagues at DIPC and CEFCA, and among them Siddharta, Gonzalo, Jonas, Silvia, Daniel, Rodrigo, Iñigo, Sara, Carmelo, Chiara, Francisco, Matteo, and all the others, for the nice time spent together.

Bibliography

Abadi, M., Barham, P., Chen, J., Chen, Z., Davis, A., Dean, J., Devin, M., Ghemawat, S., Irving, G., Isard, M., et al. (2016). Tensorflow: A system for large-scale machine learning. In *12th {USENIX} Symposium on Operating Systems Design and Implementation ({OSDI} 16)*, pages 265–283.

Abadi, M. G., Navarro, J. F., Fardal, M., Babul, A., and Steinmetz, M. (2010). Galaxy-induced transformation of dark matter haloes. *Monthly Notices of the Royal Astronomical Society*, 407:435–446.

Aihara, H., Arimoto, N., Armstrong, R., Arnouts, S., Bahcall, N. A., Bickerton, S., Bosch, J., Bundy, K., Capak, P. L., Chan, J. H. H., Chiba, M., Coupon, J., Egami, E., Enoki, M., Finet, F., Fujimori, H., Fujimoto, S., Furusawa, H., Furusawa, J., Goto, T., Goulding, A., Greco, J. P., Greene, J. E., Gunn, J. E., Hamana, T., Harikane, Y., Hashimoto, Y., Hattori, T., Hayashi, M., Hayashi, Y., Hełminiak, K. G., Higuchi, R., Hikage, C., Ho, P. T. P., Hsieh, B.-C., Huang, K., Huang, S., Ikeda, H., Imanishi, M., Inoue, A. K., Iwasawa, K., Iwata, I., Jaelani, A. T., Jian, H.-Y., Kamata, Y., Karoji, H., Kashikawa, N., Katayama, N., Kawanomoto, S., Kayo, I., Koda, J., Koike, M., Kojima, T., Komiyama, Y., Konno, A., Koshida, S., Koyama, Y., Kusakabe, H., Leauthaud, A., Lee, C.-H., Lin, L., Lin, Y.-T., Lupton, R. H., Mand elbaum, R., Matsuoka, Y., Medezinski, E., Mineo, S., Miyama, S., Miyatake, H., Miyazaki, S., Momose, R., More, A., More, S., Moritani, Y., Moriya, T. J., Morokuma, T., Mukae, S., Murata, R., Murayama, H., Nagao, T., Nakata, F., Niida, M., Niikura, H., Nishizawa, A. J., Obuchi, Y., Oguri, M., Oishi, Y., Okabe, N., Okamoto, S., Okura, Y., Ono, Y., Onodera, M., Onoue, M., Osato, K., Ouchi, M., Price, P. A., Pyo, T.-S., Sako, M., Sawicki, M., Shibuya, T., Shimasaku, K., Shimono, A., Shirasaki, M., Silverman, J. D., Simet, M., Speagle, J., Spergel, D. N., Strauss, M. A., Sugahara, Y., Sugiyama, N., Suto, Y., Suyu, S. H., Suzuki, N., Tait, P. J., Takada, M., Takata, T., Tamura, N., Tanaka, M. M., Tanaka, M., Tanaka, M., Tanaka, Y., Terai, T., Terashima, Y., Toba, Y., Tominaga, N., Toshikawa, J., Turner, E. L., Uchida, T., Uchiyama, H., Umetsu, K., Uraguchi, F., Urata, Y., Usuda, T., Utsumi, Y., Wang, S.-Y., Wang, W.-H., Wong, K. C., Yabe, K., Yamada, Y., Yamanoi, H., Yasuda, N., Yeh, S., Yonehara, A., and Yuma, S.

(2018). The Hyper Suprime-Cam SSP Survey: Overview and survey design. *Publications of the ASJ*, 70:S4.

Akaike, H. (1974). A New Look at the Statistical Model Identification. *IEEE Transactions on Automatic Control*, 19:716–723.

Alam, S., Ata, M., Bailey, S., Beutler, F., Bizyaev, D., Blazek, J. A., Bolton, A. S., Brownstein, J. R., Burden, A., Chuang, C.-H., Comparat, J., Cuesta, A. J., Dawson, K. S., Eisenstein, D. J., Escoffier, S., Gil-Marín, H., Grieb, J. N., Hand, N., Ho, S., Kinemuchi, K., Kirkby, D., Kitaura, F., Malanushenko, E., Malanushenko, V., Maraston, C., McBride, C. K., Nichol, R. C., Olmstead, M. D., Oravetz, D., Padmanabhan, N., Palanque-Delabrouille, N., Pan, K., Pellejero-Ibanez, M., Percival, W. J., Petitjean, P., Prada, F., Price-Whelan, A. M., Reid, B. A., Rodríguez-Torres, S. A., Roe, N. A., Ross, A. J., Ross, N. P., Rossi, G., Rubiño-Martín, J. A., Saito, S., Salazar-Albornoz, S., Samushia, L., Sánchez, A. G., Satpathy, S., Schlegel, D. J., Schneider, D. P., Scóccola, C. G., Seo, H.-J., Sheldon, E. S., Simmons, A., Slosar, A., Strauss, M. A., Swanson, M. E. C., Thomas, D., Tinker, J. L., Tojeiro, R., Magaña, M. V., Vazquez, J. A., Verde, L., Wake, D. A., Wang, Y., Weinberg, D. H., White, M., Wood-Vasey, W. M., Yèche, C., Zehavi, I., Zhai, Z., and Zhao, G.-B. (2017). The clustering of galaxies in the completed SDSS-III Baryon Oscillation Spectroscopic Survey: cosmological analysis of the DR12 galaxy sample. *Monthly Notices of the Royal Astronomical Society*, 470(3):2617–2652.

Albers, J., Fidler, C., Lesgourgues, J., Schöneberg, N., and Torrado, J. (2019). CosmicNet. Part I. Physics-driven implementation of neural networks within Einstein-Boltzmann Solvers. *Journal of Cosmology and Astroparticle Physics*, 2019(9):028.

Ali-Haïmoud, Y. and Bird, S. (2013). An efficient implementation of massive neutrinos in non-linear structure formation simulations. *Monthly Notices of the Royal Astronomical Society*, 428(4):3375–3389.

Amendola, L., Appleby, S., Avgoustidis, A., Bacon, D., Baker, T., Baldi, M., Bartolo, N., Blanchard, A., Bonvin, C., Borgani, S., Branchini, E., Burrage, C., Camera, S., Carbone, C., Casarini, L., Cropper, M., de Rham, C., Dietrich, J. P., Di Porto, C., Durrer, R., Ealet, A., Ferreira, P. G., Finelli, F., García-Bellido, J., Giannantonio, T., Guzzo, L., Heavens, A., Heisenberg, L., Heymans, C., Hoekstra, H., Hollenstein, L., Holmes, R., Hwang, Z., Jahnke, K., Kitching, T. D., Koivisto, T., Kunz, M., La Vacca, G., Linder, E., March, M., Marra, V., Martins, C., Majerotto, E., Markovic, D., Marsh, D., Marulli, F., Massey, R., Mellier, Y., Montanari, F., Mota, D. F., Nunes, N. J., Percival, W., Pettorino, V., Porciani, C., Quercellini, C., Read, J., Rinaldi, M., Sapone, D., Sawicki, I., Scaramella, R., Skordis, C., Simpson, F., Taylor, A., Thomas, S., Trotta, R., Verde, L., Vernizzi, F., Vollmer, A., Wang, Y., Weller, J., and Zlosnik, T. (2018). Cosmology and fundamental physics with the Euclid satellite. *Living Reviews in Relativity*, 21:2.

Angulo, R. E., Hahn, O., and Abel, T. (2013). How closely do baryons follow dark matter on large scales? *Monthly Notices of the Royal Astronomical Society*, 434(2):1756–1764.

Angulo, R. E. and Hilbert, S. (2015). Cosmological constraints from the CFHTLenS shear measurements using a new, accurate, and flexible way of predicting non-linear mass clustering. *Monthly Notices of the Royal Astronomical Society*, 448:364–375.

Angulo, R. E. and Pontzen, A. (2016). Cosmological N-body simulations with suppressed variance. *Monthly Notices of the Royal Astronomical Society*, 462:L1–L5.

Angulo, R. E., Springel, V., White, S. D. M., Jenkins, A., Baugh, C. M., and Frenk, C. S. (2012). Scaling relations for galaxy clusters in the Millennium-XXL simulation. *Monthly Notices of the Royal Astronomical Society*, 426:2046–2062.

Angulo, R. E. and White, S. D. M. (2010). One simulation to fit them all - changing the background parameters of a cosmological N-body simulation. *Monthly Notices of the Royal Astronomical Society*, 405:143–154.

Angulo, R. E., Zennaro, M., Contreras, S., Aricò, G., Pellejero-Ibañez, M., and Stücker, J. (2020). The BACCO Simulation Project: Exploiting the full power of large-scale structure for cosmology. *arXiv e-prints*, page arXiv:2004.06245.

Aricò, G., Angulo, R. E., Contreras, S., Ondaro-Mallea, L., Pellejero-Ibañez, M., and Zennaro, M. (2020a). The BACCO Simulation Project: A baryonification emulator with Neural Networks. *arXiv e-prints*, page arXiv:2011.15018.

Aricò, G., Angulo, R. E., Hernández-Monteagudo, C., Contreras, S., and Zennaro, M. (2021a). Simultaneous modelling of matter power spectrum and bispectrum in the presence of baryons. *Monthly Notices of the Royal Astronomical Society*, 503(3):3596–3609.

Aricò, G., Angulo, R. E., Hernández-Monteagudo, C., Contreras, S., Zennaro, M., Pellejero-Ibañez, M., and Rosas-Guevara, Y. (2020b). Modelling the large-scale mass density field of the universe as a function of cosmology and baryonic physics. *Monthly Notices of the Royal Astronomical Society*, 495(4):4800–4819.

Aricò, G., Angulo, R. E., and Zennaro, M. (2021b). Accelerating Large-Scale-Structure data analyses by emulating Boltzmann solvers and Lagrangian Perturbation Theory. *arXiv e-prints*, page arXiv:2104.14568.

Asgari, M., Lin, C.-A., Joachimi, B., Giblin, B., Heymans, C., Hildebrandt, H., Kannawadi, A., Stölzner, B., Tröster, T., van den Busch, J. L., Wright, A. H., Bilicki, M., Blake, C., de Jong, J., Dvornik, A., Erben, T., Getman, F., Hoekstra, H., Köhlinger, F., Kuijken, K., Miller, L., Radovich, M., Schneider, P., Shan, H., and Valentijn, E. (2020a). KiDS-1000 Cosmology: Cosmic shear constraints and comparison between two point statistics. *arXiv e-prints*.

Asgari, M., Tröster, T., Heymans, C., Hildebrandt, H., van den Busch, J. L., Wright, A. H., Choi, A., Erben, T., Joachimi, B., Joudaki, S., Kannawadi, A., Kuijken, K., Lin, C.-A., Schneider, P., and Zuntz, J. (2020b). KiDS+VIKING-450 and DES-Y1 combined: Mitigating baryon feedback uncertainty with COSEBIs. *Astronomy and Astrophysics*, 634:A127.

Auld, T., Bridges, M., and Hobson, M. P. (2008). COSMONET: fast cosmological parameter estimation in non-flat models using neural networks. *Monthly Notices of the Royal Astronomical Society*, 387(4):1575–1582.

Auld, T., Bridges, M., Hobson, M. P., and Gull, S. F. (2007). Fast cosmological parameter estimation using neural networks. *Monthly Notices of the Royal Astronomical Society*, 376(1):L11–L15.

Barreira, A., Krause, E., and Schmidt, F. (2018). Accurate cosmic shear errors: do we need ensembles of simulations? *Journal of Cosmology and Astroparticle Physics*, 2018(10):053.

Barreira, A., Nelson, D., Pillepich, A., Springel, V., Schmidt, F., Pakmor, R., Hernquist, L., and Vogelsberger, M. (2019). Separate Universe simulations with IllustrisTNG: baryonic effects on power spectrum responses and higher-order statistics. *Monthly Notices of the Royal Astronomical Society*, 488:2079–2092.

Baumann, D., Green, D., and Wallisch, B. (2018). Searching for light relics with large-scale structure. *Journal of Cosmology and Astroparticle Physics*, 2018(8):029.

Behroozi, P. S., Wechsler, R. H., and Conroy, C. (2013). The Average Star Formation Histories of Galaxies in Dark Matter Halos from z = 0-8. *The Astrophysical Journal*, 770:57.

Benitez, N., Dupke, R., Moles, M., Sodre, L., Cenarro, J., Marin-Franch, A., Taylor, K., Cristobal, D., Fernandez-Soto, A., Mendes de Oliveira, C., Cepa-Nogue, J., Abramo, L. R., Alcaniz, J. S., Overzier, R., Hernandez-Monteagudo, C., Alfaro, E. J., Kanaan, A., Carvano, J. M., Reis, R. R. R., Martinez Gonzalez, E., Ascaso, B., Ballesteros, F., Xavier, H. S., Varela, J., Ederoclite, A., Vazquez Ramio, H., Broadhurst, T., Cypriano, E., Angulo, R., Diego, J. M., Zandivarez, A., Diaz, E., Melchior, P., Umetsu, K., Spinelli, P. F., Zitrin, A., Coe, D., Yepes, G., Vielva, P., Sahni, V., Marcos-Caballero, A., Shu Kitaura, F., Maroto, A. L., Masip, M., Tsujikawa, S., Carneiro, S., Gonzalez Nuevo, J., Carvalho, G. C., Reboucas, M. J., Carvalho, J. C., Abdalla, E., Bernui, A., Pigozzo, C., Ferreira, E. G. M., Chandrachani Devi, N., Bengaly, Jr., C. A. P., Campista, M., Amorim, A., Asari, N. V., Bongiovanni, A., Bonoli, S., Bruzual, G., Cardiel, N., Cava, A., Cid Fernandes, R., Coelho, P., Cortesi, A., Delgado, R. G., Diaz Garcia, L., Espinosa, J. M. R., Galliano, E., Gonzalez-Serrano, J. I., Falcon-Barroso, J., Fritz, J., Fernandes, C., Gorgas, J., Hoyos, C., Jimenez-Teja, Y., Lopez-Aguerri, J. A., Lopez-San Juan, C., Mateus, A., Molino, A., Novais, P., OMill, A., Oteo, I., Perez-Gonzalez, P. G., Poggianti, B., Proctor, R., Ricciardelli, E., Sanchez-Blazquez, P., Storchi-Bergmann, T., Telles, E., Schoennell, W., Trujillo, N., Vazdekis, A., Viironen, K., Daflon, S., Aparicio-Villegas, T., Rocha, D., Ribeiro, T., Borges, M., Martins, S. L., Marcolino, W., Martinez-Delgado, D., Perez-Torres, M. A., Siffert, B. B., Calvao, M. O., Sako, M., Kessler, R., Alvarez-Candal, A., De Pra, M., Roig, F., Lazzaro, D., Gorosabel, J., Lopes de Oliveira, R., Lima-Neto, G. B., Irwin, J., Liu, J. F., Alvarez, E., Balmes, I., Chueca, S., Costa-Duarte, M. V., da Costa, A. A., Dantas, M. L. L., Diaz, A. Y., Fabregat, J., Ferrari, F., Gavela, B., Gracia, S. G., Gruel, N., Gutierrez, J. L. L., Guzman, R., Hernandez-Fernandez, J. D., Herranz, D., Hurtado-Gil, L., Jablonsky, F., Laporte, R., Le Tiran, L. L., Licandro, J., Lima, M., Martin, E., Martinez, V., Montero, J. J. C., Penteado, P., Pereira, C. B., Peris, V., Quilis, V., Sanchez-Portal, M., Soja, A. C., Solano, E., Torra, J., and Valdivielso, L. (2014). J-PAS: The Javalambre-Physics of the Accelerated Universe Astrophysical Survey. *ArXiv e-prints*.

Bergé, J., Amara, A., and Réfrégier, A. (2010). Optimal Capture of Non-Gaussianity in Weak-Lensing Surveys: Power Spectrum, Bispectrum, and Halo Counts. *The Astrophysical Journal*, 712(2):992–1002.

Bird, S., Rogers, K. K., Peiris, H. V., Verde, L., Font-Ribera, A., and Pontzen, A. (2019). An emulator for the Lyman-α forest. *Journal of Cosmology and Astroparticle Physics*, 2019(2):050.

Bocquet, S., Heitmann, K., Habib, S., Lawrence, E., Uram, T., Frontiere, N., Pope, A., and Finkel, H. (2020). The Mira-Titan Universe. III. Emulation of the Halo Mass Function. *The Astrophysical Journal*, 901(1):5.

Bragança, D. P. L., Lewandowski, M., Sekera, D., Senatore, L., and Sgier, R. (2020). Baryonic effects in the Effective Field Theory of Large-Scale Structure and an analytic recipe for lensing in CMB-S4. *arXiv e-prints*, page arXiv:2010.02929.

Carron, J. (2013). On the assumption of Gaussianity for cosmological two-point statistics and parameter dependent covariance matrices. *Astronomy and Astrophysics*, 551:A88.

Castorina, E., Carbone, C., Bel, J., Sefusatti, E., and Dolag, K. (2015). DEMNUni: the clustering of large-scale structures in the presence of massive neutrinos. *Journal of Cosmology and Astroparticle Physics*, 2015(7):043.

Chaves-Montero, J., Angulo, R. E., and Hernández-Monteagudo, C. (2016). Redshift uncertainties and baryonic acoustic oscillations. *ArXiv e-prints*.

Chen, S.-F., Vlah, Z., and White, M. (2020). Consistent modeling of velocity statistics and redshift-space distortions in one-loop perturbation theory. *Journal of Cosmology and Astroparticle Physics*, 2020(7):062.

Chevallier, M. and Polarski, D. (2001). Accelerating Universes with Scaling Dark Matter. *International Journal of Modern Physics D*, 10(2):213–223.

Chisari, N. E., Mead, A. J., Joudaki, S., Ferreira, P., Schneider, A., Mohr, J., Tröster, T., Alonso, D., McCarthy, I. G., Martin-Alvarez, S., Devriendt, J., Slyz, A., and van Daalen, M. P. (2019). Modelling baryonic feedback for survey cosmology. *arXiv e-prints*.

Chisari, N. E., Richardson, M. L. A., Devriendt, J., Dubois, Y., Schneider, A., Le Brun, A. M. C., Beckmann, R. S., Peirani, S., Slyz, A., and Pichon, C. (2018). The impact of baryons on the matter power spectrum from the Horizon-AGN cosmological hydrodynamical simulation. *Monthly Notices of the Royal Astronomical Society*, 480:3962–3977.

Chollet, F. et al. (2015). Keras. In -. GitHub.

Chuang, C.-H., Yepes, G., Kitaura, F.-S., Pellejero-Ibanez, M., Rodríguez-Torres, S., Feng, Y., Metcalf, R. B., Wechsler, R. H., Zhao, C., To, C.-H., Alam, S., Banerjee, A., DeRose, J., Giocoli, C., Knebe, A., and Reyes, G. (2019). UNIT project: Universe N-body simulations for the Investigation of Theoretical models from galaxy surveys. *Monthly Notices of the Royal Astronomical Society*, 487(1):48–59.

Colombi, S., Jaffe, A., Novikov, D., and Pichon, C. (2009). Accurate estimators of power spectra in N-body simulations. *Monthly Notices of the Royal Astronomical Society*, 393(2):511–526.

Contreras, S., Angulo, R. E., Zennaro, M., Aricò, G., and Pellejero-Ibañez, M. (2020a). 3 per cent-accurate predictions for the clustering of dark matter, haloes, and subhaloes, over a wide range of cosmologies and scales. *Monthly Notices of the Royal Astronomical Society*, 499(4):4905–4917.

Contreras, S., Zennaro, R. E. A. M., Aricó, G., and Pellejero-Ibañez, M. (2020b). 3\%-accurate predictions for the clustering of dark matter, haloes and subhaloes, over a wide range of cosmologies and scales. *arXiv e-prints*, page arXiv:2001.03176.

Crain, R. A., Schaye, J., Bower, R. G., Furlong, M., Schaller, M., Theuns, T., Dalla Vecchia, C., Frenk, C. S., McCarthy, I. G., Helly, J. C., Jenkins, A., Rosas-Guevara, Y. M., White, S. D. M., and Trayford, J. W. (2015). The EAGLE simulations of galaxy formation: calibration of subgrid physics and model variations. *Monthly Notices of the Royal Astronomical Society*, 450(2):1937–1961.

Dai, B., Feng, Y., and Seljak, U. (2018). A gradient based method for modeling baryons and matter in halos of fast simulations. *Journal of Cosmology and Astroparticle Physics*, 11:009.

Debackere, S. N. B., Schaye, J., and Hoekstra, H. (2020). The impact of the observed baryon distribution in haloes on the total matter power spectrum. *Monthly Notices of the Royal Astronomical Society*, 492(2):2285–2307.

DeRose, J., Wechsler, R. H., Tinker, J. L., Becker, M. R., Mao, Y.-Y., McClintock, T., McLaughlin, S., Rozo, E., and Zhai, Z. (2019). The AEMULUS Project. I. Numerical Simulations for Precision Cosmology. *The Astrophysical Journal*, 875(1):69.

DES Collaboration, Abbott, T. M. C., Aguena, M., Alarcon, A., Allam, S., Alves, O., Amon, A., Andrade-Oliveira, F., Annis, J., Avila, S., Bacon, D., Baxter, E., Bechtol, K., Becker, M. R., Bernstein, G. M., Bhargava, S., Birrer, S., Blazek, J., Brandao-Souza, A., Bridle, S. L., Brooks, D., Buckley-Geer, E., Burke, D. L., Camacho, H., Campos, A., Carnero Rosell, A., Carrasco Kind, M., Carretero, J., Castander, F. J., Cawthon, R., Chang, C., Chen, A., Chen, R., Choi, A., Conselice, C., Cordero, J., Costanzi, M., Crocce, M., da Costa, L. N., da Silva Pereira, M. E., Davis, C., Davis, T. M., De Vicente, J., DeRose, J., Desai, S., Di Valentino, E., Diehl, H. T., Dietrich, J. P., Dodelson, S., Doel, P., Doux, C., Drlica-Wagner, A., Eckert, K., Eifler, T. F., Elsner, F., Elvin-Poole, J., Everett, S., Evrard, A. E., Fang, X., Farahi, A., Fernandez, E., Ferrero, I., Ferté, A., Fosalba, P., Friedrich, O., Frieman, J., García-Bellido, J., Gatti, M., Gaztanaga, E., Gerdes, D. W., Giannantonio, T., Giannini, G., Gruen, D., Gruendl, R. A., Gschwend, J., Gutierrez, G., Harrison, I., Hartley, W. G., Herner, K., Hinton, S. R., Hollowood, D. L., Honscheid, K., Hoyle, B., Huff, E. M., Huterer, D., Jain, B., James, D. J., Jarvis, M., Jeffrey, N., Jeltema, T., Kovacs, A., Krause, E., Kron, R., Kuehn, K., Kuropatkin, N., Lahav, O., Leget, P. F., Lemos, P., Liddle, A. R., Lidman, C., Lima, M., Lin, H., MacCrann, N., Maia, M. A. G., Marshall, J. L., Martini, P., McCullough, J., Melchior, P., Mena-Fernández, J., Menanteau, F., Miquel, R., Mohr, J. J., Morgan, R., Muir, J., Myles, J., Nadathur, S., Navarro-Alsina, A., Nichol, R. C., Ogando, R. L. C., Omori, Y., Palmese, A., Pandey, S., Park, Y., Paz-Chinchón, F., Petravick, D., Pieres, A., Plazas Malagón, A. A., Porredon, A., Prat, J., Raveri, M., Rodriguez-Monroy, M., Rollins, R. P., Romer, A. K., Roodman, A., Rosenfeld, R., Ross, A. J., Rykoff, E. S., Samuroff, S., Sánchez, C., Sanchez, E., Sanchez, J., Sanchez Cid, D., Scarpine, V., Schubnell, M., Scolnic, D., Secco, L. F., Serrano, S., Sevilla-Noarbe, I., Sheldon, E., Shin, T., Smith, M., Soares-Santos, M., Suchyta, E., Swanson, M. E. C., Tabbutt, M., Tarle, G., Thomas, D., To, C., Troja, A., Troxel, M. A., Tucker, D. L., Tutusaus, I., Varga, T. N., Walker, A. R., Weaverdyck, N., Weller, J., Yanny, B., Yin, B., Zhang, Y., and Zuntz, J. (2021). Dark Energy Survey Year 3 Results: Cosmological Constraints from Galaxy Clustering and Weak Lensing. *arXiv e-prints*, page arXiv:2105.13549.

DESI Collaboration, Aghamousa, A., Aguilar, J., Ahlen, S., Alam, S., Allen, L. E., Allende Prieto, C., Annis, J., Bailey, S., Balland, C., Ballester, O., Baltay, C., Beaufore, L., Bebek, C., Beers, T. C., Bell, E. F., Bernal, J. L., Besuner, R., Beutler, F., Blake, C., Bleuler, H., Blomqvist, M., Blum, R., Bolton, A. S., Briceno, C., Brooks, D., Brownstein, J. R., Buckley-Geer, E., Burden, A., Burtin, E., Busca, N. G., Cahn, R. N., Cai, Y.-C., Cardiel-Sas, L., Carlberg, R. G., Carton, P.-H., Casas, R., Castand er, F. J., Cervantes-Cota, J. L., Claybaugh, T. M., Close, M., Coker, C. T., Cole, S., Comparat, J., Cooper, A. P., Cousinou, M. C., Crocce, M., Cuby, J.-G., Cunningham, D. P., Davis, T. M., Dawson, K. S., de la Macorra, A., De Vicente, J., Delubac, T., Derwent, M., Dey, A., Dhungana, G., Ding, Z., Doel, P., Duan, Y. T., Ealet, A., Edelstein, J., Eftekharzadeh, S., Eisenstein, D. J., Elliott, A., Escoffier, S., Evatt, M., Fagrelius, P., Fan, X., Fanning, K., Farahi, A., Farihi, J., Favole, G., Feng, Y., Fernandez, E., Findlay, J. R., Finkbeiner, D. P., Fitzpatrick, M. J., Flaugher, B., Flender, S., Font-Ribera, A., Forero-Romero, J. E., Fosalba, P., Frenk, C. S., Fumagalli, M., Gaensicke, B. T., Gallo, G., Garcia-Bellido, J., Gaztanaga, E., Pietro Gentile Fusillo, N., Gerard, T., Gershkovich, I., Giannantonio, T., Gillet, D., Gonzalez-de-Rivera, G., Gonzalez-Perez, V., Gott, S., Graur, O., Gutierrez, G., Guy, J., Habib, S., Heetderks, H., Heetderks, I., Heitmann, K., Hellwing, W. A., Herrera, D. A., Ho, S., Holland, S., Honscheid, K., Huff, E., Hutchinson, T. A., Huterer, D., Hwang, H. S., Illa Laguna, J. M., Ishikawa, Y., Jacobs, D., Jeffrey, N., Jelinsky, P., Jennings, E., Jiang, L., Jimenez, J., Johnson, J., Joyce, R., Jullo, E., Juneau, S., Kama, S., Karcher, A., Karkar, S., Kehoe, R., Kennamer, N., Kent, S., Kilbinger, M., Kim, A. G., Kirkby, D., Kisner, T., Kitanidis, E., Kneib, J.-P., Koposov, S., Kovacs, E., Koyama, K., Kremin, A., Kron, R., Kronig, L., Kueter-Young, A., Lacey, C. G., Lafever, R., Lahav, O., Lambert, A., Lampton, M., Land riau, M., Lang, D., Lauer, T. R., Le Goff, J.-M., Le Guillou, L., Le Van Suu, A., Lee, J. H., Lee, S.-J., Leitner, D., Lesser, M., Levi, M. E., L'Huillier, B., Li, B., Liang, M., Lin, H., Linder, E., Loebman, S. R., Lukić, Z., Ma, J., MacCrann, N., Magneville, C., Makarem, L., Manera, M., Manser, C. J., Marshall, R., Martini, P., Massey, R., Matheson, T., McCauley, J., McDonald, P., McGreer, I. D., Meisner, A., Metcalfe, N., Miller, T. N., Miquel, R., Moustakas, J., Myers, A., Naik, M., Newman, J. A., Nichol, R. C., Nicola, A., Nicolati da Costa, L., Nie, J., Niz, G., Norberg, P., Nord, B., Norman, D., Nugent, P., O'Brien, T., Oh, M., Olsen, K. A. G., Padilla, C., Padmanabhan, H., Padmanabhan, N., Palanque-Delabrouille, N., Palmese, A., Pappalardo, D., Pâris, I., Park, C., Patej, A., Peacock, J. A., Peiris, H. V., Peng, X., Percival, W. J., Perruchot, S., Pieri, M. M., Pogge, R., Pollack, J. E., Poppett, C., Prada, F., Prakash, A., Probst, R. G., Rabinowitz, D., Raichoor, A., Ree, C. H., Refregier, A., Regal, X., Reid, B., Reil, K., Rezaie, M., Rockosi, C. M., Roe, N., Ronayette, S., Roodman, A., Ross, A. J., Ross, N. P., Rossi, G., Rozo, E., Ruhlmann-Kleider, V., Rykoff, E. S., Sabiu, C., Samushia, L., Sanchez, E., Sanchez, J., Schlegel, D. J., Schneider, M., Schubnell, M., Secroun, A., Seljak, U., Seo, H.-J., Serrano, S., Shafieloo, A., Shan, H., Sharples, R., Sholl, M. J., Shourt, W. V., Silber, J. H., Silva, D. R., Sirk, M. M., Slosar, A., Smith, A., Smoot, G. F., Som, D., Song, Y.-S., Sprayberry, D., Staten, R., Stefanik, A., Tarle, G., Sien Tie, S., Tinker, J. L., Tojeiro, R., Valdes, F., Valenzuela, O., Valluri, M., Vargas-Magana, M., Verde, L., Walker, A. R., Wang, J., Wang, Y., Weaver, B. A., Weaverdyck, C., Wechsler, R. H., Weinberg, D. H., White, M., Yang, Q., Yeche, C., Zhang, T., Zhao, G.-B., Zheng, Y., Zhou, X., Zhou, Z., Zhu, Y., Zou, H., and Zu, Y. (2016). The DESI Experiment Part I: Science,Targeting, and Survey Design. *arXiv e-prints*, page arXiv:1611.00036.

Desjacques, V., Jeong, D., and Schmidt, F. (2018). Large-scale galaxy bias. *Physics Reports*, 733:1–193.

Dubois, Y., Pichon, C., Welker, C., Le Borgne, D., Devriendt, J., Laigle, C., Codis, S., Pogosyan, D., Arnouts, S., Benabed, K., Bertin, E., Blaizot, J., Bouchet, F., Cardoso, J.-F., Colombi, S., de Lapparent, V., Desjacques, V., Gavazzi, R., Kassin, S., Kimm, T., McCracken, H., Milliard, B., Peirani, S., Prunet, S., Rouberol, S., Silk, J., Slyz, A., Sousbie, T., Teyssier, R., Tresse, L., Treyer, M., Vibert, D., and Volonteri, M. (2014). Dancing in the dark: galactic properties trace spin swings along the cosmic web. *Monthly Notices of the Royal Astronomical Society*, 444:1453–1468.

Eifler, T., Krause, E., Dodelson, S., Zentner, A. R., Hearin, A. P., and Gnedin, N. Y. (2015). Accounting for baryonic effects in cosmic shear tomography: determining a minimal set of nuisance parameters using PCA. *Monthly Notices of the Royal Astronomical Society*, 454:2451–2471.

Eisenstein, D. J. and Hu, W. (1999). Power Spectra for Cold Dark Matter and Its Variants. *The Astrophysical Journal*, 511(1):5–15.

Euclid Collaboration, Knabenhans, M., Stadel, J., Marelli, S., Potter, D., Teyssier, R., Legrand , L., Schneider, A., Sudret, B., Blot, L., Awan, S., Burigana, C., Carvalho, C. S., Kurki-Suonio, H., and Sirri, G. (2019). Euclid preparation: II. The EUCLIDEMULATOR - a tool to compute the cosmology dependence of the nonlinear matter power spectrum. *Monthly Notices of the Royal Astronomical Society*, 484(4):5509–5529.

Euclid Collaboration, Knabenhans, M., Stadel, J., Potter, D., Dakin, J., Hannestad, S., Tram, T., Marelli, S., Schneider, A., Teyssier, R., Andreon, S., Auricchio, N., Baccigalupi, C., Balaguera-Antolínez, A., Baldi, M., Bardelli, S., Battaglia, P., Bender, R., Biviano, A., Bodendorf, C., Bozzo, E., Branchini, E., Brescia, M., Burigana, C., Cabanac, R., Camera, S., Capobianco, V., Cappi, A., Carbone, C., Carretero, J., Carvalho, C. S., Casas, R., Casas, S., Castellano, M., Castignani, G., Cavuoti, S., Cledassou, R., Colodro-Conde, C., Congedo, G., Conselice, C. J., Conversi, L., Copin, Y., Corcione, L., Coupon, J., Courtois, H. M., Da Silva, A., de la Torre, S., Di Ferdinando, D., Duncan, C. A. J., Dupac, X., Fabbian, G., Farrens, S., Ferreira, P. G., Finelli, F., Frailis, M., Franceschi, E., Galeotta, S., Garilli, B., Giocoli, C., Gozaliasl, G., Graciá-Carpio, J., Grupp, F., Guzzo, L., Holmes, W., Hormuth, F., Israel, H., Jahnke, K., Keihanen, E., Kermiche, S., Kirkpatrick, C. C., Kubik, B., Kunz, M., Kurki-Suonio, H., Ligori, S., Lilje, P. B., Lloro, I., Maino, D., Marggraf, O., Markovic, K., Martinet, N., Marulli, F., Massey, R., Mauri, N., Maurogordato, S., Medinaceli, E., Meneghetti, M., Metcalf, B., Meylan, G., Moresco, M., Morin, B., Moscardini, L., Munari, E., Neissner, C., Niemi, S. M., Padilla, C., Paltani, S., Pasian, F., Patrizii, L., Pettorino, V., Pires, S., Polenta, G., Poncet, M., Raison, F., Renzi, A., Rhodes, J., Riccio, G., Romelli, E., Roncarelli, M., Saglia, R., Sánchez, A. G., Sapone, D., Schneider, P., Scottez, V., Secroun, A., Serrano, S., Sirignano, C., Sirri, G., Stanco, L., Sureau, F., Tallada Crespí, P., Taylor, A. N., Tenti, M., Tereno, I., Toledo-Moreo, R., Torradeflot, F., Valenziano, L., Valiviita, J., Vassallo, T., Viel, M., Wang, Y., Welikala, N., Whittaker, L., Zacchei, A., and Zucca, E. (2020). Euclid preparation: IX. EuclidEmulator2 – Power spectrum emulation with massive neutrinos and self-consistent dark energy perturbations. *arXiv e-prints*, page arXiv:2010.11288.

Favole, G., Rodríguez-Torres, S. A., Comparat, J., Prada, F., Guo, H., Klypin, A., and Montero-Dorta, A. D. (2017). Galaxy clustering dependence on the [O II] emission line luminosity in the local Universe. *Monthly Notices of the Royal Astronomical Society*, 472(1):550–558.

Fedeli, C. (2014). The clustering of baryonic matter. I: a halo-model approach. *Journal of Cosmology and Astroparticle Physics*, 4:028.

Fendt, W. A. and Wandelt, B. D. (2007). Pico: Parameters for the Impatient Cosmologist. *The Astrophysical Journal*, 654(1):2–11.

Foreman, S., Coulton, W., Villaescusa-Navarro, F., and Barreira, A. (2020). Baryonic effects on the matter bispectrum. *Monthly Notices of the Royal Astronomical Society*, 498(2):2887–2911.

Foreman-Mackey, D., Hogg, D. W., Lang, D., and Goodman, J. (2013). emcee: The MCMC Hammer. *Publications of the Astronomical Society of the Pacific* , 125(925):306.

Freedman, W. L., Madore, B. F., Hatt, D., Hoyt, T. J., Jang, I. S., Beaton, R. L., Burns, C. R., Lee, M. G., Monson, A. J., Neeley, J. R., Phillips, M. M., Rich, J. A., and Seibert, M. (2019). The Carnegie-Chicago Hubble Program. VIII. An Independent Determination of the Hubble Constant Based on the Tip of the Red Giant Branch. *The Astrophysical Journal*, 882(1):34.

Garrison, L. H., Eisenstein, D. J., and Pinto, P. A. (2019). A high-fidelity realization of the Euclid code comparison N-body simulation with ABACUS. *Monthly Notices of the Royal Astronomical Society*, 485(3):3370–3377.

Giblin, B., Cataneo, M., Moews, B., and Heymans, C. (2019). On the road to per cent accuracy - II. Calibration of the non-linear matter power spectrum for arbitrary cosmologies. *Monthly Notices of the Royal Astronomical Society*, 490(4):4826–4840.

Gilman, D., Birrer, S., Nierenberg, A., Treu, T., Du, X., and Benson, A. (2020). Warm dark matter chills out: constraints on the halo mass function and the free-streaming length of dark matter with eight quadruple-image strong gravitational lenses. *Monthly Notices of the Royal Astronomical Society*, 491(4):6077–6101.

GPy (since 2012). GPy: A gaussian process framework in python. `http://github.com/SheffieldML/GPy`.

Guo, Q. and White, S. (2014). Numerical resolution limits on subhalo abundance matching. *Monthly Notices of the Royal Astronomical Society*, 437(4):3228–3235.

Guth, A. H. (1981). Inflationary universe: A possible solution to the horizon and flatness problems. *Phys. Rev. D Physical Review D: Particles, Fields, Gravitation & Cosmology*, 23(2):347–356.

Hahn, O. and Angulo, R. E. (2016). An adaptively refined phase-space element method for cosmological simulations and collisionless dynamics. *Monthly Notices of the Royal Astronomical Society*, 455(1):1115–1133.

Hand, N., Feng, Y., Beutler, F., Li, Y., Modi, C., Seljak, U., and Slepian, Z. (2018). nbodykit: An Open-source, Massively Parallel Toolkit for Large-scale Structure. *Astronomical Journal*, 156(4):160.

Harnois-Déraps, J., van Waerbeke, L., Viola, M., and Heymans, C. (2015). Baryons, neutrinos, feedback and weak gravitational lensing. *Monthly Notices of the Royal Astronomical Society*, 450:1212–1223.

Heitmann, K., Higdon, D., Nakhleh, C., and Habib, S. (2006). Cosmic Calibration. *The Astrophysical Journal Letters*, 646(1):L1–L4.

Heitmann, K., Lawrence, E., Kwan, J., Habib, S., and Higdon, D. (2014). The Coyote Universe Extended: Precision Emulation of the Matter Power Spectrum. *The Astrophysical Journal*, 780:111.

Hellwing, W. A., Schaller, M., Frenk, C. S., Theuns, T., Schaye, J., Bower, R. G., and Crain, R. A. (2016). The effect of baryons on redshift space distortions and cosmic density and velocity fields in the EAGLE simulation. *Monthly Notices of the Royal Astronomical Society*, 461:L11–L15.

Henriques, B. M. B., Yates, R. M., Fu, J., Guo, Q., Kauffmann, G., Srisawat, C., Thomas, P. A., and White, S. D. M. (2020). L-GALAXIES 2020: Spatially resolved cold gas phases, star formation, and chemical enrichment in galactic discs. *Monthly Notices of the Royal Astronomical Society*, 491(4):5795–5814.

Hikage, C., Oguri, M., Hamana, T., More, S., Mandelbaum, R., Takada, M., Köhlinger, F., Miyatake, H., Nishizawa, A. J., Aihara, H., Armstrong, R., Bosch, J., Coupon, J., Ducout, A., Ho, P., Hsieh, B.-C., Komiyama, Y., Lanusse, F., Leauthaud, A., Lupton, R. H., Medezinski, E., Mineo, S., Miyama, S., Miyazaki, S., Murata, R., Murayama, H., Shirasaki, M., Sifón, C., Simet, M., Speagle, J., Spergel, D. N., Strauss, M. A., Sugiyama, N., Tanaka, M., Utsumi, Y., Wang, S.-Y., and Yamada, Y. (2019). Cosmology from cosmic shear power spectra with Subaru Hyper Suprime-Cam first-year data. *Publications of the ASJ*, 71:43.

Hoekstra, H. and Jain, B. (2008). Weak Gravitational Lensing and Its Cosmological Applications. *Annual Review of Nuclear and Particle Science*, 58(1):99–123.

Hojjati, A., Tröster, T., Harnois-Déraps, J., McCarthy, I. G., van Waerbeke, L., Choi, A., Erben, T., Heymans, C., Hildebrandt, H., Hinshaw, G., Ma, Y.-Z., Miller, L., Viola, M., and Tanimura, H. (2017). Cross-correlating Planck tSZ with RCSLenS weak lensing: implications for cosmology and AGN feedback. *Monthly Notices of the Royal Astronomical Society*, 471(2):1565–1580.

Huang, H.-J., Eifler, T., Mandelbaum, R., and Dodelson, S. (2019). Modelling baryonic physics in future weak lensing surveys. *Monthly Notices of the Royal Astronomical Society*, 488:1652–1678.

Huterer, D., Takada, M., Bernstein, G., and Jain, B. (2006). Systematic errors in future weak-lensing surveys: requirements and prospects for self-calibration. *Monthly Notices of the Royal Astronomical Society*, 366(1):101–114.

Ivezić, Ž., Kahn, S. M., Tyson, J. A., Abel, B., Acosta, E., Allsman, R., Alonso, D., AlSayyad, Y., Anderson, S. F., Andrew, J., and et al. (2019). LSST: From Science Drivers to Reference Design and Anticipated Data Products. *The Astrophysical Journal*, 873:111.

Jenkins, A., Frenk, C. S., Pearce, F. R., Thomas, P. A., Colberg, J. M., White, S. D. M., Couchman, H. M. P., Peacock, J. A., Efstathiou, G., and Nelson, A. H. (1998). Evolution of Structure in Cold Dark Matter Universes. *The Astrophysical Journal*, 499(1):20–40.

Kennedy, J. and Eberhart, R. (1995). Particle swarm optimization. In *Proceedings of ICNN'95 - International Conference on Neural Networks*, volume 4, pages 1942–1948 vol.4.

Kilbinger, M. and Schneider, P. (2005). Cosmological parameters from combined second- and third-order aperture mass statistics of cosmic shear. *Astronomy and Astrophysics*, 442(1):69–83.

Klypin, A., Prada, F., and Byun, J. (2020). Suppressing cosmic variance with paired-and-fixed cosmological simulations: average properties and covariances of dark matter clustering statistics. *Monthly Notices of the Royal Astronomical Society*.

Knabenhans, M., Stadel, J., Marelli, S., Potter, D., Teyssier, R., Legrand, L., Schneider, A., Sudret, B., Blot, L., Awan, S., Burigana, C., Carvalho, C. S., Kurki-Suonio, H., Sirri, G., and Euclid Collaboration (2019). Euclid preparation: II. The EUCLIDEMULATOR - a tool to compute the cosmology dependence of the nonlinear matter power spectrum. *Monthly Notices of the Royal Astronomical Society*, 484(4):5509–5529.

Kobayashi, Y., Nishimichi, T., Takada, M., Takahashi, R., and Osato, K. (2020). Accurate emulator for the redshift-space power spectrum of dark matter halos and its application to galaxy power spectrum. *Phys. Rev. D Physical Review D: Particles, Fields, Gravitation & Cosmology*, 102(6):063504.

Kodwani, D., Alonso, D., and Ferreira, P. (2019). The effect on cosmological parameter estimation of a parameter dependent covariance matrix. *The Open Journal of Astrophysics*, 2:3.

Kokron, N., DeRose, J., Chen, S.-F., White, M., and Wechsler, R. H. (2021). The cosmology dependence of galaxy clustering and lensing from a hybrid N-body-perturbation theory model. *arXiv e-prints*, page arXiv:2101.11014.

Komatsu, E., Smith, K. M., Dunkley, J., Bennett, C. L., Gold, B., Hinshaw, G., Jarosik, N., Larson, D., Nolta, M. R., Page, L., Spergel, D. N., Halpern, M., Hill, R. S., Kogut, A., Limon, M., Meyer, S. S., Odegard, N., Tucker, G. S., Weiland, J. L., Wollack, E., and Wright, E. L. (2011). Seven-year Wilkinson Microwave Anisotropy Probe (WMAP) Observations: Cosmological Interpretation. *Astrophysical Journal, Supplement*, 192(2):18.

Kravtsov, A. V., Vikhlinin, A. A., and Meshcheryakov, A. V. (2018). Stellar Mass - Halo Mass Relation and Star Formation Efficiency in High-Mass Halos. *Astronomy Letters*, 44:8–34.

Kuhlen, M., Vogelsberger, M., and Angulo, R. (2012). Numerical simulations of the dark universe: State of the art and the next decade. *Physics of the Dark Universe*, 1(1-2):50–93.

Laureijs, R., Amiaux, J., Arduini, S., Auguères, J. ., Brinchmann, J., Cole, R., Cropper, M., Dabin, C., Duvet, L., Ealet, A., and et al. (2011). Euclid Definition Study Report. *ArXiv e-prints*.

Lawrence, E., Heitmann, K., Kwan, J., Upadhye, A., Bingham, D., Habib, S., Higdon, D., Pope, A., Finkel, H., and Frontiere, N. (2017). The Mira-Titan Universe. II. Matter Power Spectrum Emulation. *The Astrophysical Journal*, 847(1):50.

Le Brun, A. M. C., McCarthy, I. G., Schaye, J., and Ponman, T. J. (2014). Towards a realistic population of simulated galaxy groups and clusters. *Monthly Notices of the Royal Astronomical Society*, 441:1270–1290.

Leclercq, F. (2018). Bayesian optimization for likelihood-free cosmological inference. *Phys. Rev. D Physical Review D: Particles, Fields, Gravitation & Cosmology*, 98(6):063511.

Lesgourgues, J. (2011a). The Cosmic Linear Anisotropy Solving System (CLASS) I: Overview. *arXiv e-prints*, page arXiv:1104.2932.

Lesgourgues, J. (2011b). The Cosmic Linear Anisotropy Solving System (CLASS) III: Comparision with CAMB for LambdaCDM. *arXiv e-prints*, page arXiv:1104.2934.

Lesgourgues, J. and Tram, T. (2011). The Cosmic Linear Anisotropy Solving System (CLASS) IV: efficient implementation of non-cold relics. *Journal of Cosmology and Astroparticle Physics*, 2011(9):032.

Lewandowski, M., Perko, A., and Senatore, L. (2015). Analytic prediction of baryonic effects from the EFT of large scale structures. *Journal of Cosmology and Astroparticle Physics*, 2015(5):019.

Lewis, A. and Bridle, S. (2002). Cosmological parameters from CMB and other data: A Monte Carlo approach. *Phys. Rev. D Physical Review D: Particles, Fields, Gravitation & Cosmology*, 66:103511.

Lewis, A., Challinor, A., and Lasenby, A. (2000). Efficient Computation of Cosmic Microwave Background Anisotropies in Closed Friedmann-Robertson-Walker Models. *The Astrophysical Journal*, 538(2):473–476.

Linder, E. V. (2003). Exploring the Expansion History of the Universe. *Phys. Rev. Lett. Physical Review Letters*, 90(9):091301.

Liu, J., Bird, S., Zorrilla Matilla, J. M., Hill, J. C., Haiman, Z., Madhavacheril, M. S., Petri, A., and Spergel, D. N. (2018). MassiveNuS: cosmological massive neutrino simulations. *Journal of Cosmology and Astroparticle Physics*, 2018(3):049.

LSST Science Collaboration, Abell, P. A., Allison, J., Anderson, S. F., Andrew, J. R., Angel, J. R. P., Armus, L., Arnett, D., Asztalos, S. J., Axelrod, T. S., Bailey, S., Ballantyne, D. R., Bankert, J. R., Barkhouse, W. A., Barr, J. D., Barrientos, L. F., Barth, A. J., Bartlett, J. G., Becker, A. C., Becla, J., Beers, T. C., Bernstein, J. P., Biswas, R., Blanton, M. R., Bloom, J. S., Bochanski, J. J., Boeshaar, P., Borne, K. D., Bradac, M., Brandt, W. N., Bridge, C. R., Brown, M. E., Brunner, R. J., Bullock, J. S., Burgasser, A. J., Burge, J. H., Burke, D. L., Cargile, P. A., Chandrasekharan, S., Chartas, G., Chesley, S. R., Chu, Y.-H., Cinabro, D., Claire, M. W., Claver, C. F., Clowe, D., Connolly, A. J., Cook, K. H., Cooke, J., Cooray, A., Covey, K. R., Culliton, C. S., de Jong, R., de Vries, W. H., Debattista, V. P., Delgado, F., Dell'Antonio, I. P., Dhital, S., Di Stefano, R., Dickinson, M., Dilday, B., Djorgovski, S. G., Dobler, G., Donalek, C., Dubois-Felsmann, G., Durech, J., Eliasdottir, A., Eracleous, M., Eyer, L., Falco, E. E., Fan, X., Fassnacht, C. D., Ferguson, H. C., Fernandez, Y. R., Fields,

B. D., Finkbeiner, D., Figueroa, E. E., Fox, D. B., Francke, H., Frank, J. S., Frieman, J., Fromenteau, S., Furqan, M., Galaz, G., Gal-Yam, A., Garnavich, P., Gawiser, E., Geary, J., Gee, P., Gibson, R. R., Gilmore, K., Grace, E. A., Green, R. F., Gressler, W. J., Grillmair, C. J., Habib, S., Haggerty, J. S., Hamuy, M., Harris, A. W., Hawley, S. L., Heavens, A. F., Hebb, L., Henry, T. J., Hileman, E., Hilton, E. J., Hoadley, K., Holberg, J. B., Holman, M. J., Howell, S. B., Infante, L., Ivezic, Z., Jacoby, S. H., Jain, B., R, Jedicke, Jee, M. J., Garrett Jernigan, J., Jha, S. W., Johnston, K. V., Jones, R. L., Juric, M., Kaasalainen, M., Styliani, Kafka, Kahn, S. M., Kaib, N. A., Kalirai, J., Kantor, J., Kasliwal, M. M., Keeton, C. R., Kessler, R., Knezevic, Z., Kowalski, A., Krabbendam, V. L., Krughoff, K. S., Kulkarni, S., Kuhlman, S., Lacy, M., Lepine, S., Liang, M., Lien, A., Lira, P., Long, K. S., Lorenz, S., Lotz, J. M., Lupton, R. H., Lutz, J., Macri, L. M., Mahabal, A. A., Mandelbaum, R., Marshall, P., May, M., McGehee, P. M., Meadows, B. T., Meert, A., Milani, A., Miller, C. J., Miller, M., Mills, D., Minniti, D., Monet, D., Mukadam, A. S., Nakar, E., Neill, D. R., Newman, J. A., Nikolaev, S., Nordby, M., O'Connor, P., Oguri, M., Oliver, J., Olivier, S. S., Olsen, J. K., Olsen, K., Olszewski, E. W., Oluseyi, H., Padilla, N. D., Parker, A., Pepper, J., Peterson, J. R., Petry, C., Pinto, P. A., Pizagno, J. L., Popescu, B., Prsa, A., Radcka, V., Raddick, M. J., Rasmussen, A., Rau, A., Rho, J., Rhoads, J. E., Richards, G. T., Ridgway, S. T., Robertson, B. E., Roskar, R., Saha, A., Sarajedini, A., Scannapieco, E., Schalk, T., Schindler, R., Schmidt, S., Schmidt, S., Schneider, D. P., Schumacher, G., Scranton, R., Sebag, J., Seppala, L. G., Shemmer, O., Simon, J. D., Sivertz, M., Smith, H. A., Allyn Smith, J., Smith, N., Spitz, A. H., Stanford, A., Stassun, K. G., Strader, J., Strauss, M. A., Stubbs, C. W., Sweeney, D. W., Szalay, A., Szkody, P., Takada, M., Thorman, P., Trilling, D. E., Trimble, V., Tyson, A., Van Berg, R., Vanden Berk, D., VanderPlas, J., Verde, L., Vrsnak, B., Walkowicz, L. M., Wandelt, B. D., Wang, S., Wang, Y., Warner, M., Wechsler, R. H., West, A. A., Wiecha, O., Williams, B. F., Willman, B., Wittman, D., Wolff, S. C., Wood-Vasey, W. M., Wozniak, P., Young, P., Zentner, A., and Zhan, H. (2009). LSST Science Book, Version 2.0. *arXiv e-prints*, page arXiv:0912.0201.

Ludlow, A. D., Bose, S., Angulo, R. E., Wang, L., Hellwing, W. A., Navarro, J. F., Cole, S., and Frenk, C. S. (2016). The mass-concentration-redshift relation of cold and warm dark matter haloes. *Monthly Notices of the Royal Astronomical Society*, 460:1214–1232.

Mandelbaum, R. (2018). Weak Lensing for Precision Cosmology. *Annual Review of Astron and Astrophysics*, 56:393–433.

Marinacci, F., Vogelsberger, M., Pakmor, R., Torrey, P., Springel, V., Hernquist, L., Nelson, D., Weinberger, R., Pillepich, A., Naiman, J., and Genel, S. (2018). First results from the

IllustrisTNG simulations: radio haloes and magnetic fields. *Monthly Notices of the Royal Astronomical Society*, 480(4):5113–5139.

Martizzi, D., Teyssier, R., and Moore, B. (2013). Cusp-core transformations induced by AGN feedback in the progenitors of cluster galaxies. *Monthly Notices of the Royal Astronomical Society*, 432:1947–1954.

Mather, J. C., Cheng, E. S., Cottingham, D. A., Eplee, R. E., J., Fixsen, D. J., Hewagama, T., Isaacman, R. B., Jensen, K. A., Meyer, S. S., Noerdlinger, P. D., Read, S. M., Rosen, L. P., Shafer, R. A., Wright, E. L., Bennett, C. L., Boggess, N. W., Hauser, M. G., Kelsall, T., Moseley, S. H., J., Silverberg, R. F., Smoot, G. F., Weiss, R., and Wilkinson, D. T. (1994). Measurement of the Cosmic Microwave Background Spectrum by the COBE FIRAS Instrument. *The Astrophysical Journal*, 420:439.

Matsubara, T. (2008). Nonlinear perturbation theory with halo bias and redshift-space distortions via the Lagrangian picture. *Phys. Rev. D Physical Review D: Particles, Fields, Gravitation & Cosmology*, 78(8):083519.

McAlpine, S., Helly, J. C., Schaller, M., Trayford, J. W., Qu, Y., Furlong, M., Bower, R. G., Crain, R. A., Schaye, J., Theuns, T., Dalla Vecchia, C., Frenk, C. S., McCarthy, I. G., Jenkins, A., Rosas-Guevara, Y., White, S. D. M., Baes, M., Camps, P., and Lemson, G. (2016). The EAGLE simulations of galaxy formation: Public release of halo and galaxy catalogues. *Astronomy and Computing*, 15:72–89.

McCarthy, I. G., Bird, S., Schaye, J., Harnois-Deraps, J., Font, A. S., and van Waerbeke, L. (2018). The BAHAMAS project: the CMB-large-scale structure tension and the roles of massive neutrinos and galaxy formation. *Monthly Notices of the Royal Astronomical Society*, 476(3):2999–3030.

McCarthy, I. G., Le Brun, A. M. C., Schaye, J., and Holder, G. P. (2014). The thermal Sunyaev-Zel'dovich effect power spectrum in light of Planck. *Monthly Notices of the Royal Astronomical Society*, 440(4):3645–3657.

McCarthy, I. G., Schaye, J., Bird, S., and Le Brun, A. M. C. (2017). The BAHAMAS project: calibrated hydrodynamical simulations for large-scale structure cosmology. *Monthly Notices of the Royal Astronomical Society*, 465:2936–2965.

McClintock, T. and Rozo, E. (2019). Reconstructing probability distributions with Gaussian processes. *Monthly Notices of the Royal Astronomical Society*, 489(3):4155–4160.

McClintock, T., Rozo, E., Becker, M. R., DeRose, J., Mao, Y.-Y., McLaughlin, S., Tinker, J. L., Wechsler, R. H., and Zhai, Z. (2019). The Aemulus Project. II. Emulating the Halo Mass Function. *The Astrophysical Journal*, 872(1):53.

Mead, A., Brieden, S., Tröster, T., and Heymans, C. (2020). HMcode-2020: Improved modelling of non-linear cosmological power spectra with baryonic feedback. *arXiv e-prints*, page arXiv:2009.01858.

Mead, A. J. and Peacock, J. A. (2014a). Remapping dark matter halo catalogues between cosmological simulations. *Monthly Notices of the Royal Astronomical Society*, 440:1233–1247.

Mead, A. J. and Peacock, J. A. (2014b). Remapping simulated halo catalogues in redshift space. *Monthly Notices of the Royal Astronomical Society*, 445:3453–3465.

Mead, A. J., Peacock, J. A., Heymans, C., Joudaki, S., and Heavens, A. F. (2015). An accurate halo model for fitting non-linear cosmological power spectra and baryonic feedback models. *Monthly Notices of the Royal Astronomical Society*, 454:1958–1975.

Modi, C., Chen, S.-F., and White, M. (2020). Simulations and symmetries. *Monthly Notices of the Royal Astronomical Society*, 492(4):5754–5763.

Mohammed, I., Martizzi, D., Teyssier, R., and Amara, A. (2014). Baryonic effects on weak-lensing two-point statistics and its cosmological implications. *arXiv e-prints*.

Mootoovaloo, A., Jaffe, A. H., Heavens, A. F., and Leclercq, F. (2021). Kernel-Based Emulator for the 3D Matter Power Spectrum from CLASS. *arXiv e-prints*, page arXiv:2105.02256.

Moster, B. P., Naab, T., and White, S. D. M. (2018). EMERGE - an empirical model for the formation of galaxies since z $\sim$ 10. *Monthly Notices of the Royal Astronomical Society*, 477(2):1822–1852.

Naiman, J. P., Pillepich, A., Springel, V., Ramirez-Ruiz, E., Torrey, P., Vogelsberger, M., Pakmor, R., Nelson, D., Marinacci, F., Hernquist, L., Weinberger, R., and Genel, S. (2018). First results from the IllustrisTNG simulations: a tale of two elements - chemical evolution of magnesium and europium. *Monthly Notices of the Royal Astronomical Society*, 477(1):1206–1224.

Navarro, J. F., Frenk, C. S., and White, S. D. M. (1997). A Universal Density Profile from Hierarchical Clustering. *The Astrophysical Journal*, 490:493–508.

Nelson, D., Pillepich, A., Springel, V., Weinberger, R., Hernquist, L., Pakmor, R., Genel, S., Torrey, P., Vogelsberger, M., Kauffmann, G., Marinacci, F., and Naiman, J. (2018). First results from the IllustrisTNG simulations: the galaxy colour bimodality. *Monthly Notices of the Royal Astronomical Society*, 475(1):624–647.

Nelson, D., Springel, V., Pillepich, A., Rodriguez-Gomez, V., Torrey, P., Genel, S., Vogelsberger, M., Pakmor, R., Marinacci, F., Weinberger, R., Kelley, L., Lovell, M., Diemer, B., and Hernquist, L. (2019). The IllustrisTNG simulations: public data release. *Computational Astrophysics and Cosmology*, 6(1):2.

Nishimichi, T., Takada, M., Takahashi, R., Osato, K., Shirasaki, M., Oogi, T., Miyatake, H., Oguri, M., Murata, R., Kobayashi, Y., and Yoshida, N. (2018). Dark Quest. I. Fast and Accurate Emulation of Halo Clustering Statistics and Its Application to Galaxy Clustering. *arXiv e-prints*, page arXiv:1811.09504.

Ondaro-Mallea, L., Angulo, R. E., Zennaro, M., Contreras, S., and Aricò, G. (2021). Non-universality of the mass function: dependence on the growth rate and power spectrum shape. *arXiv e-prints*, page arXiv:2102.08958.

Orsi, Á. A. and Angulo, R. E. (2018). The impact of galaxy formation on satellite kinematics and redshift-space distortions. *Monthly Notices of the Royal Astronomical Society*, 475(2):2530–2544.

Parimbelli, G., Viel, M., and Sefusatti, E. (2019). On the degeneracy between baryon feedback and massive neutrinos as probed by matter clustering and weak lensing. *Journal of Cosmology and Astroparticle Physics*, 1:010.

Park, H., Alvarez, M. A., and Bond, J. R. (2018). The Impact of Baryonic Physics on the Kinetic Sunyaev-Zel'dovich Effect. *The Astrophysical Journal*, 853(2):121.

Pellejero-Ibañez, M., Angulo, R. E., Aricó, G., Zennaro, M., Contreras, S., and Stücker, J. (2020). Cosmological parameter estimation via iterative emulation of likelihoods. *Monthly Notices of the Royal Astronomical Society*, 499(4):5257–5268.

Perivolaropoulos, L. and Skara, F. (2021). Challenges for ΛCDM: An update. *arXiv e-prints*, page arXiv:2105.05208.

Pietroni, M. (2008). Flowing with time: a new approach to non-linear cosmological perturbations. *Journal of Cosmology and Astroparticle Physics*, 2008(10):036.

Pillepich, A., Nelson, D., Hernquist, L., Springel, V., Pakmor, R., Torrey, P., Weinberger, R., Genel, S., Naiman, J. P., Marinacci, F., and Vogelsberger, M. (2018). First results from the IllustrisTNG simulations: the stellar mass content of groups and clusters of galaxies. *Monthly Notices of the Royal Astronomical Society*, 475(1):648–675.

Planck Collaboration, Ade, P. A. R., Aghanim, N., Armitage-Caplan, C., Arnaud, M., Ashdown, M., Atrio-Barand ela, F., Aumont, J., Baccigalupi, C., Banday, A. J., Barreiro, R. B., Bartlett, J. G., Battaner, E., Benabed, K., Benoît, A., Benoit-Lévy, A., Bernard, J. P., Bersanelli, M., Bielewicz, P., Bobin, J., Bock, J. J., Bonaldi, A., Bond, J. R., Borrill, J., Bouchet, F. R., Bridges, M., Bucher, M., Burigana, C., Butler, R. C., Calabrese, E., Cappellini, B., Cardoso, J. F., Catalano, A., Challinor, A., Chamballu, A., Chary, R. R., Chen, X., Chiang, H. C., Chiang, L. Y., Christensen, P. R., Church, S., Clements, D. L., Colombi, S., Colombo, L. P. L., Couchot, F., Coulais, A., Crill, B. P., Curto, A., Cuttaia, F., Danese, L., Davies, R. D., Davis, R. J., de Bernardis, P., de Rosa, A., de Zotti, G., Delabrouille, J., Delouis, J. M., Désert, F. X., Dickinson, C., Diego, J. M., Dolag, K., Dole, H., Donzelli, S., Doré, O., Douspis, M., Dunkley, J., Dupac, X., Efstathiou, G., Elsner, F., Enßlin, T. A., Eriksen, H. K., Finelli, F., Forni, O., Frailis, M., Fraisse, A. A., Franceschi, E., Gaier, T. C., Galeotta, S., Galli, S., Ganga, K., Giard, M., Giardino, G., Giraud-Héraud, Y., Gjerløw, E., González-Nuevo, J., Górski, K. M., Gratton, S., Gregorio, A., Gruppuso, A., Gudmundsson, J. E., Haissinski, J., Hamann, J., Hansen, F. K., Hanson, D., Harrison, D., Henrot-Versillé, S., Hernández-Monteagudo, C., Herranz, D., Hildebrand t, S. R., Hivon, E., Hobson, M., Holmes, W. A., Hornstrup, A., Hou, Z., Hovest, W., Huffenberger, K. M., Jaffe, A. H., Jaffe, T. R., Jewell, J., Jones, W. C., Juvela, M., Keihänen, E., Keskitalo, R., Kisner, T. S., Kneissl, R., Knoche, J., Knox, L., Kunz, M., Kurki-Suonio, H., Lagache, G., Lähteenmäki, A., Lamarre, J. M., Lasenby, A., Lattanzi, M., Laureijs, R. J., Lawrence, C. R., Leach, S., Leahy, J. P., Leonardi, R., León-Tavares, J., Lesgourgues, J., Lewis, A., Liguori, M., Lilje, P. B., Linden-Vørnle, M., López-Caniego, M., Lubin, P. M., Macías-Pérez, J. F., Maffei, B., Maino, D., Mand olesi, N., Maris, M., Marshall, D. J., Martin, P. G., Martínez-González, E., Masi, S., Massardi, M., Matarrese, S., Matthai, F., Mazzotta, P., Meinhold, P. R., Melchiorri, A., Melin, J. B., Mendes, L., Menegoni, E., Mennella, A., Migliaccio, M., Millea, M., Mitra, S., Miville-Deschênes, M. A., Moneti, A., Montier, L., Morgante, G., Mortlock, D., Moss, A., Munshi, D., Murphy, J. A., Naselsky, P., Nati, F., Natoli, P., Netterfield, C. B., Nørgaard-Nielsen, H. U., Noviello, F., Novikov, D., Novikov, I., O'Dwyer, I. J., Osborne, S., Oxborrow, C. A., Paci, F., Pagano, L., Pajot, F., Paladini, R., Paoletti, D., Partridge, B., Pasian, F., Patanchon, G., Pearson, D., Pearson, T. J., Peiris, H. V., Perdereau, O., Perotto, L., Perrotta, F., Pettorino, V., Piacentini, F., Piat, M., Pierpaoli, E., Pietrobon, D., Plaszczynski, S., Platania, P., Pointecouteau, E., Polenta, G., Ponthieu, N., Popa, L., Poutanen, T., Pratt, G. W., Prézeau, G., Prunet, S., Puget, J. L., Rachen, J. P., Reach, W. T., Rebolo, R., Reinecke, M., Remazeilles, M., Renault, C., Ricciardi, S., Riller, T., Ristorcelli, I., Rocha, G., Rosset, C., Roudier, G., Rowan-Robinson, M., Rubiño-Martín, J. A., Rusholme, B., Sandri, M., Santos, D., Savelainen, M., Savini, G., Scott, D., Seiffert, M. D., Shellard, E. P. S., Spencer, L. D., Starck, J. L., Stolyarov, V., Stompor, R., Sudiwala, R., Sunyaev, R., Sureau, F., Sutton, D., Suur-Uski, A. S., Sygnet, J. F., Tauber, J. A., Tavagnacco, D., Terenzi, L., Toffolatti, L., Tomasi, M., Tristram, M., Tucci, M., Tuovinen, J., Türler, M., Umana, G., Valenziano, L., Valiviita, J., Van Tent, B., Vielva, P., Villa, F., Vittorio, N., Wade, L. A., Wandelt, B. D., Wehus, I. K., White, M., White, S. D. M., Wilkinson, A., Yvon, D., Zacchei, A., and Zonca, A. (2014a). Planck 2013 results. XVI. Cosmological parameters. *Astronomy and Astrophysics*, 571:A16.

Planck Collaboration, Ade, P. A. R., Aghanim, N., Armitage-Caplan, C., Arnaud, M., Ashdown, M., Atrio-Barandela, F., Aumont, J., Baccigalupi, C., Banday, A. J., and et al. (2014b). Planck 2013 results. XVI. Cosmological parameters. *Astronomy and Astrophysics*, 571:A16.

Planck Collaboration, Aghanim, N., Akrami, Y., Ashdown, M., Aumont, J., Baccigalupi, C., Ballardini, M., Banday, A. J., Barreiro, R. B., Bartolo, N., Basak, S., Battye, R., Benabed, K., Bernard, J.-P., Bersanelli, M., Bielewicz, P., Bock, J. J., Bond, J. R., Borrill, J., Bouchet, F. R., Boulanger, F., Bucher, M., Burigana, C., Butler, R. C., Calabrese, E., Cardoso, J.-F., Carron, J., Challinor, A., Chiang, H. C., Chluba, J., Colombo, L. P. L., Combet, C., Contreras, D., Crill, B. P., Cuttaia, F., de Bernardis, P., de Zotti, G., Delabrouille, J., Delouis, J.-M., Di Valentino, E., Diego, J. M., Doré, O., Douspis, M., Ducout, A., Dupac, X., Dusini, S., Efstathiou, G., Elsner, F., Enßlin, T. A., Eriksen, H. K., Fantaye, Y., Farhang, M., Fergusson, J., Fernandez-Cobos, R., Finelli, F., Forastieri, F., Frailis, M., Franceschi, E., Frolov, A., Galeotta, S., Galli, S., Ganga, K., Génova-Santos, R. T., Gerbino, M., Ghosh, T., González-Nuevo, J., Górski, K. M., Gratton, S., Gruppuso, A., Gudmundsson, J. E., Hamann, J., Handley, W., Herranz, D., Hivon, E., Huang, Z., Jaffe, A. H., Jones, W. C., Karakci, A., Keihänen, E., Keskitalo, R., Kiiveri, K., Kim, J., Kisner, T. S., Knox, L., Krachmalnicoff, N., Kunz, M., Kurki-Suonio, H., Lagache, G., Lamarre, J.-M., Lasenby, A., Lattanzi, M., Lawrence, C. R., Le Jeune, M., Lemos, P., Lesgourgues, J., Levrier, F., Lewis, A., Liguori, M., Lilje, P. B., Lilley, M., Lindholm, V., López-Caniego, M., Lubin, P. M., Ma, Y.-Z., Macías-Pérez, J. F., Maggio, G., Maino, D., Mandolesi, N., Mangilli, A., Marcos-Caballero, A., Maris, M., Martin, P. G., Martinelli, M., Martínez-González, E., Matarrese, S., Mauri, N., McEwen, J. D., Meinhold, P. R., Melchiorri, A., Mennella, A., Migliaccio, M., Millea, M., Mitra, S., Miville-Deschênes, M.-A., Molinari, D., Montier, L., Morgante, G., Moss, A., Natoli, P., Nørgaard-Nielsen, H. U., Pagano, L., Paoletti, D., Partridge, B., Patanchon, G., Peiris, H. V., Perrotta, F., Pettorino, V., Piacentini, F., Polastri, L., Polenta, G., Puget, J.-L., Rachen, J. P., Reinecke, M., Remazeilles, M., Renzi, A., Rocha, G., Rosset, C., Roudier, G., Rubiño-Martín, J. A., Ruiz-Granados, B., Salvati, L., Sandri, M., Savelainen, M., Scott, D., Shellard, E. P. S., Sirignano, C., Sirri, G., Spencer, L. D., Sunyaev, R., Suur-Uski, A.-S., Tauber, J. A., Tavagnacco, D., Tenti, M., Toffolatti, L., Tomasi, M., Trombetti, T., Valenziano, L., Valiviita, J., Van Tent, B., Vibert, L., Vielva, P., Villa, F., Vittorio, N., Wandelt, B. D., Wehus, I. K., White, M., White, S. D. M., Zacchei, A., and Zonca, A. (2018). Planck 2018 results. VI. Cosmological parameters. *arXiv e-prints*.

Planck Collaboration 2015 results XIII (2016). Planck 2015 results. XIII. Cosmological parameters. *Astronomy and Astrophysics*, 594:A13.

Pontzen, A., Slosar, A., Roth, N., and Peiris, H. V. (2016). Inverted initial conditions: Exploring the growth of cosmic structure and voids. *Phys. Rev. D Physical Review D: Particles, Fields, Gravitation & Cosmology*, 93(10):103519.

Potter, D., Stadel, J., and Teyssier, R. (2017). PKDGRAV3: beyond trillion particle cosmological simulations for the next era of galaxy surveys. *Computational Astrophysics and Cosmology*, 4(1):2.

Poveda-Ruiz, C. N., Forero-Romero, J. E., and Muñoz-Cuartas, J. C. (2016). Quantifying and Controlling Biases in Estimates of Dark Matter Halo Concentration. *The Astrophysical Journal*, 832(2):169.

Renneby, M., Hilbert, S., and Angulo, R. E. (2018). Halo mass and weak galaxy-galaxy lensing profiles in rescaled cosmological N-body simulations. *Monthly Notices of the Royal Astronomical Society*, 479:1100–1124.

Riess, A. G. (2019). The expansion of the Universe is faster than expected. *Nature Reviews Physics*, 2(1):10–12.

Riess, A. G., Filippenko, A. V., Challis, P., Clocchiatti, A., Diercks, A., Garnavich, P. M., Gilliland, R. L., Hogan, C. J., Jha, S., Kirshner, R. P., Leibundgut, B., Phillips, M. M., Reiss, D., Schmidt, B. P., Schommer, R. A., Smith, R. C., Spyromilio, J., Stubbs, C., Suntzeff, N. B., and Tonry, J. (1998). Observational Evidence from Supernovae for an Accelerating Universe and a Cosmological Constant. *Astronomical Journal*, 116:1009–1038.

Rogers, K. K., Peiris, H. V., Pontzen, A., Bird, S., Verde, L., and Font-Ribera, A. (2019). Bayesian emulator optimisation for cosmology: application to the Lyman-alpha forest. *Journal of Cosmology and Astroparticle Physics*, 2019(2):031.

Ruiz, A. N., Padilla, N. D., Domínguez, M. J., and Cora, S. A. (2011). How accurate is it to update the cosmology of your halo catalogues? *Monthly Notices of the Royal Astronomical Society*, 418:2422–2434.

Schaye, J., Crain, R. A., Bower, R. G., Furlong, M., Schaller, M., Theuns, T., Dalla Vecchia, C., Frenk, C. S., McCarthy, I. G., Helly, J. C., Jenkins, A., Rosas-Guevara, Y. M., White, S. D. M., Baes, M., Booth, C. M., Camps, P., Navarro, J. F., Qu, Y., Rahmati, A., Sawala, T., Thomas, P. A., and Trayford, J. (2015). The EAGLE project: simulating the evolution and assembly of galaxies and their environments. *Monthly Notices of the Royal Astronomical Society*, 446:521–554.

Schaye, J., Dalla Vecchia, C., Booth, C. M., Wiersma, R. P. C., Theuns, T., Haas, M. R., Bertone, S., Duffy, A. R., McCarthy, I. G., and van de Voort, F. (2010). The physics driving the cosmic star formation history. *Monthly Notices of the Royal Astronomical Society*, 402(3):1536–1560.

Schneider, A., Stoira, N., Refregier, A., Weiss, A. J., Knabenhans, M., Stadel, J., and Teyssier, R. (2020). Baryonic effects for weak lensing. Part I. Power spectrum and covariance matrix. *Journal of Cosmology and Astroparticle Physics*, 2020(4):019.

Schneider, A. and Teyssier, R. (2015a). A new method to quantify the effects of baryons on the matter power spectrum. *Journal of Cosmology and Astroparticle Physics*, 12:049.

Schneider, A. and Teyssier, R. (2015b). A new method to quantify the effects of baryons on the matter power spectrum. *Journal of Cosmology and Astroparticle Physics*, 12:049.

Schneider, A., Teyssier, R., Potter, D., Stadel, J., Onions, J., Reed, D. S., Smith, R. E., Springel, V., Pearce, F. R., and Scoccimarro, R. (2016). Matter power spectrum and the challenge of percent accuracy. *Journal of Cosmology and Astroparticle Physics*, 4:047.

Schneider, A., Teyssier, R., Stadel, J., Chisari, N. E., Le Brun, A. M. C., Amara, A., and Refregier, A. (2019). Quantifying baryon effects on the matter power spectrum and the weak lensing shear correlation. *Journal of Cosmology and Astroparticle Physics*, 2019(3):020.

Scoccimarro, R. (2000). The Bispectrum: From Theory to Observations. *The Astrophysical Journal*, 544(2):597–615.

Sefusatti, E., Crocce, M., Scoccimarro, R., and Couchman, H. M. P. (2016). Accurate estimators of correlation functions in Fourier space. *Monthly Notices of the Royal Astronomical Society*, 460:3624–3636.

Sefusatti, E. and Komatsu, E. (2007). Bispectrum of galaxies from high-redshift galaxy surveys: Primordial non-Gaussianity and nonlinear galaxy bias. *Phys. Rev. D Physical Review D: Particles, Fields, Gravitation & Cosmology*, 76(8):083004.

Seljak, U. and Zaldarriaga, M. (1996). A Line-of-Sight Integration Approach to Cosmic Microwave Background Anisotropies. *The Astrophysical Journal*, 469:437.

Semboloni, E., Hoekstra, H., and Schaye, J. (2013). Effect of baryonic feedback on two- and three-point shear statistics: prospects for detection and improved modelling. *Monthly Notices of the Royal Astronomical Society*, 434(1):148–162.

Semboloni, E., Hoekstra, H., Schaye, J., van Daalen, M. P., and McCarthy, I. G. (2011). Quantifying the effect of baryon physics on weak lensing tomography. *Monthly Notices of the Royal Astronomical Society*, 417:2020–2035.

Sijacki, D., Vogelsberger, M., Genel, S., Springel, V., Torrey, P., Snyder, G. F., Nelson, D., and Hernquist, L. (2015). The Illustris simulation: the evolving population of black holes across cosmic time. *Monthly Notices of the Royal Astronomical Society*, 452(1):575–596.

Smith, R. E. and Angulo, R. E. (2019). Precision modelling of the matter power spectrum in a Planck-like Universe. *Monthly Notices of the Royal Astronomical Society*, 486(1):1448–1479.

Smith, R. E., Peacock, J. A., Jenkins, A., White, S. D. M., Frenk, C. S., Pearce, F. R., Thomas, P. A., Efstathiou, G., and Couchman, H. M. P. (2003). Stable clustering, the halo model and non-linear cosmological power spectra. *Monthly Notices of the Royal Astronomical Society*, 341(4):1311–1332.

Spergel, D., Gehrels, N., Baltay, C., Bennett, D., Breckinridge, J., Donahue, M., Dressler, A., Gaudi, B. S., Greene, T., Guyon, O., Hirata, C., Kalirai, J., Kasdin, N. J., Macintosh, B., Moos, W., Perlmutter, S., Postman, M., Rauscher, B., Rhodes, J., Wang, Y., Weinberg, D., Benford, D., Hudson, M., Jeong, W. S., Mellier, Y., Traub, W., Yamada, T., Capak, P., Colbert, J., Masters, D., Penny, M., Savransky, D., Stern, D., Zimmerman, N., Barry, R., Bartusek, L., Carpenter, K., Cheng, E., Content, D., Dekens, F., Demers, R., Grady, K., Jackson, C., Kuan, G., Kruk, J., Melton, M., Nemati, B., Parvin, B., Poberezhskiy, I., Peddie, C., Ruffa, J., Wallace, J. K., Whipple, A., Wollack, E., and Zhao, F. (2015). Wide-Field InfrarRed Survey Telescope-Astrophysics Focused Telescope Assets WFIRST-AFTA 2015 Report. *arXiv e-prints*, page arXiv:1503.03757.

Springel, V. (2005). The cosmological simulation code GADGET-2. *Monthly Notices of the Royal Astronomical Society*, 364:1105–1134.

Springel, V. (2010). E pur si muove: Galilean-invariant cosmological hydrodynamical simulations on a moving mesh. *Monthly Notices of the Royal Astronomical Society*, 401:791–851.

Springel, V., Pakmor, R., Pillepich, A., Weinberger, R., Nelson, D., Hernquist, L., Vogelsberger, M., Genel, S., Torrey, P., Marinacci, F., and Naiman, J. (2018). First results from the IllustrisTNG simulations: matter and galaxy clustering. *Monthly Notices of the Royal Astronomical Society*, 475(1):676–698.

Springel, V., Pakmor, R., Zier, O., and Reinecke, M. (2020). Simulating cosmic structure formation with the GADGET-4 code. *arXiv e-prints*, page arXiv:2010.03567.

Springel, V., White, S. D. M., Tormen, G., and Kauffmann, G. (2001). Populating a cluster of galaxies - I. Results at [formmu2]z=0. *Monthly Notices of the Royal Astronomical Society*, 328:726–750.

Stücker, J., Hahn, O., Angulo, R. E., and White, S. D. M. (2019). Simulating the Complexity of the Dark Matter Sheet I: Numerical Algorithms. *arXiv e-prints*, page arXiv:1909.00008.

Sunyaev, R. A. and Zeldovich, Y. B. (1970). Small-Scale Fluctuations of Relic Radiation. *Astrophysics and Space Science*, 7(1):3–19.

Takahashi, R., Sato, M., Nishimichi, T., Taruya, A., and Oguri, M. (2012). Revising the Halofit Model for the Nonlinear Matter Power Spectrum. *The Astrophysical Journal*, 761:152.

Taylor, P. L., Bernardeau, F., and Huff, E. (2020). x-cut Cosmic Shear: Optimally Removing Sensitivity to Baryonic and Nonlinear Physics with an Application to the Dark Energy Survey Year 1 Shear Data. *arXiv e-prints*, page arXiv:2007.00675.

Taylor, P. L., Bernardeau, F., and Kitching, T. D. (2018a). k -cut cosmic shear: Tunable power spectrum sensitivity to test gravity. *Phys. Rev. D Physical Review D: Particles, Fields, Gravitation & Cosmology*, 98(8):083514.

Taylor, P. L., Kitching, T. D., and McEwen, J. D. (2018b). Preparing for the cosmic shear data flood: Optimal data extraction and simulation requirements for stage IV dark energy experiments. *Phys. Rev. D Physical Review D: Particles, Fields, Gravitation & Cosmology*, 98(4):043532.

Teyssier, R. (2002). Cosmological hydrodynamics with adaptive mesh refinement. A new high resolution code called RAMSES. *Astronomy and Astrophysics*, 385:337–364.

The EAGLE team (2017). The EAGLE simulations of galaxy formation: Public release of particle data. *arXiv e-prints*, page arXiv:1706.09899.

Tröster, T., Ferguson, C., Harnois-Déraps, J., and McCarthy, I. G. (2019). Painting with baryons: augmenting N-body simulations with gas using deep generative models. *Monthly Notices of the Royal Astronomical Society*, 487(1):L24–L29.

Troxel, M. A., MacCrann, N., Zuntz, J., Eifler, T. F., Krause, E., Dodelson, S., Gruen, D., Blazek, J., Friedrich, O., Samuroff, S., Prat, J., Secco, L. F., Davis, C., Ferté, A., DeRose, J., Alarcon, A., Amara, A., Baxter, E., Becker, M. R., Bernstein, G. M., Bridle, S. L., Cawthon, R., Chang, C., Choi, A., De Vicente, J., Drlica-Wagner, A., Elvin-Poole, J., Frieman, J., Gatti, M., Hartley, W. G., Honscheid, K., Hoyle, B., Huff, E. M., Huterer, D., Jain, B., Jarvis, M., Kacprzak, T., Kirk, D., Kokron, N., Krawiec, C., Lahav, O., Liddle, A. R., Peacock, J., Rau, M. M., Refregier, A., Rollins, R. P., Rozo, E., Rykoff, E. S., Sánchez, C., Sevilla-Noarbe, I., Sheldon, E., Stebbins, A., Varga, T. N., Vielzeuf, P., Wang, M., Wechsler, R. H., Yanny, B., Abbott, T. M. C., Abdalla, F. B., Allam, S., Annis, J., Bechtol, K., Benoit-Lévy, A., Bertin, E., Brooks, D., Buckley-Geer, E., Burke, D. L., Carnero Rosell, A., Carrasco Kind, M., Carretero, J., Castander, F. J., Crocce, M., Cunha, C. E., D'Andrea, C. B., da Costa, L. N., DePoy, D. L., Desai, S., Diehl, H. T., Dietrich, J. P., Doel, P., Fernandez, E., Flaugher, B., Fosalba, P., García-Bellido, J., Gaztanaga, E., Gerdes, D. W., Giannantonio, T., Goldstein, D. A., Gruendl, R. A., Gschwend, J., Gutierrez, G., James, D. J., Jeltema, T., Johnson, M. W. G., Johnson, M. D., Kent, S., Kuehn, K., Kuhlmann, S., Kuropatkin, N., Li, T. S., Lima, M., Lin, H., Maia, M. A. G., March, M., Marshall, J. L., Martini, P., Melchior, P., Menanteau, F., Miquel, R., Mohr, J. J., Neilsen, E., Nichol, R. C., Nord, B., Petravick, D., Plazas, A. A., Romer, A. K., Roodman, A., Sako, M., Sanchez, E., Scarpine, V., Schindler, R., Schubnell, M., Smith, M., Smith, R. C., Soares-Santos, M., Sobreira, F., Suchyta, E., Swanson, M. E. C., Tarle, G., Thomas, D., Tucker, D. L., Vikram, V., Walker, A. R., Weller, J., Zhang, Y., and DES Collaboration (2018). Dark Energy Survey Year 1 results: Cosmological constraints from cosmic shear. *Phys. Rev. D Physical Review D: Particles, Fields, Gravitation & Cosmology*, 98(4):043528.

Upadhye, A., Biswas, R., Pope, A., Heitmann, K., Habib, S., Finkel, H., and Frontiere, N. (2014). Large-scale structure formation with massive neutrinos and dynamical dark energy. *Phys. Rev. D Physical Review D: Particles, Fields, Gravitation & Cosmology*, 89(10):103515.

van Daalen, M. P., McCarthy, I. G., and Schaye, J. (2020). Exploring the effects of galaxy formation on matter clustering through a library of simulation power spectra. *Monthly Notices of the Royal Astronomical Society*, 491(2):2424–2446.

van Daalen, M. P., Schaye, J., Booth, C. M., and Dalla Vecchia, C. (2011). The effects of galaxy formation on the matter power spectrum: a challenge for precision cosmology. *Monthly Notices of the Royal Astronomical Society*, 415:3649–3665.

Verde, L., Treu, T., and Riess, A. G. (2019). Tensions between the early and late Universe. *Nature Astronomy*, 3:891–895.

Villaescusa-Navarro, F., Naess, S., Genel, S., Pontzen, A., Wandelt, B., Anderson, L., Font-Ribera, A., Battaglia, N., and Spergel, D. N. (2018). Statistical Properties of Paired Fixed Fields. *The Astrophysical Journal*, 867(2):137.

Villaescusa-Navarro, F., Wandelt, B. D., Anglés-Alcázar, D., Genel, S., Zorrilla Mantilla, J. M., Ho, S., and Spergel, D. N. (2020). Neural networks as optimal estimators to marginalize over baryonic effects. *arXiv e-prints*, page arXiv:2011.05992.

Vogelsberger, M., Genel, S., Sijacki, D., Torrey, P., Springel, V., and Hernquist, L. (2013). A model for cosmological simulations of galaxy formation physics. *Monthly Notices of the Royal Astronomical Society*, 436(4):3031–3067.

Vogelsberger, M., Genel, S., Springel, V., Torrey, P., Sijacki, D., Xu, D., Snyder, G., Bird, S., Nelson, D., and Hernquist, L. (2014a). Properties of galaxies reproduced by a hydrodynamic simulation. *Nature*, 509(7499):177–182.

Vogelsberger, M., Genel, S., Springel, V., Torrey, P., Sijacki, D., Xu, D., Snyder, G., Nelson, D., and Hernquist, L. (2014b). Introducing the Illustris Project: simulating the coevolution of dark and visible matter in the Universe. *Monthly Notices of the Royal Astronomical Society*, 444:1518–1547.

Watson, D. F. and Conroy, C. (2013). The Strikingly Similar Relation between Satellite and Central Galaxies and their Dark Matter Halos since z = 2. *The Astrophysical Journal*, 772(2):139.

Weinberg, D. H., Mortonson, M. J., Eisenstein, D. J., Hirata, C., Riess, A. G., and Rozo, E. (2013). Observational probes of cosmic acceleration. *Physics Reports*, 530:87–255.

Wibking, B. D., Salcedo, A. N., Weinberg, D. H., Garrison, L. H., Ferrer, D., Tinker, J., Eisenstein, D., Metchnik, M., and Pinto, P. (2019). Emulating galaxy clustering and galaxy-galaxy lensing into the deeply non-linear regime: methodology, information, and forecasts. *Monthly Notices of the Royal Astronomical Society*, 484(1):989–1006.

Winther, H. A., Casas, S., Baldi, M., Koyama, K., Li, B., Lombriser, L., and Zhao, G.-B. (2019). Emulators for the nonlinear matter power spectrum beyond Λ CDM. *Phys. Rev. D Physical Review D: Particles, Fields, Gravitation & Cosmology*, 100(12):123540.

Wong, K. C., Suyu, S. H., Chen, G. C. F., Rusu, C. E., Millon, M., Sluse, D., Bonvin, V., Fassnacht, C. D., Taubenberger, S., Auger, M. W., Birrer, S., Chan, J. H. H., Courbin, F., Hilbert, S., Tihhonova, O., Treu, T., Agnello, A., Ding, X., Jee, I., Komatsu, E., Shajib, A. J., Sonnenfeld, A., Bland ford, R. D., Koopmans, L. V. E., Marshall, P. J., and Meylan, G. (2020). H0LiCOW XIII. A 2.4% measurement of H_0 from lensed quasars: 5.3σ tension between early and late-Universe probes. *Monthly Notices of the Royal Astronomical Society*.

Zennaro, M., Angulo, R. E., Aricò, G., Contreras, S., and Pellejero-Ibáñez, M. (2019). How to add massive neutrinos to your ΛCDM simulation - extending cosmology rescaling algorithms. *Monthly Notices of the Royal Astronomical Society*, 489(4):5938–5951.

Zennaro, M., Angulo, R. E., Pellejero-Ibáñez, M., Stücker, J., Contreras, S., and Aricò, G. (2021). The BACCO simulation project: biased tracers in real space. *arXiv e-prints*, page arXiv:2101.12187.

Zennaro, M., Bel, J., Villaescusa-Navarro, F., Carbone, C., Sefusatti, E., and Guzzo, L. (2017). Initial conditions for accurate N-body simulations of massive neutrino cosmologies. *Monthly Notices of the Royal Astronomical Society*, 466(3):3244–3258.

Zhai, Z., Tinker, J. L., Becker, M. R., DeRose, J., Mao, Y.-Y., McClintock, T., McLaughlin, S., Rozo, E., and Wechsler, R. H. (2019). The Aemulus Project. III. Emulation of the Galaxy Correlation Function. *The Astrophysical Journal*, 874(1):95.

Appendices

Appendix A

Class setup

In this Appendix we provide some details on our `CLASS` setup and compare its predictions against those of `CAMB` .

In our `CLASS` calculations, we set the primordial helium fraction to $Y_{\mathrm{He}} = 0.24$, the optical depth at reionisation $\tau_{\mathrm{reio}} = 0.0952$, the number of (degenerate) massive neutrinos to $N_\nu = 3$, and the number of relativistic species $N_r = 3.046$. The neutrino to photon temperature is computed accounting for non-instantaneous neutrino decoupling and spectral distortions induced by the reheating, $T_\nu = 0.71611$.

To get an estimate of the absolute accuracy of the `CLASS` power spectra, we make a comparison against the predictions of another Boltzmann solver, `CAMB` (Lewis and Bridle, 2002). We use in `CAMB` , whenever possible, an analogous setup, specifying a degenerate neutrino hierarchy, and furthermore setting to True the *accurate_massive_neutrino_transfer* and *Reionization* options.

We compare both codes in 100 points distributed as a Latin hyper-cube, in a pure ΛCDM scenario, adding massive neutrinos, in a ΛCDM plus $w_0 w_{\mathrm{a}}$ dynamical dark energy, and finally in our full *extended* cosmological space. In Fig. A.1 we show the results of this comparison.

In the minimal ΛCDM scenario and in the $w_0 w_{\mathrm{a}}$ cosmologies, the two codes agree at the 0.1% level, except for $k > 10h\,\mathrm{Mpc}^{-1}$ where `CAMB` underestimates the `CLASS` solution by 0.2%, likely due to `CAMB` neglecting the impact of reionisation on the baryon sound speed (Lesgourgues, 2011b). When considering the massive neutrinos, the agreement degrades to a 0.5%, a value larger than what found in Lesgourgues and Tram (2011) but in agreement with Zennaro et al. (2017).

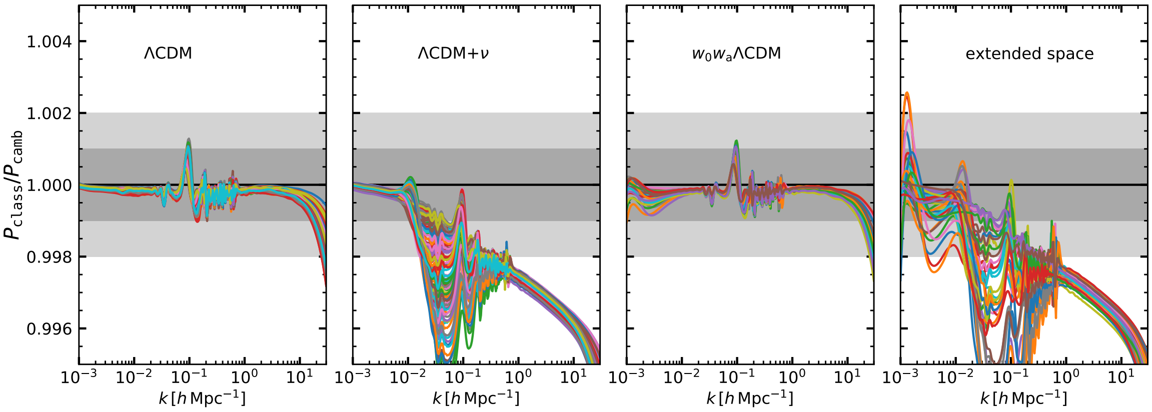

Figure A.1: Comparison of the linear power spectrum provided by two independent Bolztmann solvers `CLASS` and `CAMB` . Each panel displays the ratio for multiple cosmologies in the minimal ΛCDM model, ΛCDM plus neutrinos, ΛCDM plus dynamical dark energy, and in ΛCDM plus neutrinos and dynamical dark energy.

Appendix B

Analytical profiles of baryons and dark matter

In this appendix we report the analytical formulae used in this work to compute the density profiles of each component of the BCM. In the end, we obtain a total "baryon corrected" mass profile that we have to invert in order to find the Lagrangian displacement required to make the halo particles match the new profile. For every halo of the simulation, we fit a NFW profile, and we model our initial, gravity-only density profile as follow:

$$\rho_{\mathrm{GrO}}(x) = \begin{cases} \rho_0 \cdot x^{-1}(1+x)^{-2} & r \leq r_{200} \\ 0 & r > r_{200}, \end{cases} \tag{B.1}$$

where $x = r/r_s$ and r_s is the scale radius. We sharply truncate the profile at $r = r_{200}$, so that $M_{TOT} \equiv M_{200}$, where M_{TOT} is the integral of equation B.1 to infinity, r_{200} is the radius which enclose a mass M_{200} where the density is 200 times the critical density $\rho_c(z) \equiv 3H(z)^2/8\pi G$, $H(z)$ is the Hubble function and G the gravitational constant. The truncation of the initial profile imply a null displacement of the particles beyond r_{200}, hence we can consider just the particles inside r_{200}. Furthermore, we can avoid the modelling of the background as in Schneider and Teyssier (2015b), or the computationally expensive measurement of the 2-halo term e.g. Schneider et al. (2019).

We can compute now the four different components of the final profile. The different density profiles are normalised such as that for each component $M_i(r) = \int_0^\infty 4\pi r^2 \rho_i(r) dr = f_i \cdot M_{200}$, so that $\sum M_i(r) = M_{200}$, thus obviously $\sum f_i = 1$. Furthermore we truncate all the density profile at r_{200}, except for the ejected gas.

The central galaxy is modelled with a power-law with an exponential cut-off (Mohammed et al., 2014),

$$\rho_{\mathrm{CG}}(r) = f_{\mathrm{CG}} \cdot \frac{M_{200}}{4\pi^{3/2} R_h r^2} \cdot \exp\left(-\left(\frac{r}{2R_h}\right)^2\right), \tag{B.2}$$

where the half-mass radius is approximated as $R_h \approx 0.015 \cdot r_{200}$ (Kravtsov et al., 2018). There is no need to truncate the galaxy profile, because the exponential cut-off assures that the density at r_{200} is practically zero.

The hot, bound gas is modelled assuming hydrostatic equilibrium (Martizzi et al., 2013) up to $r < r_{200}/\sqrt{5}$, after which the gas is considered collisionless, thus following the NFW profile (Eq. B.1):

$$\rho_{\rm BG}(x) = f_{\rm BG} \cdot \begin{cases} y_0 \cdot (x^{-1}\ln(1+x))^{\Gamma_{eff}(c)} & r < r_{200}/\sqrt{5} \\ y_1 \cdot x^{-1}(1+x)^{-2} & r \leq r_{200} \\ 0 & r \geq r_{200}, \end{cases} \tag{B.3}$$

The effective polytropic index $\Gamma_{\rm eff}$ is defined such that the hydrostatic gas has the same slope of the NFW at $r = r_{200}/\sqrt{5}$:

$$\Gamma_{\rm eff}(c) = \frac{(1+3c/\sqrt{5})\ln(1+c/\sqrt{5})}{(1+c/\sqrt{5})ln(1+c/\sqrt{5}) - c/\sqrt{5}}, \tag{B.4}$$

where $c = r_{200}/r_s$ is the halo concentration. The normalisation factors y_0 and y_1 are defined such that the profile is continuous and $\int_0^\infty 4\pi r^2 \rho_{\rm BG}(r)dr = f_{\rm BG} \cdot M_{200} = M_{\rm BG}(r)$.

The ejected gas profile is computed assuming a Maxwell-Boltzmann velocity distribution of the particles expelled by the AGN, and behave as a constant with an exponential cut-off,

$$\rho_{\rm EG}(r) = \frac{M_{200}}{(2\pi r_{\rm ej}^2)^{3/2}} \exp\left(-\frac{1}{2}\left(\frac{r}{r_{\rm ej}}\right)^2\right), \tag{B.5}$$

where the *ejected radius* $r_{\rm ej}$ is the maximum radius reached by the expelled gas:

$$r_{\rm ej} \equiv \eta \cdot 0.75\, r_{\rm esc}, \tag{B.6}$$

with η as a free parameter. The halo escape radius is estimated assuming a constant halo escape velocity and a time-scale of a half Hubble time:

$$r_{\rm esc} \equiv \Delta t \cdot v_{\rm esc} \approx \Delta t\sqrt{\frac{8}{3}\pi G \Delta_{200}\rho_{\rm crit}} \approx \frac{1}{2}\sqrt{\Delta_{200}}r_{200}. \tag{B.7}$$

Finally, we compute the dark matter profile, defined as a piece-wise function: a NFW up to a scale r', a constant $\rho_{DM}(r_{200})$, between r' and r_{200} and 0 afterward. We make sure that the density profile is continuous at all scales by forcing the matching of the profiles at r_{200} and at r'. Within r_{200}, the density is given by the sum of all our BCM components, whereas beyond r_{200} the only contribution is given by the ejected gas, that must be be summed to the initial GrO density of the halo: $\sum \rho_i(r_{200}) = \rho_{EG}(r_{200}) + \rho_{GrO}(r_{200})$. Since $\rho_{CG}(r_{200}) \approx 0$, we obtain $\rho_{DM}(r_{200}) = \rho_{GrO}(r_{200}) - \rho_{BG}(r_{200})$; we force the new NFW to pass through the point $(r',\ \rho_{DM,200})$,

$$\rho_{\rm NFW}(x', \rho_0') = \frac{\rho_0'}{x'(1+x')^2}, \tag{B.8}$$

where $x' = r'/r_s$. We also impose the mass conservation, i.e.

$$\int_0^{r'} 4\pi r^2 \rho_{\rm NFW}(r, \rho_0'){\rm dr} + \int_{r'}^{r_{200}} 4\pi r^2 \rho_{\rm NFW}(r')dr = M_{DM}. \tag{B.9}$$

We can obtain r' and the new normalisation ρ'_0 minimising the function

$$r'(r_s + r')^2 \left[\rho_{\mathrm{GrO}}(r_{200}) - \rho_{\mathrm{BG}}(r_{200})\right] \left[\ln\left(1 + \frac{r'}{r_s}\right) - \frac{r'}{r' + r_s}\right] = \\ = -\frac{\rho_{\mathrm{GrO}}(r_{200}) - \rho_{\mathrm{BG}}(r_{200})}{3}\left(r_{200}^3 - r'^3\right) + \frac{f_{\mathrm{DM}} M_{200}}{4\pi}. \quad \text{(B.10)}$$

We compute then the expected baryonic back-reaction on the dark matter. We allow the dark matter profile to relax, so that the particles will expand (contract) depending if the total gravitational potential is shallower (deeper). Let us call M_i the initial mass contained in a sphere of radius r_i, whereas M_f will be the mass after relaxation inside a final radius r_f. Numerical simulations show that the halo relaxation is not perfectly adiabatic, i.e. $r_f/r_i \neq M_i/M_f$, but it follows the equation

$$\frac{r_f}{r_i} = 1 + a\left[\left(\frac{M_i}{M_f}\right)^n - 1\right], \quad \text{(B.11)}$$

where $a = 0.3$ and $n = 2$ (Abadi et al., 2010). Considering

$$\begin{cases} M_i(r_i) = M_{\mathrm{OG}}(r_i) \\ M_f(r_f) = f_{\mathrm{DM}} M_i + M_{\mathrm{EG}}(r_f) + M_{\mathrm{BG}}(r_f) + M_{\mathrm{CG}}(r_f), \end{cases} \quad \text{(B.12)}$$

we can solve the system of Eq.s B.12 and B.11 iteratively for $\xi = r/r_i$, furthermore imposing that $\xi(r_{200}) = 1$. The relaxed dark matter mass profile is thus

$$M_{\mathrm{RDM}}(r) = f_{\mathrm{DM}} \cdot M_{\mathrm{GrO}}(r/\xi), \quad \text{(B.13)}$$

and the density profile will be

$$\rho_{\mathrm{RDM}}(r) = \frac{1}{4\pi r^2}\frac{d}{dr} M_{\mathrm{RDM}}(r). \quad \text{(B.14)}$$

We now report the components mass fractions used in this work. The dark matter fraction is fixed at the cosmic density value, $f_{\mathrm{RDM}} = 1 - \Omega_b/\Omega_m$. The central galaxy fraction is given by the parametrisation from abundance matching by Behroozi et al. (2013):

$$f_{\mathrm{CG}}(M_{200}) = \epsilon\left(\frac{M_1}{M_{200}}\right) 10^{g(\log_{10}(M_{200}/M_1)) - g(0)}, \quad \text{(B.15)}$$

$$g(x) = -\log_{10}(10^{\alpha x} + 1) + \delta\frac{(\log_{10}(1 + \exp(x)))^\gamma}{1 + \exp(10^{-x})}. \quad \text{(B.16)}$$

We use the best-fitting parameters at $z = 0$ given by Kravtsov et al. (2018), while assuming the redshift dependence given by Behroozi et al. (2013):

$$\nu(a) = \exp(-4a^2)$$

$$\begin{aligned}
\log_{10}(M_1) &= M_{1,0} + (M_{1,a}(a-1) + M_{1,z}z)\nu \\
\log_{10}(\epsilon) &= \epsilon_0 + (\epsilon_a(a-1))\nu + \epsilon_{a,2}(a-1) \\
\alpha &= \alpha_0 + (\alpha_a(a-1))\nu \\
\delta &= \delta_0 + (\delta_a(a-1) + \delta_z z)\nu \\
\gamma &= \gamma_0 + (\gamma_a(a-1) + \gamma_z z)\nu,
\end{aligned} \tag{B.17}$$

with $M_{1,a} = -1.793$, $M_{1,z} = -0.251$, $\epsilon_0 = \log_{10(0.023)}$, $\epsilon_a = -0.006$, $\epsilon_{a,2} = -0.119$, $\alpha_0 = -1.779$, $\alpha_a = 0.731$, $\delta_0 = 4.394$, $\delta_a = 2.608$, $\delta_z = -0.043$, $\gamma_0 = 0.547$, $\gamma_a = 1.319$, $\gamma_z = 0.279$.

We set the characteristic halo mass, $M_{1,0}$, for which the galaxy-to-halo mass fraction is ϵ_0, as a free parameter of the model. Notice that, however, we quote throughout the paper the derived parameter M_1.

The hot gas mass fraction reads

$$f_{\rm BG}(M_{200}) = \frac{\Omega_b/\Omega_m - f_{\rm CG}}{(1 + (M_c/M_{200})^{\beta})}, \tag{B.18}$$

with M_c and β free parameters. Notice that, for $M_c = M_{200}$ we obtain $f_{\rm BG} = 0.5\,\Omega_b/\Omega_m - f_{\rm CG}$, i.e. half of the gas is retained in the halo.

The ejected gas mass fraction is simply

$$f_{\rm EG}(M_{200}) = \Omega_b/\Omega_m - f_{\rm CG}(M_{200}) - f_{\rm BG}(M_{200}). \tag{B.19}$$

In this way, high values of M_c imply that all the gas is expelled even from massive haloes, and vice versa for low values of M_c progressively smaller halos are gas rich.

To recap, in our modelling we have four free parameters: η, directly proportional to the halo ejected radius, escape radius and critical radius; M_c is the characteristic halo mass for which half of the gas is retained; β describes how fast the depletion of gas increase going toward smaller haloes; M_1, which is the characteristic halo mass that host a central galaxy of a given mass.

Appendix C

Subsampling of components particles

Once we have the galaxy, hot gas, ejected gas and dark matter analytical profiles, we can tag and re-scale the mass of the gravity-only particles to match those profiles. In this way, we can get a "baryonic" simulation. The main steps of the algorithm are the following:

- Compute the theoretical cumulative and differential mass profiles of the different components;
- Compute the theoretical bin/total mass fraction for each component f;
- Count the number of halo particles per radial bin C;
- The quantity $\mathcal{N} = f \cdot C$ gives the number of particles per radial bin per component;
- Iteratively add to $\mathcal{N}$ the particles missing for discretisation (roundoff);
- The mass of the particles per component and per radial bin is given by

  $$m = m_p \cdot \frac{C}{\mathcal{N}} \frac{M_c}{M_{bcm}}, \tag{C.1}$$

  where m_p is the particle mass in the gravity-only original simulation and M_c and M_{bcm} are the component and the total *baryonic correction* differential mass profiles, respectively.

Appendix D

Convergence of the *baryon* simulation

We have test the convergence of the *baryonic* suppression by running three simulations with increasing volume and number of particles, while keeping same resolution. In particular, we have run simulations with $64\,h^{-1}\mathrm{Mpc}$, $128\,h^{-1}\mathrm{Mpc}$ and $256\,h^{-1}\mathrm{Mpc}$ of box side, with $N = 192$, $N = 384$ and $N = 768$ cubic particles, respectively. All the simulations share the same initial conditions, and for each different volume we have run two simulations with fixed amplitude and shifted phases as reported in §3.2. In Fig. D.1 we show the suppression $S(k)$, defined as the ratio between baryonic and gravity only matter power spectra, for the three simulations at $z = 0$. We consider a BCM with the following parameters: $M_c = 1.2 \cdot 10^{14}\,h^{-1}\mathrm{M}_{\odot}$, $\eta = 0.5$, $\beta = 0.6$, $M_1 = 2.2 \cdot 10^{11} h^{-1}\mathrm{M}_{\odot}$. We note that even if the cosmic variance is consistently different, this contribution is canceled out at first order in the ratio of the power spectra, which are consistent with each other well within 1%. In the bottom panel of Fig. D.1, we show the difference in suppression between using standard and *paired and fixed* simulations. For the biggest volume considered the suppression is practically the same (solid line), and even for the smallest volume the difference is well within 1% (dotted line).

We have investigated moreover the contribution of different halo masses to the total baryonic suppression. As shown in the upper panel of D.1, the biggest relative contribution is given by haloes of mass $M = 10^{14} - 10^{15}\,h^{-1}\mathrm{M}_{\odot}$ and $10^{13} - 10^{14}\,h^{-1}\mathrm{M}_{\odot}$. It appears that the number of very massive haloes ($M \geq 10^{15}\,h^{-1}\mathrm{M}_{\odot}$) is not sufficient to produce an effect lager than 1%, even for the largest simulation considered in this work. Haloes with masses $M \leq 10^{13}\,h^{-1}\mathrm{M}_{\odot}$ have an impact of $\approx 2\%$ on small scales, $k \approx 5\,h\,\mathrm{Mpc}^{-1}$.

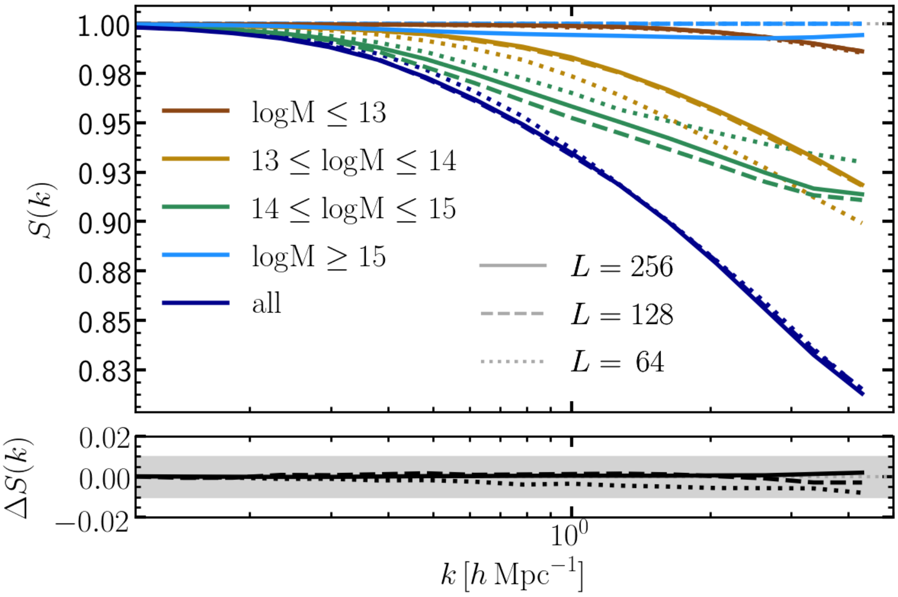

Figure D.1: *Upper panel:* Baryon suppression of the matter power spectrum, defined as $S(k) \equiv P_{\mathrm{BCM}}/P_{\mathrm{GrO}}$ at $z = 0$. Solid, dashed and dotted lines are computed with simulations of box side 256, 128 and 64 h^{-1}Mpc and 768^3, 384^3 and 192^3 particles, respectively. Colors are referred to different halo mass bins, expressed in decimal logarithm of $h^{-1}\mathrm{M}_{\odot}$, with which the baryon corrections have been computed, according to the legend. *Lower panel:* Difference in suppression between two *paired and fixed* simulations and a single one, for the three different volumes specified in the legend of the upper panel.

Appendix E

Convergence test

In this Appendix, we show the tests we have performed to assure that the baryonic effects on the clustering measurements have converged.

First, we test the convergence with the simulation box size. For this, we have used our suite of simulations with $64\,h^{-1}\mathrm{Mpc}$, $128\,h^{-1}\mathrm{Mpc}$, $256\,h^{-1}\mathrm{Mpc}$, and $512\,h^{-1}\mathrm{Mpc}$ of box side, with $N = 192$, $N = 384$, $N = 768$ and $N = 1536$ cubic particles, respectively. All the simulations have same force and mass resolution, and share the same initial conditions. For each different volume we have run two simulations with fixed amplitude and shifted phases as reported in §4.2.

In Fig. E.1 we show the suppression $S(k)$, defined as the ratio between baryonified and gravity-only matter power spectra and equilateral bispectra, measured in the four different boxes at $z = 0$.

We have also separated the contribution to the clustering of different halo masses, to get more insight on the origin of the discrepancies between the different boxes. As expected, we note that the boxsize does not affect sensibly haloes of $M \leq 10^{14}\,h^{-1}\mathrm{M}_{\odot}$. However, the abundance of massive haloes ($M = 10^{14} - 10^{15}\,h^{-1}\mathrm{M}_{\odot}$) varies consistently among the various boxes, leading to discrepancies in the baryonic effects that are still within 1% in the power spectrum, but slightly higher in the bispectrum ($3 - 4\%$).

In the bottom panels of Fig. E.1 we display the impact of using a *paired and fixed simulation* against a single realisation. Also in this case, the biggest impact is found in the bispectrum, with a maximum of $\approx 2.5\%$ bias when using a $64\,h^{-1}\mathrm{Mpc}$ box, whereas we detect a maximum of $\approx 1\%$ in the power spectrum. In the analysis, we make use of a single realisation of the $256\,h^{-1}\mathrm{Mpc}$ box, which is shown to be converged within 2%.

We have performed also a mass resolution test, by using four simulation with the same box size, $133\,h^{-1}\mathrm{Mpc}$, and different number of particles: $N = 256^3$, $N = 384^3$, $N = 512^3$, $N = 768^3$ particles. Also in this case, we split the contribution of different halo mass bins. As shown in Fig. E.2, we have found that resolution effects are larger in large haloes, and their impact in the power spectrum and bispectrum is within $\approx 2\%$.

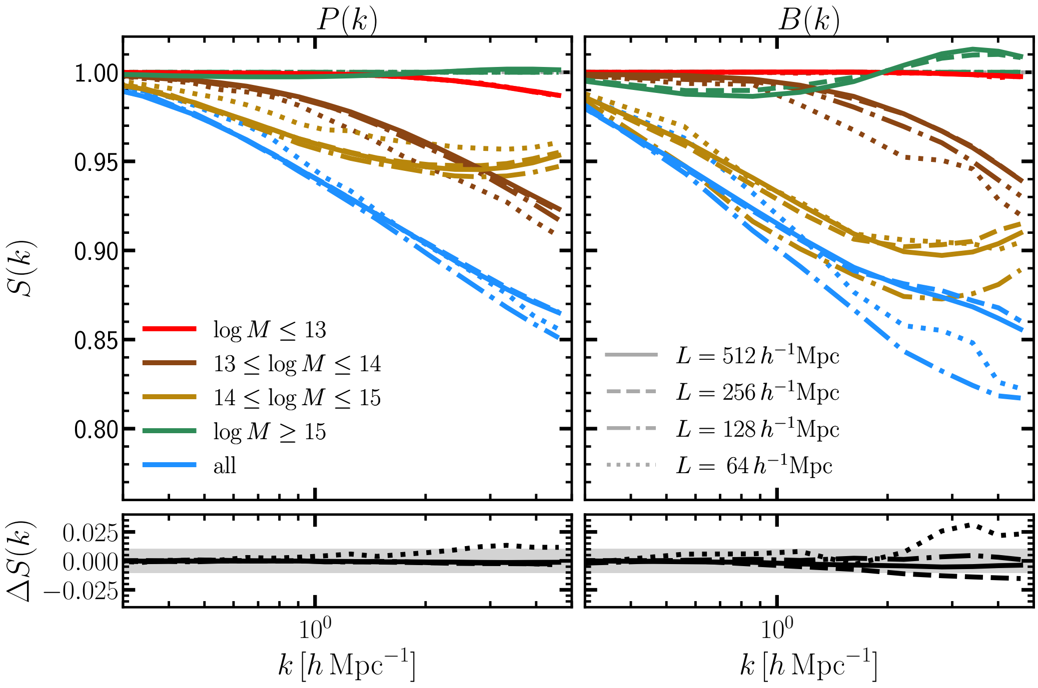

Figure E.1: *Upper panel:* Baryon suppression of the matter power spectrum (left) and reduced bispectrum (right), defined as $S(k) \equiv T(k)_{\mathrm{BCM}}/T(k)_{\mathrm{GrO}}$ for $T(k) = P(k), Q(k)$, at $z = 0$. Solid, dashed, dashed-dotted and dotted lines are computed with simulations of box side 512, 256, 128 and $64\,h^{-1}\mathrm{Mpc}$ and 1536^3, 768^3, 384^3 and 192^3 particles, respectively. Colors are referred to different halo mass bins, expressed in decimal logarithm of $h^{-1}\mathrm{M}_{\odot}$, with which the baryon corrections have been computed, according to the legend. *Lower panel:* Difference in suppression between a *paired and fixed* simulation and a single realisation, for the four different volumes specified in the legend of the upper panel.

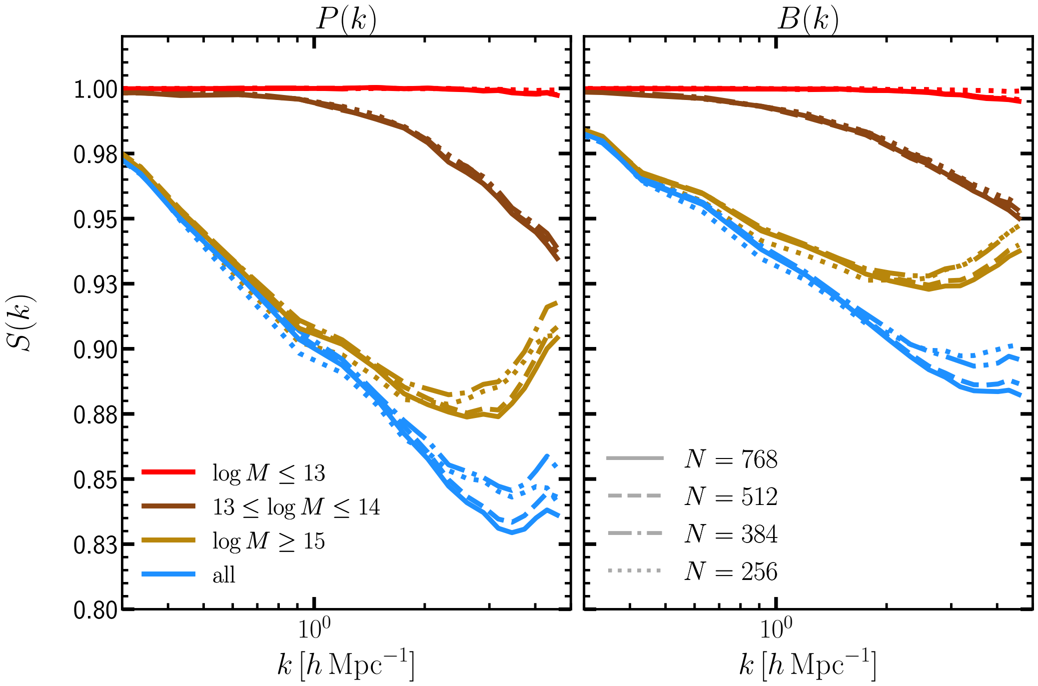

Figure E.2: Baryon suppression of the matter power spectrum (left) and reduced bispectrum (right), defined as $S(k) \equiv T(k)_{\mathrm{BCM}}/T(k)_{\mathrm{GrO}}$ for $T(k) = \{P(k), Q(k)\}$, at $z = 0$. Solid, dashed, dashed-dotted and dotted lines are computed with simulations of box side 133 h^{-1}Mpc and 768^3, 512^3, 384^3 and 256^3 particles, respectively. Colours are referred to different halo mass bins, expressed in decimal logarithm of $h^{-1}\mathrm{M}_{\odot}$, with which the baryon corrections have been computed, according to the legend.

Appendix F

Folding of the particle distribution

Measuring the three-point clustering with the classical Fourier estimators can be very expensive in terms of memory and CPU, especially when using covering larger dynamical ranges. In fact, it is easy to see that, being $k_{\rm Ny} = \pi N_g/L_{\rm box}$ the Nyquist frequency of the grid, increasingly large number of grid points N_g are required to get a given accuracy at a fixed wavenumber, when using progressively larger simulation boxes $L_{\rm box}$. Additionally, when using "interlacing" to suppress aliasing, the number of grids used must be doubled (Sefusatti et al., 2016).

However, since our measurements are limited by discreteness noise (and not cosmic variance), we can obtain accurate estimates of Fourier statistics on small scales by folding the density field (Jenkins et al., 1998; Colombi et al., 2009). The idea is to fold the particle distribution by re-applying the periodic boundary conditions assuming a new boxsize $L' = L/f$, where we call f the number of foldings. If L' is large enough to assure that the modes inside the new box are uncorrelated, we can measure in principle the clustering from a new effective fundamental wavenumber $k'_{\rm f} = 2\pi/L'$ up to a new effective Nyquist frequency, given by $k'_{\rm Ny} = \pi N_g/L'$. For instance, by folding the box 4 times, we will get to Nyquist frequency 4 times higher.

In Fig. F.1 we apply this technique to our $512h^{-1}{\rm Mpc}$ simulation, folding the particles up to 6 times, and reaching a $k_{\rm Ny} \approx 2h\,{\rm Mpc}^{-1}$ with a 64^3 and a 128^3 grid for the power spectrum and the bispectrum, respectively. Even using a TSC scheme on interlaced grids, we note that it is safer to use the measurements up to $k = k'_{Ny}/2$ in the bispectrum. Also, the measurement of the largest modes of the folded box are noisy because they are sparsely sampled; for this reason, it is convenient to discard these modes, taking for instance wavenumbers $k > 10k'_{\rm f}$.

Using these precautions, we show in Fig. F.2 that using this technique we can achieve an accuracy well within 1% in the estimation of the ratios, using a small fraction $1 - 10\%$ of the computational resources. Although it is common to use the folding technique to compute power spectra, to our knowledge, this is the first time it has been shown to be accurate for bispectrum measurements.

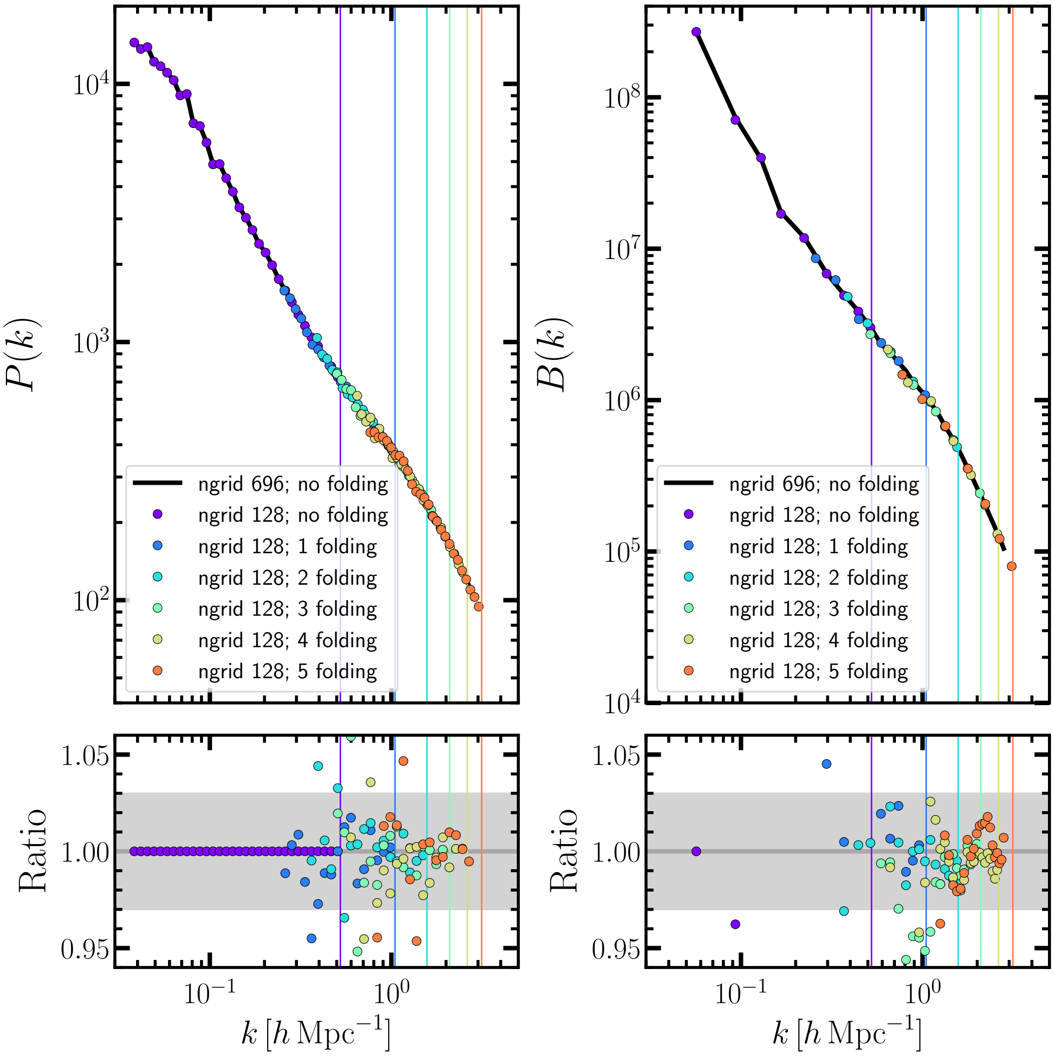

Figure F.1: *Left panels:* Matter power spectrum measured in a 64^3 (interlaced) mesh, folding the box up to 6 times, following the technique explained in the text (coloured dots). For comparison, the matter power spectrum measured with a 696^3 mesh and not folding the box is plotted as a black solid lines. The equivalent Nyquist frequencies for each folded box is plotted as a solid line. In the bottom panel, we display the ratio between the power spectrum measure with a 64^3 and a 696^3 mesh. *Right panels:* Similarly to the left panels, we display the measured bispectra using a 128^3 mesh and the folding of the box, and compare with a not-folded 696^3 mesh.

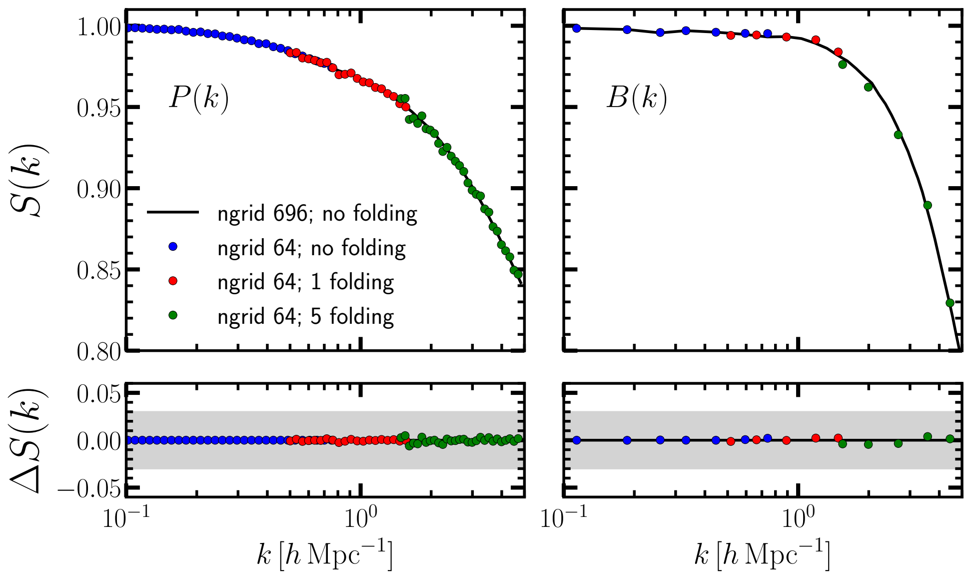

Figure F.2: *Left panels:* Ratio of baryonified and GrO matter power spectra $S(k)$, measured in a 64^3 (interlaced) mesh, folding the particles up to 6 times, following the technique explained in the text (coloured dots). For comparison, the measurements with a 696^3 mesh is plotted as a black solid lines. The equivalent Nyquist frequencies for each folded box is plotted as a coloured solid line. In the bottom panel, we display the difference of the ratios $\Delta S(k)$ measured with a 64^3 and a 696^3 mesh. *Right panels:* Similar to the left panels, but displaying the matter bispectrum instead of the power spectrum.

Appendix G

Impact of cosmic variance

In this Appendix, we explore the expected impact of cosmic variance in our analysis. In particular, in the training process, § 2.3, we feed the Neural Network with power spectra computed by applying the cosmology scaling to a $512h^{-1}\mathrm{Mpc}$ box simulation. Furthermore, in § 5.2.5 we validate the combination of baryonification and cosmology scaling algorithms by using $256\,h^{-1}\mathrm{Mpc}$ simulations. To estimate the expected impact of the cosmic variance, we compare the power spectrum suppression obtained by applying the baryonification to a box of $256\,h^{-1}\mathrm{Mpc}$, $512\,h^{-1}\mathrm{Mpc}$, and $1440\,h^{-1}\mathrm{Mpc}$, while keeping the same mass resolution. We vary four different BCM set of parameters, chosen to reproduce the clustering of EAGLE, Illustris, Illustris TNG-300, and BAHAMAS. We note that, generally, we do not expect the same level of convergence for different baryonic parameter sets. In fact, models with strong feedback, which expel large amount of gas even from very massive haloes, are more dependent on the high-mass end of the halo mass function. Therefore, we expect such models to be more sensitive to the shot noise in the mass function when using small boxes. Nevertheless, as reported in Fig. G.1, we find that in all cases we get results converged at 1%, even when not using the "pairing and fixing" technique. Given that, after the scaling process, our box has typically a size between $300 - 700\,h^{-1}\mathrm{Mpc}$, we are reasonably confident that the cosmic variance have a negligible impact on our predictions.

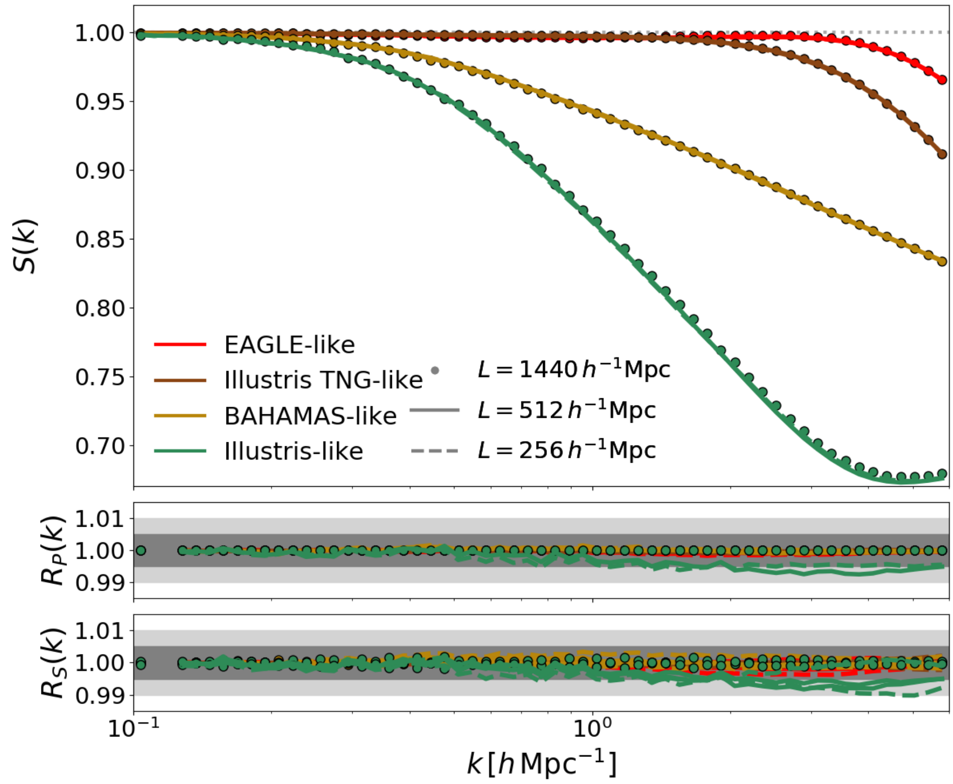

Figure G.1: *Upper panel:* Suppression $S(k)$ in the matter power spectrum caused by baryons as predicted by baryonification in four different scenarios, as reported in the legend. The simulations used are run with the "pairing and fixing" technique to suppress the cosmic variance, and have box sizes of $1440h^{-1}$Mpc (symbols), $512h^{-1}$Mpc (solid lines), and $256h^{-1}$Mpc (dashed lines). *Lower panels:* Ratios of the suppressions $S(k)$ over the suppression predicted by our $1440h^{-1}$Mpc-side box simulation, averaging between two "paired and fixed" simulations (upper panel) and using single realisations (lower panel).

Appendix H

Joint accuracy of cosmology rescaling and baryonification

In this Appendix, we extend the analysis done in §5.2.5 to validate the joint use of cosmology rescaling and baryonification algorithms. In §5.2.5 we have shown the accuracy of our framework when varying a single parameter, here we discuss the case when all the parameters are simultaneously varied. We use a set of 20 cosmological simulations disposed as two random Latin hypercubes of 10 points each, one defined varying the standard ΛCDM parameters, and the other varying all the parameters, included M_ν, w_0, w_a. Similarly to our test suite, these simulations have a box size chosen to match the re-scaled box from a $L = 256 h^{-1}\mathrm{Mpc}$ simulation, while keeping the same mass and force resolution. We refer to the Appendix A of Contreras et al. (2020a) for more details on these simulations. We measure the power spectra of these simulations after applying to each of them 4 different baryonification models, which mimic the clustering of the BAHAMAS, EAGLE, Illustris and Illustris TNG hydrodynamical simulations. Similarly, we measure the power spectra after applying the same baryonification models on a set of simulations obtained rescaling our main `bacco` simulations to the cosmologies of the Latin hypercubes. We display the comparison between these two sets of power spectra in Fig.H.1. We find that in most of the cases, the accuracy is within 1%, with few extreme models being within 2%. This results are in broad agreement with what found in §5.2.5, and thus support the robustness and reliability of our framework.

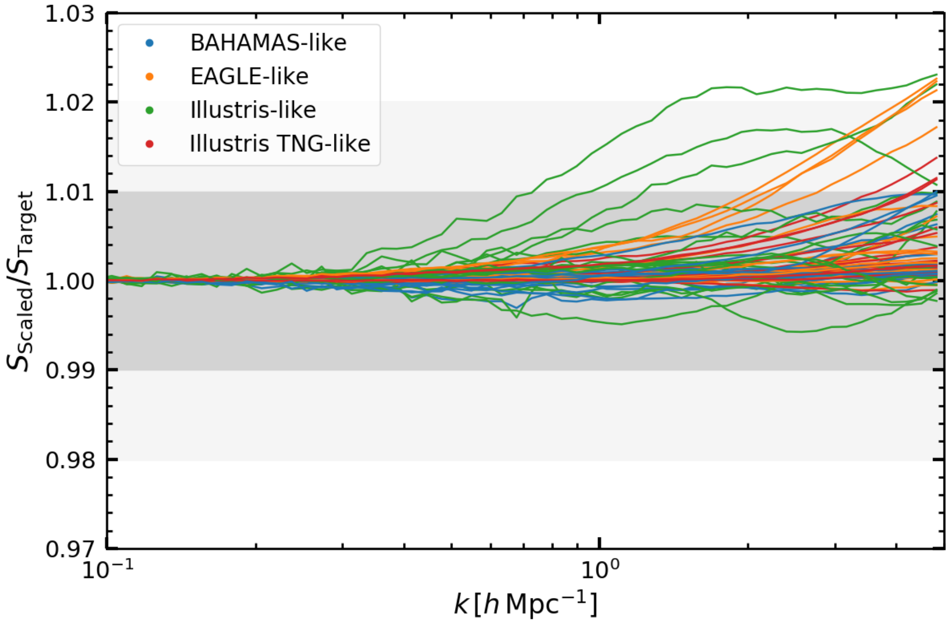

Figure H.1: Accuracy of the cosmology rescaling algorithm with baryonification at $z = 0$. We display the ratios of $S \equiv P_{\mathrm{bcm}}/P_{\mathrm{GrO}}$ estimated on a simulation whose cosmology has been rescaled (S_{scaled}) over the same quantity but computed on a simulation carried out directly with the target cosmology S_{target}. We test 20 cosmologies, and 4 baryonic models for each cosmology. Different colours show the results adopting 4 different baryonification parameter sets consistent with the modifications predicted by different hydrodynamical simulations, according to the legend. The grey bands highlight 1% and 2% accuracy in the resulting "baryonified" power spectrum.